STUDIES ON STRUCTURAL, OPTICAL, DIELECTRIC AND MAGNETIC PROPERTIES OF ALKALI AND TRANSITION METAL DOPED TIN SELENIDE

THESIS

SUBMITTED IN PARTIAL FULFILMENT OF THE REQUIREMENTS FOR THE AWARD OF THE DEGREE OF

DOCTOR OF PHILOSOPHY

IN

PHYSICS

BY

NERELLA MANJULA

[ROLL NO: 701639]

UNDER THE SUPERVISION OF

Prof. B. SOBHA

DEPARTMENT OF PHYSICS

NATIONAL INSTITUTE OF TECHNOLOGY

WARANGAL-506004, TELANGANA, INDIA

DECEMBER-2022

DEDICATED TO

MY PARENTS & TEACHERS

DECLARATION

This is to certify that the work presented in the thesis entitled "**STUDIES ON STRUCTURAL, OPTICAL, DIELECTRIC AND MAGNETIC PROPERTIES OF ALKALI AND TRANSITION METAL DOPED TIN SELENIDE**" is a bonafide work done by me under the supervision of Prof. B. Sobha, and was not submitted elsewhere for the award of any degree.

I declare that this written submission represents my ideas in my own words and where others' ideas or words have been included, I have adequately cited and referenced the original sources. I also declare that I have adhered to all principles of academic honesty and integrity and have not misrepresented or fabricated or falsified any idea/data/fact/source in my submission. I understand that any violation of the above will be a cause for disciplinary action by the Institute and can also evoke penal action from the sources which have thus not been properly cited or from whom proper permission has not been taken when needed.

N. Manjula

Nerella Manjula
(Roll No. 701639)

Date: 26/12/2022.

i

CERTIFICATE

This is to certify that the work presented in the thesis entitled "**STUDIES ON STRUCTURAL, OPTICAL, DIELECTRIC AND MAGNETIC PROPERTIES OF ALKALI AND TRANSITION METAL DOPED TIN SELENIDE**" is a bonafide work carried out by **Mrs. Nerella Manjula (Roll No. 701639)** under our supervision and was not submitted elsewhere for the award of any degree.

B. Sobha

Prof. B. SOBHA
Research supervisor
Professor
Department of Physics
National Institute of Technology
Warangal

Date: 26/12/2022.

ii

ACKNOWLEDGEMENTS

First and foremost, I'd like to express my gratitude to the Almighty for providing me with this opportunity, strength, and good health to complete all of my research work without difficulty.

I express my heartfelt gratitude to my supervisor, Prof. B. Sobha, Department of Physics, National Institute of Technology Warangal, for her guidance, unrelenting support, and motivation, which encouraged me to progress and complete my Ph.D. Her valuable advice and conversations always helped me to focus and achieve the purpose of this study.

I thank Prof. N. V. Ramana Rao, Director, NITW for allowing me to pursue my Ph. D in this reputed institute.

I also thank Prof. T. Venkatappa Rao, Head, Department of Physics, NITW for providing the necessary support during my Ph. D tenure. I would also like to take this opportunity to express my gratitude to the former heads of the Department of Physics at NITW for their invaluable assistance and support.

I ought to show my thankfulness to my Doctoral Scrutiny Committee members, Prof. P. Syam Prasad, Dr. Kusum Kumari, and Prof. T. D Gunneshwar Rao (Department of civil engineering), for their insightful comments and suggestions that aided the progress of my Ph. D work.

I am thankful to farmer faculty members of our department, Prof. M. Sai Sankar, Prof. R. L. N. Sai Prasad, Prof. L Ram Gopal Reddy, and Prof. K.V.G. Reddy for their encouragement and support.

I extend my sincere gratitude to the faculty members, Prof. D. Dinakar, Prof. P. Abdul Azeem, Prof. Sourabh Roy, Prof. K. Thangaraju, Prof. D Haranath, Dr. D. Paul Joseph, Dr. V. Jayalakshmi, Dr. R. Rakesh Kumar, Dr. K. Uday Kumar, Dr. Vijay Kumar, Dr. Surya K. Ghosh, Dr. Hitesh Borkar, Dr. Aalu Boda, Department of Physics, National Institute of Technology, Warangal for their valuable advice, encouragement and moral support in my career.

I especially thank Dr. Madireddy Buchi Suresh, Scientist-F, ARCI Hyderabad, for his guidance, support, and motivation throughout my Ph. D thesis work. His extensive research ideologies have always inspired me to approach a scientific problem in a significant and simple manner.

I express my sincere thanks to MHRD, New Delhi for the financial support in the form of a fellowship.

I thank the Head, UGC-NRC, School of Physics, the University of Hyderabad for allowing me to utilize the FESEM facility. I thank the head, of SRM-NRC, Chennai, Tamilnadu for allowing me to utilize the UV-DRS and VSM characterization facility.

I would also like to acknowledge the TEM FACILITY, STIC Thiruvananthapuram and CENS Bangalore.

I thank the head, of OU FOR XPS facility.

I thank the Director, ARCI Hyderabad for the dielectric measurement facility.

I am also indebted to the following friends and research colleagues for various reasons related to my Ph. D work, all of whom deserve special mention: Dr. P Kishore, Dr. S. Raj Kumar, Dr. V. Himamaheshwar Rao, Dr. Ashish Kumar, Dr. PVN Kishore, Dr. Harikrishna, Dr. M. Mohan Babu, Dr. R. Ramarajan, Dr. M. Shiva Prasad, Dr. Macherla Nagaraju, Dr. N. Purushotham Reddy, Dr. Lalsingh Guguloth, Dr. Gnyaneshwar Dasi, Mr. B Ramesh, Dr. Akshay Kranth, Ms. Mahalakshmi, Ms. T Lavanya, Mrs. Ramadevi, Mr. R. Muniramaiah.

I also thank my research colleagues from other departments, Dr. Mohammad Ali, Mr. Shiva Kumar, and Dr. Abhey Ram Nithin for their help in the research work.

I also express my thankfulness to all other present and past research scholars of the Department of Physics NITW and all the teaching and non-teaching staff of the Dept. of Physics for their constant support during my Ph.D.

I express my special thanks to Dr. Bunty Rani Roy from Kakatiya University, who motivated me to study Ph.D.

I take this opportunity to show my deepest gratitude to my gurus from my schooling to till today for not only educating me and also making me strong enough to face the challenges encountered during my entire life.

I am infinitely indebted to my loving parents Mrs. Nerella Bhagya Lakshmi and Mr. Nerella Thirupathi, without their motivation I would not have been what I am. Their unconditional love and affection always inspired me to achieve my goals and gave me the strength and confidence to complete impossible tasks more than my strength, including my Ph.D. I always remember and cherish the encouragement and inspiration provided by my mother and father during my research work.

I would like to thank my sister Mrs. Tejaswi (Padma), and brother-in-law, Mr. Suresh, and also I thank my brother Mr. Vinay Kumar, and Sister-in-law Mrs. Keerthy (Anusha) for their moral support. Special thanks to my son and daughter, Sriman, Aadyasri, and nephew Rudraved for making me happy, relaxed, and feel fresh all the time to pursue my research work with full of confidence.

Finally, I'd like to express my deepest gratitude to my soul mate Dr.M.Nagaraju for his constant support, healthy discussions about the research problem, and for lifting my confidence with his motivational words and lots of love to my baby daughter Kumari Jaisvika, who recently arrived in our life.

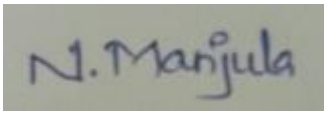

NERELLA MANJULA

Date: 26/12/2022.

ABSTRACT

Recently metal chalcogenide semiconductors have attracted extensive importance in different fields due to their exceptional electrical and magnetic properties. Among them, the IV-VI metal chalcogenide with precise dielectric and magnetic properties are in good demand for several microelectronic and spintronic applications. Tin Selenide (SnSe) is the most promising material among all of the above, due to its extraordinary physical and chemical properties. Doping of suitable elements into SnSe can alter electrical and magnetic properties. Hence in this regard, the present thesis focussed on the synthesis of alkali (Na, K) and transition (Co, Fe) doped Tin Selenide (SnSe) polycrystals using hydrothermal method. The alkali metals, Sodium (Na) and Potassium (K) will effectively tune the concentration of charge carriers thereby affecting the electric and dielectric properties of the host lattice SnSe. The transition metals, Cobalt (Co) and Iron (Fe) doping into SnSe will induce magnetism which is useful for spintronic applications. The dielectric properties of alkali and transition metal doped SnSe were investigated from room temperature to 523 K in a frequency range of 100 Hz- 12 MHz. Among all the dopants, $Na_{0.20}Sn_{0.80}Se$ exhibited good dielectric properties such as high dielectric constant ($1.35x10^{10}$) and AC conductivity at 523 K. The variation of frequency exponent 's' in all the doped samples showed that Correlated Barrier Hopping (CBH) is the probable mechanism for the hopping of charge carriers in all the samples. Electrical modulus studies for all the alkali and transition metal doped SnSe showed a single semi-circular arc indicating a non-Debye type relaxation mechanism. The values of dielectric parameters will find promising applications of the alkali and transition metal doped SnSe in microelectronic, capacitive storage, electro-optic, and high-frequency related devices. Room temperature ferromagnetism is observed in both the Co and Fe doped SnSe. The $Co_{0.10}Sn_{0.90}Se$ (0.1342 emu/g) and $Fe_{0.10}Sn_{0.90}Se$ (0.14087 emu/g) have obtained large saturation magnetization values respectively. These transition metal-doped SnSe polycrystals have applications in data storage and spintronic devices. The cost-effective hydrothermally synthesized alkali (Na, K) and transition (Co, Fe) metal-doped SnSe polycrystals are promising candidates for microelectronic and Spintronic device applications.

TABLE OF CONTENTS

LIST OF ABBREVIATIONS & SYMBOLS

DS	Dielectric Spectroscopy
DMS	Diluted Magnetic Semiconductors
TM	Transition Metals
RKKY	Ruderman–Kittel–Kasuya–Yosida (RKKY) Interaction
BMP	bound magnetic polaron
E	Electric field
ε'	Dielectric constant
ε''	Dielectric Loss
C	Capacitance
C_o	Capacitance of free space
ε_o	Absolute permittivity
A	Cross sectional area
d	Thickness of the pellet
tan δ	Dielectric loss tangent
σ_{ac}	AC conductivity
σ_{dc}	DC conductivity
s	Frequency exponent factor
E_a	Activation energy
W_m	Maximum barrier height
k_B	Boltzmann constant
M'	Real part of electric modulus
M''	Imaginary part of electric modulus
M_s	Saturation magnetization
H_C	Coercivity
M_R	retentivity
SnSe	Tin Selenide
$Na_xSn_{1-x}Se$	Sodium doped Tin Selenide
$K_xSn_{1-x}Se$	Potassium doped Tin Selenide
$Co_xSn_{1-x}Se$	Cobalt doped Tin Selenide
$Fe_xSn_{1-x}Se$	Iron doped Tin Selenide
CdTe	Cadmium Telluride
CIGS	Copper Indium Gallium Selenium

ZnTe	Zinc Telluride
Cds	Cadmium Sulphide
CdSe	Cadmium Selenide
GaAs	Gallium Arsenide
InAs	Indium Arsenide
SnS	Tin Sulphide
TiO_2	Titanium Oxide
ZrO_2	Zirconium Oxide
SnO_2	Tin Oxide
$SnCl_2.2H_2O$	Tin Chloride dihydrate
$CoCl_2.6H_2O$	Tin Chloride hexahydrate
$FeCl_2.4H_2O$	Tin ChlorideTetrahydrate
NaCl	Sodium Chloride
NaOH	Sodium Hydroxide
KOH	Potassium Hydroxide
KCl	Potassium Chloride
$NaBH_4$	Sodium Borohydrate
SeO_2	Selenium dioxide
EDTA	Ethylenediaminetetraacetic acid
XRD	X-Ray Diffraction
FESEM	Field Emission Scanning Electron Microscopy
EDAX	Energy dispersive X-ray Analysis
UV-Vis-NIR DRS	Ultra Violet-visible-near infrared Diffuse Reflectance Spectroscopy
HRTEM	High-Resolution Transmission Electron Microscopy
XPS	X-Ray Photoelectron Spectroscopy
B.E.	Binding Energy
K.E.	Kinetic energy
VSM	Vibrating Sample Magnetometer
mg	Milli gram
ml	Milli liter
L	Litre
DI	Deionized

M	Molarity
kg	kilogram
cm	centimetre
g	gram
^{o}C	Degree centigrade
MPa	Mega Pascal
Hz	Hertz
DI water	Deionized water

LIST OF FIGURES

CHAPTER 5

LIST OF TABLES

CHAPTER 1: Introduction

1.1 IV-VI metal chalcogenides

Semiconductor materials are now the pillars of advanced technology. There would be no electronics, photonic, or fiber optic communication industries without them. There is little advanced optical equipment available, and there are some significant gaps in conventional manufacturing engineering. The advancement of semiconducting material synthesis and epitaxial technology is in high demand due to its critical role in the progress of numerous important areas such as the fabrication of high-efficiency photovoltaic cells and detectors for alternative energy and medicine, as well as the production of light emitting diodes. Many metal chalcogenides, which are metal and non-metal compounds containing S, Se, or Te, are important in new technologies. These "high-tech" chalcogenides have numerous applications. The rapidly expanding field of applied material science requires materials to be affordable, non-toxic, environmentally benign, simple to synthesis, and highly competitive in performing specific tasks. Due to their use virtually in every industry, versatile materials have recently attracted a lot of attention. Group IV-VI monochalcogenide materials have demonstrated considerable potential for applications in energy, electrical, and optoelectronic devices. Research in these areas is a fast-expanding field of study. In recent times, the IV-VI metal chalcogenide semiconductors have attained great research importance due to their novel physical and chemical properties. These properties of IV-VI metal chalcogenides have resulted in diverse applications in several fields such as thermoelectric [1,2], solar cells [3,4], Li-ion batteries [5], supercapacitors [6], photo catalysis [7,8], optoelectronics [9], phase-change memory devices [10], and photovoltaic [11]. The IV-VI metal chalcogenide semiconducting materials with precise dielectric properties are in good demand for several electronic, optoelectronic, and solar cell device applications [9,12,13]. Among IV–VI layered compounds, Tin Selenide (SnSe) has attracted considerable attention on account of its semiconducting, anisotropic, and optical properties.

1.1.1 Tin Selenide (SnSe)

Tin Selenide (SnSe) is non-toxic, inexpensive, and available abundantly on the earth. It is a narrow band gap p-type semiconductor material having indirect (0.9 eV) and direct band gaps (1.3 eV) respectively [14]. SnSe has a layered orthorhombic structure with *pnma* space group at room temperature and undergoes a phase transition to the *cmcm*

space group at 800 K. The phase diagram and crystal structure of SnSe is given in fig. 1.1 [15]. Its crystal structure is similar to SnS. SnSe also possesses a very high absorption coefficient and hence can be used in various applications, such as in the fabrication of high-performance electronic devices and as an absorber layer in solar cells to replace other toxic and expensive absorber layers like CdTe and Copper Indium Gallium Selenium (CIGS). Tin selenide is found in two forms: SnSe and $SnSe_2$. SnSe has two crystallographic phases, orthorhombic (α-SnSe) and cubic (π-SnSe), and $SnSe_2$ has a hexagonal crystal structure [12]. The π-SnSe material is mechanically stable and energetically comparable to α-SnSe and has already shown potential in the piezoelectric application [15]. SnSe exhibits extreme anisotropy in its lattice vibrational, optical, and electronic properties and perhaps shows some characteristic features of the two-dimensional or layer-type semiconductors [2,16]. Some researchers have observed another phase, Sn_2Se_3, but this phase is the superposition of SnSe and $SnSe_2$ [17].

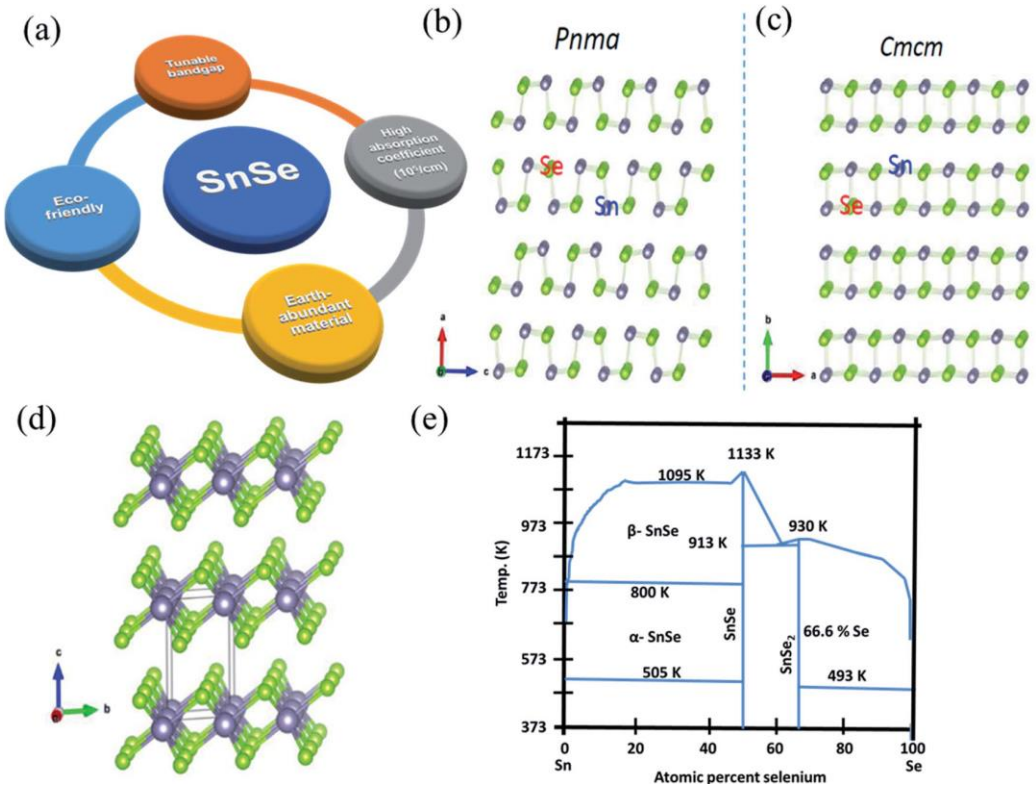

Figure 1.1 Crystal structure and phase diagram of SnSe. This figure is adapted from ref.15.

Tin selenide has proven to be versatile in a variety of applications, including topological insulators, photodetectors, phase change memory, gas sensor, solar cells, photocatalysis, and thermoelectric. These applications heavily rely on the SnSe characteristics (optical, electrical and micro-structural, etc.). Material synthesis techniques, in addition to material attributes, are crucial for producing high-quality materials. Doping is an important parameter to improve the physical properties of semiconductors and results in

remarkable effects compared to undoped material. SnSe exhibits a p-type electrical conductivity and its conductivity can be altered by using different dopants such as Na, K, Ag, Cu, Zn, La, Bi, Co, Fe etc.,. SnSe can be prepared by traditional fabrication techniques such as melting and mechanical alloying. However, it is challenging to achieve morphological control of the prepared SnSe products. Advanced aqueous synthesis-based solution techniques have been successfully applied to polycrystalline SnSe to address this problem and are one of the most practical ways to produce SnSe polycrystals. Advanced aqueous synthesis-based solution approaches provide distinct benefits over conventional melting and mechanical alloying methods, including convenient morphological control to produce high anisotropy and remarkable high doping solubility. A specific number of aqueous solution methods have been developed to prepare SnSe polycrystals are:

1.1.1.1 Co-precipitation method

In this method a salt precursor (chloride, nitrite etc.) is dissolved in water or other solvents to precipitate the oxohydroxide form with the help of a base. The resulting chloride salts are subsequently rinsed away. Only metal hydroxide may occasionally precipitate; this metal hydroxide is then calcined to produce the final powder after filtration and washing. One disadvantage of this method is the difficulty to control particle size distribution.

1.1.1.2 Facile Surfactant-Free Synthesis

This approach is used because the substance can be synthesised without surfactants. On the other hand, the procedures using organic surfactants or solvents have extremely low yields, i.e., milligram amounts of materials, whereas the surfactant-free synthesis can produce high yields, i.e., nanoparticles in gram quantities.

1.1.1.3 Solvothermal Method

Solvothermal process incorporates the chemical reaction under high pressure (ranging between and low temperature within an enclosed system with the existence of non-aqueous solvent. It is engrossing to note that the desired powder can be derived directly from the solution in contrary to other methods. This technique is significantly effective in the preparation of the materials containing well defined and distinct geometrical shape (0D, 1D, 2D and 3D). Such morphologies have been regulated by using the appropriate surfactant at monitored pH. This identical process is presumed to be hydrothermal if the non-aqueous solvent is replaced with water. It proves to be an excellent solvent for ionic compounds as well as can dissolve non-ionic compounds even under the influence of high pressure along with the suitable temperature. Various

solvents possess different characteristics, such as boiling point, vapor pressure, and solubility of precursors.

1.1.1.4 Hydrothermal Method

Water is used as the solvent in the hydrothermal technique of material preparation, which can dissolve, react, and crystallize precursors like the conventional aqueous solution route. The difference is that hydrothermal reactions take place at high pressures and temperatures, typically above the point at which water begins to boil. This allows for a high vapour pressure, which in turn enables the reaction to fulfill certain essential conditions. As a result, post-treatment is applied to the synthesized products, which includes washing, drying, and separation. In a typical hydrothermal synthesis, a water solution is utilized as the reaction medium in a specialized closed reaction vessel (autoclave) to produce a high-temperature (>100 °C), high-pressure (1-100 MPa), reaction environment by heating the reaction vessel, causing the typically insoluble precursors to be dissolved, reacted, and/or converted.

We chose the hydrothermal method over the other methods because of its advantages, including complete crystal growth, controllable crystal size, uniform distribution, weak agglomeration, significant efficiency, competitive productivity, and increased cost-effectiveness due to the use of relatively inexpensive raw materials, as well as ease of achieving the desired stoichiometry and crystal form at a much lower temperature.

Part-I:

1.2 Dielectric Spectroscopy

Dielectric Spectroscopy (DS) is a powerful and easy tool used to investigate dielectric properties of materials as a function of frequency which is based on the interaction of electric dipole moment with an external field. We have chosen this technique for investigating the electrical properties of alkali and transition metal doped SnSe because of its sensitivity to any weak change in structure and dynamics. This technique operates in a wide range of frequencies (10^{-6} - 10^{12} Hz); however, all frequency ranges have not been equally available for measurement as it requires complex and expensive equipment. The study of dielectric properties of nano-sized materials is important for both fundamental and application-oriented research. Grains and grain boundaries present in nano-sized materials play important role in determining their electrical properties. The majority of atoms are present in the grain boundary or within a few atomic layers of it. The interface regions are bound to have a high

concentration of vacancies, vacancy clusters, dangling bonds, and other properties that can control the properties of these materials. In the writing of this section of the thesis, we aim to demonstrate some of the basic concepts used to explain the dielectric properties of investigated samples. Depending upon the nature of the given material, there are four types of polarizations [18].

1.2.1 Types of polarizations

i. Space charge/interfacial polarization

Space charge or interfacial polarization appears in those dielectric substances in which the charge carriers can travel to some distance inside the material and as a consequence it macroscopic field gets distorted. This type of polarization is the only kind that involves macroscopic charge transport. In this polarization, charges are accumulated at the interface of the two materials, the interface of two regions of the same material (grain boundary), and the material-electrode interface. This polarization is further divided into hopping and interfacial polarizations. The hopping mechanism of polarization is observed due to the hopping of localized charge carriers from one site to another inside the dielectric material. The interfacial polarization is caused by the external electric field via the separation of positive and negative charges. The interfacial/space polarization usually appears in the polycrystalline/amorphous materials and at the lower frequency side.

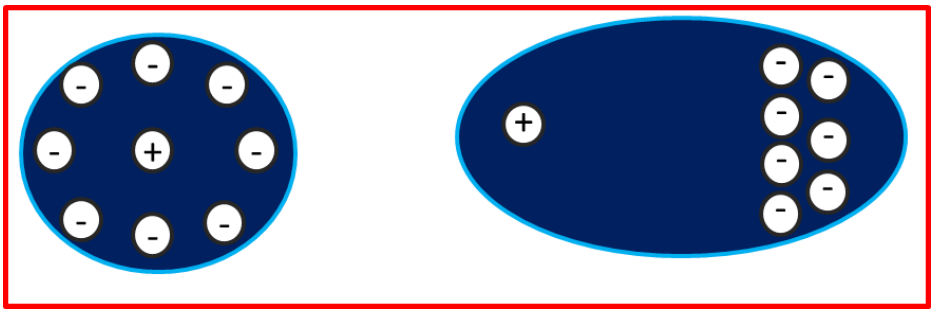

Figure 1.2 Schematic representation of Space charge polarization.

ii. Orientation/dipolar polarization

This kind of polarization happens in materials having permanent dipole moments. In the absence of an electric field, the thermal agitation arranges the dipoles in a way to cancel out the dipole moment. As a result of this, the net dipole moment of the material becomes zero. But under the effect of an external electric filed, the dipoles get orientated in the direction of the applied field giving rise to the net dipole moment and this type of polarization is known as orientation (dipolar) polarization. The dipole polarization is limited to the microwave frequency domain and shows inverse temperature dependence.

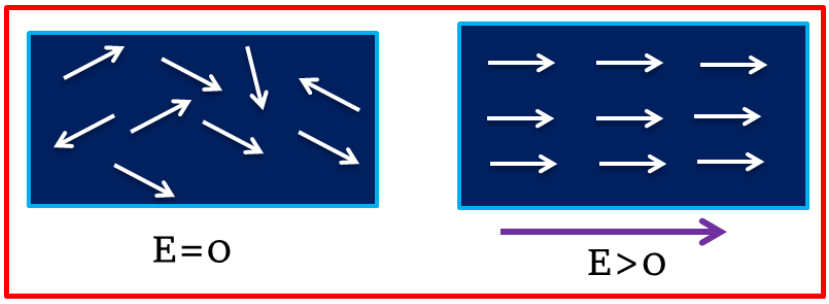

Figure 1.3 Schematic representation of orientation polarization.

iii. Ionic polarization

Ionic polarization exists in molecular crystals in which the constituent atoms are connected via ionic bonding. In the absence of an external field, these ionic crystals have zero net polarization as the dipole moments of the positive and negative ions cancel each other. But under the external field, the ions get displaced from their equilibrium positions giving rise to the induced polarization which is known as ionic polarization. The ionic polarizability is often 10 times larger than the electronic polarizability, as a result, the ionic materials are known to have high dielectric constant. Ionic polarization is temperature independent and active below infrared frequency domain.

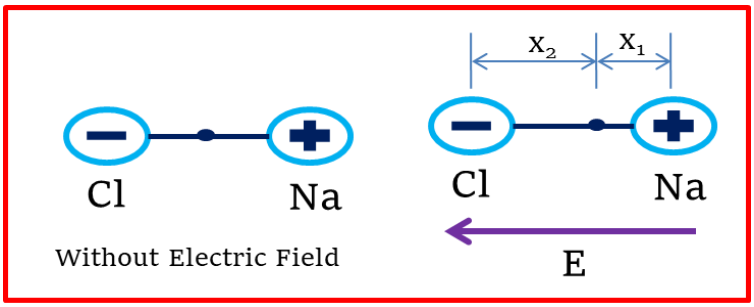

Figure 1.4 Schematic representation of ionic polarization.

iv. Atomic/electronic polarization

Electronic/atomic polarization is observed in all dielectric materials and is a microscopic polarization, which is found to be the most fundamental polarization mechanism shown by dielectric materials. Electronic polarization appears when a dielectric material is subjected to an external electric field. Then the center of charge of the electron cloud and positively charged nucleus get displaced from their original positions which leads to the generation of induced dipoles and thus gives rise to electronic polarization. This polarization is also temperature independent and active in almost the entire frequency domain.

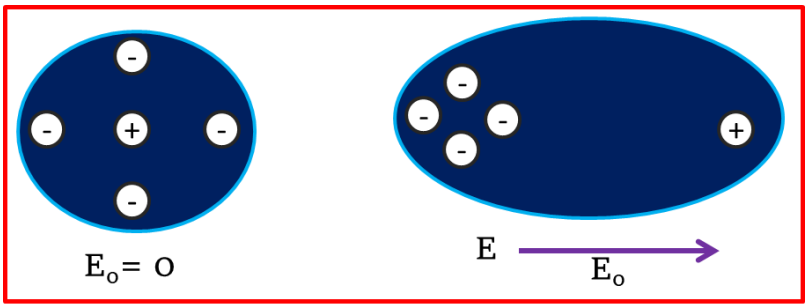

Figure 1.5 Schematic representation of atomic polarization.

1.2.3 Applications of dielectric materials

High dielectric materials are of greater technological importance due to their potential in integrated electronic devices, tuneable microwave devices applications, and as bypass capacitors in microelectronics and energy-storing devices [19]. Capacitors are crucial components in electrical and electronic circuits because they perform a variety of tasks, such as blocking, coupling, and decoupling, separating AC from DC, filtering, adjusting power factors, and storing energy.

Part-II

1.3 Spintronics-Brief history

In the current era of technology, the advancement of developing functional magnetic semiconductors is much needed to bring revolutionary changes in designing and fabrication of a device. In conventional integrated circuits and high-frequency devices, capacitors and semiconductors used the charge to process binary digits of information (0 and 1). Magnetic recordings, on the other hand, stored information using spin alignments. These separate processes used to necessitate a lot of energy and space. Later, using the charge and spin magnetic moments of the electron, the researchers were able to combine the electrical and magnetic properties in a single device. The association of the charge with the spin has thus given rise to a new intrinsic property called spintronic property, which has greatly alleviated the issues of high energy consumption and bigger size. These devices are based on spin transport electronics and require little space, little energy, and function quickly like in spin-dependent transport structures. To produce exceptional modernistic sturdy gadgets, spintronics includes spin transport of electronics.

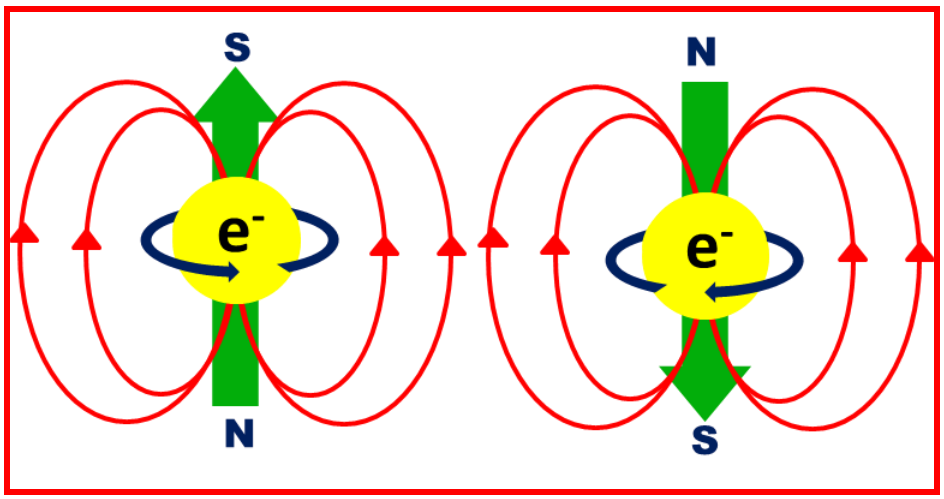

Figure 1.6 Schematic representation of electron's behavior as a tiny magnet.

1.3.1 Diluted Magnetic Semiconductors

Diluted magnetic semiconductors (DMS) are semi-magnetic semiconductors with a lattice that contains some substitutional magnetic atoms. The exchange interaction between the spins of the dopant atoms and the carriers in the semiconductor host is expected to produce ferromagnetic order throughout the lattice. Spintronics, also known as magneto electronics, is a new technology that uses the electron's intrinsic spin as well as its associated magnetic moment, in addition to its fundamental electronic charge. There is a boundless search for new dilute magnetic semiconductors that are ferromagnetic at ambient temperature due to their promising spintronic applications. DMS can be employed for information processing and data storage functionalities. They also can be used in multifunctional fields such as optical, gas sensing, and optoelectronic devices.

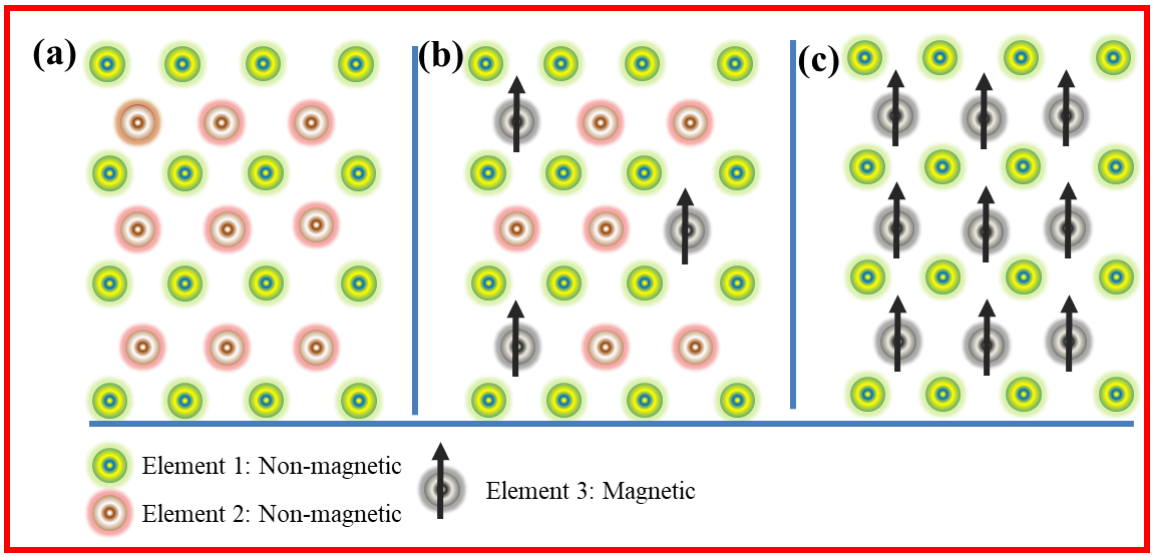

Figure 1.7 (a) A non-magnetic semiconductor, **(b)** a magnetic semiconductor; and **(c)** a diluted magnetic semiconductor. The two types of circles represent the two different atoms making up the compound semiconductor.

To achieve control upon both electronic charge and spin, the II-VI, II-V, III-V, and IV-VI binary compounds can be doped by transition metals which will further influence the electrical and magnetic properties over applied external electric fields. In particular, nowadays research has been focussed on the transition metal doped IV-VI semiconductors which can exhibit carrier concentration changes by way of governing native defects and also can be utilized to manipulate ferromagnetism. Among the IV-VI semiconductors, Tin Selenide (SnSe) is an important material because of its unique properties. DMSs are classified into different groups such as

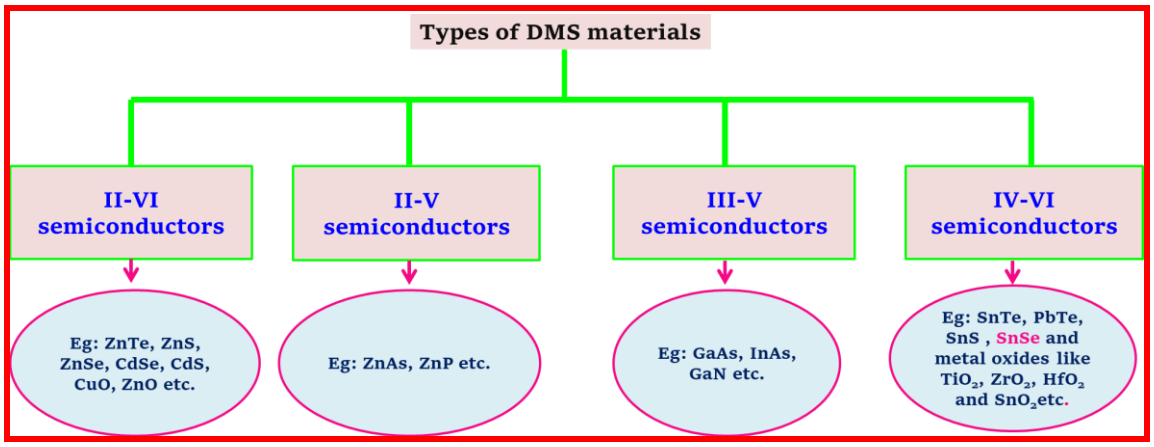

Figure 1.8 Schematic representations of different DMS materials.

1.3.2 Models explaining ferromagnetism in DMS

Since the discovery of DMSs, several different theoretical models have been proposed to explain the origin of ferromagnetism in DMSs, but the true nature of the mechanisms responsible for its origin is not fully understood and explained even today.

Amongst many few of the most commonly used theoretical models that have been used to explain ferromagnetism in DMSs are summarized as:

1.3.2.1 Direct Exchange Interaction

These interactions are short-range couplings between magnetic atoms that are robust magnetic interactions. According to Mathias Getzlaff (2008) [20], these interactions are possible between very close magnetic atoms when their wave functions overlap due to minimal columbic interactions. When two magnetic atoms are very close together, there is a high probability that an electron will pass between the two nuclei. If the electron spins are anti-parallel it is understood as negative exchange (antiferromagnetism) and if electron spins are in parallel then it is understood to result in positive interaction (ferromagnetic interaction). The balance between the kinetic and columbic energy determines the value of this interaction.

1.3.2.2 Indirect Exchange interaction

An indirect exchange couple spins over a long distance. Metal electrons overlap with an intermediate medium for each other. The medium for these indirect exchange interactions is lattice defects or conduction band electrons.

i. Super exchange Interaction

The magnetic interactions between d electrons of transition metal ions are mediated by the intermediate anions. This is known as a superexchange interaction. Because of the sp-d exchange interaction, based on their spin orientation, the electrons in the valence band will be attracted or repulsed by a given magnetic ion. If the band is completely filled, this causes a spatial separation between spin-down and spin-up electrons. This separation causes anti-ferromagnetic interactions between neighbouring localized spins. The super exchange interaction explains the coupling of nearest neighbouring transition metals via a shared cation. The 'p' and 'd' orbitals are completely filled by virtual hopping.

ii. Double Exchange Interaction

This interaction occurs when the width of the carrier band (W) is less than the exchange energy, which is typical for bands originating from d states. As observed in another study by Zener[21], spin ordering enables carrier hopping over the d states, the ferromagnetic transition is driven by a decrease in carrier energy caused by an increase in carrier band (W). As a result, spin ordering is always accompanied by a significant rise in conductivity, resulting in colossal magneto resistance, which is normally greater in magnitude than the giant magneto resistance, as observed in multilayer magnetic metals. The interaction between distinct oxidation states of cation in a medium of non-magnetic anion is known as double-exchange interaction. In 1951, Zener proposed the Double-exchange interaction mechanism using Mn^{4+} O^{2-} Mn^{3+}[21]. The electron shifts from the Mn^{3+} ion to the nonmagnetic anion, then to the Mn^{4+} cations.

iii. Ruderman–Kittel–Kasuya–Yosida (RKKY) Interaction

Above mentioned theoretical models have been used frequently to explain the origin of expected magnetism where carrier concentrations are not so high. In contrast to this, if the available carrier concentration is sufficiently high, as in the case of a metallic system, the carrier-mediated exchange interactions (Ruderman–Kittel–Kasuya–Yosida (RKKY) interaction) are found more reliable. The indirect exchange coupling between the magnetic ion and the band electrons is described by the Ruderman-Kittel-Kasuya-Yoshida (RKKY) mechanism. Interactions between delocalized band electron conduction and localized electrons in the d or f shells. The electrons in the conduction

band interact with magnetic ion electrons and become magnetized as a result of the interactions. Polarized electrons oscillate, inducing an antiferromagnetic behaviour of ferromagnetic interactions. In the end, a long-distance exchange interaction leads to net magnetization in the entire system. The distance between magnetic ions determines whether they are ferromagnetic or anti-ferromagnetic.

1.3.2.3 Bound magnetic polarons

The concept of the bound magnetic polaron (BMP) model was first proposed by Torrance et al. (1972) [22]. This model was developed to explain the low-temperature metal-to-insulator transition in oxygen-deficient EuO compounds. In this case, oxygen acts as an electron donor, and electron trapping in oxygen vacancies retains the insulating nature. The orbital of the host lattice orbital is occupied by the trapped electrons, and the magnetic polarons cause long-range exchange interactions between the cation and oxygen vacancies. The weak interaction between nearest neighbouring polarons seems to be a paramagnetic exchange interaction. This model explains the formation of bound magnetic polarons as the result of the exchange interaction between many localized transition metal ion spins and a much smaller number of weakly localized charge carriers. When more than two or more neighbouring magnetic polarons overlap each other, it directs to a long-range ferromagnetic ordering, and when the polaron size equals the sample size, the ferromagnetic transition occurs. According to Coey [23] (Coey, J. M. D. et al., 2005) when this model is applied to diluted magnetic semiconductors, the shallow donor electrons trapped by the vacancies tend to form bound magnetic polarons within their hydrogenic orbits, which mediate the ferromagnetic exchange coupling of transition metal ions in n-type diluted magnetic semiconductors.

1.3.3 Applications of DMS

The DMS materials are used to work as functional materials which can transport spin and electrons at room temperature, namely spintronics. It is possible to transfer reading and writing information using spin rather than by charge. And also the possible applications of DMS include magnetic sensors and actuators, and integrated magnetic electronic and optical devices.

1.4 Literature review related to dielectric properties of SnSe

The research reported till now related to dielectric properties of SnSe-based thin films and single crystals only [24,25]. For example, Solanki et.al. reported the dielectric properties of pure SnSe nanoparticles using chemical precipitation method and Te doped SnSe using direct vapor transport technique [26,27]. In literature, researchers

have studied the dielectric properties of various metal chalcogenide semiconductors which include SnS nanoparticles [28], SnS doped with Co, Fe and Ni [29–31], PbS and PbTe nanomaterials [32], PbS nanostructures[33],[34] Two-dimensional lead sulfide nanosheets [34], MC-PbS polymer nanocomposite films [35], PbS nano sheets with Ni doping [36], CdS nano particles [37], Bi_2S_3 [38] and NiS_2 [39] nano particles which are excellent materials for dielectric applications. Tin Selenide (SnSe) is the IV-VI layered semiconductor that is well-studied for thermoelectric applications. Several research works have been reported for the thermoelectric properties of Na, K-doped SnSe [40–49]. However, there is no sufficient literature regarding the dielectric properties of pure SnSe, alkali, and transition metal doped SnSe.

S.No	Material	Method of preparation	Property		Reference
			Dielectric constant (order of)	AC conductivity (order of) (S/m)	
1	PbS and PbTe nanomaterials	Hydrothermal method	10^5-10^7	10^{-3} to 10^{-5}	[32]
2	PbS nanostructures	Surfactant-assisted reflux synthesis	10^4-10^9	-	[33]
3	Two-dimensional lead sulphide nanosheets	solid state reaction method	10^4	10^{-2}	[34]
4	MC-PbS polymer nanocomposite films	In situ chemical reduction	10^4	10^{-3} to 10^{-4}	[35]
5	PbS nano sheets with Ni doping	solid state reaction method	10^2	10^{-3}	[36]
6	Co-doped SnS	Co-precipitation	10^5	0.6	[29]
7	$Sn_{1-x}Ni_xS$ (x_{Ni}=0–10)	Co-precipitation	10^5	0.9	[31]
8	Fe doped SnS	Co-precipitation	10^5	0.5	[30]

9	Tin Sulphide nano particles	Wet chemical synthesis	10^{2}	-	[28]
10	Tin Selenide Films	Thermal evaporation	10^{1}	-1.28	[24]
11	TIN SELENIDE THIN FILMS	Encapsulated selenization	10^{1}	10^{-5}	[25]
12	$SnSe_{0.5}Te_{0.5}$ Crystals	Direct Vapor transport Technique (DVT)	10^{2}	10^{-6}	[27]
13	Tin Selenide Nanoparticles	Chemical precipitation	10^{3}	-	[26]

1.5 Literature review related to magnetic properties of SnSe

Recently, few researchers have investigated the electrical and magnetic studies of transition metal-doped SnSe by computing their first-principle calculations using Density Functional Theory [50–53]. Lu et.al. concluded that 3d-orbits of transition elements efficiently change the bandgap and spin polarization of the SnSe monolayers and also these narrowband transition metal-doped DMS can have probable advantages in the fields of optoelectronic and spintronic devices [51]. However, most of them focused on magnetic studies and coupling of Mn and Fe doped SnSe monolayers. Isber et al. reported the crystal growth and magnetic studies of Eu doped SnSe single crystals obtained using the Bridgeman method [54]. Recently, Liu et al. prepared Co doped SnSe thin films by thermal evaporation and investigated the thermoelectric and magnetic properties which have concluded that Co induces magnetism in SnSe lattice [55].

S.No	Title	Synthesis method	Property	Reference
1	Co-doped SnS	Co-precipitation	M_S of 0.0065 emu/g for x=0.02	[29]
2	Ni-doped SnS	Co-precipitation	M_S of 0.037 emu/g for x=0.10	[31]
3	Fe doped SnS	Co-precipitation	M_S of 0.0076 emu/g for x=0.10	[30]

4	SnSe with transition metal doping	Thermal evaporation	-	[53]
5	SnSe doped by transition metals:	encapsulated selenization	-	[52]
6	Transition-Metal Dopants in β-SnSe	Direct Vapor Transport technique (DVT)	-	[50]
7	SnSe Monolayer via Doping of Transition-Metal Atoms	Chemical precipitation	-	[51]
8	$Sn_{1-x}Eu_xSe$	Bridgmen method	-	[54]
9	Co doped SnSe films	Vacuum thermal evaporation	magnetic moment is 20 emu/cm3	[55]

1.6 Motivation

As observed from the literature, SnSe is well-studied for thermoelectric, photovoltaic, and optoelectronic applications**.** Our work will not focus on thermoelectric studies. We focussed on the preparation of this material with alkali metal and transition metal dopants. This was aimed at applying this material for dielectrics and spintronics applications. Doping of Group-I alkali metals like Na and K into SnSe leads to change the carrier concentration and effect bandgap of the host lattice. There by Na, K will influence the structural, morphological, optical, and dielectric properties. The transition metals like Co and Fe doping into SnSe change the electrical, and optical properties and induces magnetism in SnSe. Literature survey indicates that experimental investigations on the effects of doping SnSe with alkali metals and transition metals for dielectric and magnetic properties are scarce.

Various synthesis methods have been used for the preparation of polycrystalline SnSe. These include solid-state reaction, vacuum melting, mechanical alloying, wet chemical methods such as hydrothermal, solvothermal, and chemical precipitation. The solid-state reaction, vacuum melting, and mechanical alloying methods employ high processing temperatures; demand the use of special equipment, and the need to work with toxic reagents. The solvothermal method utilizes organic solvents while the morphology of the sample cannot be controlled in the chemical precipitation method. In

comparison, the hydrothermal method has the advantage that it can be carried out in an aqueous medium at low temperatures is economical, and easy to synthesize.

To date, no research has been reported on the effect of alkali and transition metal doped into SnSe prepared by hydrothermal method for its dielectric and magnetic properties in particular. Therefore the study of morphological, optical, and dielectric studies has been undertaken keeping in mind the simplicity and cost-effectiveness of the hydrothermal approach for all cases. In addition, magnetic property studies have been studied in transition metal doped SnSe.

1.7 Objectives of the Thesis Work

The objective of the present study is to carry out the under-mentioned investigations. The dielectric measurements in all cases have been undertaken in the temperature range of 323K -523 K and in the frequency range of 100 Hz to 12 MHz. The magnetic studies were undertaken at room temperature.

- Synthesis and characterization of alkali metal (a) Na , (b) K doped SnSe polycrystals through hydrothermal method and understand their structural, morphological properties
- Study of the optical and dielectric properties of alkali doped SnSe for the application of optoelectronic and dielectric devices. This includes temperature and frequency dependent dielectric and electric modulus studies of alkali doped SnSe
- Preparation and characterization of transition metal (c) Co (d) Fe doped SnSe polycrystals using hydrothermal method.
- The optical and dielectric properties of transition metal doped SnSe for the application of optoelectronic and dielectric devices. This includes temperature and frequency dependent dielectric and electric modulus studies of transition metal Co, Fe doped SnSe polycrystals.
- Study the room temperature magnetic studies of Co doped SnSe and Fe doped SnSe for spintronic applications.

1.8 Organization of the thesis

The thesis is organized in to seven chapters as mentioned below

Chapter 1

The first chapter discusses the recent research on IV-VI metal chalcogenide semiconductors for various applications in the fields of dielectric and magnetic properties of materials. The background for diluted magnetic semiconductors (DMS) which are useful for data processing and spintronic applications is discussed. The

specific properties of SnSe that make it important among the IV-VI layered semiconductors, is discussed. The various preparation methods for SnSe polycrystals were explained. In comparison to other methods hydrothermal method is used due to its advantages over the other methods.

Chapter 2

This chapter deals with the synthesis procedure and material characterization techniques used in the current study. Further, the details of the characterizations and dielectric and magnetic property measurement techniques that are used in the present work have been discussed in this chapter. Structural parameters like average crystallite size and lattice parameters have been calculated by PAN-Analytical powder X-ray Diffraction (XRD). Morphological studies are obtained using Scanning Electron Microscope (Tescan, Vega 3 LMU), (SEM), Field emission scanning electron microscope (FESEM), and High Resolution Transmission Electron Microscopy (HRTEM) (HR-TEM, Jeol/JEM 2100). Elemental composition was confirmed by Energy Dispersive X-Ray Analysis (EDAX) (Tescan, Vega 3 LMU). The direct and indirect bandgaps were determined using UV-Vis-NIR Diffuse Reflectance Spectroscopy (Carry 5000). The valence states of atoms are revealed by X-ray photoelectron spectroscopy (XPS)) (K-Alpha electron spectrometer, Thermofisher). The dielectric parameters such as dielectric constant, dielectric loss, dielectric loss tangent and, AC conductivity were measured by using the Solartron SI1260A impedance/gain-phase analyzer for frequencies from 100 Hz to 12 MHz. The Room temperature magnetic parameters like Saturation magnetization (M_S), Coercivity (H_C), and retentivity (M_R) were investigated in the range of -15000 G to +15000 G by Vibrating Sample Magnetometer (Lake Shore).

Chapter 3

This chapter provides information about the structural, morphological, optical, and dielectric properties of Na-doped SnSe polycrystals prepared by hydrothermal method at 170 ^oC. The structural properties were investigated using XRD. The morphology for x=0.20, the sample showed 3D flower-like structure. The optical studies showed that both indirect and direct bandgaps are narrowed as Na doping increases into SnSe. Further, the room temperature and high temperature dielectric studies were discussed in detailed.

Chapter 4

This chapter gives the detailed synthesis procedure for K-doped SnSe using hydrothermal method 170 ^oC. The single phase structural parameters and morphological

studies were explored. Then optical studies were measured for K-doped SnSe. Later, dielectric studies discussed in detail at room and high temperature respectively.

Chapter 5

In this chapter the Co-doped SnSe polycrystals were successfully prepared by hydrothermal method at 150^{o}C. Then the structural and morphological studies for the prepared Co doped SnSe were investigated. The bandgap values revealed the optical properties of the prepared samples. The oxidation states of the elements present in Co-doped SnSe were obtained using XPS. Later the room temperature and temperature dependent dielectric studies were discussed in detail. Further, magnetic properties for Co doped SnSe were measured at room temperature.

Chapter 6

This chapter illustrates the preparation of Fe doped SnSe by hydrothermal method at 150 ^{o}c. Then the structural and morphological studies were discussed. To obtain the bandgap values for Fe doped SnSe polycrystals, optical studies were investigated. The chemical states of the elements present in Fe doped SnSe were obtained using XPS. Then dielectric studies for Fe doped SnSe were discussed at room temperature and high-temperature respectively. Finally, room temperature magnetic properties for Fe doped SnSe were measured which are having applications in spintronic devices.

Chapter 7

Chapter 7 represents the summary and conclusions taken from the studies on structural, morphological, optical, dielectric and magnetic properties of alkali (Na, K) and transition (Co, Fe) metal doped SnSe prepared by hydrothermal method. Finally it gives the future scope of the thesis.

CHAPTER 2: Material Characterization and Measurements

This chapter provides the complete information about the synthesis methods followed for the preparation of alkali and transition metal doped Tin Selenide compounds. Further, it gives the insight into the characterization and measurement techniques used to evaluate structural, morphological, optical, dielectric and magnetic properties of synthesized materials are discussed. It also explains steps followed to prepare pellets for dielectric measurements

The advantages and reasons for selection of hydrothermal method adopted for sample preparation has been covered in the previous chapter.

2.1. Hydrothermal method

The Hydrothermal reaction takes place under the conditions of high-pressure and high-temperature. Generally above the boiling temperature of water in order to achieve a high vapor pressure and meet specific critical conditions. This process blends precursor materials with an aqueous solution in a specific end-product stoichiometry. The mixture is sealed in an autoclave. The solution become pressurized and subjected to a temperature above the solvent critical point for chemical reactions. Finally, the autoclave was allowed to cool to room temperature. The obtained products are then subjected to a post-treatment process that includes isolation, washing, and drying. The obtained product is ground into a fine powder for later use.

2.2 Materials Characterization

2.2.1 X-ray diffraction

X-ray Diffraction (XRD) is one of the most traditional, basic non-destructive techniques to analyse the crystal structure of the materials. The information about the crystal structure is obtained by the interaction of X-rays with the atoms in a crystal plane of the samples. When a monochromatic X-ray beam incident on the sample it is diffracted at different angles that are received by the detector. The diffraction of X-ray beam is originated from the boundaries of atoms present in a crystal planes. When the diffracted X-rays originated from different set of crystal planes are in-phase, they undergo constructive interference and to produce maximum intensity at that particular glancing angle (θ). Besides, when the diffracted X-rays are in out of phase then they interfere destructively and produced minimum intensity. The crystal structure is determined by Bragg's law using the interference of these diffracted beams from the various crystal planes. Bragg’s law is first proposed in 1913 by Lawrence Bragg and his

father, William Henry Bragg. According to Bragg, every diffracted beam has a set of crystal planes from which it appears to be spectacularly reflected [56,57]. These reflected X-rays interfere and produce diffraction pattern only when the Bragg's law is satisfied. The Bragg's condition for obtaining the diffraction pattern of the material is that the path difference between two x-ray beams that are diffracted from the two successive crystal planes is equal to the integral multiple of incident X-ray wavelength which is given in below equation.

$$2d \sin\theta = n\lambda \qquad (2.1)$$

Where n is an integer (n=1, 2, 3, etc) and λ is the wavelength of X-ray (λ= 1.5406 Å), and d is Lattice spacing. The peak positions i.e., the angle of diffraction and peak intensities are the important parameters to analyse the crystal structure of the materials. Each peak present in the diffraction pattern is corresponding to the set of crystal planes which are indicated by miller indices (h k l). These miller indices values and the lattice d-spacing are used to calculate the lattice parameters (a, b, c) of all the samples using the relation given below.

$$\frac{1}{d^2} = \frac{h^2}{a^2} + \frac{k^2}{b^2} + \frac{l^2}{c^2} \qquad (2.2)$$

The crystalline size (D) of the particles can be calculated by using Scherrer equation:

$$D = \frac{k\lambda}{\beta Cos\theta} \qquad (2.3)$$

Where k is the geometrical factor and is equals to 0.9, and β is the full width at half maximum (FWHM). The strain is calculated using the Stokes Wilson formula given by Eqn. (3) [58]

$$Strain\ (\varepsilon) = \frac{\beta}{4\tan\theta} \qquad (2.4)$$

The dislocation density is calculated using Eqn. (4) [58]

$$Dislocation\ density\ (\delta) = \frac{1}{D^2} \qquad (2.5)$$

In this thesis, XRD patterns of the powder samples are obtained by using a PAN Analytical powder X-ray diffractometer equipped with Cu K_{α}-radiation of wavelength equals to 1.54 Å.

Figure 2.1 Photograph of PAN Analytical powder X-ray diffractometer.

2.2.2 Scanning electron microscopy and Energy dispersive x-ray analysis

Scanning Electron Microscope (SEM) is a microscopic technique that uses an electron beam instead of light to scan the surface of the material. It is an image processing technique that produces features of the specimen such as surface morphology, structure, and composition. The surface images are produced by scanning a high-energy focussed electron beam on the surface of the specimen. The beam of electrons is generated either by a thermionic gun where a tungsten filament is heated at high temperatures to produce electrons or a field emission gun where a high electric

field is applied to the tungsten wire. The electron beam is focussed vertically onto the surface of the specimen by using an electromagnetic lenses system. When the electron beam interacts with the surface, it produces signals mainly secondary electrons, backscattered electrons, and characteristic x-rays. These secondary and backscattered electrons are collected and processed to produce surface images of the materials [59–62]. To produce high-quality images using SEM, the sample surface must be conductive to prevent the charging effect which blurs the image quality. To avoid this, generally, the surface of the sample is sputtered with the conducting surface layer. In this thesis, we have used FESEM (CARL ZEISS, ULTRA55) and SEM (TESCAN, VEGA-3 LMU). For sample preparation, a few mg of powder samples is spread over the copper adhesive tape and gold coating is performed using the sputtering technique.

Energy dispersive x-ray analysis (EDAX) is used to estimate the composition of the sample and determine the elements that are present in the sample. The EDAX analysis is always coupled with an electron microscope. In this technique, the sample surface is exposed to an electron. When the electron beam interacts with the atoms that are present in the samples, ejection of the elections which are bounded tightly with the nucleus of the atom (inner shell) will take place. The vacated position of the ejected electrons is filled by the electrons which are present in the outer shell. During this shifting from outer shell to inner shell, certain energy will release in the form of X-Rays. The energy released during this process is depends on the shells from which the electron transferring is taking place. The emitted x-rays provide the characteristic information about the element which is present in the sample. Every element releases x-rays with unique amount of energy. Therefore, the x-rays emitted from the surface of the sample are collected and analysed using EDAX spectrum. EDAX spectrum relates the x-rays energy with intensity. Peak position is used to determine the element present in the sample and intensity of the peak is used to estimate the concentration of the particular element present.

Figure 2.2 Photograph of Scanning Electron Microscope attached with Energy Dispersive X-Ray Analysis (TESCAN, VEGA-3 LMU).

2.2.3 Transmission electron microscopy

Transmission Electron Microscopy (TEM) is also a microscopy technique, similar to SEM; it also uses a highly focussed electron beam to produce the images of the specimen. In this technique, the specimen should be thin in such a way that it should pass the electron beam through the sample. Sample preparation is extremely important because this technique works on the transmission of electrons through the samples. In this technique, electron beam focussed on the sample is interacted with the sample and transmit through it. The interaction of electron beam transmitted through the specimen is further processed by an image detection system to produce the images of the samples. TEM is useful to evaluate the microstructure, pore arrangement, and crystallinity of the electrode material [63].

The TEM instrument also generates a diffraction pattern from a large distribution of identical electrons known as selected area electron diffraction (SAED). The SAED pattern makes it simple to determine the crystal structure and calculate the lattice parameters for a given crystal system. The diffracted electron's de-Broglie wave length is 0.025, which corresponds to energy of 200 keV, which is used to generate an SAED pattern. When these low-energy electrons interact with the sample, they create a small glancing angle of approximately 0.4 ° with respect to each plane. As a result, all planes appear to be parallel to the incident electron, and all planes' reciprocal vectors occur in the plane of the incident beam. Since the glancing angle is so small, the Bragg's equation for a crystal structure from an SAED pattern is expressed as $d.2\theta = \lambda$. The 2θ

value can also be expressed as $2\theta = r/L$, where r is the distance from the diffracted spot to the spot where the incident beam strikes the screen and L is Camera length i.e., the distance from the screen to the sample.. As a result, d value can be determined using the formula $d = L\lambda/r$, where L is kept constant.. In this thesis, High-Resolution Transmission Electron Microscopy (HRTEM, Thermofisher, Talos F200S) is used to obtain the TEM images of the electrode materials. For sample preparation, powdered samples are dispersed in ethanol solvent by ultra-sonication and drop cast over a Cu grid.

2.2.4 X-ray photoelectron spectroscopy

X-ray photoelectron spectroscopy (XPS) is broadly used to quantify the surface elemental composition and chemical state of the sample being studied [64]. The interaction of x-rays with the sample surface at a depth of a few nanometres produces the XPS spectrum. The photoelectric effect is the backbone of XPS. Core-shell photoelectrons are ejected when the x-rays hit the atoms present on the surface of the specimen. The electrons present in each shell of an element have their unique binding energies (B.E.). Therefore, the electron in the core shell orbital consumes some of energy of incident x-rays which is equivalent to the sum of its binding energy and work function. The emitted electron also possess Kinetic energy (K.E.) which is given by the relation $(K.E) = h\upsilon - B.E. - \phi$, where ϕ is work function. By measuring the K.E of the emitted photoelectrons using electron energy analyzer, B.E is obtained [65,66]. The elemental identity, chemical state, and quantity of a detected element can be determined by analysing the xps spectrum which is the plot between the B.E and Intensity. The main components of an X-ray Photoelectron Spectrometer are the X-ray source, sample stage, electron energy analyzer, and detector. In the present study, XPS studies were carried out using a K-alpha electron spectrometer equipped with an *Al* X-ray beam source.

2.2.5 UV–Vis–NIR spectroscopy

The energy band gap (E_g), a key characteristic of semiconductors, governs how they are used in optoelectronics. Semiconducting materials are often examined using UV-Vis absorption spectroscopy. Thin films, liquids, and solids can all be studied using this spectroscopic method. Knowing the thickness of solid films makes it simple to derive the E_g values from their absorption spectra due to their low scattering. It is simple to assess the energy gap for samples of transparent liquids using the absorption spectrum. However, with colloidal samples, if the particle size is too large then it precipitates, and the resultant absorption spectra results in a wrong interpretation. It is preferable to

employ diffused reflectance spectroscopy (DRS), which allows us to determine the E_g of solid materials. The DRS spectrum is determined by measuring diffused radiation that is reflected from a surface of the sample is being analyzed. Only a tiny layer of the sample surface is examined in this procedure, which allows the use of powder samples directly. The radiated beam is focused on the surface of the sample and it get reflected from and collected in a large solid angle. Radiation from the samples is reflected in all directions as a result of the particles' random orientation. Although it cannot be completely prevented, measuring geometries have been designed to reduce the effect of regular reflection. The contributions of transmission, internal, specular reflectance components and scattering mechanisms in the collected energy, can show both absorbance and reflectance characteristics. There are numerous theories that have been proposed to describe the diffuse reflectance phenomenon based on the sample's optical response. In DRS, the model proposed by Kubelka-Munk in 1931 is commonly utilized. Both the scattering coefficient (s) and the absorption coefficient (k) affect the intensity of the light that is reflected. By using the Kubelka-Munk equation, the reflectance data can be transformed to absorbance. Kubelka-Munk equation [67] is

$$F(R) = \frac{(1-R)^2}{2R} \qquad (2.6)$$

where R is absolute reflectance. We have calculated the bandgaps of all the compositions using the Tauc plot by the following Eqn.

$$F(R)h\upsilon = A(h\upsilon - E_g)^n \qquad (2.7)$$

where h, υ, E_g, and n are the Planck constant, frequency of radiation, bandgap, and constant related to a mode of transition, respectively. For allowed direct transition the value of n is ½ and it is 2 for the indirect transition.

In the current study, Carry 5000 spectrophotometer is utilized for measuring the reflectance spectra in the range of 400-2000 nm at room temperature.

Figure 2.3: Photograph of UV–Vis–NIR spectroscopy.

2.2.6 Dielectric measurements

Dielectric analysis can be used to determine how the physical characteristics of polar materials, such as polarization, permittivity, and conductivity, change with respect to temperature and frequency. By examining the dielectric properties, it is possible to study the conduction characteristics of the materials. Specifically, it highlights the relationship between temperature and frequency and the dielectric characteristics. Using the results of the dielectric analysis, materials capacity for storing and transmitting electric charge is carefully examined. Due to the increased number of grains on the surface of the nanostructure material, its dielectric properties are closely related to its opto-electric properties. Dielectric constant (ε') and dielectric loss (ε'') are two complex quantities that are measured to determine the dielectric characteristics of materials. The dielectric constant is the capacity to store energy from the applied electric field. Dielectric loss, which occurs when energy is lost as a result of defects and charge accumulation at the interphase layers, is most noticeable in nanoscale materials. The basic components of dielectric analysis include an LCR meter and an electrode holder into which the sample is placed. The computer is externally linked to the system that records the data. The obtained data are used to calculate various dielectric properties of materials using the formulae 2.8 to 2.18. The preparation of the sample is an important factor in the measurement of electric properties. Typically, the sample is made in the shape of a disc, and the flat surface is coated with silver paint to enhance electrical contact. The sample is placed in the holder, and the electrodes are adjusted to make contact with the sample. Vernier calipers are used to measure the thickness and diameter of the sample. Schematic of steps involved in dielectric measurements are depicted in figure below.

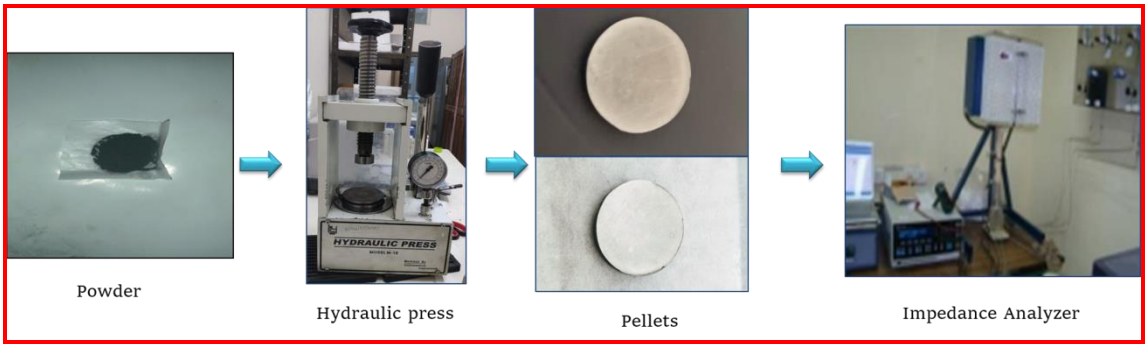

Figure 2.4 Steps involved during pelletization and dielectric measurements.

2.2.6.1 Dielectric properties

The dielectric properties of a material can be understood by three theories i.e, i) Maxwell-Wagner model ii) Koop's phenomenological theory and iii) Jonscher's power law [68]. According to Maxwell-Wagner theory, interfacial polarization is prominent in the low-frequency region which causes charge trapping at grain boundaries. Because grain boundaries act as a barrier to charge carrier movement. In the low-frequency region, the relationship of ac conductivity with frequency was described using Koop's theory. According to this theory, grain boundaries with large resistance generate constant conductivity in a low frequency region. In a high frequency region, grains with high conductivity than grain boundaries leads to an increase in ac conductivity value [68]. The electrical conductivity of various types of disordered solids is described by Jonscher's power law. This law states that the conduction mechanism of a material can be explained by various theoretical models that correlate the conduction mechanism with s behaviour. In the literature, a number of models [67] based on the two separate processes of classical hopping across a barrier and quantum-mechanical tunnelling, or some of their variants or combinations, have been put forth. The quantum mechanical tunnelling (QMT), correlated barrier hopping (CBH), overlapping large-polaron tunnelling (OLPT), and non-overlapping small polaron tunnelling (NSPT) models are the four different models, respectively.

i. **Dielectric constant (ε')**

The complex dielectric constant (ε) of a material is given by the relation $\varepsilon = \varepsilon' + i\varepsilon''$, where ε' is the real part of dielectric constant and ε'' is the imaginary part of dielectric constant. The dielectric constant (ε') is calculated using the following relation

$$\varepsilon' = \frac{C}{C_o} \qquad (2.8)$$

$$\text{Where } C_o = \frac{A\varepsilon_o}{d} \qquad (2.9)$$

where C is the capacitance, d is the pellet thickness, A is the cross-sectional active area of the pellet, ε_o is the absolute permittivity ($\varepsilon_o = 8.85 \times 10^{-12}$ Fm^{-1}).

ii. **Dielectric loss (ε")**

The dielectric loss describes the electrical energy loss of a material when the field penetrates the material. The dielectric loss (ε") is calculated using the relation

$$\varepsilon'' = \varepsilon' \tan\delta \qquad (2.10)$$

iii. **Dielectric loss tangent (tan δ)**

The energy dissipation in the dielectric material can be described using loss tangent or dissipation factor (tan δ) and it is calculated using the relation

$$\tan\delta = \frac{1}{2\pi f RC} \qquad (2.11)$$

iv. **AC conductivity**

The frequency dependence of AC conductivity can be explained by the Jonscher's relation given by Eqn. (5) below:

$$\sigma(\omega) = \sigma_{dc} + A\omega^{s} \qquad (2.12)$$

where σ_{dc} is the frequency-independent conductivity, A is the pre-exponential factor, and 's' is the frequency exponent which depends on temperature and lies between 0 and 1. In CBH model, the value of exponent 's' is temperature dependent and it is decreases with increase in temperature. According to the CBH model the value of 's' can be calculated using Eqn. (2.13) .

$$s = 1 - \frac{6k_BT}{W_m + [k_BT\ln(\omega\tau_o)]} \qquad (2.13)$$

where k_B is Boltzmann's constant, τ_o is the relaxation time, T is the absolute temperature and Wm is the maximum barrier height. For larger values of Wm/kT, the Eqn. (2.13) approximates to Eqn. (2.14)

$$s = 1 - \frac{6k_BT}{W_m} \qquad (2.14)$$

v. **Activation energy**

The temperature-dependent activation energy (E_a) is calculated using the relation

$$\sigma(T) = \sigma_o \exp^{\left(-\frac{\Delta E_a}{k_BT}\right)} \qquad (2.15)$$

where σ_o is the pre-exponential factor, ΔE_a is the activation energy, and k_B is the Boltzmann constant.

vi. **Electrical modulus**

Complex electrical modulus spectroscopy is a very useful technique to extract bulk response and to obtain a better understanding of relaxation and conduction mechanisms on the complex plane of M' versus M" at different temperatures. It gives information

about the differentiation between electrode polarization and grain boundary conduction[69]. To remove high loss effects at the low-frequency region, electrical modulus studies have been investigated at different temperatures. The complex electrical modulus and it's real (M') and imaginary (M") parts are calculated using the relations given below

$$M^* = \frac{1}{\varepsilon^*} = M' + iM'' \qquad (2.16)$$

$$M' = \frac{\varepsilon''^2}{\varepsilon'^2+\varepsilon''^2} \qquad (2.17)$$

$$M'' = \frac{\varepsilon'^2}{\varepsilon'^2+\varepsilon''^2} \qquad (2.18)$$

2.2.7 Magnetic measurements

The vibrating sample magnetometer VSM, invented by S. Foner, is a simple and useful technique for illustrating magnetic material properties. VSM has become widely accepted tool to examine the magnetic behavior of a wide range of materials, including diamagnetic, paramagnetic, ferromagnetic, ferrimagnetic, and anti-ferromagnetic materials. Owing to its simplicity, robustness, ease of measurement, and relatively high sensitivity. Temperature dependent magnetic properties can also be measured using VSM. The operation of VSM is based on Faraday's law of electromagnetic induction, which is dependent on the measurement of emf created in a coil of wire given by

$$\varepsilon = -N\frac{d}{dt}(BA\cos\theta) \qquad (2.19)$$

Where N denotes the number of turns in the coil, A denotes the coil area, B denotes the magnetic field, and θ is the angle between the B field and the direction normal to the coil surface.

In the current study, a VSM (Lake Shore Model 7410) based on Foner's design was used for determining the magnetization measurements. A photograph of the VSM is shown in Fig. 2.5.

A sample is connected to a vibrating rod and made to vibrate in an electromagnetically generated magnetic field in VSM. The magnetic properties of the sample are deduced from measurements of the voltage caused in the stationary detection coils by the oscillating magnetic field of the vibrating sample. A secondary voltage is produced by a reference sample, which could be a tiny permanent magnet known as an electromagnet (referred to as the reference signal). The voltage from the reference is then proportional to the known portion of the voltage, which is then related to the magnetic moment of the sample after it has been phased to balance the voltage from the sample. This method

makes measurements insensitive to changes in vibration amplitude, frequency, minor magnetic field instabilities, non-uniform magnetic field, amplifier gain, and amplifier gain variation.

Figure 2.5 Photograph of the vibrating sample magnetometer.

2.3 Conclusions

This chapter covered the complete information about synthesized materials and various techniques that are used to characterize the samples. An understanding of the basics behind each technique will provide a clear insight about the properties of material. In addition to that the knowledge about the fundamental principle of various techniques will pave a way to where and when to use the technique. In this unit the synthesis of material by hydrothermal method is discussed in detail. Hence the complete knowledge about the synthesis procedure and the characterization technique of will give a broad insight about the synthesis and characterization of the materials. In the following chapters the details of synthesis procedure for various dopants (Na, K, Co, Fe) and the results of characterization will be presented along with relevant discussion of results

CHAPTER 3: Effect of Na doping on structural, Optical, and dielectric properties of SnSe polycrystals

3.1 Introduction:

We have observed that a few literature is available related to the dielectric properties of SnSe prepared by different methods other than hydrothermal method as mentioned in chapter 1 [24–27]. Doping of Group-I alkali metals like sodium (Na) into SnSe lattice can influence the structural, morphological, optical, electric transport, and thermoelectric properties. Mainly the influence of Na doping in SnSe on its transport and thermoelectric properties prepared by several methods has been studied [40,42,43,49,70]. However, to the best of our knowledge, no research work has been reported till now concerning the influence of Na doping in SnSe on the morphological, optical, and dielectric properties in hydrothermally prepared polycrystals. Hence, the present work is aimed at reporting the effects of Na doping into SnSe on the above properties to understand its suitability for optical and dielectric applications.

In the present work, we have synthesized Na doped SnSe ($Na_xSn_{1-x}Se$) polycrystals using hydrothermal method by varying the concentration (x) of Na (0.00 – 0.20 with an increment of 0.05). The changes that occurred in the structural, morphological optical and dielectric properties of SnSe due to Na doping were discussed. A detailed study was conducted on dielectric properties and various parameters such as permittivity, dielectric loss, dielectric loss tangent, AC conductivity, activation energy, and electrical modulus, etc. are reported.

3.2 Synthesis of $Na_xSn_{1-x}Se$ polycrystals

$SnCl_2.2H_2O$ (99.9%), Se metal powder (98%), NaCl (99.9%), KOH (85%), and $NaBH_4$ (99.9%) were purchased from MERCK. All chemicals were utilized in an as-received state without further purification. The concentrations of $SnCl_2.2H_2O$ and NaCl are varied to obtain $Na_xSn_{1-x}Se$ (where x = 0.00 to 0.20 with a step of 0.05) polycrystals using the hydrothermal method. Initially, stoichiometric amounts of $SnCl_2.2H_2O$ and NaCl were mixed in 100 ml of deionized water and stirred for 5 min. Then, 6 g of KOH was added to the solution. After 15 min of continuous stirring, the solution was turned transparent. Next, a stoichiometric amount of Se metal powder was added to the above solution followed by stirring for 15 min. This changed the color of the solution to greyish black. After that, 2 g of $NaBH_4$ was mixed into the solution and stirred for another 30 min. At this step, the color of the solution became pale yellow. Then, the solution was poured into an autoclave of 120 ml capacity and was kept in an oven at 170 ^oC for 12 h. Finally, it was cooled to room

temperature naturally. The solution was washed and filtered with ethanol and deionized water several times. The final product was dried in an oven at 80 ^{o}C overnight. The schematic of the detailed synthesis procedure is displayed in Fig. 3.1.

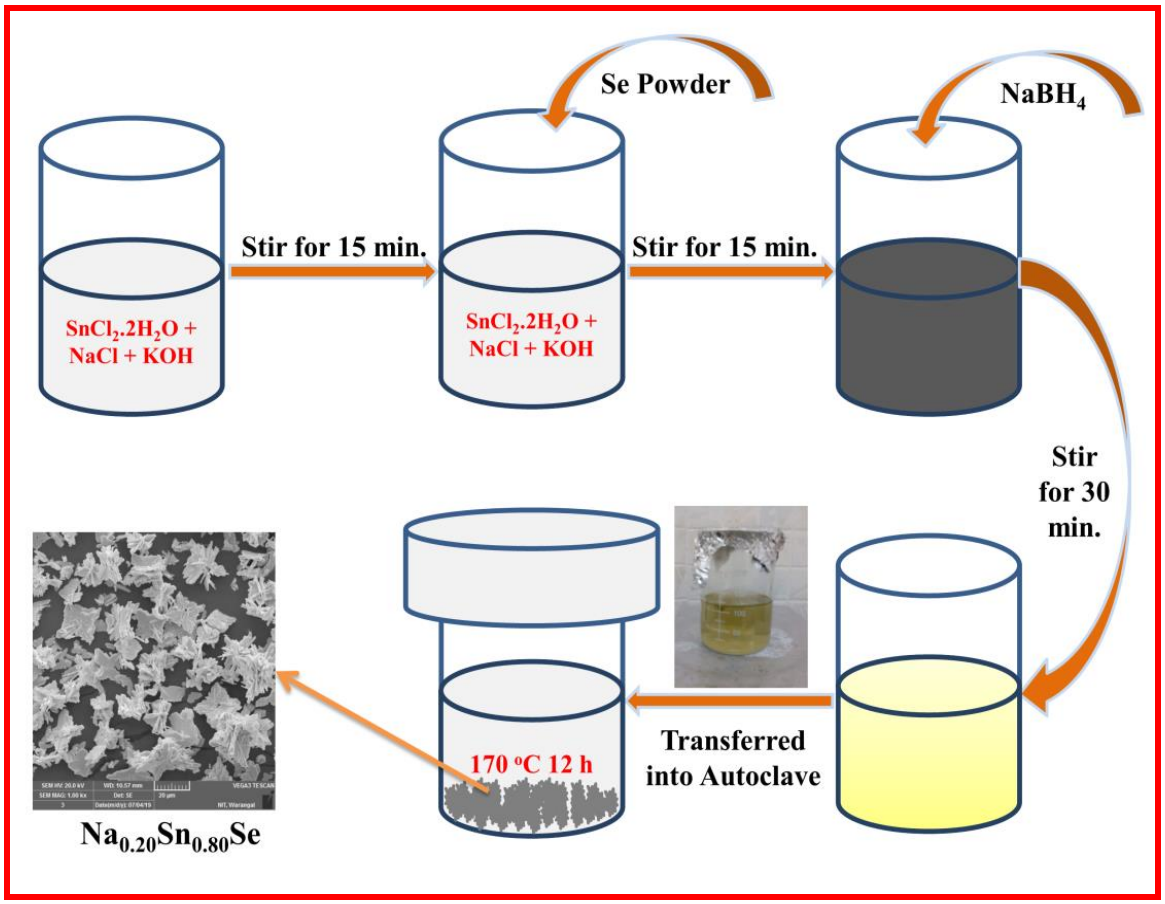

Figure 3.1 Schematic representation of the synthesis procedure of $Na_xSn_{1-x}Se$ using the hydrothermal method.

3.3 Results and Discussion

3.3.1 X-Ray Diffraction

Figure 3.2(a) shows XRD patterns of $Na_xSn_{1-x}Se$ for x = 0.00, 0.05, 0.10, 0.15, and 0.20 polycrystals. All the samples are resulted in single-phase and are well-indexed. The reflections occurred along the lattice planes (2 0 1), (2 1 0), (1 1 1), (4 0 0), (3 1 1), (4 1 1), (0 2 0), (5 0 1), (5 1 1) and (4 2 0) are in good agreement with standard PDF file no: #48-1224 [58,71]. The strongest intensity and preferred orientation for all the compositions is along (4 0 0). With increasing concentration of the Na as dopant, the intensity of the plane (4 0 0) decreased, whereas the intensity of the (1 1 1) plane increased. In Fig. 3.2(b), the values of lattice parameters are plotted against Na concentration (x). They are found to be matching well with the standard values (a= 11.49 Å, b = 4.153 Å, c = 4.44 Å, PDF#48-

1224). The lattice parameter values show a decreasing trend with an increasing concentration of Na. This might be due to the replacement of the large-sized Sn atom (0.112 nm) with the small-sized Na atom (0.102 nm) leading to lattice shrinkage and hence decrease of lattice constant [42].

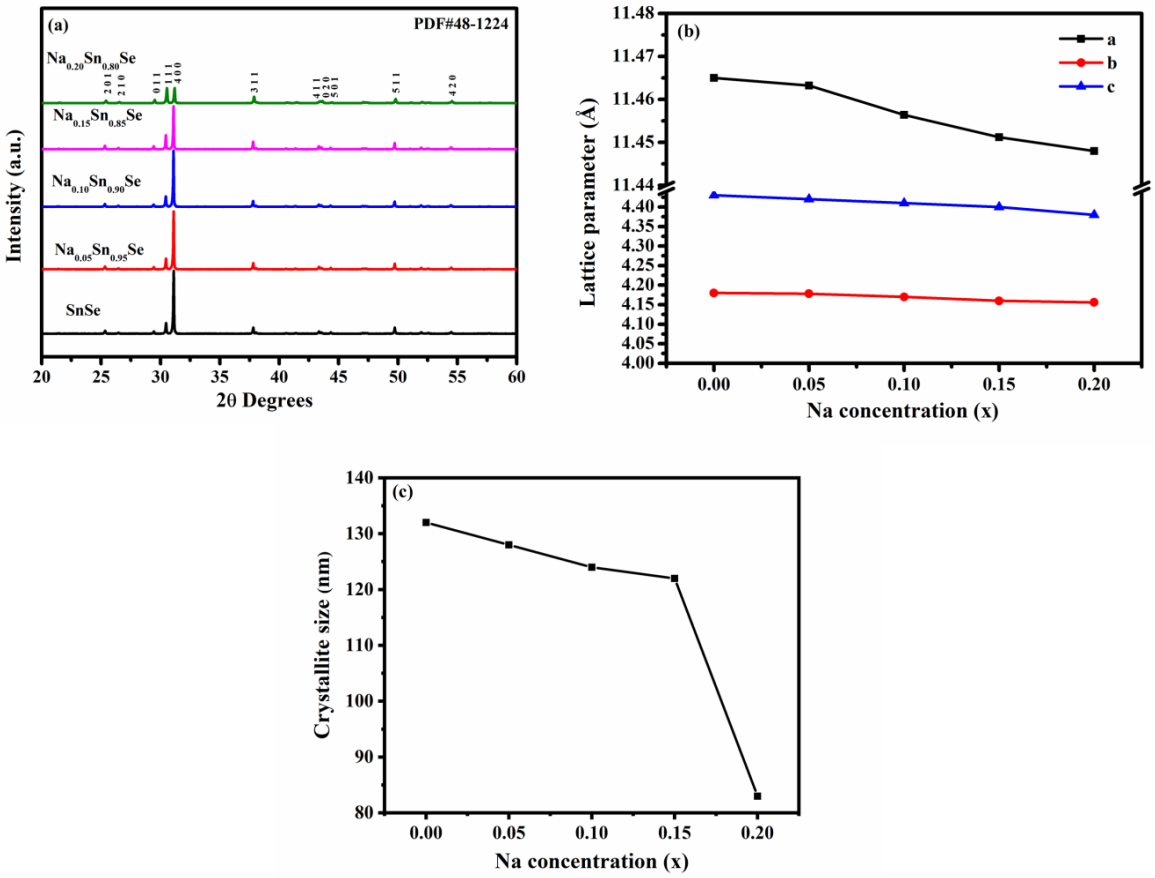

Figure 3.2 (a) XRD pattern of $Na_xSn_{1-x}Se$ polycrystals, (b) Variation of Lattice parameter to Na concentration(x), (c) Crystallite size versus Na doping concentration.

The value of average crystallite size (D) is found to decrease from 132 to 83 nm with increasing concentration of Na as shown in Fig. 3.2(c). Table 3.1 gives the values of lattice parameters, crystallite size, cell volume, and density of all the samples.

Table 3.1 Lattice constants, the crystallite size (D), cell volume, and density of all the compositions.

Sample	Lattice constants			Cell volume(Å)^3	D (nm)	Density (ρ) (g/cm^3)
	a (Å)	b (Å)	c (Å)			
SnSe	11.465	4.18	4.43	212.30	132	5.85
$Na_{0.05}Sn_{0.95}Se$	11.4632	4.178	4.42	211.69	128	5.86
$Na_{0.10}Sn_{0.90}Se$	11.4564	4.17	4.41	210.68	124	5.83
$Na_{0.15}Sn_{0.85}Se$	11.4512	4.16	4.4	209.60	122	5.94
$Na_{0.20}Sn_{0.80}Se$	11.448	4.156	4.38	208.40	83	6.05

3.3.2 Morphological studies

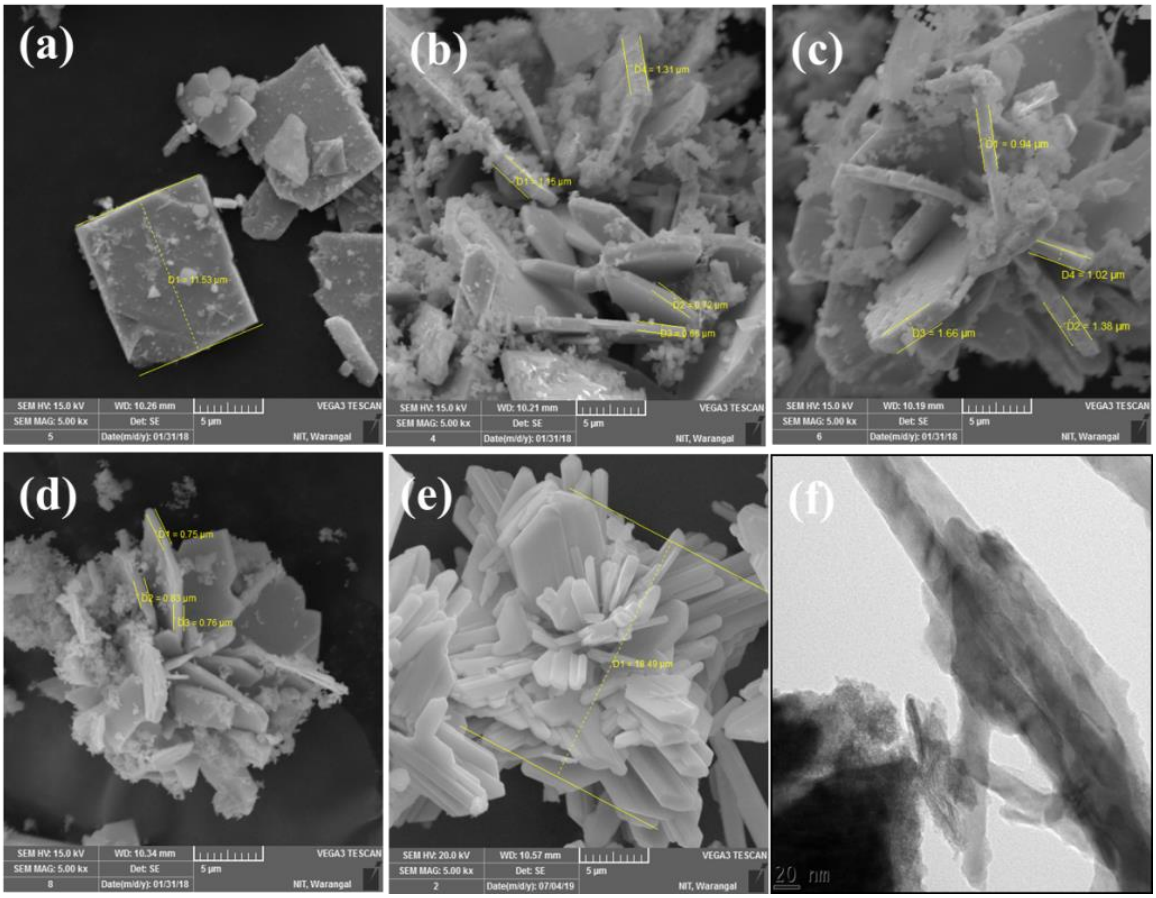

Figure 3.3 SEM images of $Na_xSn_{1-x}Se$ polycrystals (a) x = 0.00, (b) x = 0.05, (c) x = 0.10, (d) x = 0.15, (e) x = 0.20, and (f) HRTEM image of $Na_{0.20}Sn_{0.80}Se$.

Figure 3.3(a)-(e), shows overall morphology of $Na_xSn_{1-x}Se$ for x = 0.00 to x = 0.20 respectively. A 2D plate-like morphology is observed for pure SnSe crystals (Fig. 3.3(a)). The average length of a 2D plate is around 12 µm and the thickness is approximately 1µm. The thickness of the 2D plates gradually decreased as the concentration of Na increased and reached a value of 0.8 µm for $Na_{0.15}Sn_{0.85}Se$. The 2D plate-like morphology gradually changed to a 3D flower-like structure when Na was added to SnSe. It can be observed that these uniform flower-like structures are constructed from 2D plates. The size of the plates decreased and the plates got agglomerated together to form 3D-flowers at x = 0.20, having an average diameter of around 18 µm. As revealed by XRD, the orientation of 2D plates gradually changed from (4 0 0) to (1 1 1). At x = 0.20, the 2D plates are preferentially oriented in (1 1 1) direction. Fig. 3.3(f) shows the HRTEM image of $Na_{0.20}Sn_{0.80}Se$ shows petal of the 3D flower.

3.3.3 UV-VIS-NIR Diffuse Reflectance Spectroscopy

Figure 3.4a shows the reflectance spectra of all the samples. The plots for indirect and direct band gaps of all $Na_xSn_{1-x}Se$ samples are depicted in figs. 3.4(b & c), respectively. The indirect bandgap of SnSe (0.938 eV) is found to be in good agreement with the theoretical band gap (0.9eV). Further, it is observed that the indirect band gap of the doped samples gradually decreases from 0.938 eV to 0.830 eV with increasing Na concentration (Table 3.2). The direct bandgap measured for undoped SnSe turns out to be 0.981eV in comparison to the theoretical value of 1.3 eV. With increasing the doping concentration of Na, the direct band gap is found to decrease. The reduction in the average crystallite size with increasing Na doping results in a decrease in the grain size, which in turn results in a band gap decrease [72,73]. The variation of band gap versus concentration of Na is shown in fig. 3.4(d).

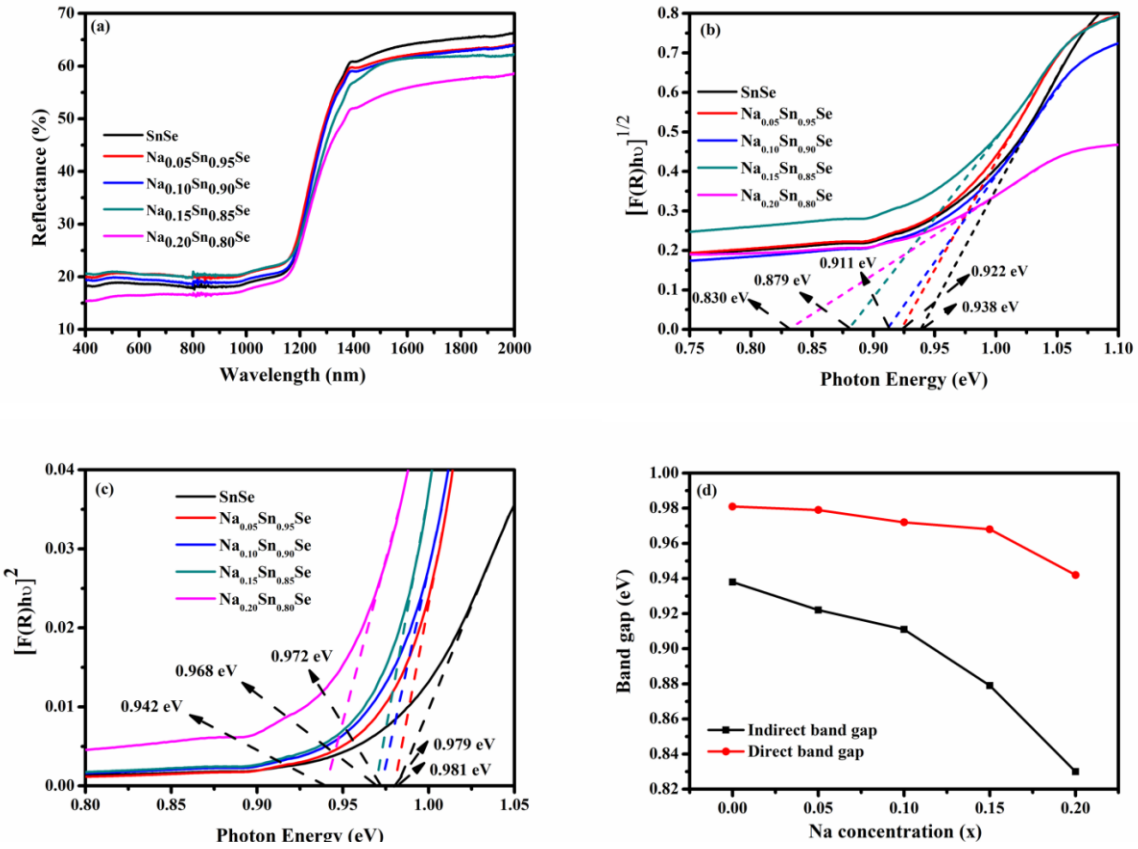

Figure 3.4 (a) Reflectance spectra of $Na_xSn_{1-x}Se$ polycrystals, (b) Tauc Plot for indirect band gap, (c) Tauc plot for direct bandgap, (d) Variation of indirect and direct band gaps as a function of Na concentration.

Table 3.2 Indirect and Direct band gap values of $Na_xSn_{1-x}Se$ polycrystals

Na concentration (x)	Indirect band gap (eV)	Direct band gap (eV)
0.00	0.938	0.981
0.05	0.922	0.979
0.10	0.911	0.972
0.15	0.879	0.968
0.20	0.830	0.942

3.3.4 Dielectric studies

3.3.4.1 Room temperature dielectric studies

Figure 3.5(a) displays the effect of frequency on ε' for $Na_xSn_{1-x}Se$ samples at room temperature. In the low-frequency region the ε' is large in all the samples. It is increased as the Na concentration increases into SnSe. The reason for exhibiting high values of ε' is because of the happening of space charge polarization in the low-frequency region. When the external ac field is applied the space charges move at grain boundaries and experience space charge polarization. The composition $Na_{0.20}Sn_{0.80}Se$ exhibited a large dielectric constant amongst other samples. The ε' decreases as frequency increases and become independent of frequency in the high-frequency region around 10 kHz. At high frequencies, much time is required for the dipoles to rotate themselves in the applied field direction. Due to the lack of enough time the dipoles begin to lag behind the AC field. Further, it leads to a decrease in the ε' value. Hence ε' reaches a constant value at high frequencies.

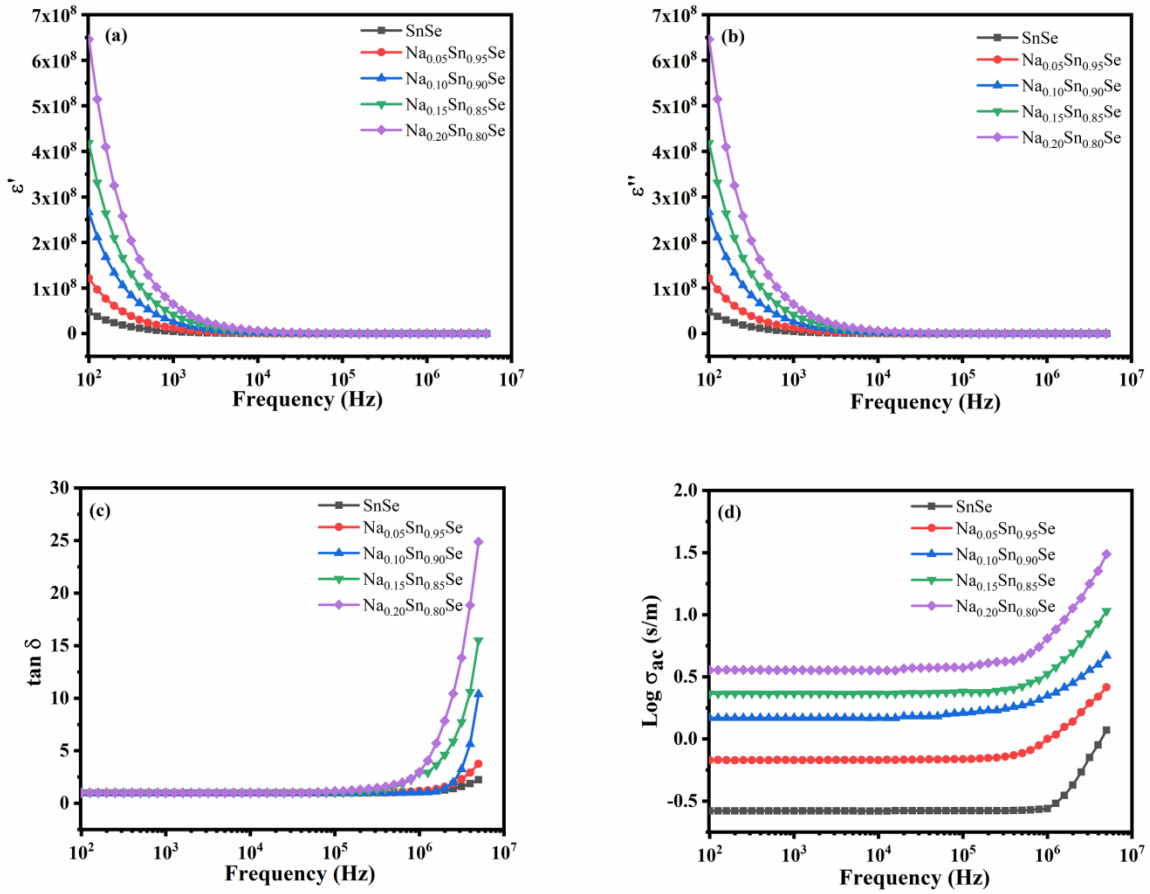

Figure 3.5 (a) Dielectric constant vs. frequency, (b) Dielectric loss vs. frequency, (c) Dielectric loss tangent vs. frequency, and (d) AC conductivity vs. frequency for all $Na_xSn_{1-x}Se$ samples at room temperature.

The effect of frequency on dielectric loss at room temperature for $Na_xSn_{1-x}Se$ is depicted in fig. 3.5(b). The ε" is high for all the $Na_xSn_{1-x}Se$ samples in the low-frequency region and becomes low and independent of frequency at the high-frequency region. The composition $Na_{0.20}Sn_{0.80}Se$ exhibited maximum dielectric loss compared to all other Na-doped SnSe samples. The effect of frequency on loss tangent (tan δ) for $Na_xSn_{1-x}Se$ polycrystals at room temperature is displayed in fig. 3.5(c). The tan δ values are low and independent of frequency between 100 Hz-100 kHz for all the samples. After that, the tan δ values for all the samples increase gradually. The sample $Na_{0.20}Sn_{0.80}Se$ has obtained a high value of tan δ. Figure 3.5(d) shows the effect frequency on ac conductivity for all the $Na_xSn_{1-x}Se$ samples. It is observed that two regions are observed in the ac conductivity plot of $Na_xSn_{1-x}Se$ samples: i) plateau region in the frequency range of 100 Hz -1 MHz corresponds to DC conductivity which is frequency independent, ii) the increasing portion in the frequency range of 1 MHZ- 10 MHz corresponds to ac conductivity. The ac conductivity increases as Na doping into SnSe increases and the largest value of ac conductivity is obtained for the composition $Na_{0.20}Sn_{0.80}Se$.

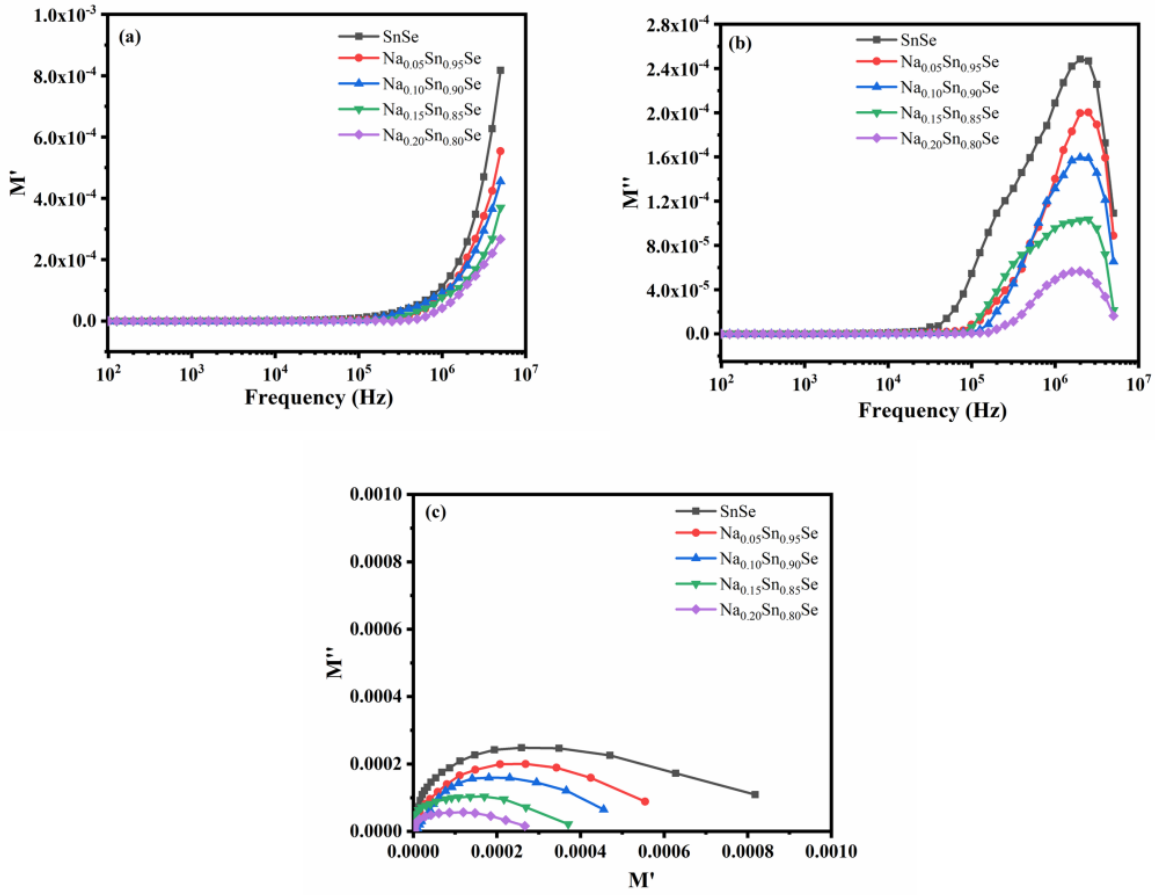

Figure 3.6 (a) Variation of M' as a function Frequency, (b) Variation of M" as a function of Frequency, and (c) Variation M" vs. M' for all $Na_xSn_{1-x}Se$ samples.

The effect of frequency on M' for all the $Na_xSn_{1-x}Se$ samples at room temperature is depicted in fig. 3.6(a). The values of M' is low and independent of frequency till 100 KHz. After that, the value of M' for all the samples increases as frequency rises and showed dispersion in the high-frequency region. The less values of M' indicate the negligible polarization effect at low frequencies. M' increases as frequency rises in all the samples. Figure 3.6(b) displays the effect of frequency on M'' for $Na_xSn_{1-x}Se$ samples at room temperature. The M'' values are very less in the low-frequency region and show an increasing trend as frequency rises for all the samples. Relaxation peaks are observed in the frequency region of 100 kHz- 10M Hz for all the compositions at various temperatures. The peak intensity is decreased as the Na doping increases. The peaks shifted in the direction of the higher frequency side as Na concentration increased. The M'' curves showed asymmetric behaviour represents a non-Debye type relaxation phenomenon. The area below the peak maximum is because of the long-range conduction of charge carriers whereas short-range conduction of mobile ions is responsible for the region above the peak maximum. The variation of M' vs M'' for $Na_xSn_{1-x}Se$ samples is depicted in fig.3.6(c) at room temperature. Semi-circular arcs are observed for all the compositions having their centres below the x-axis. It is also noticed that the radii of the arcs were found to be decreased with an increase in the composition of Na. The presence of semi-circular arcs indicates the existence of grain boundaries in all the Na-doped SnSe samples in the low-frequency region. The incomplete formations of semi-circular arcs indicate the non-Debye type relaxation is present in all the samples.

3.3.4.2 Temperature dependent dielectric studies

It is observed from fig. 3.7(a-e), that all the samples showed a decreasing trend in the value ε' with an increase in frequency. The $Na_{0.20}Sn_{0.80}Se$ has a larger number of grain boundaries in comparison to other compositions due to its 3D flower-like morphology [74]. The increase in ε' is due to the accumulation of space charges at grain boundaries which become active due to the trapping of charges. This is one of the reasons for the nanostructures to have larger values of dielectric constant than bulk forms. Because of space charge polarization, the value of electrostatic binding energy will be less, which increases the dielectric constant. The increase of the ε' with sample temperature for any composition can be described by the fact that as temperature increases there is more possibility of the orientation of the dipoles along the direction of the electric field. The high value of ε' obtained for Na doped SnSe suggests the material in the applications of high-density energy storage devices and microelectronic materials [74,75]. It is also

observed from Fig. 3.7(a-e), that ε' attains a constant value around a frequency of 10 kHz and saturates at high frequencies. With increasing frequency, the contribution by space charge polarisation decreases resulting in the decrease of ε'. At high frequencies, the dipoles do not have enough time to orient themselves towards the applied field direction. The dielectric constant obtained for $Na_{0.20}Sn_{0.80}Se$ in the current study at room temperature is less than the value obtained at high temperature. From this, it is understood that the temperature rise causes an increase in the dielectric constant.

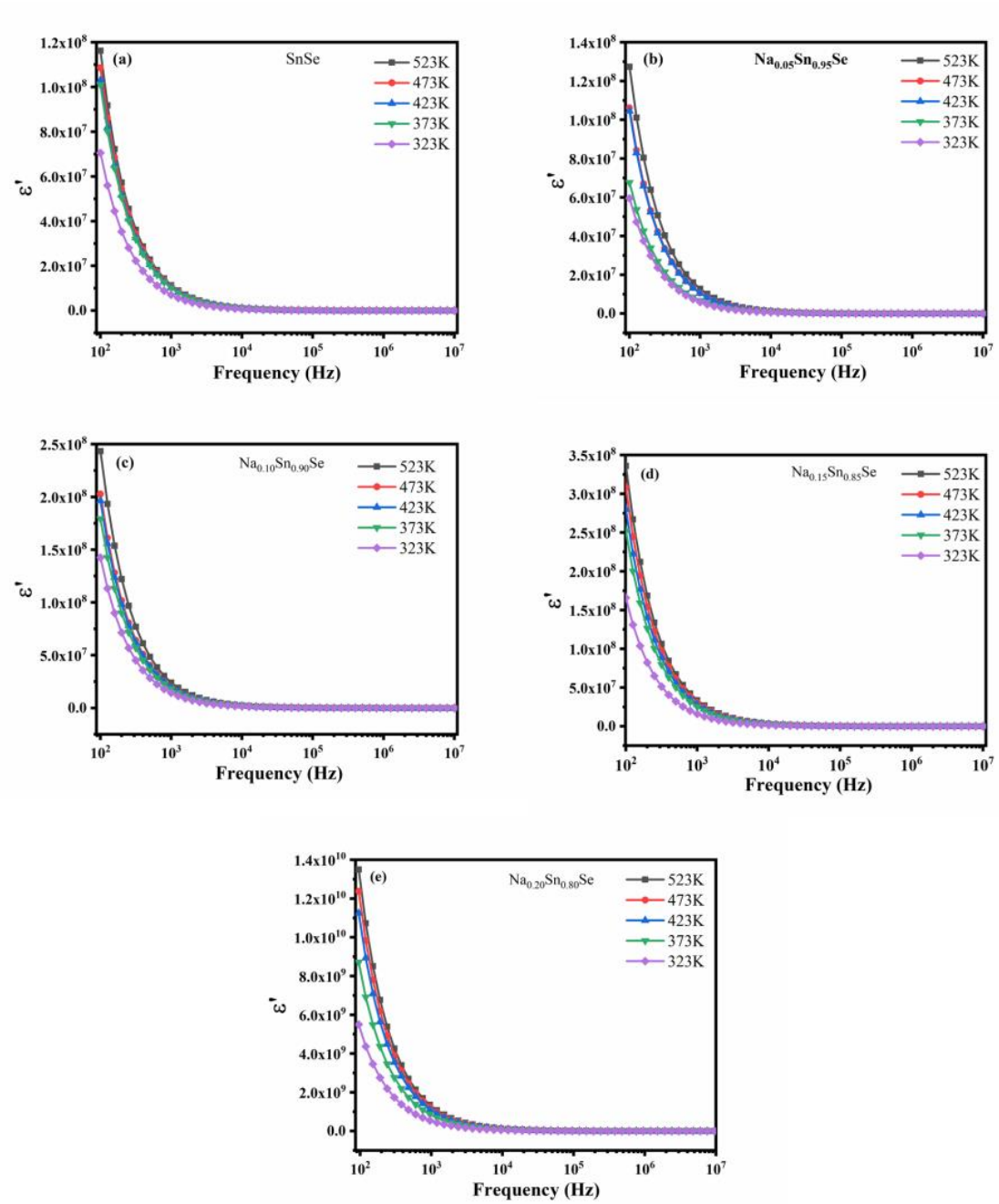

Figure 3.7 Dielectric constant vs Frequency of (a) SnSe, (b) $Na_{0.05}Sn_{0.95}Se$, (c) $Na_{0.10}Sn_{0.90}Se$, (d) $Na_{0.15}Sn_{0.85}Se$, and (e) $Na_{0.05}Sn_{0.95}Se$ respectively.

The dielectric loss describes the electrical energy loss of a material when the field penetrates the material. As seen from Fig. 3.8(a-e), the value of ε" also increased for all compositions from 323 K to 523 K. The maximum amount of loss is observed in the case of $Na_{0.20}Sn_{0.80}Se$. The ε" value for all compositions is observed to decrease with increasing frequency. The saturation at higher frequencies implies the absence of losses owing to dielectric relaxation. The low values of dielectric constant and dielectric losses at higher frequencies will find promising applications for electro-optic, photonic, and solar cell device fabrication [12,76,77].

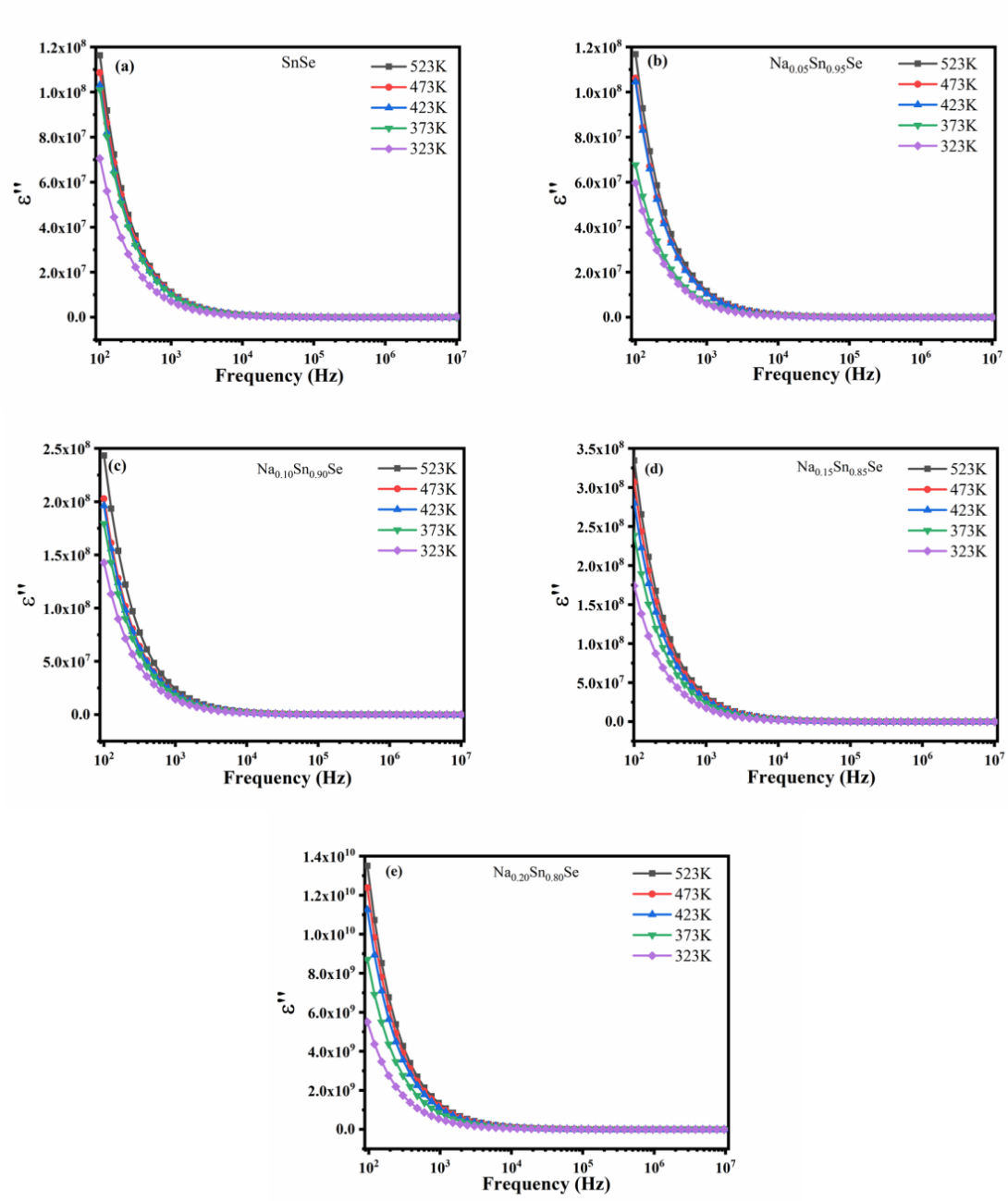

Figure 3.8 The imaginary part of permittivity versus Frequency of (a) SnSe, (b) $Na_{0.05}Sn_{0.95}Se$, (c) $Na_{0.10}Sn_{0.90}Se$, (d) $Na_{0.15}Sn_{0.85}Se$, and (e) $Na_{0.20}Sn_{0.80}Se$ respectively.

The dielectric loss tangent is found to increase for all compositions of $Na_xSn_{1-x}Se$ with an increase in frequency and temperature in each case as shown in fig. 3.9(a-e). The Maxwell Wagner model can be used to explain the changes occurring in the dielectric constant and dielectric loss tangent [78]. In polycrystalline materials, the grains are separated by grain boundaries. Space charge polarization arises when electrons get accumulated at the grain boundaries. In the high-frequency region, as the AC field increases, more electrons will accumulate at the grain boundaries [31].

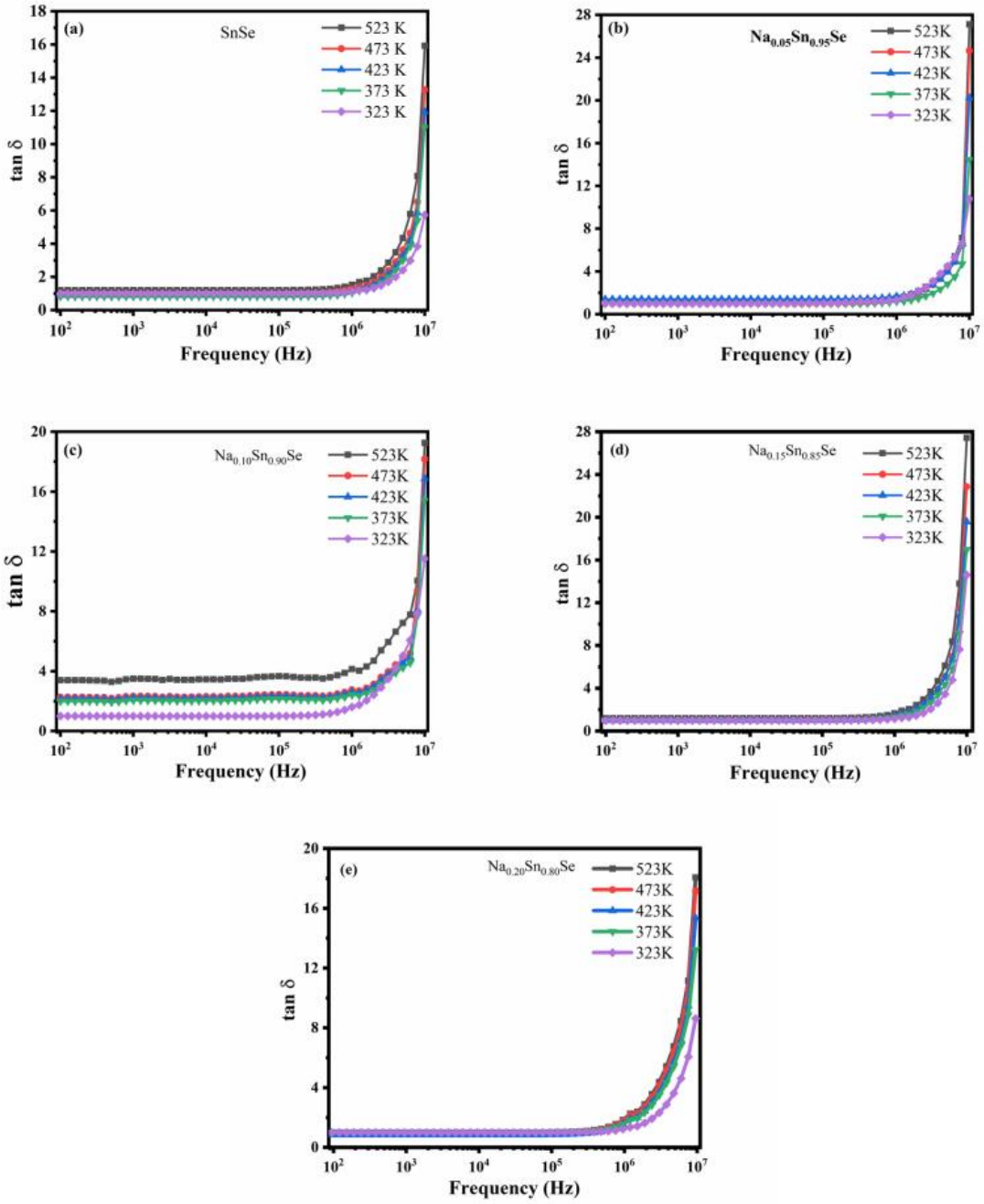

Figure 3.9 Variation of loss tangent versus Frequency of (a) SnSe, (b) $Na_{0.05}Sn_{0.95}Se$, (c) $Na_{0.10}Sn_{0.90}Se$, (d) $Na_{0.15}Sn_{0.85}Se$, and (e) $Na_{0.20}Sn_{0.80}Se$ respectively.

The results for the AC conductivity measurements for all compositions of $Na_xSn_{1-x}Se$ and temperatures from 323 to 523 K are depicted in fig. 3.10(a-e). From fig. 3.10(a-e), it is observed that there is a plateau region that corresponds to dc contribution σ_{dc} starting from the low frequency of measurement to around 3.16 MHz. The $\sigma_{dc,}$ increases as the temperature increases for all compositions. The dispersion in conductivity seen at lower frequencies can be attributed to non-adiabatic hopping of charge carriers between impurity sites.

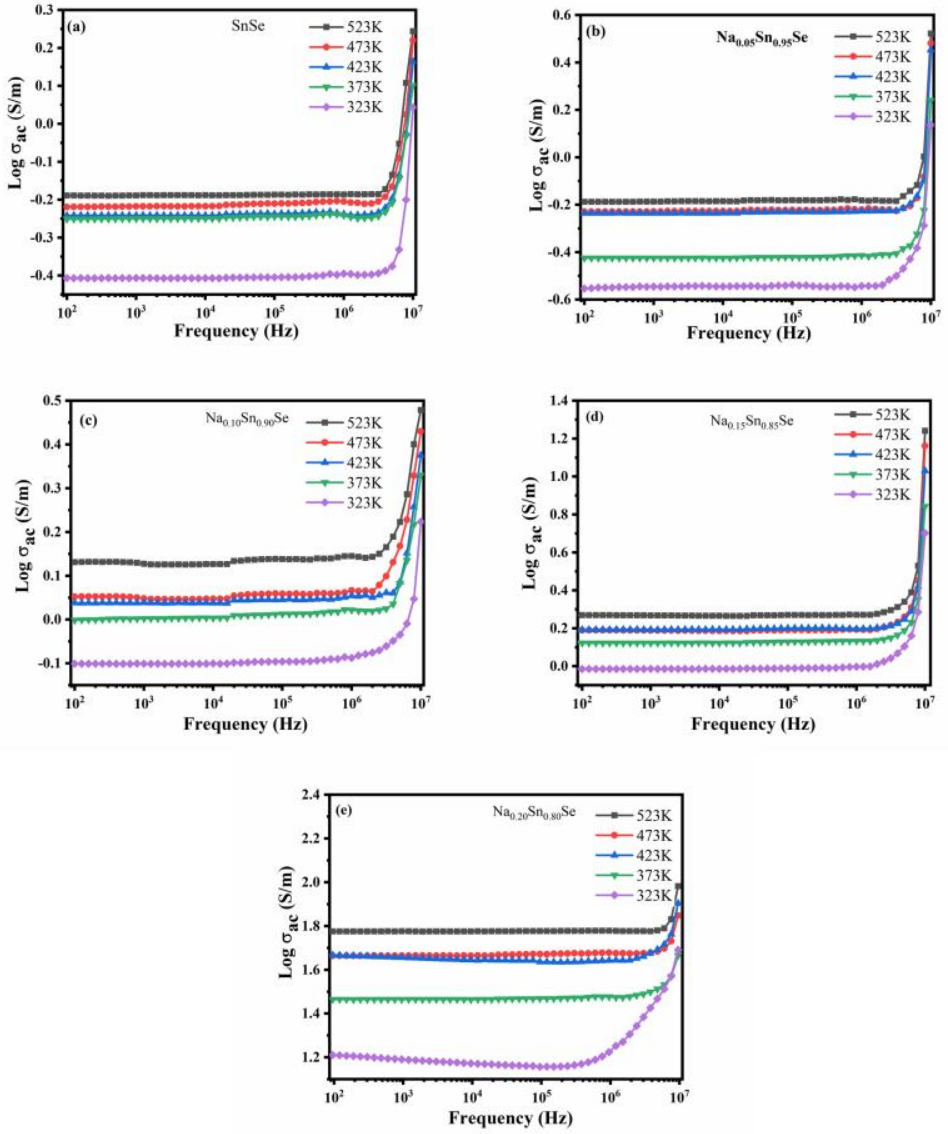

Figure 3.10 Variation of AC conductivity versus Frequency of (a) SnSe, (b) $Na_{0.05}Sn_{0.95}Se$, (c) $Na_{0.10}Sn_{0.90}Se$, (d) $Na_{0.15}Sn_{0.85}Se$, and (e) $Na_{0.20}Sn_{0.80}Se$ respectively.

The value of AC conductivity increases with Na concentration and temperature. A high value of AC conductivity is obtained for $Na_{0.20}Sn_{0.80}Se$ amongst all compositions. We believe that the possible reason for the high AC conductivity in Na doped samples is due to the presence of Na at grain boundaries combined with lowered porosity obtained due to a

high density of 97% achieved (Table 3.1). The effects of high pressures on $Na_xSn_{1-x}Se$ have been reported by B.Cai et.al [79] wherein for the samples with densities up to 94%, the electrical conductivity was found to increase with Na concentration. The enhancement of electrical conductivity by Na doping has also been reported by T R Wai et.al [49]. In compacted disk-shaped pellets of polycrystalline materials, a large number of defects are generated at the grain boundaries such as porosities, dangling bonds, etc. However, the degree of existence of these defects is dependent on the pressure and duration of temperature applied simultaneously during compaction. Further, the decrease in the crystallite size also causes an increase in electrical conductivity with an increase in Na concentration. The reduced crystallite size also favours grain boundary ionic diffusivity [32,80]. The value of 's' is obtained from the slope of Frequency versus Log σ_{ac} in the increasing portion (after subtraction of the dc component) as shown in fig. 3.11(a) and the values are found to vary from 0.05 to 0.793. The value of 's' decreases as temperature increases implying a correlated barrier hopping (CBH) mechanism. Variation of (1-s) as afunction of temperature is shown in fig. 3.11(b). Figure 3.11(c) shows the Arrhenius plot for all $Na_xSn_{1-x}Se$ samples at a frequency of 100 kHz. The activation energy is calculated from the slopes of the plots and is found to increase with the concentration of Na as seen in fig. 3.11(d).

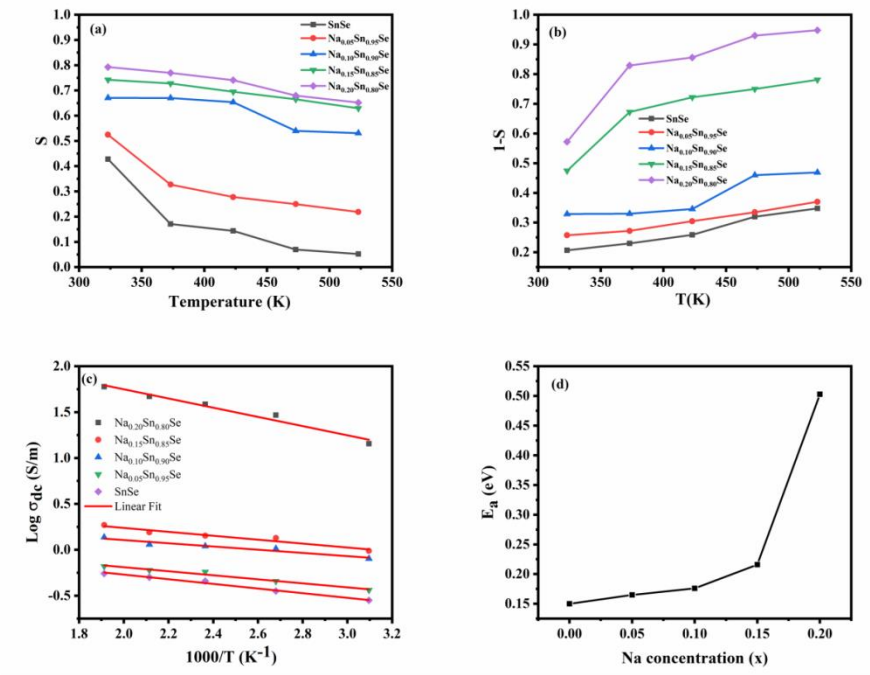

Figure 3.11 (a) Variation of frequency exponent 's' versus temperature, (b) Variation of (1-s) versus temperature, (c) Arrhenius plot for calculation of activation energy at 100 kHz, and (d) Variation of activation energy versus concentration of Na.

Table 3.3 Values of frequency exponent 's', activation energy (E_a), and maximum barrier height (W_m) at different temperatures for all $Na_xSn_{1-x}Se$ samples.

Composition	Temperature (K)	Frequency exponent (s)	Activation Energy (E_a) (eV)	W_m (meV)
SnSe	323	0.793		
	373	0.770		
	423	0.741	0.150	1.800
	473	0.680		
	523	0.652		
$Na_{0.05}Sn_{0.95}Se$	323	0.743		
	373	0.728		
	423	0.695	0.165	1.530
	473	0.665		
	523	0.623		
$Na_{0.10}Sn_{0.90}Se$	323	0.671		
	373	0.670		0.680
	423	0.654	0.176	
	473	0.540		
	523	0.531		
$Na_{0.15}Sn_{0.85}Se$	323	0.525		
	373	0.328		
	423	0.278	0.216	0.560
	473	0.250		
	523	0.219		
$Na_{0.20}Sn_{0.80}Se$	323	0.428		
	373	0.171		
	423	0.144	0.503	0.685
	473	0.070		
	523	0.052		

Complex electrical modulus spectroscopy is a very useful technique to extract bulk response and to obtain a better understanding of relaxation and conduction mechanisms on the complex plane of M' versus M'' at different temperatures. It gives information about the differentiation between electrode polarization and grain boundary conduction. To remove high loss effects at the low-frequency region, electrical modulus studies have been investigated for all $Na_xSn_{1-x}Se$ samples at different temperatures. Figure 3.12(a-e) depicts the frequency dependence of M' for $Na_xSn_{1-x}Se$ (x=0.00 to 0.20) respectively. In the low-frequency region, the M' values are found to be very low and tend to zero indicating the elimination of electrode polarization. The values of M' increases with frequency for all compositions and is dispersed at high frequencies. The dispersion in M' at high frequencies is related to the short-range conduction of charge carriers. The M' value decreases with temperature in the high-frequency region for all compositions. This behaviour of M' is due to the increased hopping rate influenced by thermal agitations.

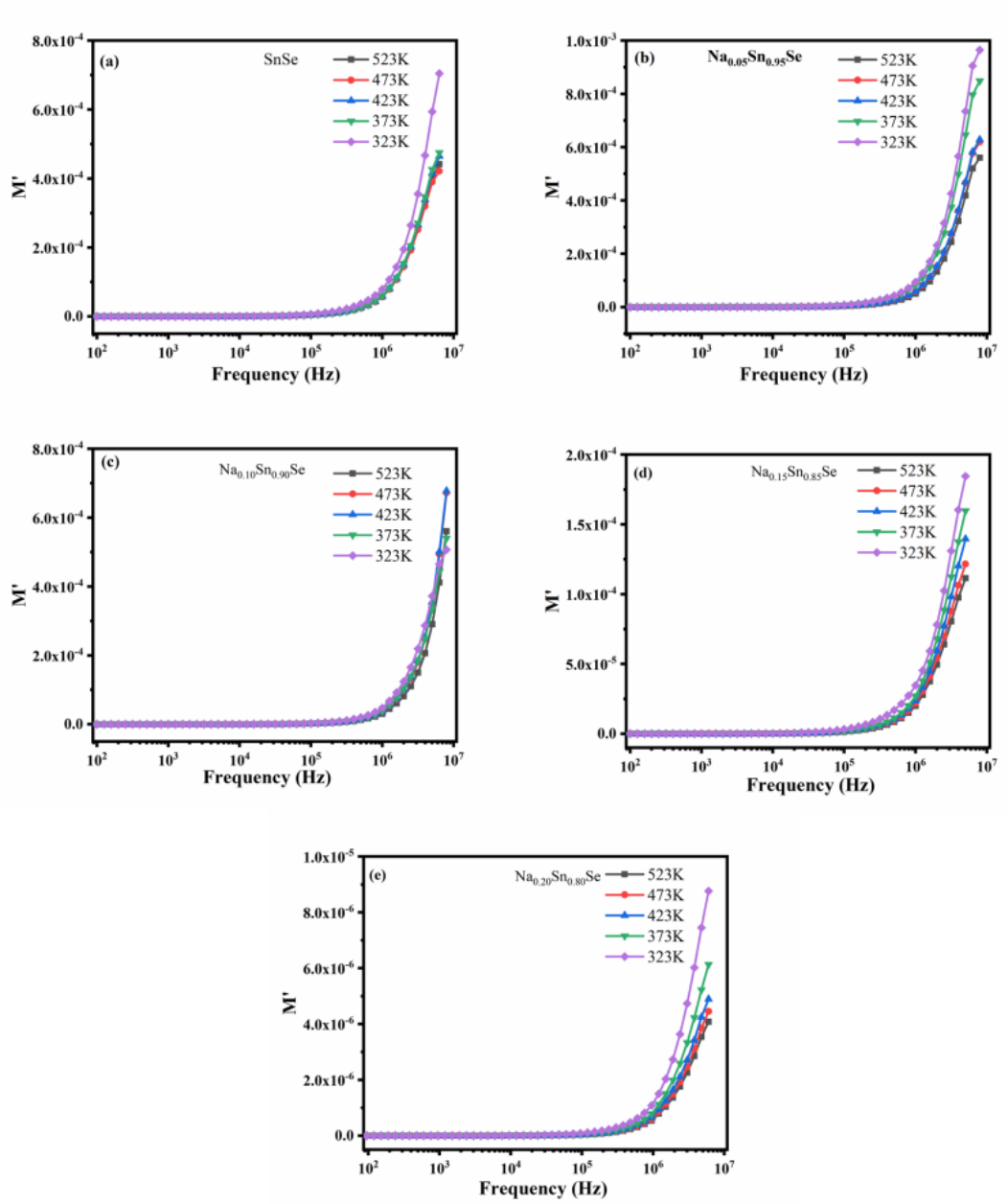

Figure 3.12 Variation of the real part of electrical modulus versus Frequency of **(a)** SnSe, **(b)** $Na_{0.05}Sn_{0.95}Se$, **(c)** $Na_{0.10}Sn_{0.90}Se$, **(d)** $Na_{0.15}Sn_{0.85}Se$, and **(e)** $Na_{0.20}Sn_{0.80}Se$ respectively.

Figure 3.13(a-e) shows the frequency dependence of M" for $Na_xSn_{1-x}Se$ (x=0.00 to 0.20) respectively. The M" for all $Na_xSn_{1-x}Se$ samples increases with frequency. It reaches a maximum at 3.8 MHz and decreases thereafter. This indicates the long-range mobility of charge carriers. The occurrence of long-range mobility is related to the hoping mechanism [81]. For frequencies beyond the peak frequency, the carriers are confined to potential wells being mobile over a short distance [82]. The peak is shifted towards the high-frequency region as temperature increases and this shift represents the conductivity. The peak amplitude also decreases with increasing temperature for all compositions.

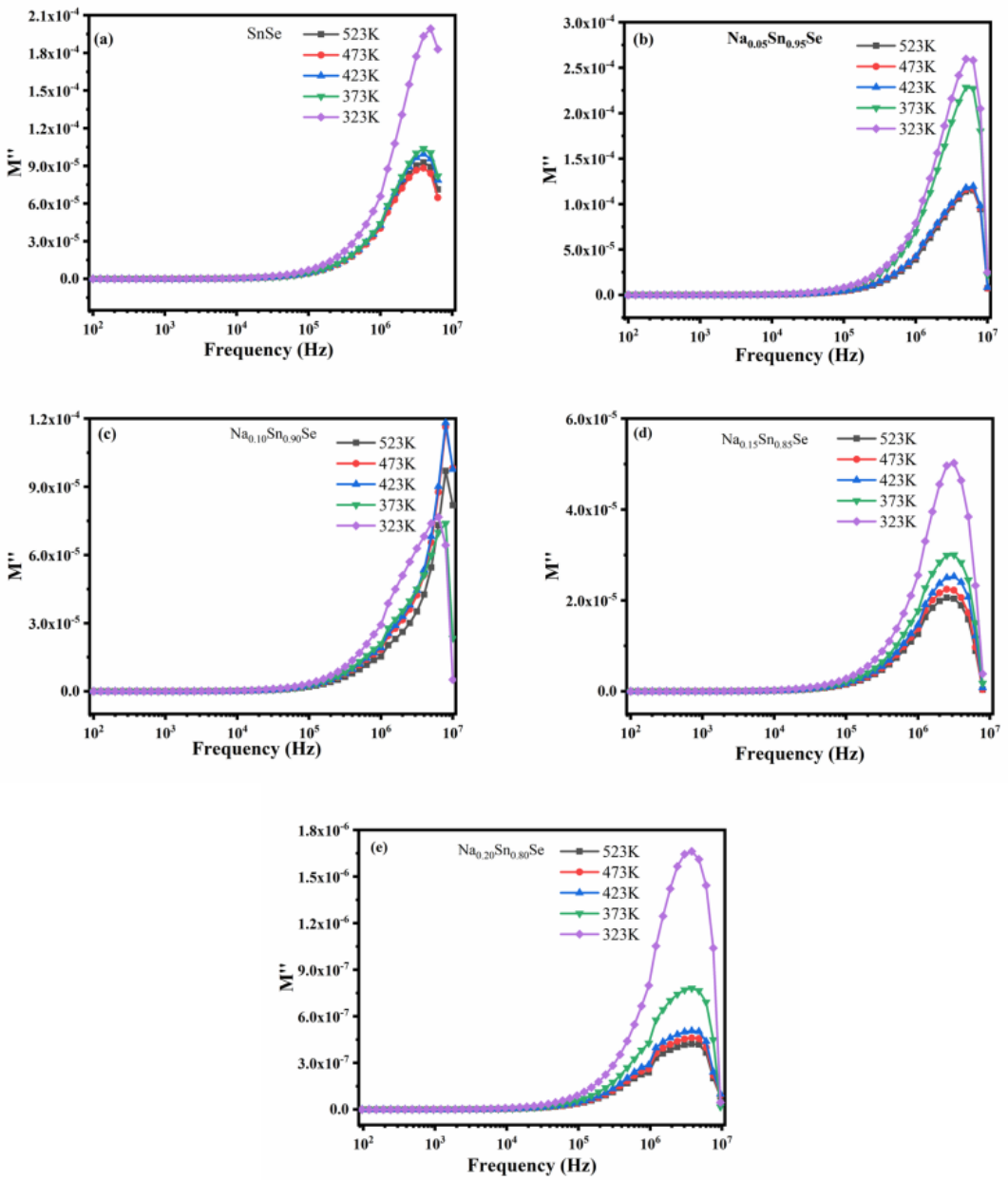

Figure 3.13 Variation of the imaginary part of electrical modulus versus Frequency of **(a)** SnSe, **(b)** $Na_{0.05}Sn_{0.95}Se$, **(c)** $Na_{0.10}Sn_{0.90}Se$, **(d)** $Na_{0.15}Sn_{0.85}Se$,and **(e)** $Na_{0.20}Sn_{0.80}Se$ respectively.

The complex electrical modulus spectrum (M' versus M'') for all the samples are shown in fig. 3.14(a-e). Non-Debye type relaxation is observed due to an incomplete formation of single semi-circular arcs. The semi-circles are found distorted with their centers located below the x-axis. The semi-circular arcs in the low-frequency region represent the presence of grain boundaries. It can also be concluded that the radius of semi-circular arcs decreases as temperature increases suggesting that the conduction processes may be due to temperature-dependent hopping conduction.

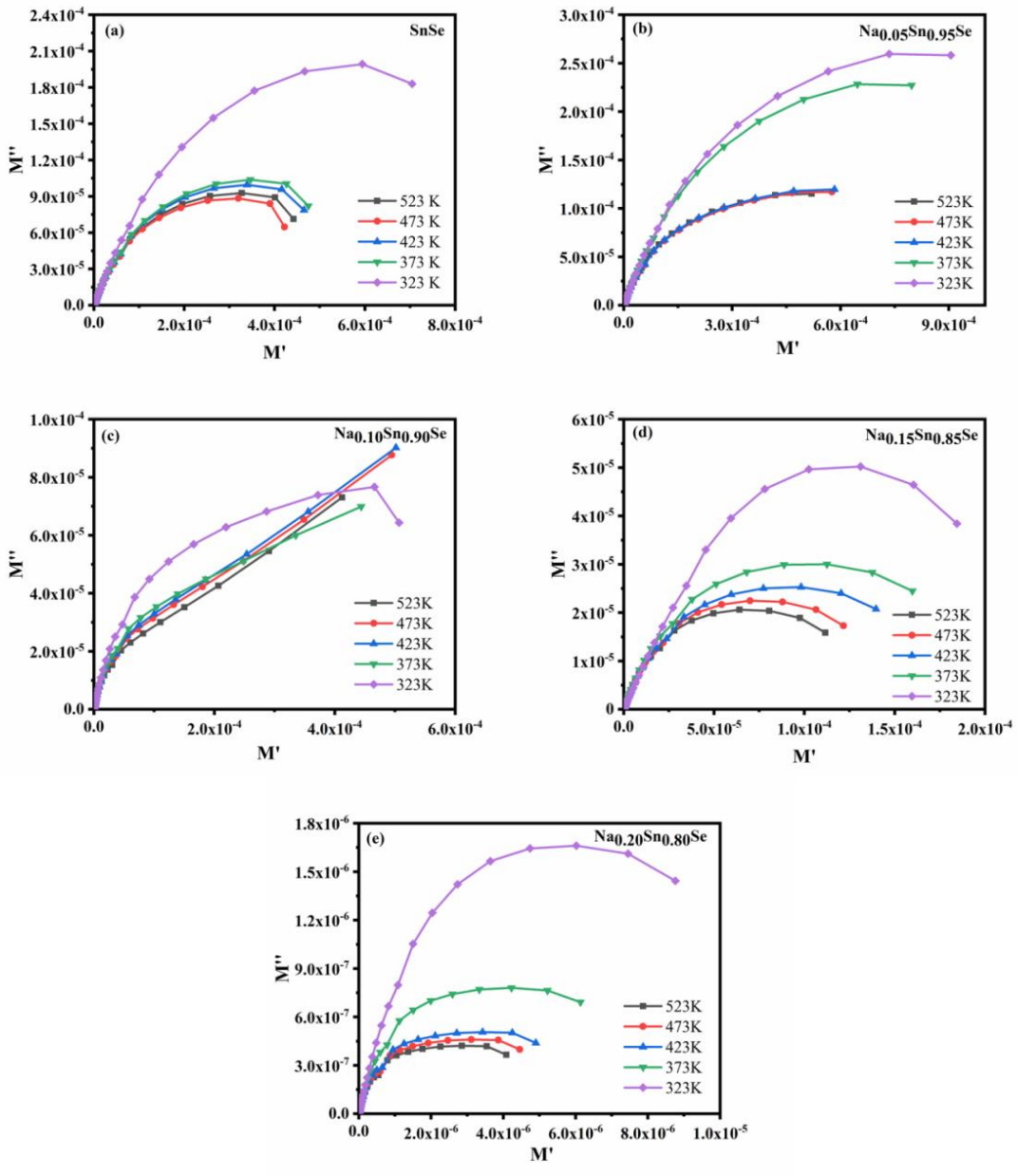

Figure 3.14 Variation of Imaginary part of electrical modulus versus Real part of electrical modulus of (a) SnSe, (b) $Na_{0.05}Sn_{0.95}Se$, (c) $Na_{0.10}Sn_{0.90}Se$, (d) $Na_{0.15}Sn_{0.85}Se$,and (e) $Na_{0.20}Sn_{0.80}Se$ respectively.

3.4 Conclusions

$Na_xSn_{1-x}Se$ polycrystals (x = 0.00 to 0.20 with a step of 0.05) were successfully synthesized by hydrothermal method. XRD studies confirmed that all the samples were in single phase and the average crystallite size decreased from 132 to 83 nm as Na doping increases. SEM images revealed a 2D plate-like morphology for undoped SnSe. With increasing Na concentration, these 2D plate-like structures cross-linked to each other and formed 3D flower-like structure at x = 0.20. Further, this flower-like morphology helped in enhancing the dielectric properties of $Na_xSn_{1-x}Se$ polycrystals. The optical bandgap studies

revealed that both direct and indirect bandgap values decreased as doping concentration increased which can contribute to an increase in AC conductivity. This feature suggests that the $Na_xSn_{1-x}Se$ polycrystals will find promising applications in optoelectronic devices, photo catalytic materials, and thermoelectrics, etc. The room temperature dielectric study shows that $Na_{0.20}Sn_{0.80}Se$ exhibited high value of ac conductivity and dielectric constant. The temperature-dependent dielectric studies showed that the maximum values of the real part of permittivity and dielectric losses were obtained for higher doping concentration at low frequencies and there is no remarkable change observed at higher frequencies. The low value of the dielectric constant and dielectric loss at high frequencies appears to be promising for electro-optic and solar cell devices. The doping concentration (Na) has a significant effect on AC conductivity and it is found to be maximum for $Na_{0.20}Sn_{0.80}Se$ sample at high temperature (523 K). The AC conductivity follows Jonscher's power-law relation and the variation of the 's' parameter with temperature indicated that the CBH model is responsible for the charge carriers in the hopping mechanism. The temperature-dependent dc conductivity (σ_{dc}) is a thermally activated process and the activation energy (E_a) increased with Na concentration. The electrical modulus studies revealed the dispersive nature and impact of grain boundary effects in all the $Na_xSn_{1-x}Se$ samples. The high values of the real part of permittivity and AC conductivity will find the possible application of $Na_xSn_{1-x}Se$ polycrystals in high-energy capacitive storage devices.

CHAPTER 4: Optical and Dielectric properties of Potassium doped Tin Selenide polycrystals

4.1 Introduction

We have discussed earlier that doping of alkali metals can influence the structural, optical, and electrical properties, In the previous work, we have investigated the structural, optical, and dielectric properties of Na doped SnSe [83]. Recently Chan-Chieh reported that potassium can enhance electrical transport properties with good solubility in SnSe [46]. Yue-Xing Chen et al reported that the introduction of K into SnSe has a dual effect: it enhances the carrier concentration and reduces the Sn oxides [47]. However, to the best of our knowledge, no reports are available on AC conductivity and dielectric properties of K-doped SnSe in a broad temperature range hence; an effort is made to study the optical and dielectric properties of K-doped SnSe samples. A very few reports exist on the K-doped SnSe prepared by solid-state methods such as mechanical alloying and conventional melting [46–49,84]. No reports exist on K-doped SnSe using aqueous solution methods. In the current study, we used hydrothermal method to prepare K-doped SnSe polycrystals, due to its advantages that have been explained earlier.

In the present study, we have synthesized K-doped SnSe polycrystals using a simple hydrothermal method. The influence of K on the structural, morphological, and optical studies of SnSe was studied. Further temperature-dependent dielectric studies were investigated in a frequency range of 100 Hz-10 MHz and over a temperature range of 323-523 K.. We concluded that Correlated Barrier Hopping (CBH) is the possible mechanism for the electronic transport of charge carriers. Electrical modulus studies for all the samples revealed that there is a non-Debye type relaxation is present in all the samples

4.2 Synthesis of $K_xSn_{1-x}Se$ polycrystals

$K_xSn_{1-x}Se$ polycrystalline samples with x= 0.00, 0.05, 0.10, 0.15 and 0.20 were synthesized by hydrothermal method. The chemical reagents used in the synthesis procedure are procured from MERCK and used as it is without any further purification process. Equimolar solutions of $SnCl_2.2H_2O$ (99.9%), Se metal powder (98%) were taken as precursors of Sn^{+2} and Se^{-2} sources respectively and KCl (99.9%) is used as potassium precursor. Initially, to prepare K-doped SnSe, the stoichiometric molar concentration of $SnCl_2.2H_2O$ was taken into 100 ml of De-ionized water and it is stirred

for 5 min. Then the stoichiometric molar concentration of KCl is added to the previous mixture and stirred for another 5 min. Further, 6 g of NaOH (85%) is added to the solution and stirred for 10 min. The color of the solution is turned transparent. The stoichiometric molar concentration of Se metal powder is added to the transparent solution followed by stirring for 15 min. Then to reduce the Se source 2 g of $NaBH_4$ (99.9%) is mixed into the obtained solution and stirred for 30 min. After the reaction time is over the final solution is transferred into a hydrothermal autoclave of capacity 120 ml. the autoclave was kept in a vacuum oven at 170 ^oC for 12 h. For different K doping, concentrations of $SnCl_2.2H_2O$ and KCl are varied. Finally, the autoclave was allowed to cool to room temperature. Further, the solution was taken out from the autoclave and washed, filtered with ethanol and DI water several times. Then the obtained product was kept in an oven for drying at 80 ^oC overnight. Pure SnSe was also prepared by the same procedure explained above without the addition of potassium precursor.

4.3 Results and Discussion

4.3.1 X-Ray Diffraction

Figure 4.1(a) shows X-Ray diffraction pattern of $K_xSn_{1-x}Se$ for x = 0.00, 0.05, 0.10, 0.15, and 0.20 polycrystals. The samples are in single-phase and indexed well by indicating the lattice planes (2 0 1), (2 1 0), (1 1 1), (4 0 0), (3 1 1), (4 1 1), (0 2 0), (5 0 1), (5 1 1) and (4 2 0). The XRD data is in good agreement with standard PDF file no: #48-1224 [14,85]. All the $K_xSn_{1-x}Se$ compositions have the strongest intensity along the direction of the (4 0 0) plane indicating that the preferred orientation is along (4 0 0) direction. With increasing concentration of the dopant K to 0.05, the intensity of the (1 1 1) plane is increased, followed by a decrease for compositions x=0.10 and 0.15, and thereafter it showed a slight increase for x=0.20. However, the intensity of (4 0 0) plane is decreased for all the compositions with increasing K doping concentration. In Fig. 1b, the lattice parameters values are plotted against K concentration (x). The calculated lattice parameters are matched well with the standard values (a = 11.49 Å, b = 4.153 Å, c = 4.44 Å, PDF#48-1224). From fig. 4.1(b), it is shown that the lattice parameter 'a' values slightly increase as the concentration of K increases whereas there is less variation along the b and c axis. This is because the intensity of (4 0 0) peak is higher than that of other peaks in all the samples suggesting preferential orientation along a-axis [47]. The increase in the values of lattice parameters happens when the small-sized Sn atom (0.112 nm) is substituted with the small-sized K atom (0.138 nm) which leads

to lattice expansion and increase of lattice constant. The unit cell volume corresponding to the lattice parameters shows an increasing trend with K doping. The value of average crystallite size (D) is decreased as the doping concentration of K increases and it is varied from 136 to 97 nm as depicted in fig. 4.1(c). The lattice parameter values, crystallite size, and cell volume for all samples were shown in Table 4.1.

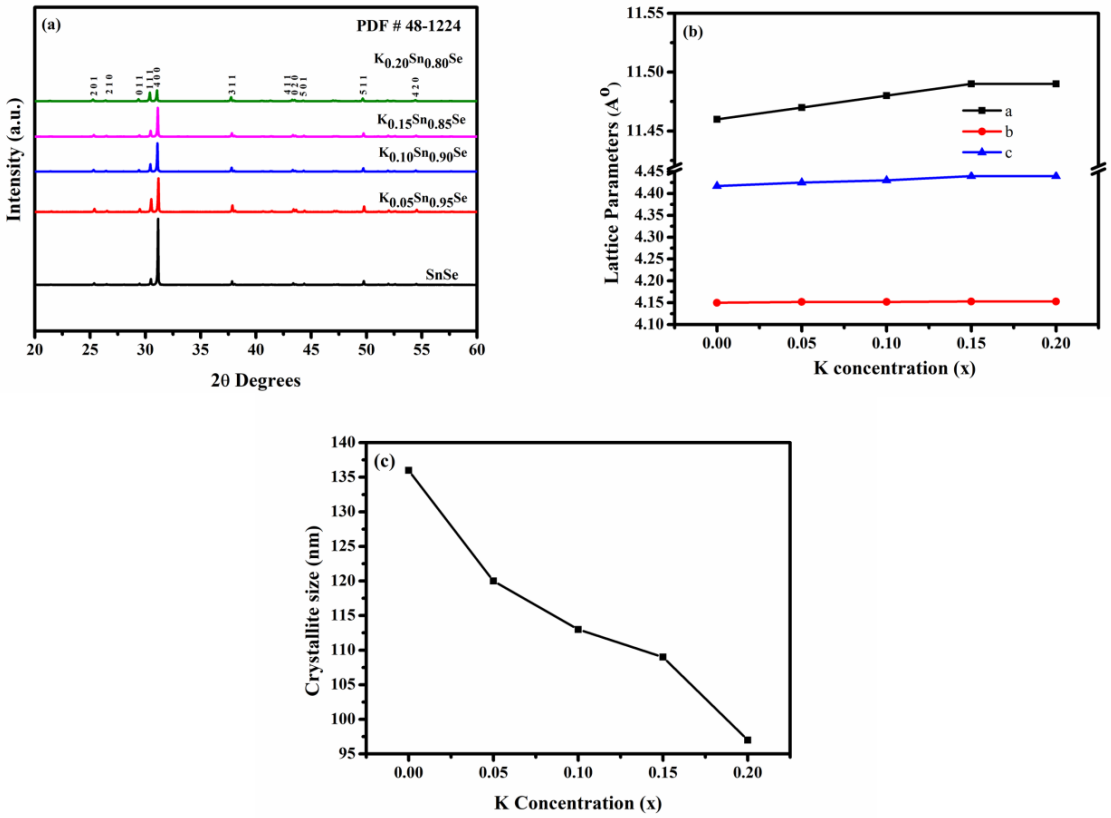

Figure 4.1 (a) XRD pattern of all $K_xSn_{1-x}Se$ samples, (b) Lattice parameter variation with concentration (x) of K, and (c) crystallite size Vs. K doping concentration.

Table 4.1 Lattice constants, cell volume, and crystallite size (D) of all the $K_xSn_{1-x}Se$ compositions.

Sample	Lattice constants			Cell volume(Å)^3	D
	a (Å)	b (Å)	c (Å)		(nm)
SnSe	11.46	4.15	4.417	210.0	136
$K_{0.05}Sn_{0.95}Se$	11.47	4.152	4.425	210.7	120
$K_{0.10}Sn_{0.90}Se$	11.48	4.152	4.43	211.2	113
$K_{0.15}Sn_{0.85}Se$	11.49	4.153	4.44	211.7	109
$K_{0.20}Sn_{0.80}Se$	11.49	4.153	4.44	211.7	97

4.3.2 Morphology and elemental analysis

Figure 4.2 (a-e) reveals the SEM images of all the $K_xSn_{1-x}Se$ polycrystals. It is seen that the undoped SnSe revealed a profile of non-uniform plate-like structures (fig. 4.2(a)). The size of the plates is decreased as the K doping into SnSe increases (fig.4.

2(b-d)). In addition, for $K_{0.20}Sn_{0.80}Se$ composition (fig.4.2(e)), it is noticed that there is a combination of small plate-like structures that get agglomerated with small nano rod-like structures. The decrease in the size of the plate-like structures with K doping is possibly due to the lattice distortion induced by the replacement of small-sized Sn with large-sized K and also due to the decrease in average crystallite size when K doping increases. This results in a decrease in grain size [86]. The elemental composition was confirmed for all the samples through EDAX as shown in fig. 4.3(a-e). The Edax spectra show the existence of Sn, Se, and K in the stoichiometric compositions. The atomic ratio for pure SnSe is 1.06:1 which is nearly stoichiometric and is in good agreement with the standard value [85,87,88]. The ratio is lowered significantly as K doping into SnSe increases because Sn composition decreases due to the substitution of K into it.

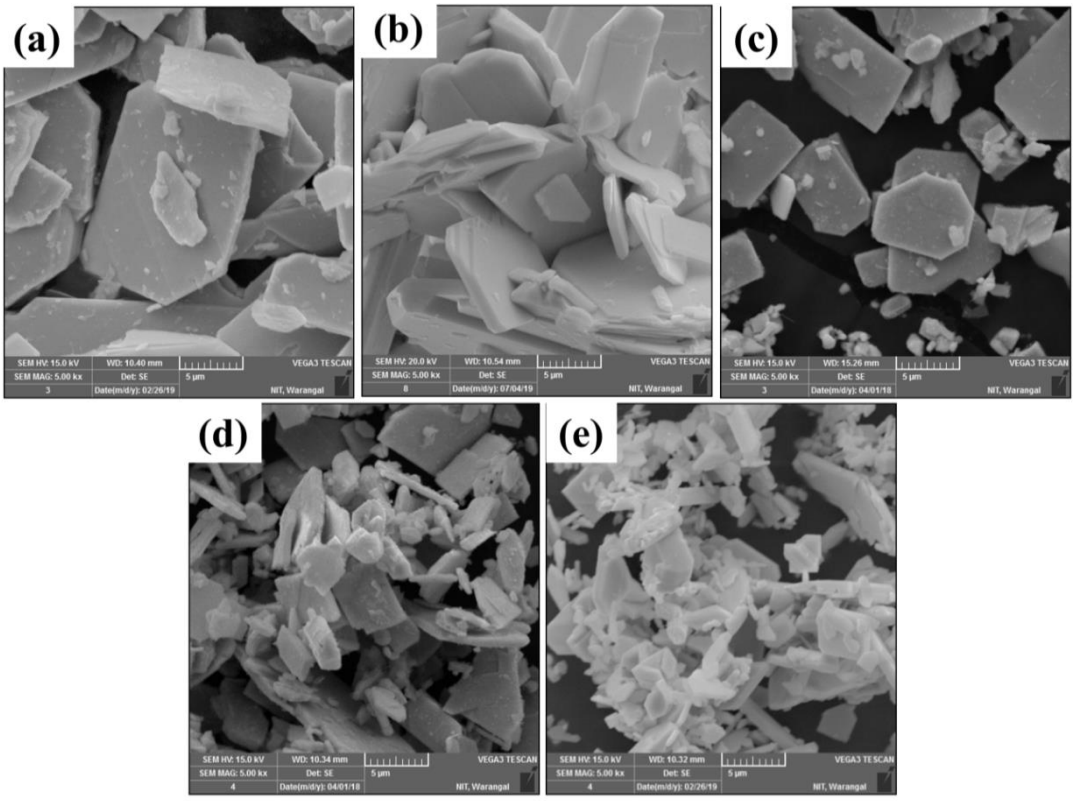

Figure 4.2 SEM images of $K_xSn_{1-x}Se$ polycrystals **(a)** x = 0.00, **(b)** x = 0.05, **(c)** x = 0.10, **(d)** x =0.15, and **(e)** x = 0.20 at 5 μm range.

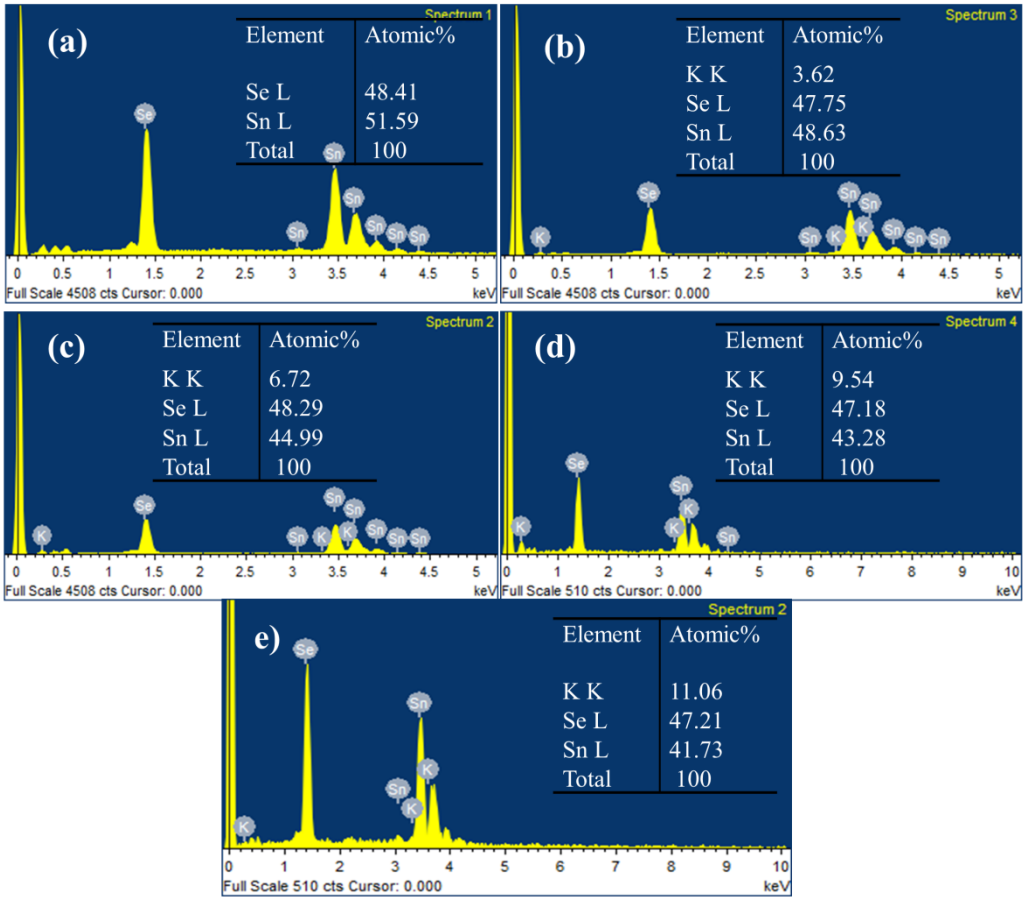

Figure 4.3 EDAX spectra of $K_xSn_{1-x}Se$ polycrystals (a) x = 0.00, (b) x = 0.05, (c) x = 0.10, (d) x = 0.15, and (e) x = 0.20.

To further understand the morphology of K-doped SnSe samples high-resolution transmission electron microscope studies were carried out. Figure 4.4(a) shows the TEM image of the $K_{0.20}Sn_{0.80}Se$ sample. From fig.4.4(a) and (b), it is observed that the sample possesses a rectangular plate-like structure, which is connected with small Nano rods at the edges and is inconsistent with the SEM observation for $K_{0.20}Sn_{0.80}Se$ [14,89]. The selected area diffraction pattern for the $K_{0.20}Sn_{0.80}Se$ sample is shown in fig.4.4(c), and it displays the formation of diffraction rings confirming the polycrystalline nature of the sample indicating the planes (2 1 0), (4 0 0), (3 1 1) and (5 1 1) which are observed from XRD pattern. Figure.4.4(d) shows the high-resolution TEM image of the $K_{0.20}Sn_{0.80}Se$ sample showing lattice fringes with d-spacing of 3.3 Å and 2.88 Å corresponding to (2 1 0) and (4 0 0) planes respectively.

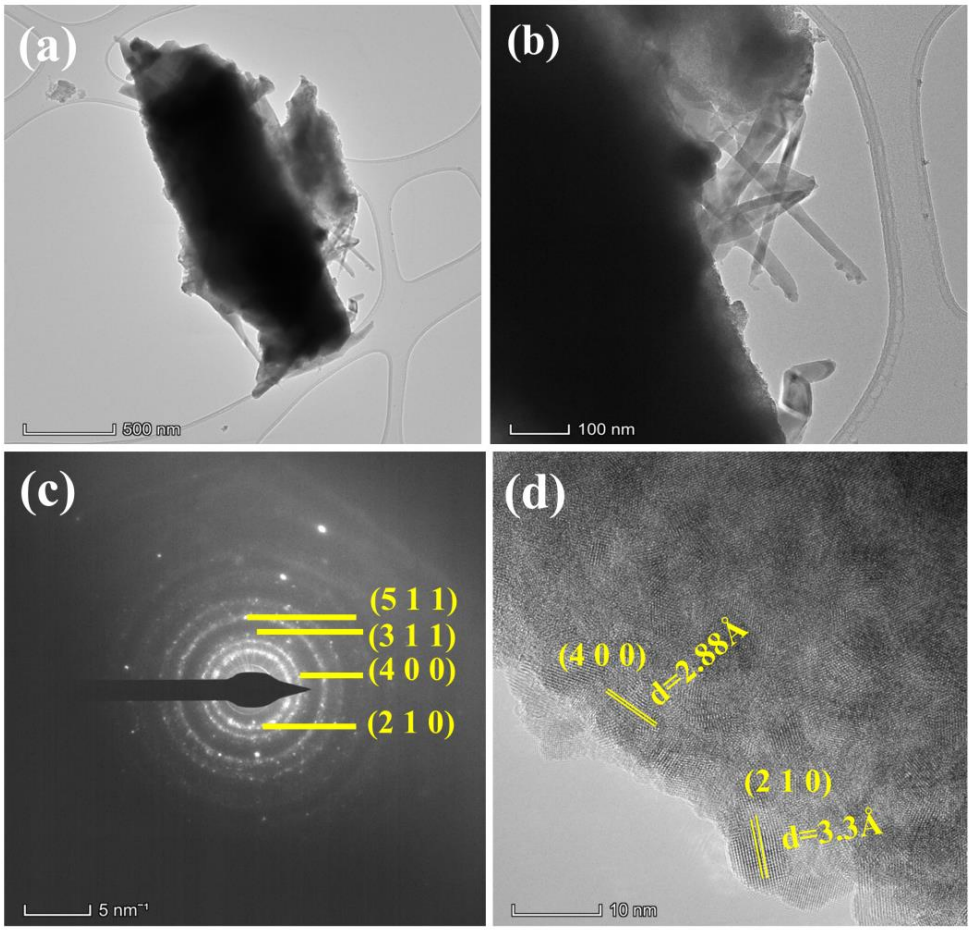

Figure 4.4 (a) TEM image of $K_{0.20}Sn_{0.80}Se$ sample, (b) Magnified TEM image of $K_{0.20}Sn_{0.80}Se$ sample, (c) SAED pattern of $K_{0.20}Sn_{0.80}Se$ sample, and (d) High-resolution TEM image of $K_{0.20}Sn_{0.80}Se$ sample indicating d-spacing.

4.3.3 UV-VIS-NIR Diffuse Reflectance Spectroscopy

Figure 4.5(a) shows the reflectance spectra for all $K_xSn_{1-x}Se$ samples. Figs. 4.5(b &c) depict the tauc plots of indirect and direct band gaps for all $K_xSn_{1-x}Se$ samples respectively. The indirect bandgap for the pristine SnSe is obtained as 0.817 eV, which is less and in close agreement compared to the theoretical band gap (0.9 eV). Further, it is noticed that the indirect bandgap of the K doped samples decreased from 0.817 eV to 0.709 eV as K composition increased. The direct bandgap calculated for undoped SnSe is 0.946 eV is in agreement with the theoretical value of 1.3 eV. The direct bandgap is also found to be decreased as K concentration increases into SnSe. The decrease in both the bandgaps is due to the reduction in the crystallite size as K doping increases [83]. The indirect bandgaps (0.817 eV-0.709 eV) and the direct bandgaps (0.946 eV-0.906 eV) are widely tuned after K doping into SnSe can have new possible applications in electronic and optoelectronic devices [48]. Figure 4.5(d) shows the variation of indirect and direct bandgaps as a function of K concentration. The bandgap values for $K_xSn_{1-x}Se$ polycrystals are shown in Table 4.2.

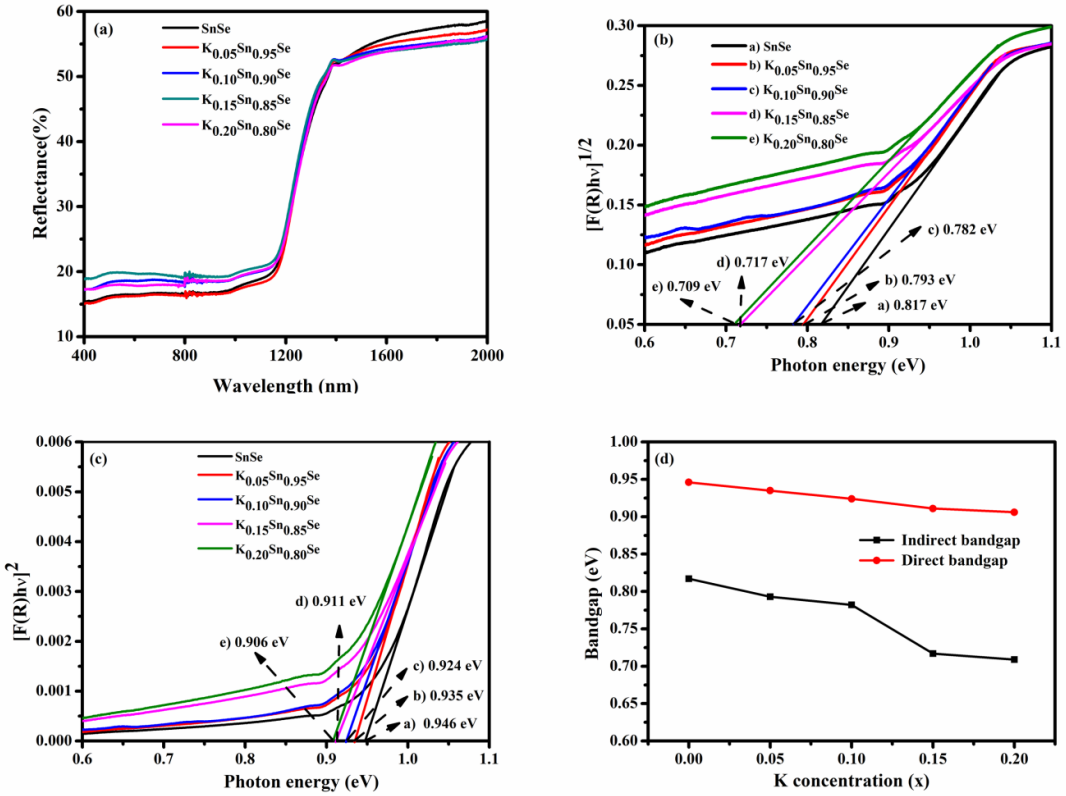

Figure 4.5 (a) Reflectance spectra of $K_xSn_{1-x}Se$ polycrystals, (b) Determination of indirect band gap using tauc plot, (c) Determination of direct bandgap using tauc plot, and (d) Indirect and direct band gaps vs. K concentration**.**

Table 4.2 Bandgap values of $K_xSn_{1-x}Se$ polycrystalline samples.

K doing concentration (x mol %)	Indirect bandgap (eV)	Direct bandgap (eV)
0	0.817	0.946
5	0.793	0.935
10	0.782	0.924
15	0.717	0.911
20	0.709	0.906

4.3.4 Dielectric studies

4.3.4.1 Room temperature dielectric studies

The dielectric properties of the materials can be influenced by various kinds of polarizations such as ionic, orientation, electronic, and space charge polarization. Dielectric properties are related to the electro-optic properties of the materials. The microelectronics industry requires materials with low dielectric constants as interlayer dielectric [90].

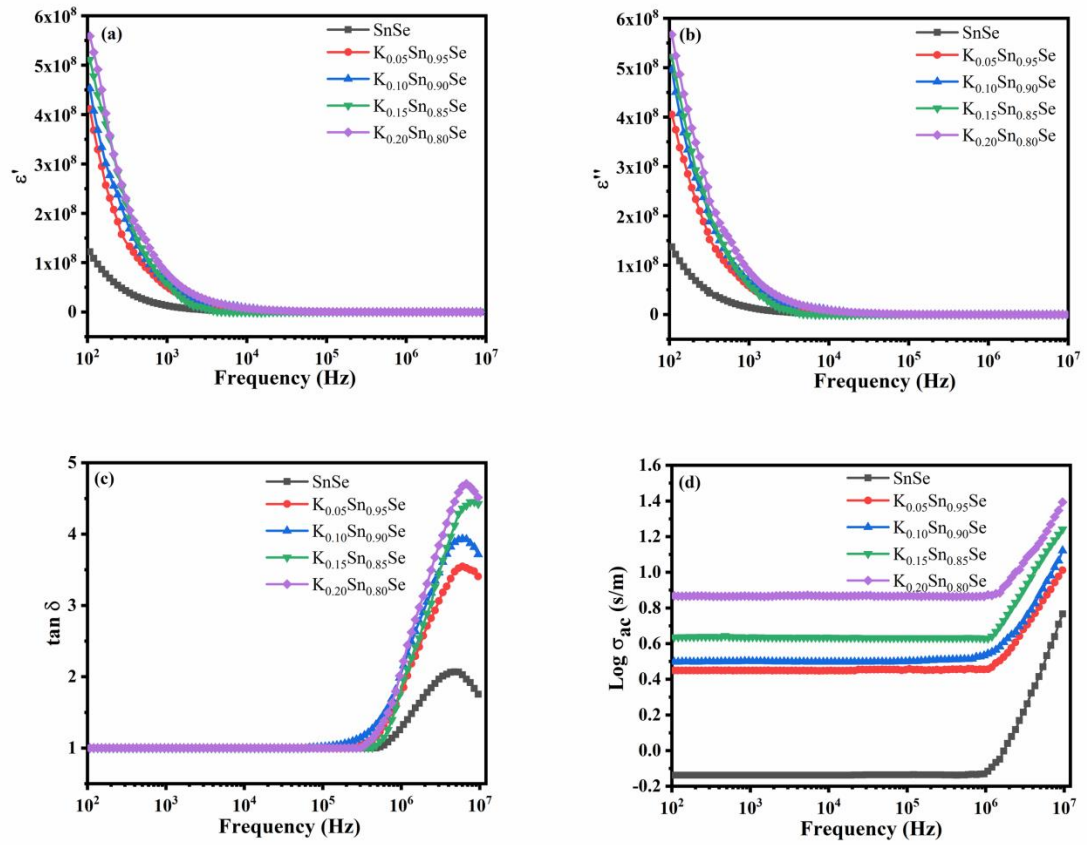

Figure 4.6 (a) Dielectric constant vs. frequency, (b) Dielectric loss vs. frequency, and (c) Dielectric loss tangent vs. frequency (d) AC conductivity vs. frequency for all $K_xSn_{1-x}Se$ samples at room temperature.

Figure 4.6(a) depicts the effect of frequency on ε' for all the $K_xSn_{1-x}Se$ samples. The trend observed in the frequency dependence of dielectric constant for $K_xSn_{1-x}Se$ samples is the same as observed in $Na_xSn_{1-x}Se$ samples. The ε' increases with K doping and a large value of it is observed for $K_{0.20}Sn_{0.80}Se$. One of the reasons for the increase in ε' is due to the morphology exhibited by the samples. For pure SnSe plate-like structures were observed. The sizes of the plates are reduced due to K doping which causes the increase in the number of grain boundaries. The $K_{0.20}Sn_{0.80}Se$ have a large number of grain boundaries due to the lowest size hence exhibited a large value of ε' compared to all other samples. The increase in the number of grain boundaries causes more charge carriers to get trapped at their boundaries which can further increase ε'. The variation of dielectric loss for all $K_xSn_{1-x}Se$ samples with frequency is depicted in fig. 4.6(b). All the samples showed high dielectric loss in low frequency region. The dielectric loss gradually decreases with increase in frequency and becomes independent of frequency in the high frequency region. The $K_{0.20}Sn_{0.80}Se$ sample exhibited large value of dielectric loss. The frequency dependence of dielectric loss tangent is shown in fig. 4.6(c). The tan δ increases as frequency increases and relaxation peaks are observed in

the high-frequency region of 1 MHz-10 MHz. The peak intensity increases and the peaks are shifted towards the high-frequency region as K doping into SnSe increases. The value of tan δ is high for the composition $K_{0.20}Sn_{0.80}Se$. Fig. 4.6(d) displays the dependence of ac conductivity on frequency for the $K_xSn_{1-x}Se$ samples. The same behavior is obtained for $K_xSn_{1-x}Se$ samples as observed in the case of $Na_xSn_{1-x}Se$ samples. The $K_{0.20}Sn_{0.80}Se$ has obtained a large value of ac conductivity among all the K-doped SnSe samples. However, $Na_{0.20}Sn_{0.80}Se$ exhibited a large value of ac conductivity than $K_{0.20}Sn_{0.80}Se$. This might be due to the large doping ability of Na than K into SnSe and also morphology also plays a crucial role in the value of ac conductivity. $Na_{0.20}Sn_{0.80}Se$ exhibited 3D flower-like morphology which has more number of grain boundaries produces a high ac conductivity due to the accumulation of charges at the boundaries increasing ac conductivity. Whereas $K_{0.20}Sn_{0.80}Se$ exhibited plate-like combined with rod-like morphology has less number of grain boundaries compared to $Na_{0.20}Sn_{0.80}Se$.

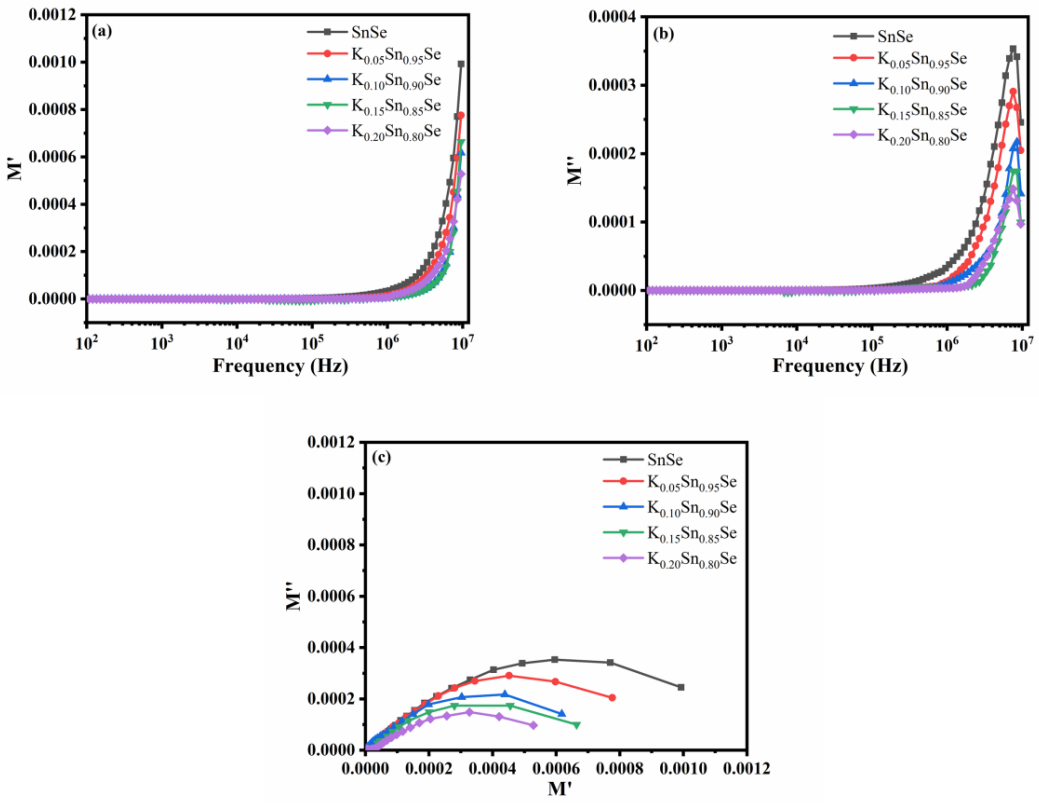

Figure 4.7 (a) Variation of M' as a function Frequency, (b) Variation of M'' as a function of Frequency, and (c) Variation M'' vs. M' for all $K_xSn_{1-x}Se$ samples.

Figure 4.7(a) displays the effect of frequency on M' for $K_xSn_{1-x}Se$ samples. The values of M' is low and constant for all the K-doped SnSe samples till 320 KHz. The M' values increase as frequency increases. Dispersion is seen in the high-frequency region in all

the samples. Figure 4.7(b) displays the effect of frequency on M" for all the $K_xSn_{1-x}Se$ samples. The M" values are less and independent of frequency in the low-frequency region till 100 kHz. The rise in frequency causes the M" values to increase and relaxation peaks are observed in the high-frequency region of 1 MHz- 10 MHz. The peaks are shifted towards the high-frequency region as K doping into SnSe increases. Figure 4.7(c) shows the variation of M' vs M" for $K_xSn_{1-x}Se$ samples at room temperature. Similar behaviour is observed for $K_xSn_{1-x}Se$ samples as exhibited by $Na_xSn_{1-x}Se$ samples.

4.3.4.2 Temperature dependent dielectric studies

The dielectric constants for all the K-doped SnSe samples are depicted in fig. 4.8(a-e) in the temperature range 323 K-523 K. The ε' value is high at the low-frequency region and it found decreasing and become independent of frequency around 10 kHz as the frequency increases. The dipoles do not have sufficient time to orient themselves quickly in the direction of the ac field as frequency increases so that they begin to lag behind the applied ac field. Further, the increase in frequency causes the dipoles to completely not able to follow the applied field and the orientation of the dipoles is stopped. Hence the value of ε' reaches a constant value at high frequencies. The high value of ε' at the low-frequency region is because of the occurrence of space charge polarization. The space charges move at grain boundaries when the external ac field is applied. The dipole moments will be created which causes space charge polarization. The increase in K doping into SnSe causes an increase in the value of ε' and it is found to be highest for $K_{0.20}Sn_{0.80}Se$. One of the reasons for the increase in ε' value as K increases is due to the morphology exhibited by the samples. For undoped SnSe large plate-like structures were observed. The K doping causes the size of the plates to be reduced and thereby increases the number of grain boundaries. The $K_{0.20}Sn_{0.80}Se$ exhibited the lowest size of the plates which have a large number of grain boundaries produces an increase in the value of ε'. The increase in the number of grain boundaries causes more charge carriers to get trapped at their boundaries which can further increase ε'. The possibility of an increase in ε' as a function of temperature in each case can be attributed to the alignment of the maximum number of dipoles in the direction of the electric field as dipoles are less oriented at low temperatures. Whereas, dipoles can rotate freely at high temperatures thus increases the orientation polarization, which increases ε'. The value of ε' is increased as the temperature increased in each composition of K-doped SnSe. When the temperature increases more charge carriers

move which in results increases the value of ε'. The high values of dielectric constants for K-doped SnSe make the material excellent for applications in capacitive storage devices [37].

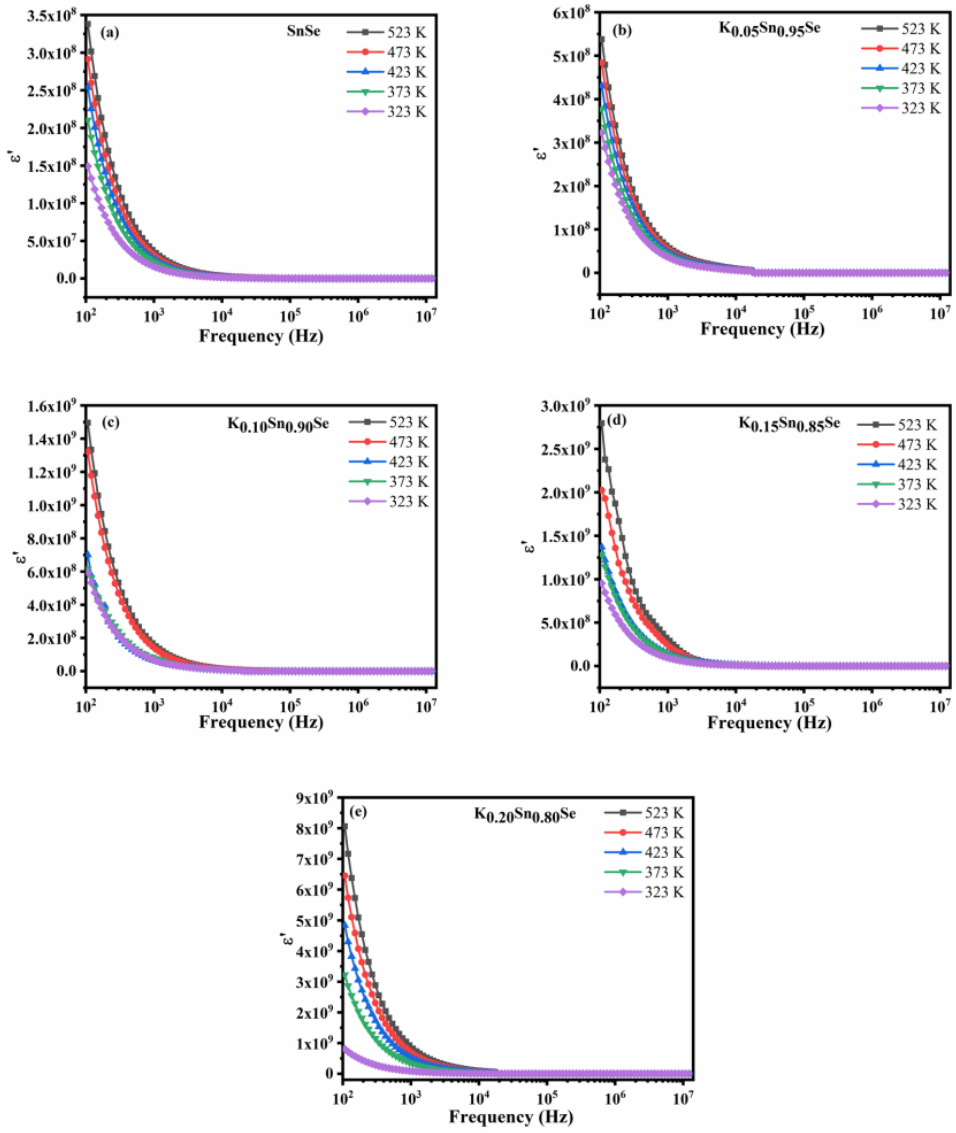

Figure 4.8 Dielectric constant vs. Frequency of (a) SnSe, (b) $K_{0.05}Sn_{0.95}Se$, (c) $K_{0.10}Sn_{0.90}Se$, (d) $K_{0.15}Sn_{0.85}Se$, and (e) $K_{0.20}Sn_{0.80}Se$ respectively in the temperature range of 323 -523 K.

The variation of dielectric loss with frequency at various temperatures for all the K-doped SnSe is shown in fig. 4.9(a–e). The ε" follows the same trend as the dielectric constant. The dielectric constant decreases and becomes constant at higher frequencies. The low value of the dielectric loss at high frequencies suggests the suitability of the material used in high-frequency-related devices [9, 31–33]. The behaviour of exhibiting low values of dielectric constant and dielectric loss at high frequencies in a sample implies that the sample possesses greater optical quality with smaller defects and this

parameter is crucial for different electro-optic devices and their applications [12,76,83,90].

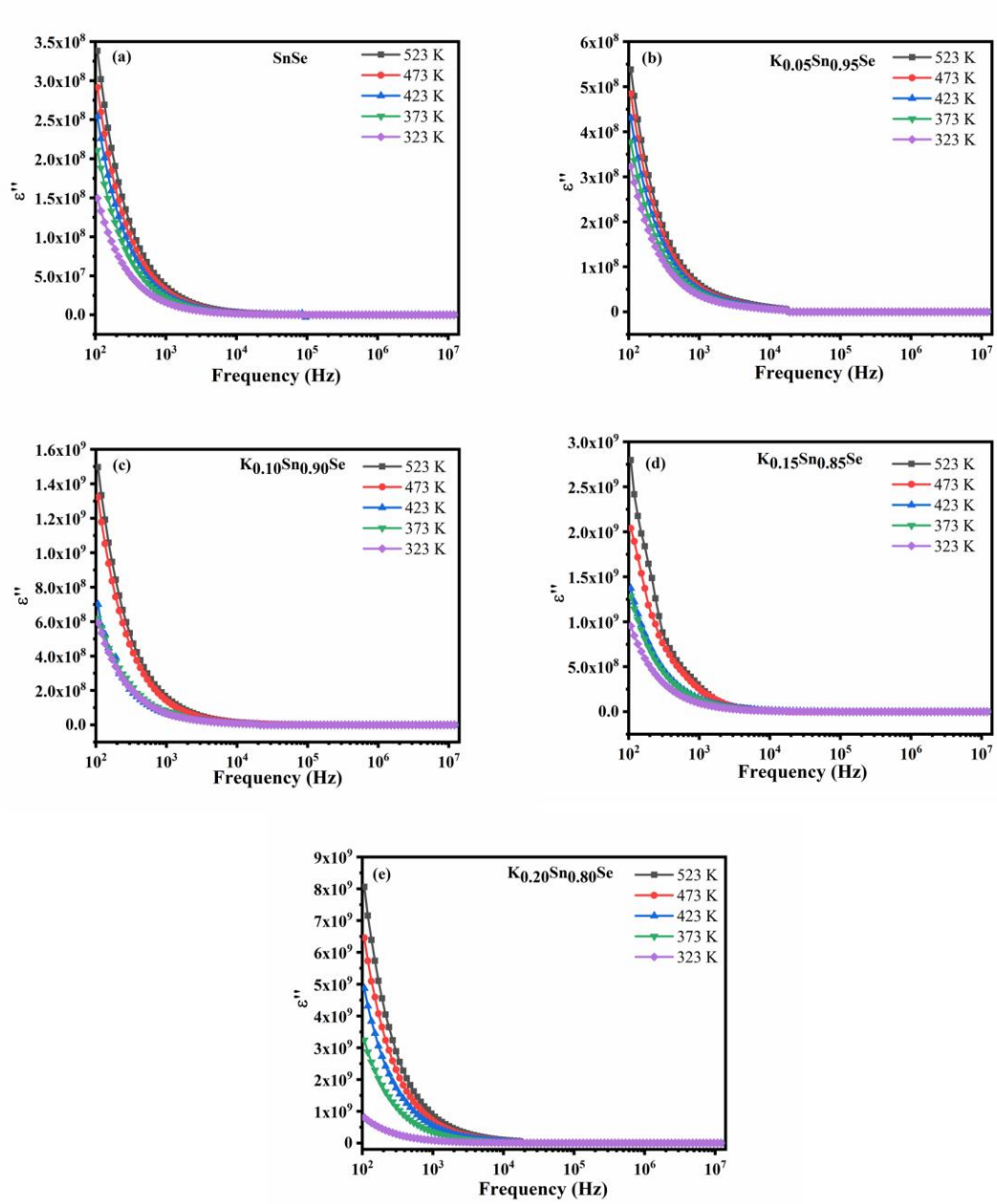

Figure 4.9 Dielectric loss vs. Frequency of (a) SnSe, (b) $K_{0.05}Sn_{0.95}Se$, (c) $K_{0.10}Sn_{0.90}Se$, (d) $K_{0.15}Sn_{0.85}Se$, and (e) $K_{0.20}Sn_{0.80}Se$ respectively in the temperature range of 323-523 K.

The variation of loss tangent as a function frequency at different temperatures for pure and K-doped samples is shown in fig. 4.10(a-e). It is low and independent of frequency for all the samples in the low-frequency region. The loss tangent increases as frequency increases and relaxation peaks are observed in the high-frequency region (1.2-12 MHz). The intensity of the peak increases as temperature increases and the peaks are shifted towards the high-frequency region with an increase in temperature. The value of tan δ

increases as temperature increases in each composition of K doped SnSe shows strong temperature dependence.

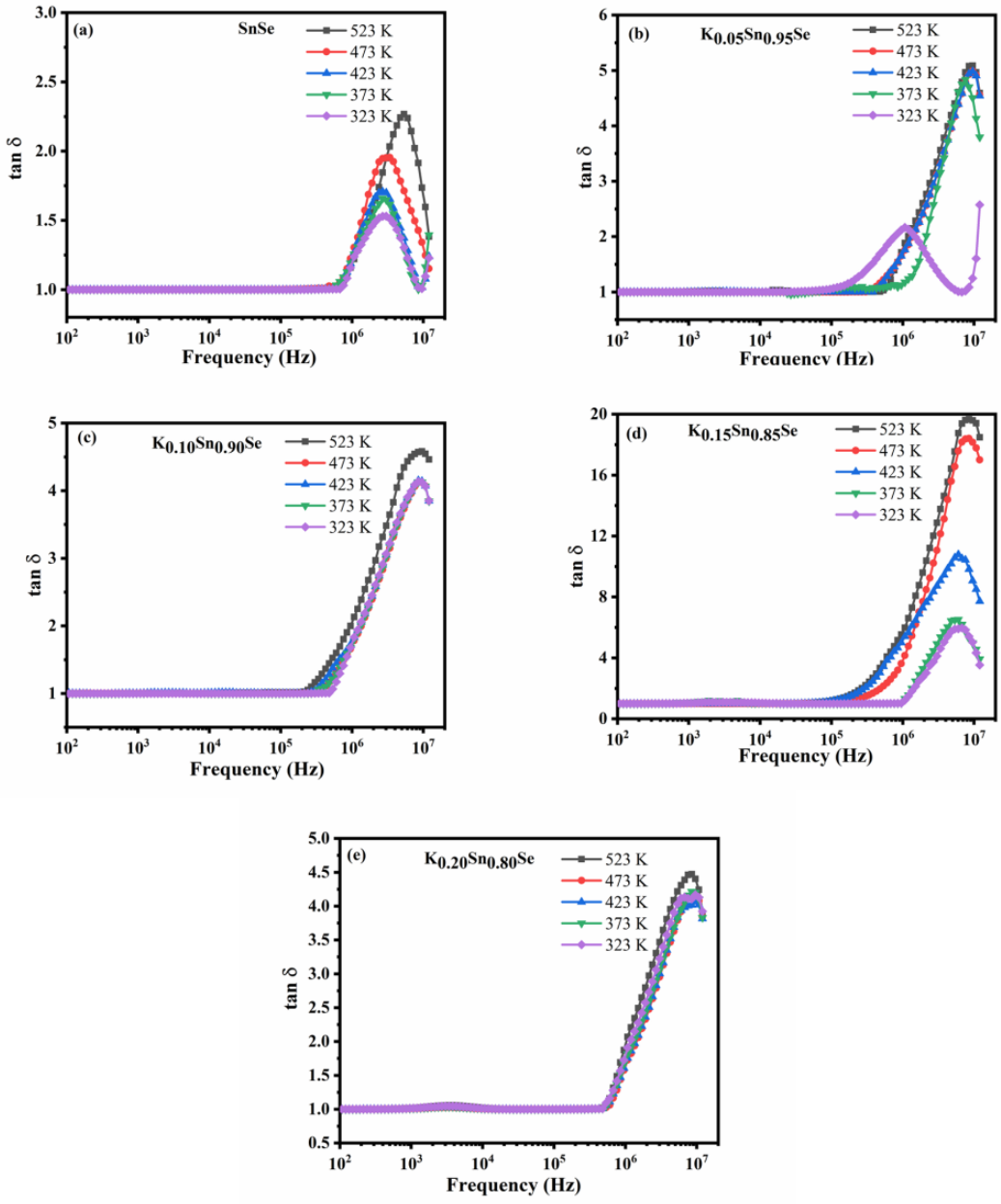

Figure 4.10 Dielectric loss tangent vs. Frequency of (a) SnSe, (b) $K_{0.05}Sn_{0.95}Se$, (c) $K_{0.10}Sn_{0.90}Se$, (d) $K_{0.15}Sn_{0.85}Se$, and (e) $K_{0.20}Sn_{0.80}Se$ respectively in the temperature range of 323-523 K.

The variation of ac conductivity as a function of frequency for all the K-doped SnSe samples is shown in fig.4.11(a-e). It is observed that in all the samples there is a plateau corresponding to dc conductivity and it is independent of frequency in the low-frequency region. The increased conductivity at high frequencies indicates ac conductivity. It increases as frequency increases and follows the relation $\sigma = A\omega^s$ in each case. It also increases for temperature in all the samples showing the

semiconductor nature of the sample. The increase in ac conductivity with temperature is due to the tunnelling and thermionic emission of charge carriers across the barrier [90]. Because the size of the particles is small the charge carriers more easily move to the surface of the particles and allow charge transfer by tunnelling or thermionic emission to increase conductivity. The ac conductivity increases as the doping concentration of K increases into SnSe. The highest value of ac conductivity is obtained for the composition $K_{0.20}Sn_{0.80}Se$. One more possible reason for the increase in conductivity as K doping increases is a decrease in the bandgap values. The $K_{0.20}Sn_{0.80}Se$ has obtained the least values of bandgaps compared to others and exhibited a high value of ac conductivity.

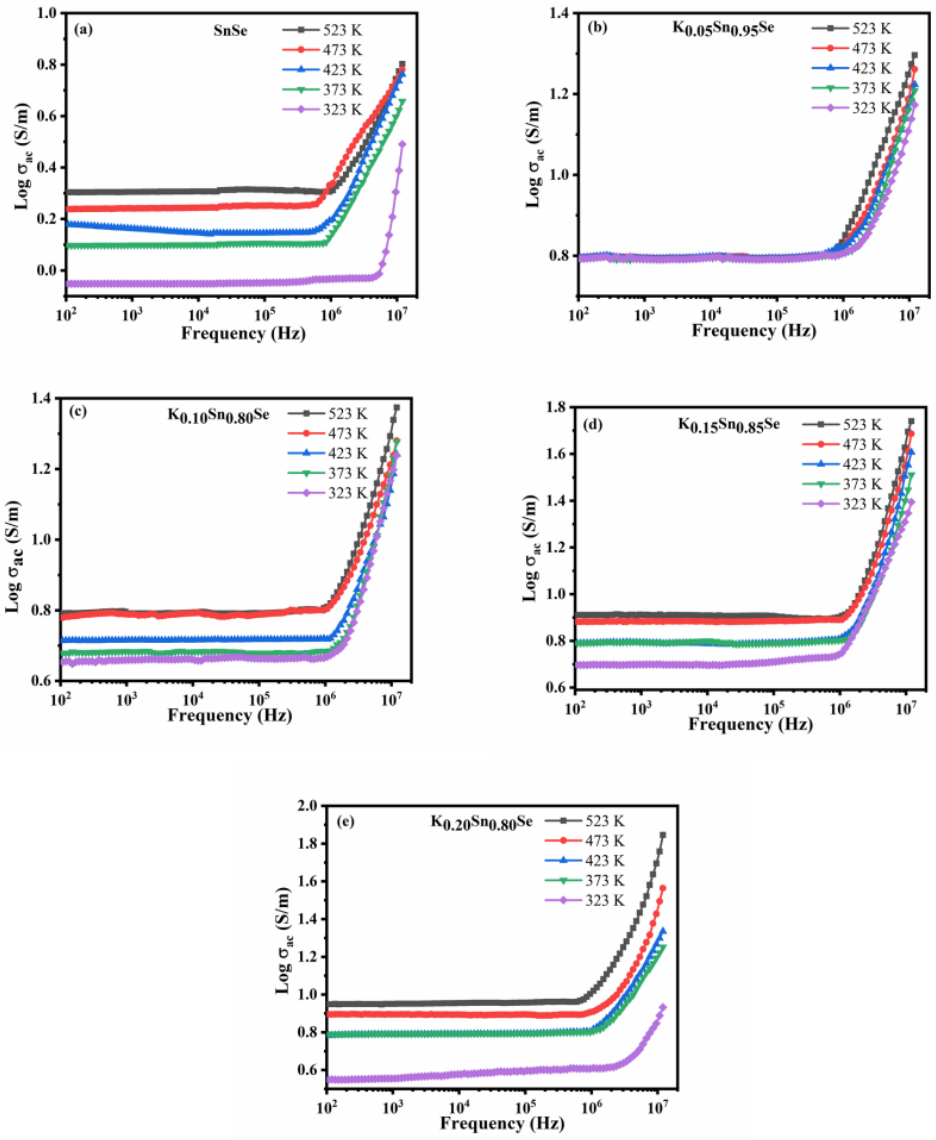

Figure. 4.11 Variation of AC conductivity vs. Frequency of (a) SnSe, (b) $K_{0.05}Sn_{0.95}Se$, (c) $K_{0.10}Sn_{0.90}Se$, (d) $K_{0.15}Sn_{0.85}Se$, and (e) $K_{0.20}Sn_{0.80}Se$ respectively in the temperature range of 323 -523 K.

The frequency exponent ‘s’ has been determined from the slopes of Frequency versus Log σ_{ac} (increasing region of ac conductivity) plots for all the samples as depicted in fig. 4.12(a). The value of ‘s’ is found to be decreased as temperature increases and the values are lie between 0.406-0.932 are less than 1. Hence the variation of s is in good agreement with the Correlated Barrier Hopping (CBH) mechanism. Figure 4.12(b) shows the variation of (1-s) with temperature.

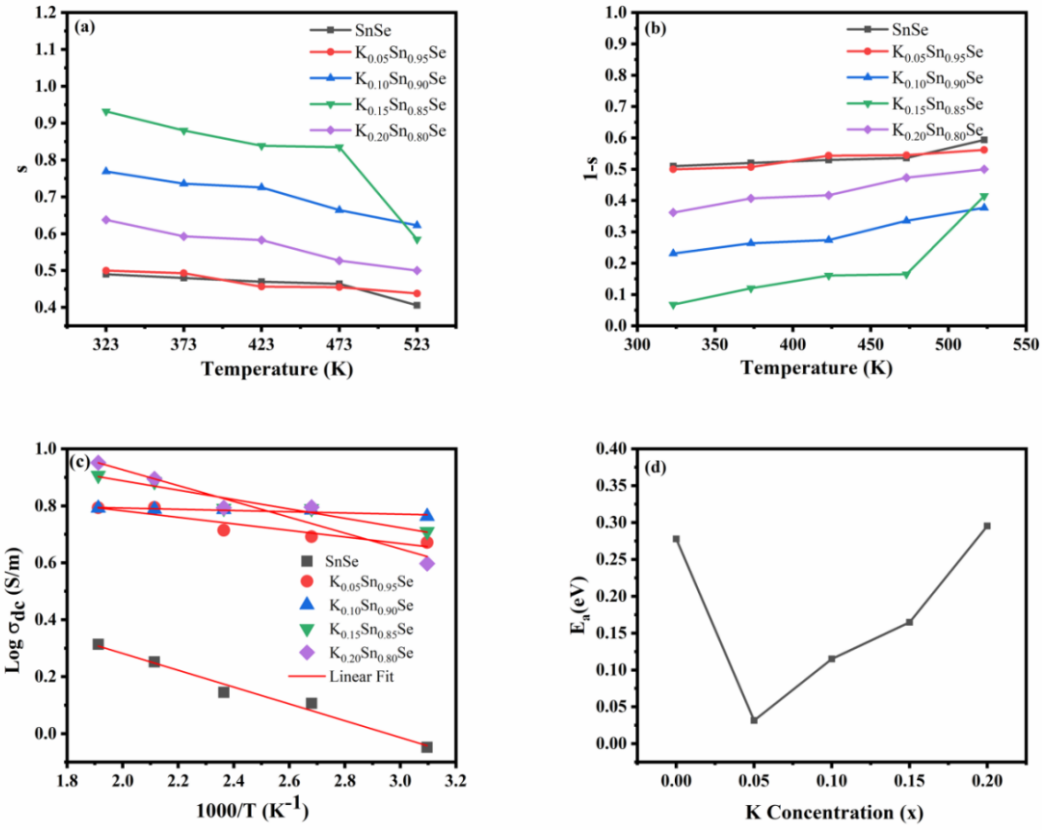

Figure 4.12 (a) Frequency exponent ‘s’ vs. temperature, (b) Variation of 1-s vs. Temperature, (c) Arrhenius plot for determining activation energy at 100 kHz, and (d) Activation energy vs. concentration of K.

Figure 4.12(c) shows the Arrhenius plot for all K-doped SnSe samples at a frequency of 100 kHz. The activation energy is obtained from the slopes after linear fitting as displayed in fig. 4.12(c). It is found to decrease with an increase in K till x=0.05 after that it again increases as depicted in fig. 4.12(d). The values of E_a for all the samples are listed in Table 4.3.

Table 4.3 Frequency exponent 's', activation energy (E_a), and maximum barrier height (W_m) values at various temperatures for all K-doped SnSe samples.

Composition	Temperature (K)	Frequency exponent (s)	Activation Energy (E_a) (eV)	W_m (meV)
SnSe	323	0.490		
	373	0.480		
	423	0.470	0.295	0.368
	473	0.464		
	523	0.406		
$K_{0.05}Sn_{0.95}Se$	323	0.500		
	373	0.493		
	423	0.4565	0.031	0.324
	473	0.455		
	523	0.438		
$K_{0.10}Sn_{0.90}Se$	323	0.769		
	373	0.736		
	423	0.726	0.115	0.728
	473	0.664		
	523	0.623		
$K_{0.15}Sn_{0.85}Se$	323	0.932		
	373	0.880		
	423	0.839	0.164	0.148
	473	0.835		
	523	0.585		
$K_{0.20}Sn_{0.80}Se$	323	0.638		
	373	0.593		
	423	0.583	0.277	0.684
	473	0.527		
	523	0.500		

The complex electrical modulus provides useful information about the electrical transport properties and relaxation process that occur in the material. It explains the relaxation phenomenon of a material as a microscopic property of ionic solids. The electrical transport phenomenon for the smallest capacitance can be studied by it. It is very advantageous compared to impedance spectroscopy in terms of discrimination between electrode polarization and grain boundary conduction. The frequency dependence variation of the real part of electrical modulus (M') for all K-doped SnSe samples at various temperatures is shown in fig. 4.13(a-e). The values of M' are low for all the samples at all temperatures indicates the negligible polarization effect at low frequencies. M' increases as frequency increases for all the samples. The variation of M'' as a function of frequency at various temperatures is shown in fig. 4.14(a-e). M'' is very less in the low-frequency region and shows an increasing trend as frequency increases. Relaxation peaks are observed for all the compositions at various temperatures. The peak intensity is decreased as the temperature increases in each

composition. The M'' curves showed asymmetric behaviour indicates a non-Debye type relaxation phenomenon. The peaks shifted in the direction of the higher frequency side as temperature increased due to the correlated motion of mobile ions. The region below the peak maximum is due to the long-range conduction of charge carriers whereas short-range conduction of mobile ions is responsible for the region above the peak maximum.

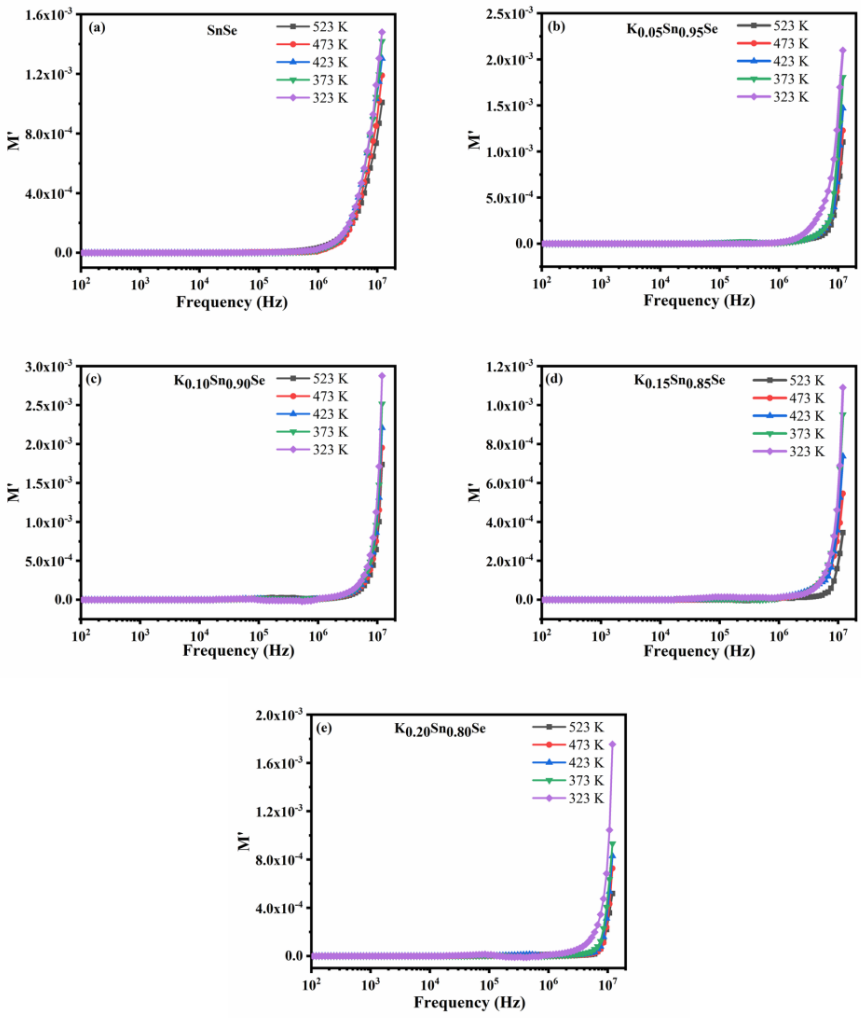

Figure 4.13 Variation of the M' vs. Frequency of (a) SnSe, (b) $K_{0.05}Sn_{0.95}Se$, (c) $K_{0.10}Sn_{0.90}Se$, (d) $K_{0.15}Sn_{0.85}Se$, and (e) $K_{0.20}Sn_{0.80}Se$ respectively in the temperature range of 323-523 K.

The variation of M' vs. M'' is depicted in fig. 4.15(a-e). The figures show semi-circular arcs are observed for all compositions at all temperatures with their centers lying below the x-axis. It is also noticed that the radii of the arcs were found to be decreased with an increase in the temperature. The presence of semi-circular arcs in the low-frequency region indicates the existence of grain boundaries in all the K-doped SnSe samples. The incomplete formations of semi-circular arcs indicate the non-Debye type relaxation is present in all the samples.

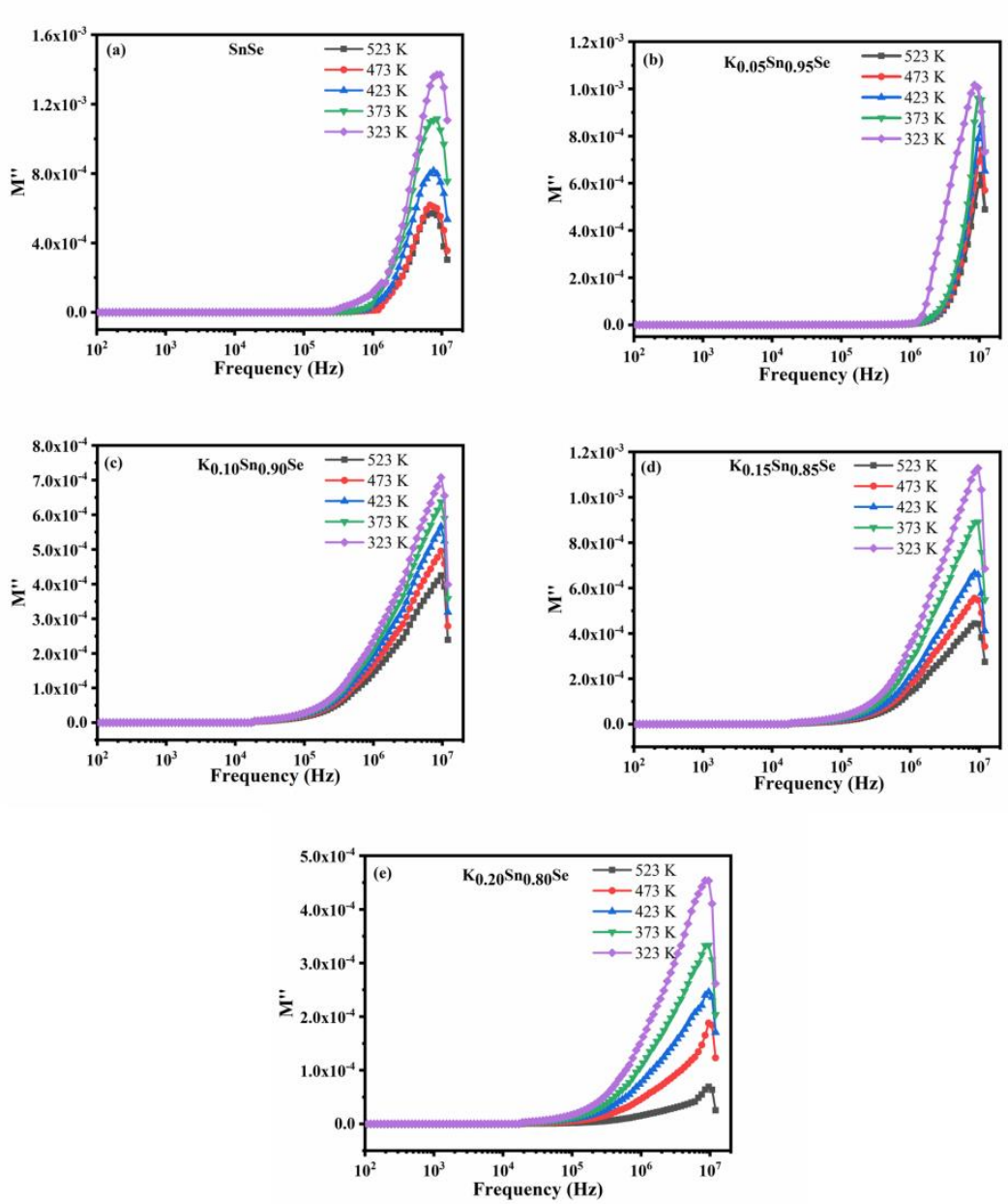

Figure 4.14 Variation of M'' vs. Frequency of (a) SnSe, (b) $K_{0.05}Sn_{0.95}Se$, (c) $K_{0.10}Sn_{0.90}Se$, (d) $K_{0.15}Sn_{0.85}Se$, and (e) $K_{0.20}Sn_{0.80}Se$ respectively in the temperature range of 323-523 K.

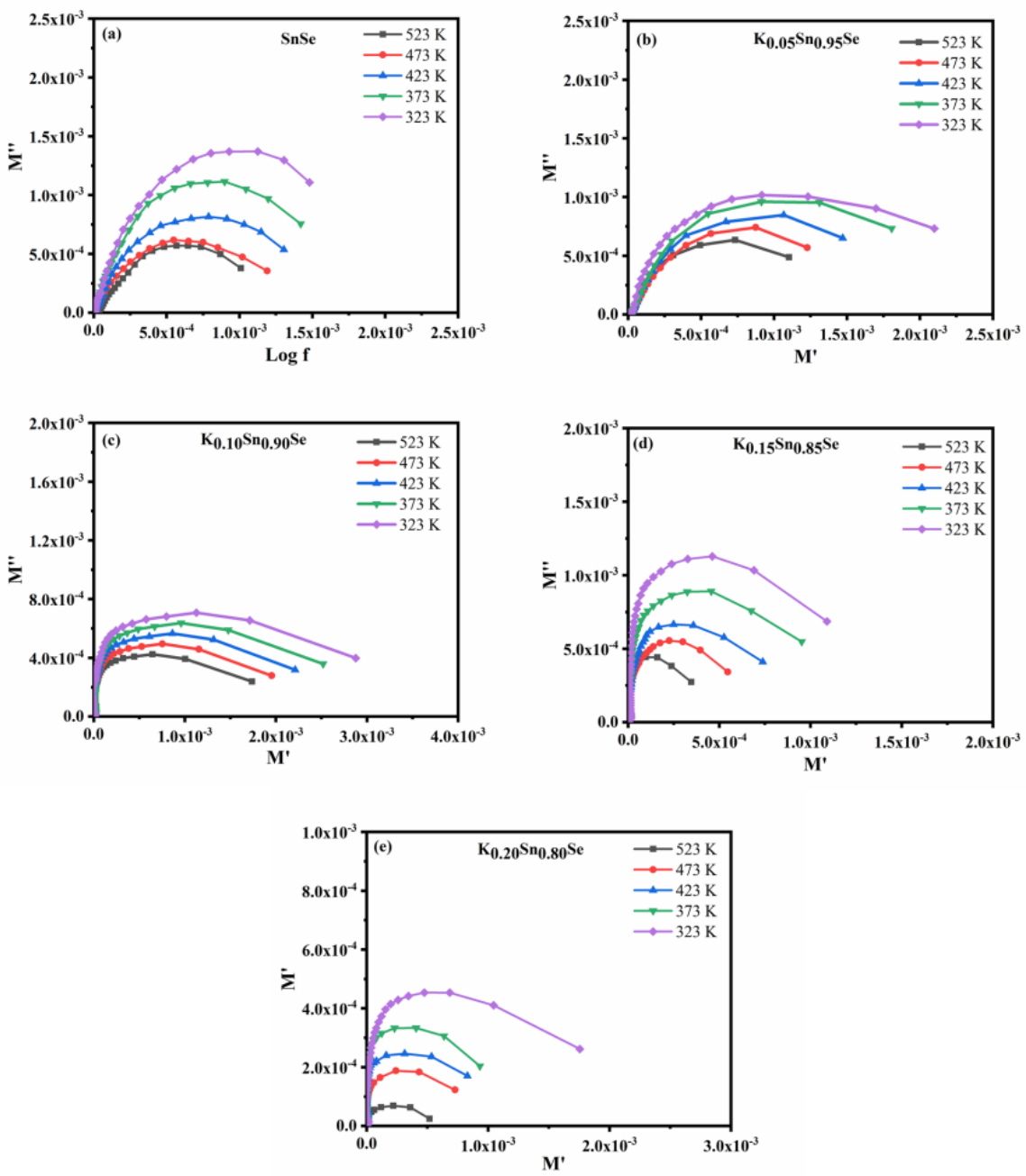

Figure 4.15 M'' vs. M' of (a) SnSe, (b) $K_{0.05}Sn_{0.95}Se$, (c) $K_{0.10}Sn_{0.90}Se$, (d) $K_{0.15}Sn_{0.85}Se$, and (e) $K_{0.20}Sn_{0.80}Se$ respectively in the temperature range of 323 -523 K.

4.4 Conclusions

$K_xSn_{1-x}Se$ polycrystals (x = 0 to 20 mol % with a step of 5 mol %) were prepared by hydrothermal method. The single phase of all the samples was confirmed through XRD. The average crystallite size is found to be varied from 97-136 nm with K doping increases into SnSe. The SEM images revealed that there is a decrease in the size of the plate-like structures with K doping. The TEM analysis exhibited the combination of plate-like structures with small nanorods at high resolution. The indirect and direct bandgap values are reduced with an increase in K concentration and further lead to enhance the ac conductivity with K doping. The room temperature studies

showed that the large value of dielectric constant and ac conductivity was obtained for the composition $K_{0.20}Sn_{0.80}Se$. The temperature-dependent dielectric studies exhibited maximum values of dielectric constant and dielectric losses for $K_{0.20}Sn_{0.80}Se$ at low frequencies. The K doping has significantly affected the AC conductivity and it is found to be maximum for the $K_{0.20}Sn_{0.80}Se$ sample at 523K. The calculated value of the parameter 's' suggested that the CBH model is the possible mechanism for the charge carriers of the hopping mechanism. The impact of grain boundary effects is revealed by electrical modulus studies and indicated non-Debye type relaxation in all the K-doped SnSe samples. The results suggest the possible application of the material in microelectronic, electro-optic, and capacitive storage devices.

CHAPTER 5: Room temperature ferromagnetism and dielectric properties of Cobalt doped Tin Selenide

5.1 Introduction

It has already stated in the previous occasions that SnSe is well studied for thermoelectric, photovoltaic, and optoelectronic applications. Doping of transition metals like Co and Fe into SnSe can alter its optical, electrical and magnetic properties. To realize the applications of this material for dielectrics and spintronic application, it is needed to investigate the doping effect of transition metal in SnSe on the dielectric and magnetic properties respectively. Few researchers have investigated the electrical and magnetic studies of transition metal-doped SnSe by computing their first-principle calculations using Density Functional Theory (DFT) [50–53]. Jiating Lu et al. concluded that 3d-orbits of transition elements efficiently change the bandgap and spin polarization of the SnSe monolayers and also these narrowband transition metal-doped DMS can have probable advantages in the fields of optoelectronic and spintronic devices [51]. However, most of them focused on magnetic studies and coupling of Mn and Fe doped SnSe monolayers. Isber et al. reported the crystal growth and magnetic studies of Eu doped SnSe single crystals obtained using the Bridgeman method [54]. Recently, Shiying Liu et al. prepared cobalt-doped SnSe thin films by thermal evaporation and investigated the thermoelectric and magnetic properties which have concluded that Co induces magnetism into SnSe lattice [55]. However, experimental investigations on Cobalt-doped SnSe for magnetic properties are scarce in the literature. Dielectric investigations will provide information about the underlying conduction mechanism by revealing the significant roles of grains and grain boundaries. The response of the material to the incident ac field will give information about the dependence on dielectric characteristics. To date, very few reports exist on the dielectric properties of pure and doped SnSe [24–27]. No one has reported the effect of Co on SnSe prepared by hydrothermal method for its dielectric and magnetic properties. Therefore the analysis of magnetic properties combined with dielectric studies has been undertaken keeping in mind the simplicity and cost-effectiveness of the hydrothermal approach.

In the present study, $Co_xSn_{1-x}Se$ polycrystals with x= 0.00, 0.01, 0.03, 0.05, 0.10 and 0.20 were synthesized using hydrothermal method. The effect of Co doping on structural, morphological, and optical studies of SnSe was discussed. In addition, dielectric properties, ac conductivity studies, and electrical modulus analysis were

explored to understand the underlying conduction mechanism of SnSe with a function of the applied ac field. Magnetic studies were also explained to understand the behavior of the material for a potential application in data storage and spintronic devices.

5.2 Synthesis of $Co_xSn_{1-x}Se$ polycrystals

Analytical grades of $SnCl_2.2H_2O$ (99.9%), SeO_2 metal powder (98%), $CoCl_2.6H_2O$ (99.9%), NaOH (85%), $NaBH_4$ (99.9%), and Ethylenediaminetetraacetic acid (EDTA) were procured from MERCK and utilized as received without conducting any further purification process. The pure and $Co_xSn_{1-x}Se$ samples were synthesized by a simple hydrothermal method. For undoped SnSe, initially, 10 mmol of $SnCl_2.2H_2O$ was mixed into 100 ml of deionized (DI) water and the solution is stirred for 5 min. Then 4 g of NaOH was mixed into the solution and stirred for another 5 min. Then 10 mmol of SeO_2 was added to the above mixture and stirred for 15 min. To reduce the SeO_2, 1g of $NaBH_4$ is added to the solution and stirred for 30 min. Later, 1.46 g of EDTA was added to the mixture and stirred for 15 min. Finally, the resulting solution was shifted into a stainless steel autoclave with Teflon lining having 120 ml capacity and kept in an oven at 150 ^oC for 12 h. After completing the reaction time, the autoclave was allowed to cool naturally to room temperature. Then the solution obtained was cleaned and filtered with DI water and ethanol many times to get the resultant product. Further, the product was dried in the air at 80 ^oC overnight. The $Co_xSn_{1-x}Se$ for x= 0.01, 0.03, 0.05, 0.10, and 0.20 samples are synthesized by the similar process as explained above. The molar concentrations of $SnCl_2.2H_2O$ and $CoCl_2.6H_2O$ are varied to obtain the specific compositions. The schematic of the synthesis process is presented in fig. 5.1.

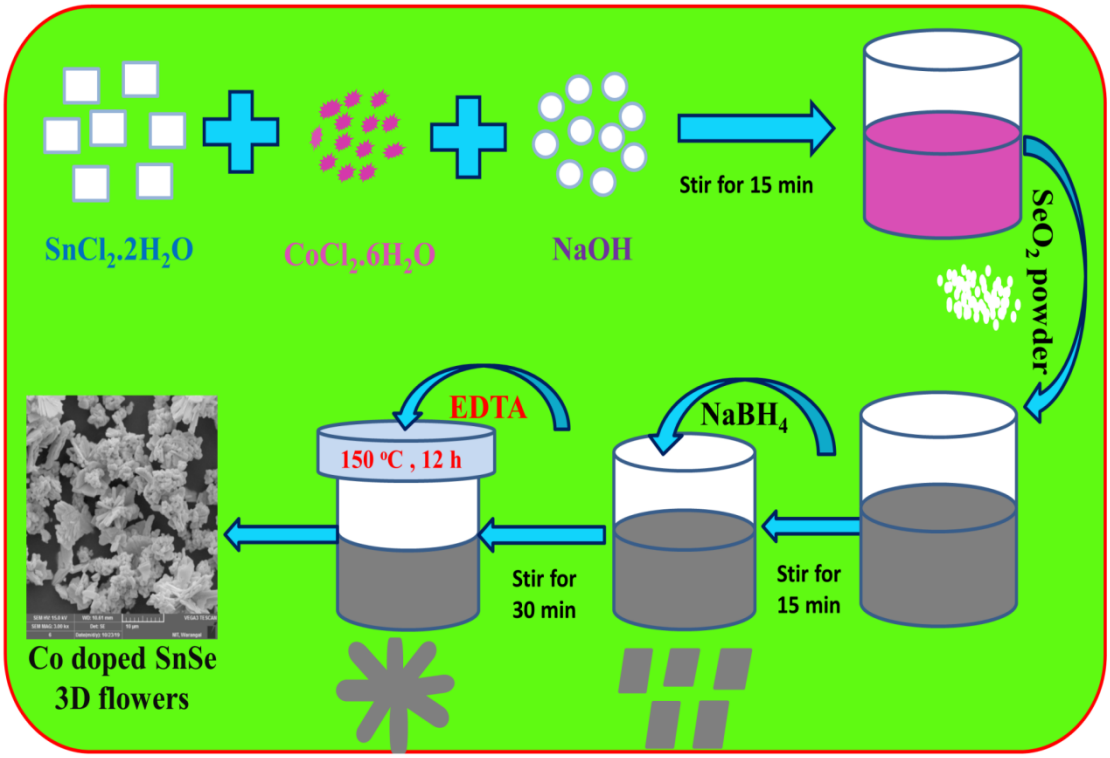

Figure 5.1 Schematic representation of the synthesis procedure of $Co_xSn_{1-x}Se$ using the hydrothermal method.

5.3 Results and Discussion

5.3.1 X-Ray Diffraction

Figure 5.2(a) shows X-Ray diffraction pattern of $Co_xSn_{1-x}Se$ for x = 0.00, 0.01, 0.03, 0.05, 0.10 and 0.20 polycrystals. Single-phase with the orthorhombic structure is found in undoped and all Co-doped SnSe samples. No secondary phases belonging to SnSe (i.e., $SnSe_2$, Sn_2Se_3) or Co impurity (i.e., $CoSe_2$ or CoO) are observed. From the Fig. 2(a), it is noticed that the diffraction peaks occur mainly from the planes (2 0 1), (2 1 0), (0 1 1), (1 1 1), (4 0 0), (3 1 1), (4 1 1), (5 1 1) and (4 2 0). All the planes are well-indexed, and well-matched with standard PDF file no: #48-1224 [58,71,85]. The diffraction intensity for the plane (4 0 0) increases as the concentration of Co reaches 0.05, which shows the increase in crystalline nature. This type of behavior in the diffraction intensity of the plane (4 0 0) is due to the residual stresses that occur by the mismatch of ionic size between Co^{+2} (0.65 Å) and Sn^{+2} (0.93 Å). Increasing the Co concentration to 0.10 and 0.20 again the intensity of the peak (4 0 0) is found to decrease. This could be due to the occurrence of defects or stacking faults in the SnSe lattice, which will decrease the diffraction intensity [29].

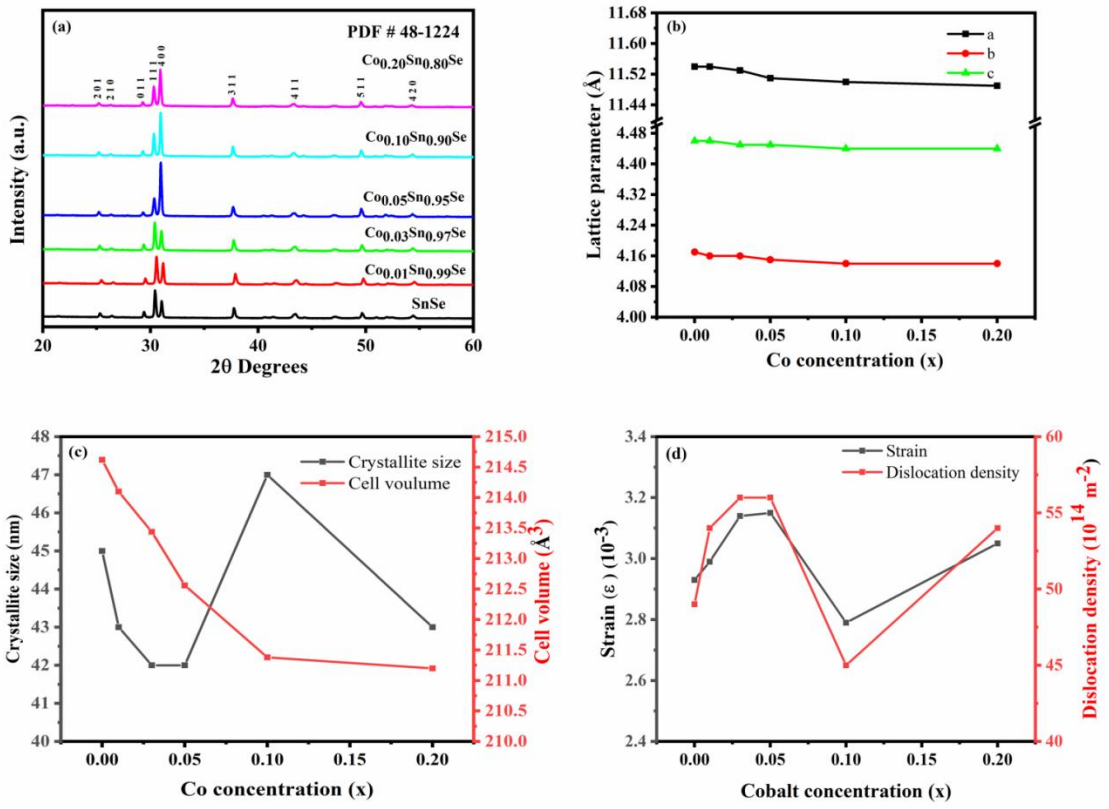

Figure 5.2 (a) XRD pattern of all $Co_xSn_{1-x}Se$ samples, (b) Lattice parameter variation with concentration (x) of Co, (c) crystallite size, and Cell volume vs. Co doping concentration, and (d) Variation of strain and dislocation density with Co concentration.

The values of lattice parameters are plotted against Co concentration as shown in fig. 5.2(b) and it is noticed that as the Co concentration increases the lattice parameters show a decreasing trend. This is due to the replacement of Sn^{+2} in the SnSe lattice with Co^{+2} with a lesser ionic radius than Sn^{+2}. This leads to lattice shrinkage and a decrease in lattice constant. The calculated lattice parameters are shown in Table 5.1. The cell volume is also calculated ($V=a*b*c$ (Å^3)) and values are displayed in Table 5.1. The calculated values are shown in Table 5.1. The value of D is found to be 45 nm for undoped SnSe. With increasing values of x from 0.00 to 0.05, the crystallite size decreased and thereafter attained a maximum value for x = 0.10 following which it decreased at x = 0.20. The calculated crystallite size values of undoped SnSe are in good agreement with existing literature values [91]. The noticed behavior of the average crystallite size is because of the lattice strains that are produced while synthesizing the $Co_xSn_{1-x}Se$ samples [29]. The cell volume and crystallite size are shown in the plot fig. 5.2(c). Lattice imperfections occur due to Co doping into SnSe lattice and they lead to occur strain in the host lattice. The average crystallite size decreases with an increase in Co concentration till x=0.05. Further, it increases slightly for x=0.10 and thereafter decreases. A similar trend is followed for strain but in opposite direction. The increase

in the value of strain is due to the changes in the crystallite size and broadening of the peaks (1 1 1) and (4 0 0) for x= 0.05. The broadening of peaks (1 1 1) and (4 0 0) are reduced and the crystallite size is slightly increased for x=0.10 which results in a decrease in the strain value [92,93]. The broadening of the peaks can be explained as a function of FWHM. As strain is inversely related to average crystallite size, the variation in the average crystallite size will alter the related deformations in the sample [94]. The values of FWHM and strain are shown in Table 5.1. The strain and dislocation densities are plotted against Co concentration and are shown in fig. 5.2(d). The obtained strain and dislocation density values are very small and can increase the free motion of electrons further which improves the mobility of the charge carriers in the SnSe lattice [29]. The dislocation density increased from x= 0.00 to x= 0.05, and further it decreased to x=0.10 and again increased for x=0.20. The increase in dislocation density and decrease in crystallite size at the higher composition of Co is due to the presence of doping atoms at grain boundaries [95]. However, the dislocation density is inversely related to crystallite size. Table 5.1 shows the values of XRD parameters such as lattice parameters, crystallite size, cell volume, strain, and dislocation density for all the $Co_xSn_{1-x}Se$ samples.

Table 5.1 XRD parameters of all $Co_xSn_{1-x}Se$ compositions.

Sample	Lattice constants			Cell volume $(Å)^3$	FWHM	D (nm)	Strain (10^{-3})	Dislocation density $(10^{14}$ lines/cm$^2)$
	a (Å)	b (Å)	c (Å)					
SnSe	11.54	4.17	4.46	214.62	0.195	45	2.93	49
$Co_{0.01}Sn_{0.99}Se$	11.54	4.16	4.46	214.10	0.210	43	2.99	54
$Co_{0.03}Sn_{0.97}Se$	11.53	4.16	4.45	213.44	0.208	42	3.14	56
$Co_{0.05}Sn_{0.95}Se$	11.51	4.15	4.45	212.56	0.224	42	3.15	56
$Co_{0.10}Sn_{0.90}Se$	11.50	4.14	4.44	211.38	0.190	47	2.79	45
$Co_{0.20}Sn_{0.80}Se$	11.49	4.14	4.44	211.20	0.219	43	3.05	54

5.3.2 Morphological studies and elemental analysis

The surface morphology of all $Co_xSn_{1-x}Se$ (x = 0.00 - 0.20) polycrystals are shown in fig. 5.3(a)-(f) at 10 μm range and it is evident that cobalt doping into SnSe influences the morphology greatly. Pure SnSe exhibits non-uniform 2D plate-like structures that are agglomerated and interconnected to form non-uniform 3D flower-like structures. For SnSe with x = 0.01, 0.03, and 0.05, there is a decrease in the size of the 3D flowers and they grow into a more compact structure because the plate-shaped petals have become thicker and denser as the composition of Co increases. The decrease in the size of the flowers is due to the pinning effects at the grain boundaries caused by the

addition of Co and these results in the decrease of grain size. However, with an increase in Co content further to x = 0.10, agglomeration disappears and the plate-like structures are changed into uneven rod-like structures. The rods are interconnected to form 3D flowers. Furthermore, for x= 0.20, the 3D flowery nature has disappeared and the size of the rods is decreased. Figure 5.4 shows the morphology of $Co_{0.20}Sn_{0.80}Se$ at higher magnification i.e., at 2 μm range. The average size of the rod is 800 nm as seen from fig.5.4.

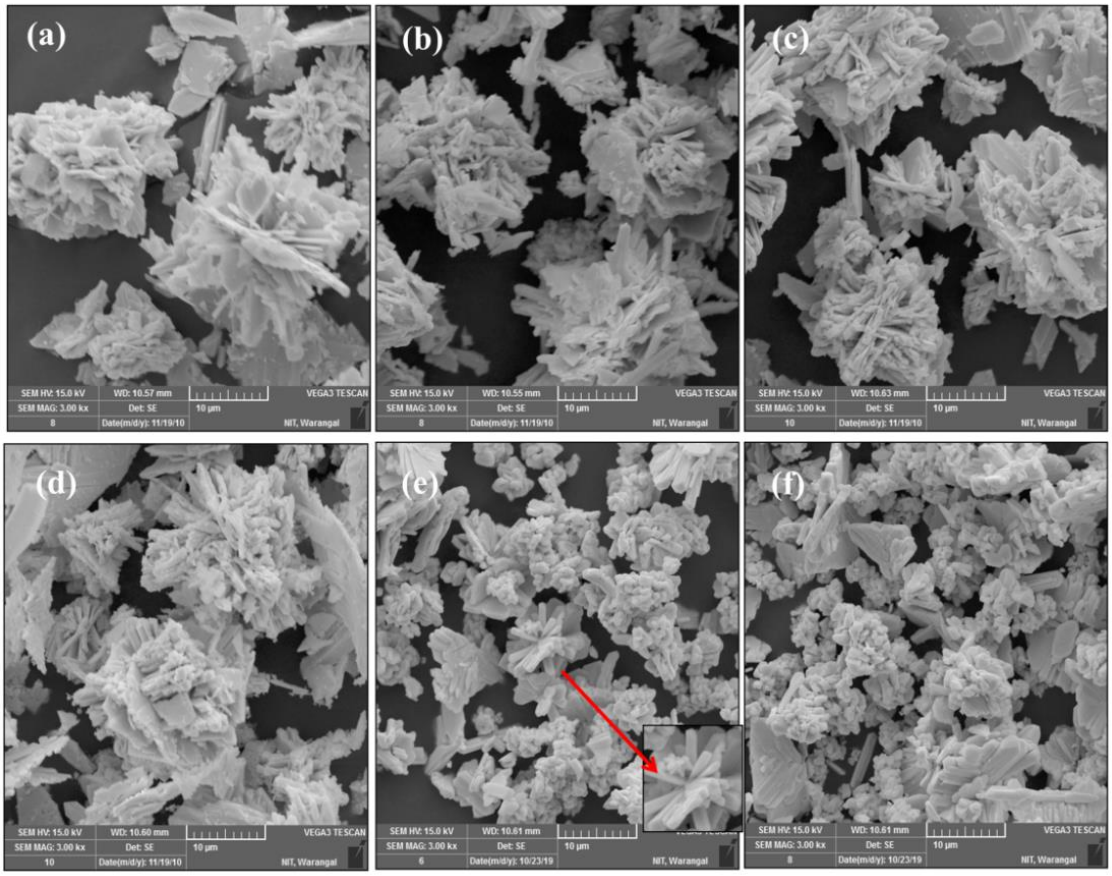

Figure 5.3 SEM images of $Co_xSn_{1-x}Se$ polycrystals (a) x = 0.00, (b) x = 0.01, (c) x = 0.03, (d) x = 0.05, (e) x = 0.10, and (f) x=0.20 at 10 μm range.

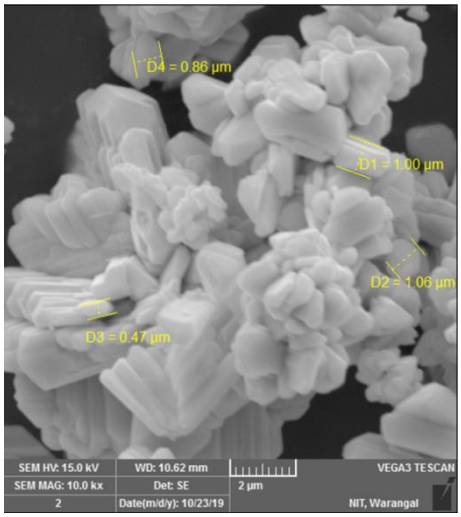

Fig. 5.4 SEM image of Co-doped SnSe at x=0.20 at 2 µm range.

Further, to understand more about the morphology of Co-doped SnSe polycrystals, high-resolution transmission electron microscope studies were investigated. Figure 5.5(a) shows the HRTEM image of $Co_{0.05}Sn_{0.95}Se$ sample showing plate-like structure at higher magnification. The rod-like structure is seen from the HRTEM image as shown in fig. 5.5(b) for the sample $Co_{0.10}Sn_{0.90}Se$. Figure 5.5(c) shows the agglomeration of small nano rods for the sample $Co_{0.20}Sn_{0.80}Se$. No cluster formation is observed from the HRTEM results in all the samples. The HRTEM results are consistent with the observed SEM results. The SAED pattern for $Co_{0.10}Sn_{0.90}Se$ from fig. 5.5(d) depicts the polycrystalline nature of the sample. The SAED pattern shows a set of rings corresponding to the lattice planes (2 0 1), (4 0 0), and (3 1 1) are matched with the XRD data. Fig. 5.5(e) depicts d-spacing of 2.88 Å corresponding to the plane (4 0 0) and grain boundary from the HRTEM image of $Co_{0.10}Sn_{0.90}Se$. The HRTEM image of $Co_{0.10}Sn_{0.90}Se$ from fig.5.5(f) shows the dotted circles representing the dislocations that occurred in the sample [96]. The d-spacing of 2.88 Å and 3.5 Å corresponding to the planes (4 0 0) and (2 0 1) are represented in fig. 5.5(f) which are matched with the XRD data. Figure 5.5(g-f) shows the Inverse Fast Fourier Transform (IFFT) images of the circles represented in fig. 5.5(f). From the IFFT images, it is noticed that the red marked regions are denoting the dislocations present in the $Co_{0.10}Sn_{0.90}Se$ sample [97].

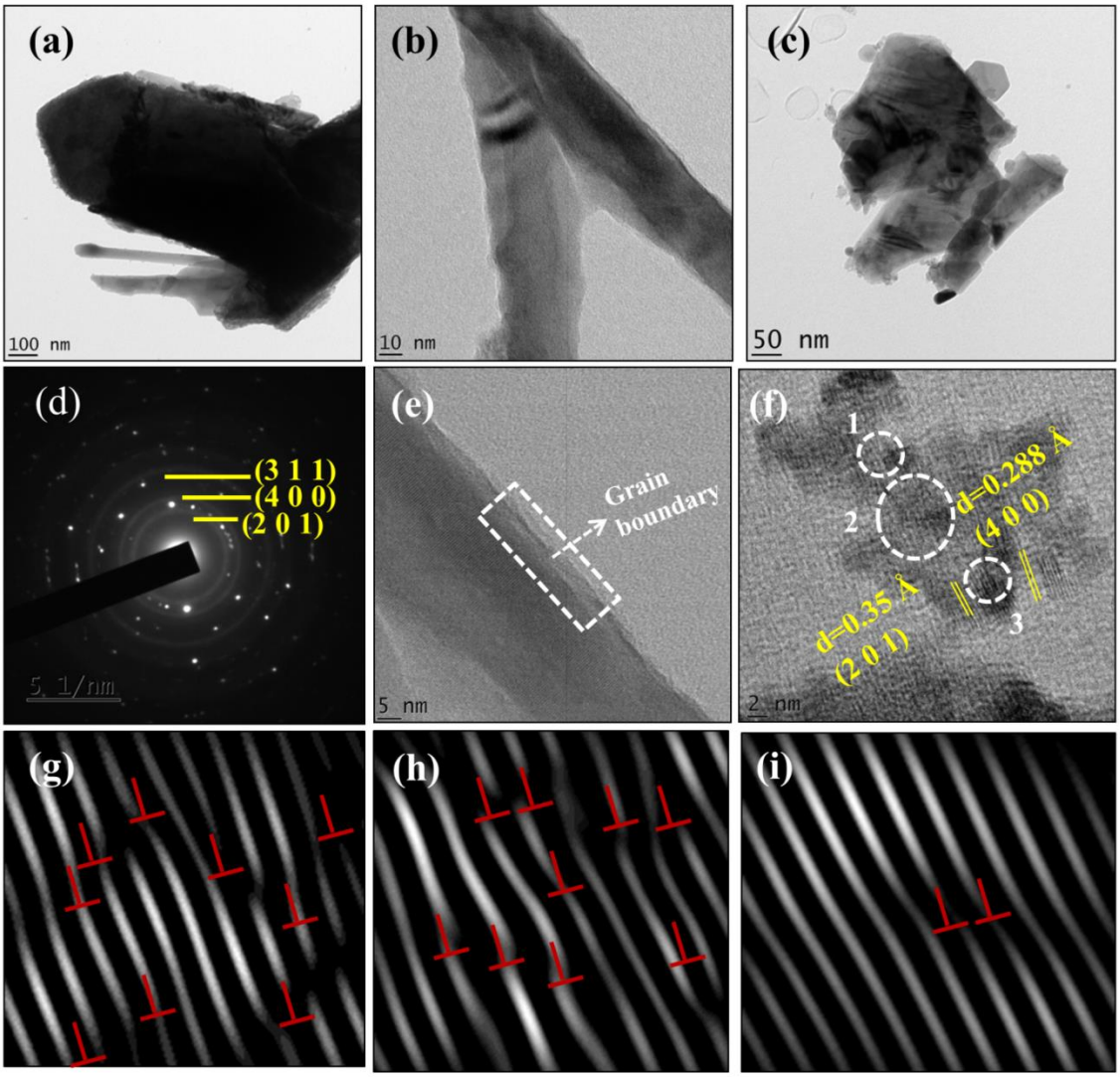

Figure 5.5 HRTEM images of $Co_xSn_{1-x}Se$ polycrystals (a) x = 0.05, (b) x = 0.10, (c) x = 0.20, and (d) SAED pattern and (e) HR-TEM image of $Co_{0.10}Sn_{0.90}Se$ representing grain boundaries, (f) HR-TEM image of $Co_{0.10}Sn_{0.90}Se$ with dotted circles representing dislocations and (g),(h)&(i) are the IFFT images of the dotted circles 1,2 and 3 respectively as numbered in 5(f).

The elemental composition of pure and Co-doped SnSe samples is confirmed through EDAX. Figure 5.6(a-f) shows the EDAX spectra for all the compositions. The sharp peaks related to Sn, Se, and Co are seen in fig. 5.6(a-f) which confirms the existence of Sn, Se, and Co in the EDAX spectra. No other impurities were found other than the elements Sn, Se, and Co.

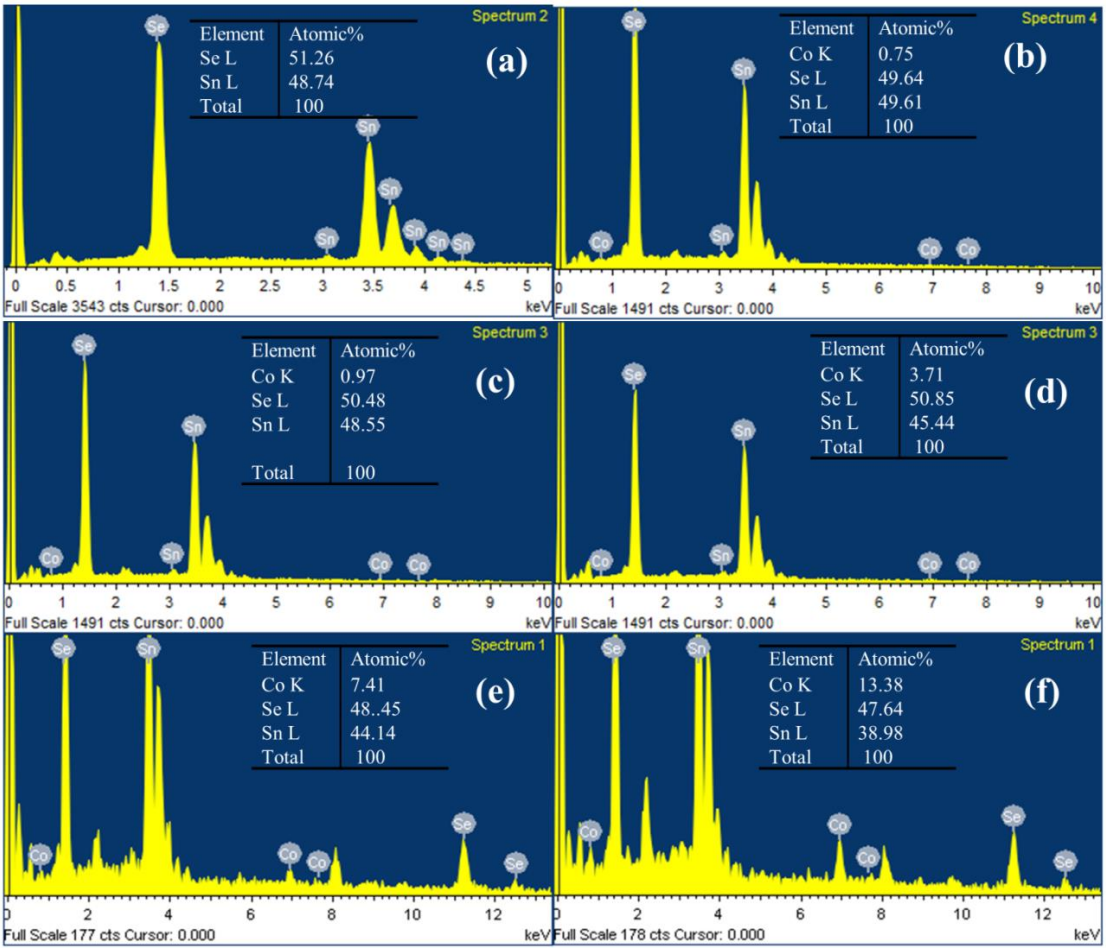

Figure 5.6 (a-f) EDAX spectra of all $Co_xSn_{1-x}Se$ samples.

5.3.3 UV-VIS-NIR Diffuse Reflectance Spectroscopy

Figure 5.7(a) displays the reflectance spectra for all $Co_xSn_{1-x}Se$ samples. The absorption edges are shifted toward the higher wavelength sides as Co concentration increases into SnSe, indicating a redshift except for x= 0.10. The plot for indirect bandgap $((F(R)h\upsilon)^{1/2}$ versus $h\upsilon$) and direct bandgap $((F(R)h\upsilon)^2$ versus $h\upsilon$) are depicted in fig. 7(b,c) respectively. The optical bandgaps are calculated by extrapolating the linear region of the plots onto the $h\upsilon$ axis. The indirect bandgap for SnSe (0.93 eV) and direct bandgap (1.023 eV) are well-matched with the theoretical indirect bandgap of 0.9 eV and direct bandgap of 1.3 eV respectively. Both the bandgap values decrease as Co concentration increases till x= 0.05, followed by a slight increase at x=0.10 before it shows a decrease as the concentration approaches x= 0.20. The sp-d exchange interactions between the band electrons of the host lattice and the d electrons of Co^{+2} ions cause changes in the bandgap values [98]. Further, the variation of bandgap values is related to the variation in the crystallite size for all the samples. The bandgap values decreased for values of x=0.00 to x=0.05 and also again for x=0.20. This is due to the decreasing trend of average crystallite size which will cause the grain size to decrease [72,99]. However, at

x=0.10 the bandgap values show a slight increase. This can be attributed to an increase in the value of crystallite size. The variation of indirect and direct bandgaps as a function of Co concentration is shown in fig. 5.7(d). The bandgap values are shown in Table 5.2.

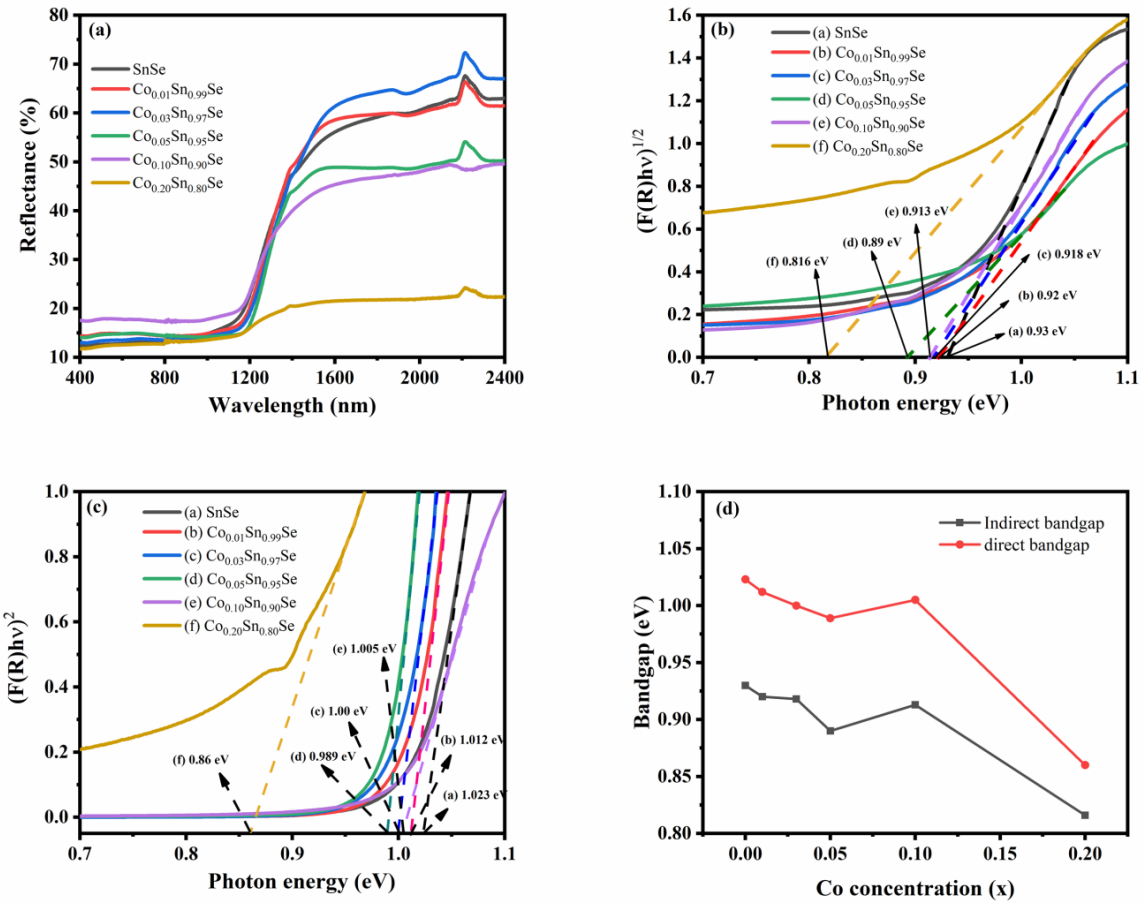

Figure 5.7 (a) Reflectance spectra of $Co_xSn_{1-x}Se$ samples, (b) $(F(R)h\upsilon)^{1/2}$ versus $h\upsilon$ for indirect bandgap, (c) $(F(R)h\upsilon)^2$ versus $h\upsilon$ Tauc plot for direct bandgap, and (d) Variation of indirect and direct bandgaps as a function of Co concentration.

Table 5.2 Values of indirect and direct bandgaps of $Co_xSn_{1-x}Se$ polycrystals

Composition	Indirect bandgap (eV)	Direct bandgap (eV)
SnSe	0.93	1.023
$Co_{0.01}Sn_{0.99}Se$	0.92	1.012
$Co_{0.03}Sn_{0.97}Se$	0.918	1.000
$Co_{0.05}Sn_{0.95}Se$	0.89	0.989
$Co_{0.10}Sn_{0.90}Se$	0.913	1.005
$Co_{0.20}Sn_{0.80}Se$	0.816	0.86

5.3.4 X-ray Photoelectron spectroscopy

XPS is recorded for the sample $Co_{0.10}Sn_{0.90}Se$ to know the chemical states and to confirm the formation of $Co_{0.10}Sn_{0.90}Se$ as shown in fig. 5.8(a-c). Figure 5.8(a) shows a high-resolution spectrum of Sn 3d showing doublet peaks at 486.7 eV and 495.5 eV corresponding to $3d_{5/2}$ and $3d_{3/2}$ respectively which confirming that the valence state of Sn is +2. Figure 5.8(b) shows the deconvolution spectra of Se 3d showing two peaks at 54.4 eV and 55.7 eV are ascribed to $3d_{5/2}$ and $3d_{3/2}$ respectively which are associated with the -2 oxidation state of Se. The XPS results for both Sn and Se are in good agreement with the literature [91,100]. The peaks at 781.8 eV and 797.6 eV are corresponding to Co $2p_{3/2}$ and Co $2p_{5/2}$ respectively as depicted in fig.5.8(c). The binding energy difference between the two peaks is 15.8 eV. The results reveal that the cobalt in our sample is in +2 state [101]. There is no evidence for the formation of metallic Co because if metallic Co is formed the binding energies of Co $2p_{3/2}$ and Co $2p_{1/2}$ should be around 778 and793 eV with a difference of binding energies between those two states is 15.05 eV [102].

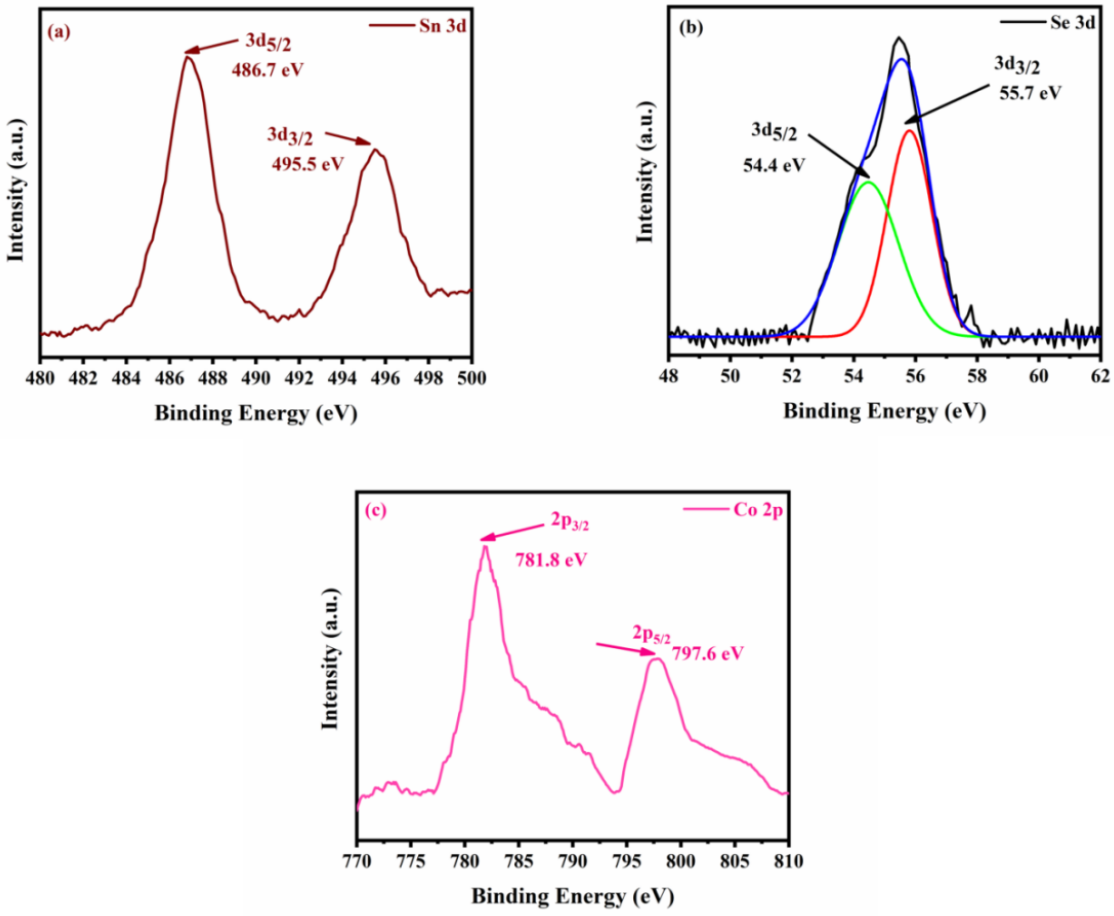

Figure 5.8 (a) XPS spectra of Sn3d, (b) Se3d, and (c) Co2p of $Co_{0.10}Sn_{0.90}Se$ sample.

5.3.5 Dielectric studies

5.3.5.1 Room temperature dielectric studies

The variation of ε' as a function of the frequency is shown in fig. 5.9(a). The value of ε' is greater in the low-frequency region for all $Co_xSn_{1-x}Se$ samples due to space charge polarization. The space charge polarization arises due to the charges getting trapped at grain boundaries when an electric field is applied. Due to the trapping of charges at grain boundaries, they become active which causes an increase in ε'. The value of ε' is increased as Co concentration increases up to x= 0.05 in the low-frequency region. The largest value of ε' is obtained for $Co_{0.05}Sn_{0.95}Se$. This is due to the reduction in the average crystallite size of the 3D flower-like microstructure which further produces a high number of grain boundaries. Hence the value of ε' is large for $Co_{0.05}Sn_{0.95}Se$. For values of Co concentration above x= 0.05, the microstructure exhibits small rod-like nature and the crystallite size is high for x= 0.10 compared to other compositions. The increase in the value of crystallite size causes a decrease in the number of grain boundaries which further decreases the dielectric constant. It is also noticed from fig. 5.9(a), that ε' tends to decrease with an increase in frequency, becomes constant, in the region of high-frequencies. This is due to the lagging of polarization behind the frequency at a certain point in the high-frequency region. Further, there is no sufficient time for the dipoles to accommodate themselves in the direction of the applied ac field. The influence of space charge polarization declines which results in the decrease of ε'. The dielectric loss elucidates the loss of electrical energy of material when an external electric field passes into the material; hence conduction mechanism mainly depends on dielectric loss. The ε" value for all Co-doped SnSe samples is noticed to decrease with increasing frequency and finally, it becomes constant and independent of frequency which shows that the losses vanish at high frequencies as seen from fig. 5.9(b). The decrease in ε" at high frequencies is due to the relaxation phenomenon. The ε" is high in the low-frequency region due to the enhancement in the carrier mobility by the free charge motion. The dielectric loss is observed to be the largest in the case of $Co_{0.05}Sn_{0.95}Se$. It is seen from fig. 5.9(c); the dielectric loss tangent is constant and is independent of the frequency in the low-frequency region. It increases with frequency and peaks are observed in loss spectra for all compositions caused due to the dipole relaxation phenomenon. This is due to the space charges and defects in different defect states in nanocrystalline materials**.** The Maxwell Wagner model and Koop theories [103,104] are known to demonstrate the changes observed in the dielectric parameters.

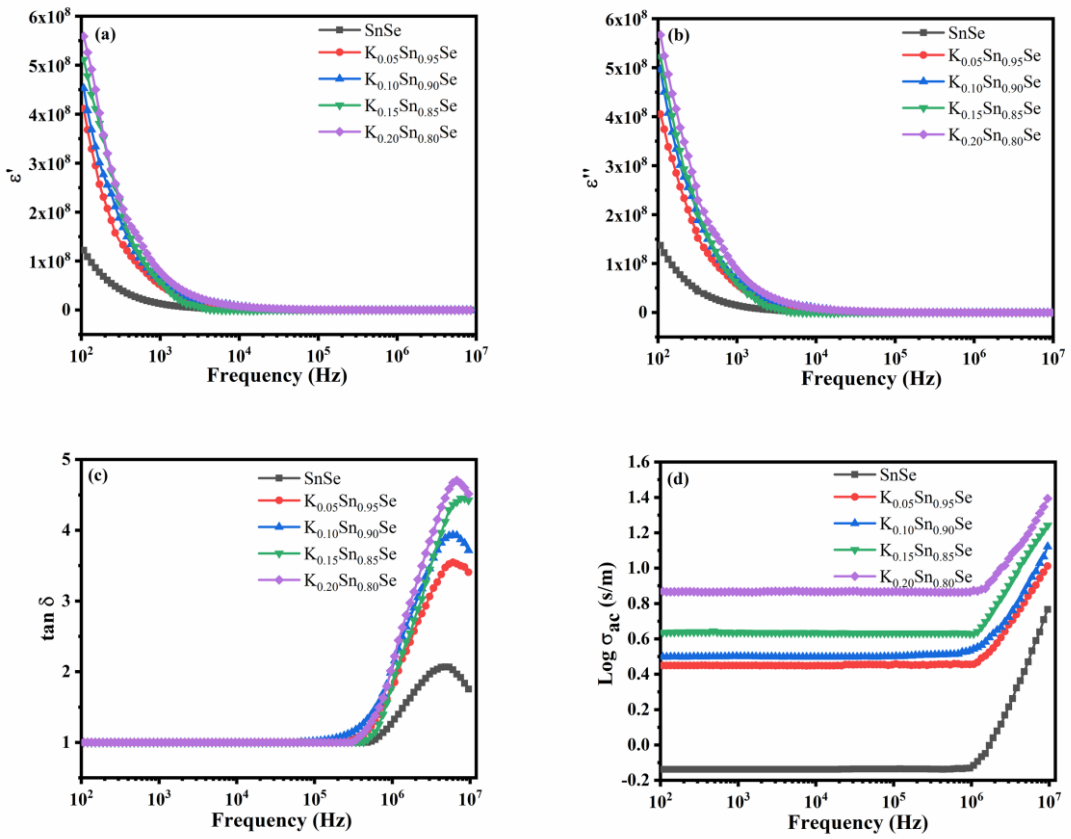

Figure 5.9 (a) Dielectric constant vs. frequency, (b) Dielectric loss vs. frequency, and (c) Dielectric loss tangent vs. frequency, and (d) AC conductivity vs. frequency for all $Co_xSn_{1-x}Se$ samples at room temperature.

It is observed from fig. 5.9(d), that there is a plateau region at low frequencies which corresponds to dc conductivity $\sigma_{dc.}$ It is also seen that $\sigma_{dc,}$ increases with Co composition till x=0.05 and thereafter decreases. The increasing portion of conductivity at high frequencies corresponds to ac conductivity. This conduction occurs due to the migration of ions inside the material. The σ_{ac} shows an increasing trend with Co doping which indicates that doping of Co induces impurity sites within the bandgap of SnSe lattice. Though Co doping enhances the carrier concentration the testing frequency needs to be high for achieving a fully ionized state and enhancement of conductivity. The $Co_{0.05}Sn_{0.95}Se$ has achieved a high value of ac conductivity due to the reduction in the value of crystallite size. The decrement in the value of crystallite size with Co concentration also improves grain boundary ionic diffusivity. The ac conductivity is decreased for higher compositions of Co viz; x=0.10 and 0.20. This is due to the rise in the value of crystallite size for these compositions which causes a decrease in the number of grain boundaries resulting in the decrease of ac conductivity.

Complex electrical modulus spectroscopy is helpful for the extraction of the electrical response and thus provides a better understanding of the relaxation phenomenon. It gives detailed information about the conduction mechanism in polycrystalline materials and describes the electrical relaxation phenomenon of ionic solids as a microscopic property of materials. To eliminate extreme loss effects, at low frequencies the electrical modulus has been studied for all $Co_xSn_{1-x}Se$ samples at room temperature. The variation of M' as a function of frequency for all $Co_xSn_{1-x}Se$ samples is depicted in fig.5.10(a). It is obvious from fig. 5.10(a) that the M' values are low and tend to zero in the low-frequency region due to the non-contribution of electrode polarization. The M' values increase with frequency for all compositions due to the relaxation phenomenon and absence of space charge effect at high frequencies.

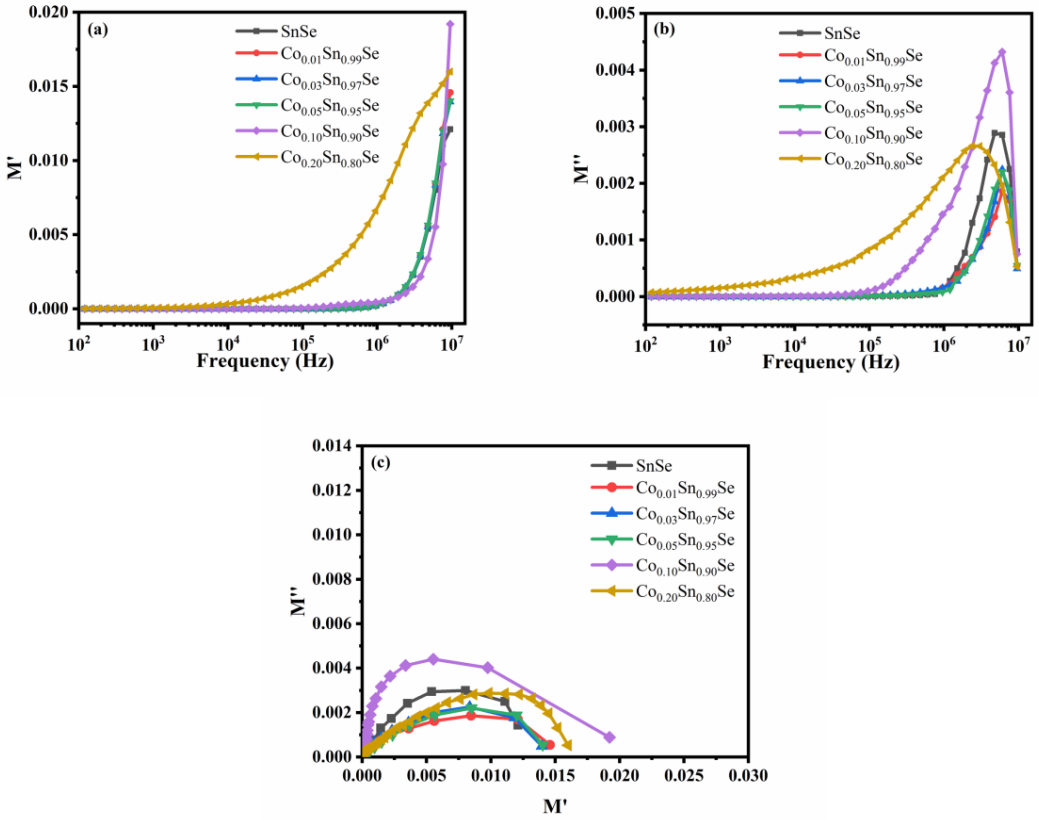

Figure 5.10 (a) Variation of M' as a function Frequency, (b) Variation of M'' as a function of Frequency, and (c) Variation M'' vs. M' for all $Co_xSn_{1-x}Se$ samples.

The frequency dependence of M'' for $Co_xSn_{1-x}Se$ system of samples is shown in fig. 5.10(b). The M'' values for all $Co_xSn_{1-x}Se$ samples increase with frequency and peaks in the high-frequency region. The ions are free to move over long-range distances involving hopping mechanisms in the region below the peak maximum. In the region above the peak maximum, the ions are restricted to potential wells and hence can move over short distances i.e., can move within the local site [105]. The area where the peak

occurs specifies the transformation of long-range conduction of charge carriers to short-range conduction. The shifting of the peak towards the high frequencies for Co concentration up to x=0.05 combined with the increase in peak strength. The peak shift towards the high-frequency region corresponds to conductivity. For Co concentrations of x= 0.10 to 0.20, a shift towards low frequencies is observed with maximum peak strength being observed for x= 0.10. This shift towards the low-frequency side as the Co composition increases is caused due to the increase in relaxation time [81]. The complex electrical modulus spectrum (M' vs M'') of all the $Co_xSn_{1-x}Se$ samples at room temperature is shown in fig. 5.10(c). It is noticed that there is a formation of asymmetric semi-circular arc in every sample. This confirms the dominance of the bulk effect towards electrical conduction. The appearance of arcs in the spectra represents the single phase of the samples. The centers of the semi-circular arcs that lie below the x-axis indicate a non-Debye type relaxation. The semi-circular arcs observed in the low-frequency region represent the existence of grain boundaries. The radii of semi-circular arcs decrease with an increase in Co concentration till x= 0.05. The radius is maximum for x= 0.10, and thereafter decreases for x= 0.20. This would mean that the conduction processes depend on the doping concentration [106].

5.3.5.2 Temperature dependent dielectric studies

Figure 5.11(a-f) depicts the frequency dependence of dielectric constants (ε') for all the $Co_xSn_{1-x}Se$ samples in the temperature range 323 K-523 K. The value of ε' is large in the low-frequency region and decreases with frequency increase for all the compositions at all temperatures. It becomes independent of frequency above 10 kHz. There is no remarkable change observed in the ε' value at the high-frequency region in all cases at all temperatures. The combined contribution of interfacial, electronic, atomic, and ionic polarization results in net polarisation in the low-frequency region. When the measuring frequency is lower than the relaxation frequency, all kinds of polarizations will influence the dielectric constant. The large value of the dielectric constant is due to interfacial polarization attributed to grain boundaries in the low-frequency region.

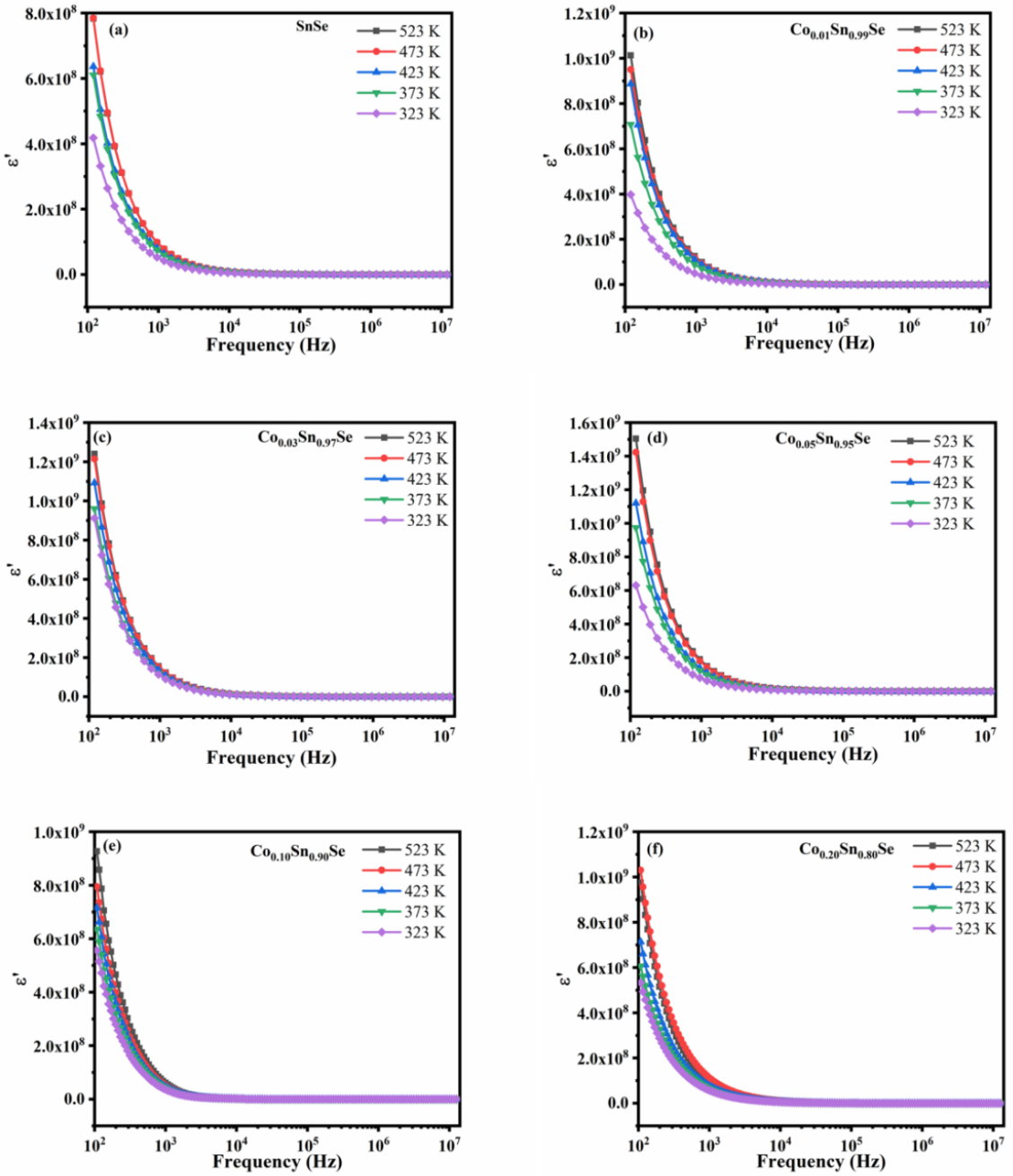

Figure 5.11 Variation of Dielectric constant vs. Frequency of (a) SnSe, (b) $Co_{0.01}Sn_{0.99}Se$, (c) $Co_{0.03}Sn_{0.97}Se$, (d) $Co_{0.05}Sn_{0.95}Se$, (e) $Co_{0.10}Sn_{0.90}Se$, and (f) $Co_{0.20}Sn_{0.80}Se$ respectively in the temperature range of 323 -523 K.

The variation of dielectric constant with frequency is explained by Maxwell-Wagner's [10] theory of interfacial polarization. This theory agrees with Koop's theory [15]. According to this theory, interfacial polarization is prominent in the low-frequency region which causes charge trapping at grain boundaries. Because grain boundaries act as a barrier to charge carrier movement. In the low-frequency region, the large value of the dielectric constant can be illustrated in two ways. The first one is, that the Co-doped SnSe polycrystals have a high density of disordered positive ions of Cobalt and Tin

gaps and negative ions of Selenium vacancies which act as shallow acceptors at grain boundaries. The arrangement of these Cobalt, Tin gaps, and Selenium vacancies in Co-doped SnSe polycrystals may result in the formation of dipole moments. Thus applying an external field will rotate the dipole moments at grain boundaries and contribute to increasing the dielectric constant value. The second is that at high pressure, the grain boundaries in compacted pellets must have a lot of, vacancies, porosities, defects, and dangling bonds. These defects at grain boundaries can alter the space charge distribution of negative and positive charges. The positive and negative space charges move towards the negative and positive poles at grain boundaries when an external field is applied. This generates a large number of dipole moments, resulting in a high dielectric constant value. In each case, the increase in dielectric constant with temperature can be attributed to charge carrier thermal conduction as the temperature rises. The value of ε' is increased with Co-doping into SnSe and it is found to be large for the composition $Co_{0.05}Sn_{0.95}Se$ due to the high 3D flowery nature of the sample compared to other samples. This composition has more grain boundaries due to the increased flowery nature. This can cause the trapping of more number of charge carriers at the boundaries which raise the ε' value. The dielectric constant decreases for $Co_{0.10}Sn_{0.90}Se$ due to the decrease in flowery nature. A slight increase is observed for $Co_{0.20}Sn_{0.80}Se$ composition due to the small rod-like morphology having large grain boundaries. The value of ε' ≈¬50-1400 is in the frequency-independent region above 10 kHz. Similar behaviour has been observed in PbS nanosheets [16], Bi2S3 nanorods [17] and NiS2 [18] nanoparticles where ε' ≈¬200 above 10 kHz, ε' ≈20 above 100 kHz, and ε' ≈150 above 1 kHz respectively. When frequency increases, the dipoles do not have rapid orientation in the applied ac field direction. As a result, dipole oscillations lag behind frequency and ε' decreases in the high-frequency region. Further, the dipoles are no longer able to follow the applied ac field as the frequency rises, and their orientation is lost. Hence, at high frequencies, ε' reaches a constant value. The values of ε' obtained for the Co-doped SnSe have possible applications in microelectronic and capacitive storage devices [19]. Figure 5.12(a-f) depicts the variation of dielectric loss (ε") as a function of frequency at different temperatures for all the Co-doped SnSe. For all compositions, the value of ε" decreases with increasing frequency and increases with increasing temperature. It is high in the low-frequency region, and the composition $Co_{0.05}Sn_{0.95}Se$ has the highest dielectric loss. Low dielectric constants and losses may have applications in electro-optic and high-frequency devices [21–23].

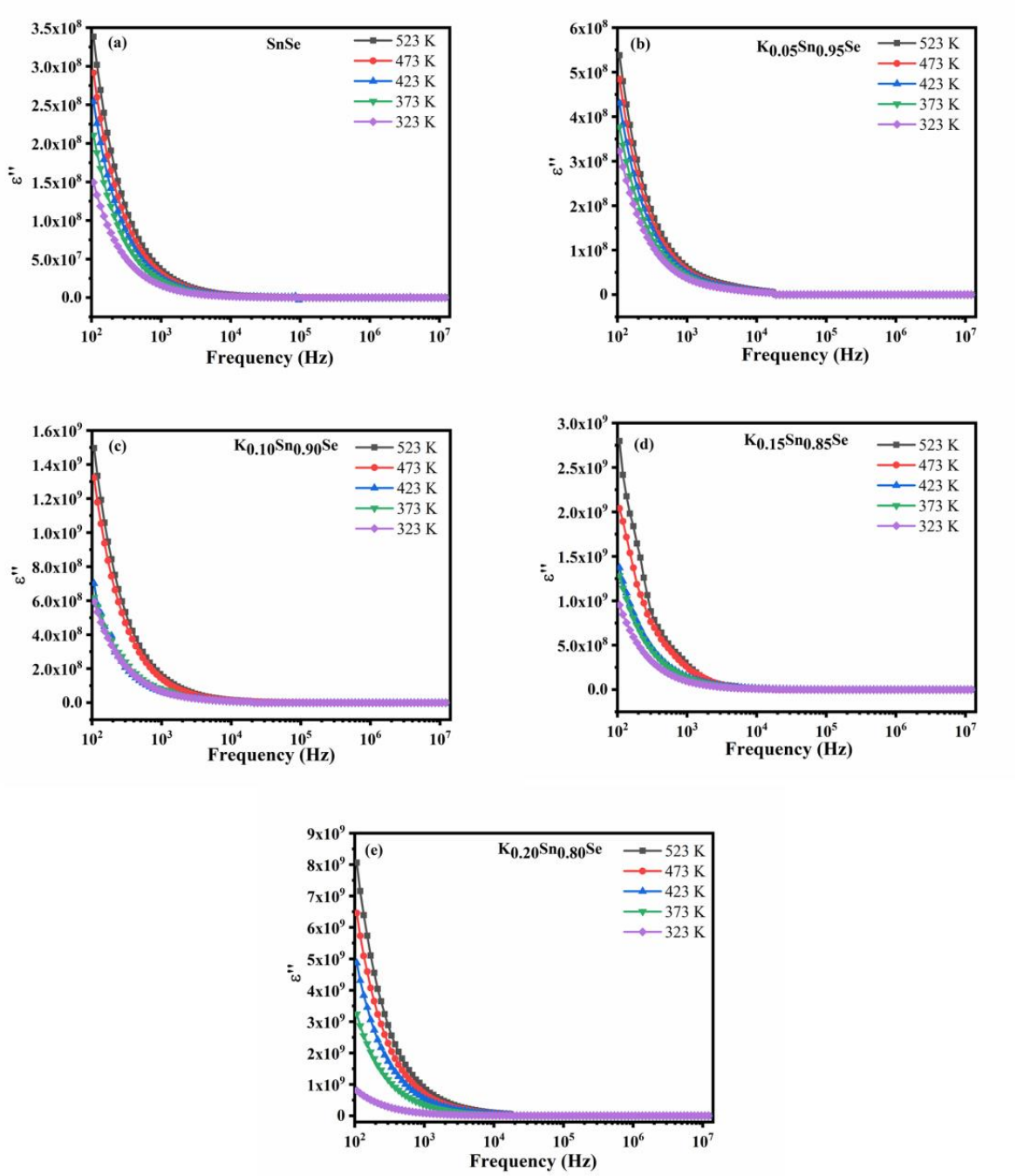

Figure 5.12 Variation of Dielectric loss vs. Frequency of (a) SnSe, (b) $C_{0.01}Sn_{0.99}Se$, (c) $Co_{0.03}Sn_{0.97}Se$, (d) $Co_{0.05}Sn_{0.95}Se$, (e) $Co_{0.10}Sn_{0.90}Se$, and (f) $Co_{0.20}Sn_{0.80}Se$ respectively in the temperature range of 323 -523 K.

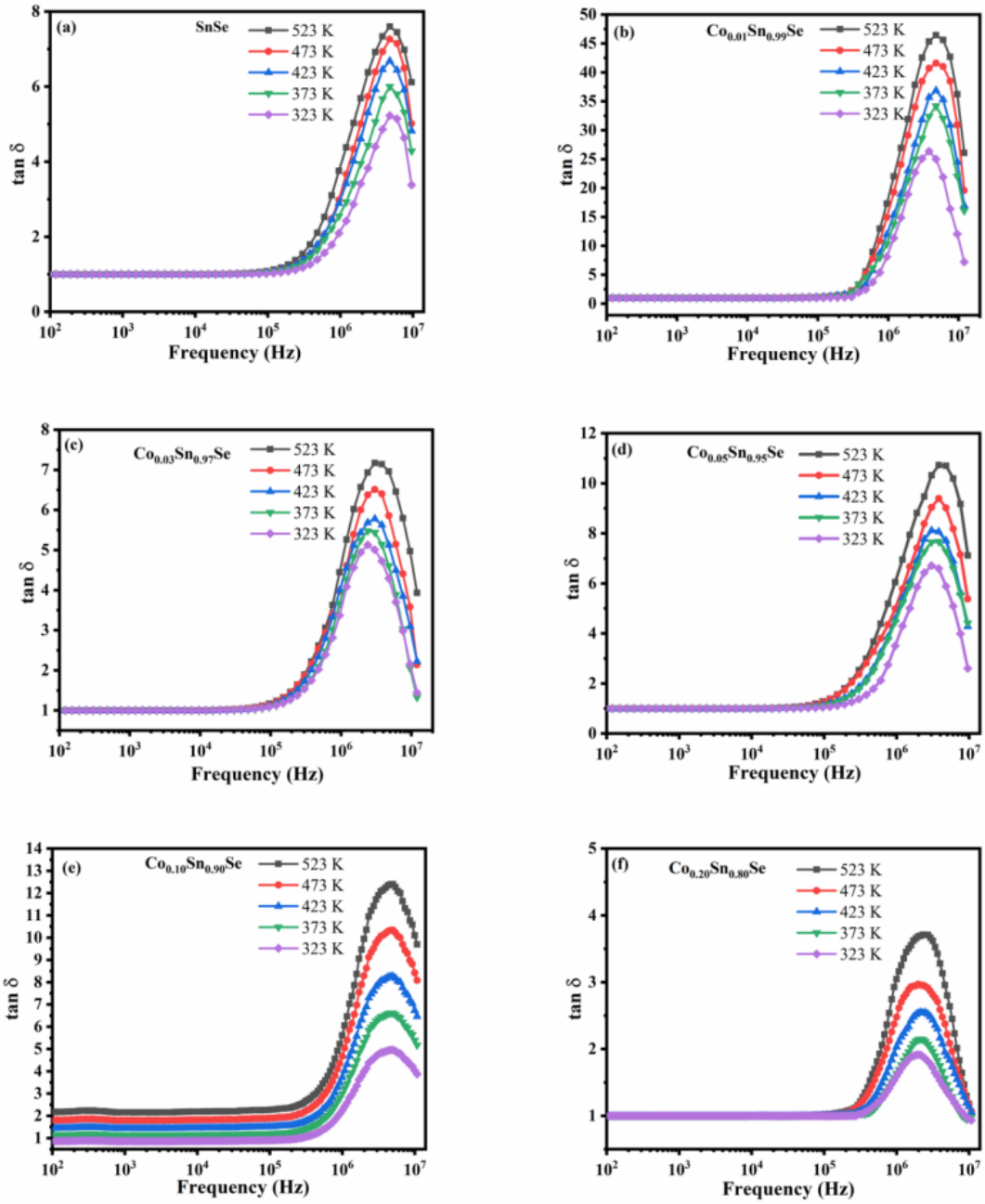

Figure 5.13 Variation of Dielectric loss tangent vs. Frequency of (a) SnSe, (b) $Co_{0.01}Sn_{0.99}Se$, (c) $Co_{0.03}Sn_{0.97}Se$, (d) $Co_{0.05}Sn_{0.95}Se$, (e) $Co_{0.10}Sn_{0.90}Se$, and (f) $Co_{0.20}Sn_{0.80}Se$ respectively in the temperature range of 323 -523 K.

In fig. 5.13(a-f), the variation of the dielectric loss tangent (tan δ) as a function of frequency is shown for all compositions. At low frequencies, the tan δ is low and frequency independent for all of the compositions, but it increases as the frequency increases. The tan δ shows a maximum value before it shows decreasing trend in the region of high frequencies. Relaxation peaks are observed for all the compositions in the high-frequency region of 1 MHz-10 MHz. After the occurrence of the relaxation peaks, the tan δ shows decreasing trends which indicates that the sample reveals almost

zero dielectric loss at higher frequencies [24]. The peak intensity is increased as the temperature increases for all the compositions. The peaks are shifted to the low-frequency region as the temperature rises.

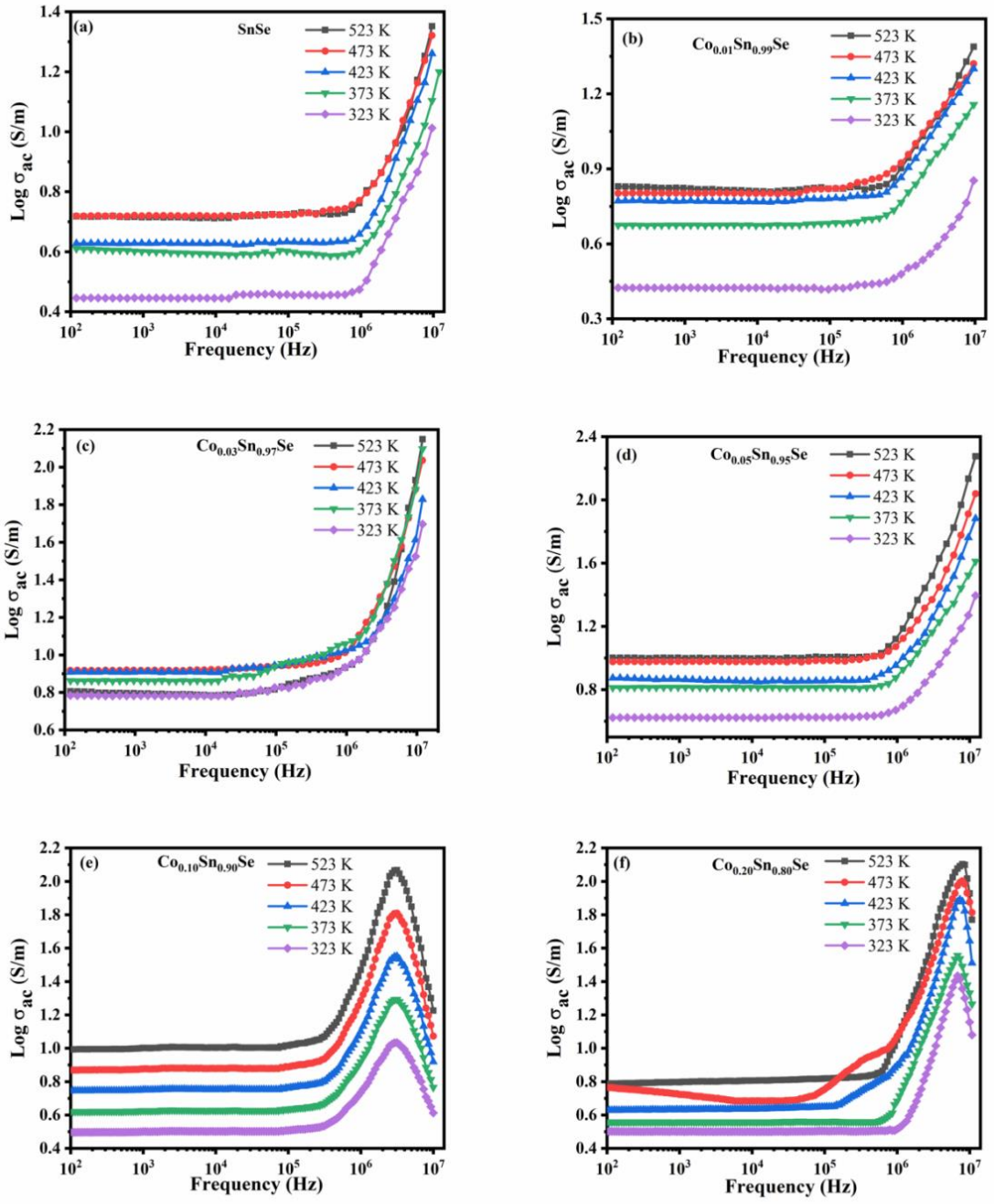

Figure 5.14 Variation of AC conductivity vs. Frequency of (a) SnSe, (b) $Co_{0.01}Sn_{0.99}Se$, (c) $Co_{0.03}Sn_{0.97}Se$, (d) $Co_{0.05}Sn_{0.95}Se$, (e) $Co_{0.10}Sn_{0.90}Se$, and (f) $Co_{0.20}Sn_{0.80}Se$ respectively in the temperature range of 323 -523 K.

From fig.5.14(a-f), the following two regions can be identified: (i) plateau region (100 Hz-100 kHz) which is frequency independent in the low-frequency region for all the compositions corresponding to DC conductivity, and (ii) the increasing portion in the frequency-dependent high-frequency region (100 kHz- 10 MHz) which

indicates the AC conductivity. Thus the conduction mechanism in all the samples follows Jonscher's power law. The dispersion region in the AC conductivity shifted toward high frequencies as the temperature rises which shows the bulk relaxation of the materials [26]. Relaxation peaks are observed for x=0.10 and x=0.20 compositions in the frequency range of 1 MHz-10 MHz. As the temperature rises, the peaks shift to the high-frequency region. The increase in temperature causes an increase in the thermal conduction of charge carriers in all compositions, resulting in an increase in AC conductivity in each case. The rise in temperature causes more charge carriers to move over the barrier and increase the electrical conductivity. The AC conductivity variation in all the cases can also be related to the average crystallite size and surface morphology of the samples. At 523 K, the composition $Co_{0.05}Sn_{0.95}Se$ exhibits a high AC conductivity. This is due to the sample's heavy flowery nature and the low average crystallite size of $Co_{0.05}Sn_{0.95}Se$, which has a large number of grain boundaries that can trap more charge carriers at the interface. In the high-frequency region, there are relaxation peaks for x=0.10 and 0.20.

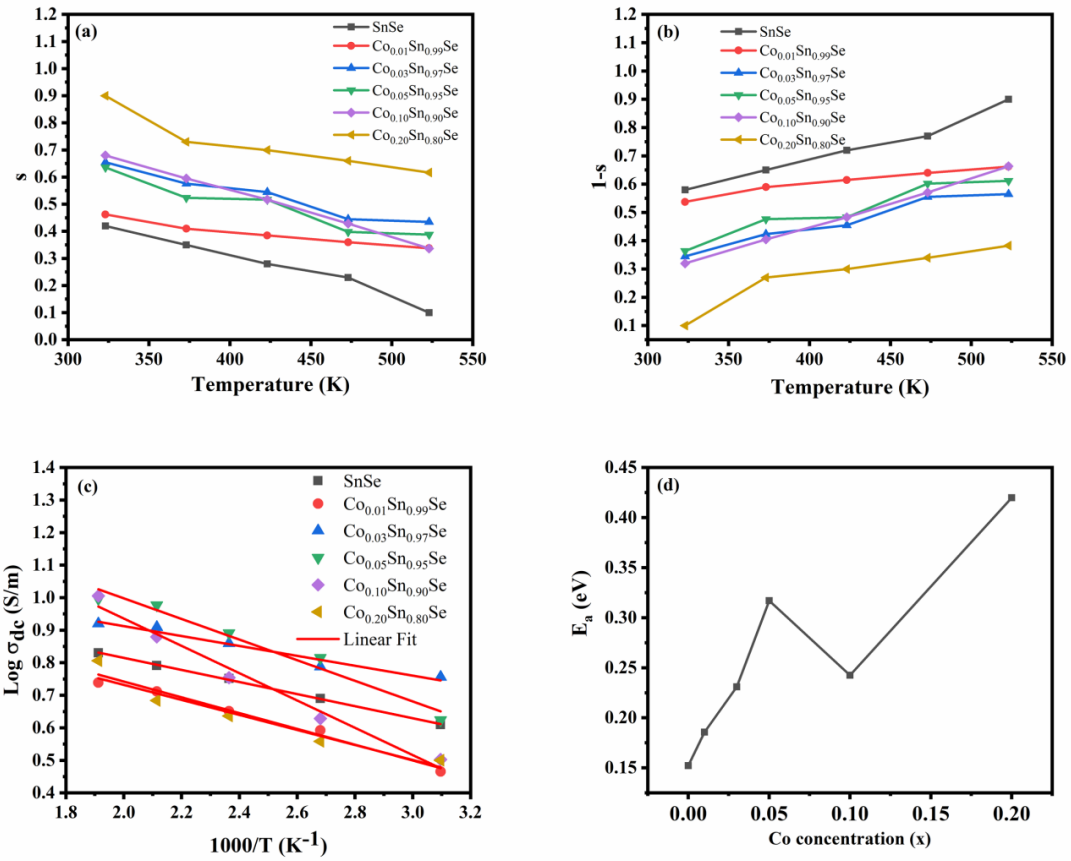

Figure 5.15 (a) Variation of frequency exponent 's' vs. temperature, (b) Variation of 1-s vs. Temperature, (c) Arrhenius plot for determining activation energy at 100 kHz, and (d) Activation energy vs. Dopant concentration (x).

Table 5.3 Frequency exponent 's', activation energy (E_a), and maximum barrier height (W_m) values at various temperatures for all Co-doped SnSe samples

Composition	Temperature (K)	Frequency exponent (s)	Activation Energy (E_a) (eV)	W_m (meV)
SnSe	323	0.42		
	373	0.35		
	423	0.28	0.152	1.52
	473	0.23		
	523	0.1		
$Co_{0.01}Sn_{0.99}Se$	323	0.4625		
	373	0.41		
	423	0.385	0.185	0.598
	473	0.36		
	523	0.338		
$Co_{0.03}Sn_{0.97}Se$	323	0.655		
	373	0.576		
	423	0.545	0.231	1.14
	473	0.445		
	523	0.435		
$Co_{0.05}Sn_{0.95}Se$	323	0.636		
	373	0.5235		
	423	0.517	0.317	1.24
	473	0.398		
	523	0.388		
$Co_{0.10}Sn_{0.90}Se$	323	0.68		
	373	0.595		
	423	0.517	0.242	1.71
	473	0.429		
	523	0.3367		
$Co_{0.20}Sn_{0.80}Se$	323	0.9		
	373	0.73		
	423	0.7	0.419	1.27
	473	0.66		
	523	0.617		

The slopes of Frequency vs. Log ac (the increasing portion of AC conductivity) plots for all $Co_xSn_{1-x}Se$ samples are used to calculate the frequency exponent 's'. The values of 's' for all samples are found to decrease with temperature rise, and values ranging from 0.1 to 0.9, which are less than 1 and are shown in fig.5.15(a) with the variation of temperature. From the manner of variation of 's', it can be concluded that the conduction process follows Correlated Barrier Hopping (CBH) mechanism. Table 5.3 shows the values of 's' for all of the samples at various temperatures. The valence band and conduction band are separated by localized states which are created due to the defects that occur in the material. Every localized state is separated by a barrier of height W_m. Under normal circumstances, charge carriers are confined to localized states. When external energy is supplied, charge carriers will move from filled localized

states to unfilled localized states, resulting in hopping. Since the hopping mechanism is taking place over the barrier, activation energy (ΔE_a) is needed by the charge carriers to cross across the barrier. The values of 's' can be calculated according to the CBH model using the Eqn. (8)[107]. Figure. 5.15(c) shows the frequency dependence of dc conductivity for all $Co_xSn_{1-x}Se$ samples at 100 kHz. The activation energy is estimated from the slopes of frequency vs. Log σ_{dc} after linear fitting as depicted in fig. 5.15(c). It is found to increase with Co doping till x=0.05, thereafter it decreases for x=0.10 slightly and further increases for x=0.20 as displayed in fig. 5.15(d). Table 5.3 shows the activation energy (E_a) values for all of the samples.

The frequency dependence of the real part of electrical modulus (M') for all the Co-doped SnSe samples at various temperatures are displayed in fig. 5.16(a-f). M' is nearly zero and frequency independent in the low-frequency region up to 1MHz. After that as frequency increases, M' value increased for all the compositions at all temperature. The variation of M'' with frequency is shown in fig. 5.17(a-f). The M'' is constant and frequency independent in the region of low frequencies. M'' increases with frequency, and relaxation peaks can be seen in the high-frequency region (1 MHz-10 MHz). The region beneath the peak maximum corresponds to charge carrier long-range conduction. Charge carriers are constrained to potential wells by short distances above the peak maximum. As the temperature rises, the relaxation peaks shift to the high-frequency side.

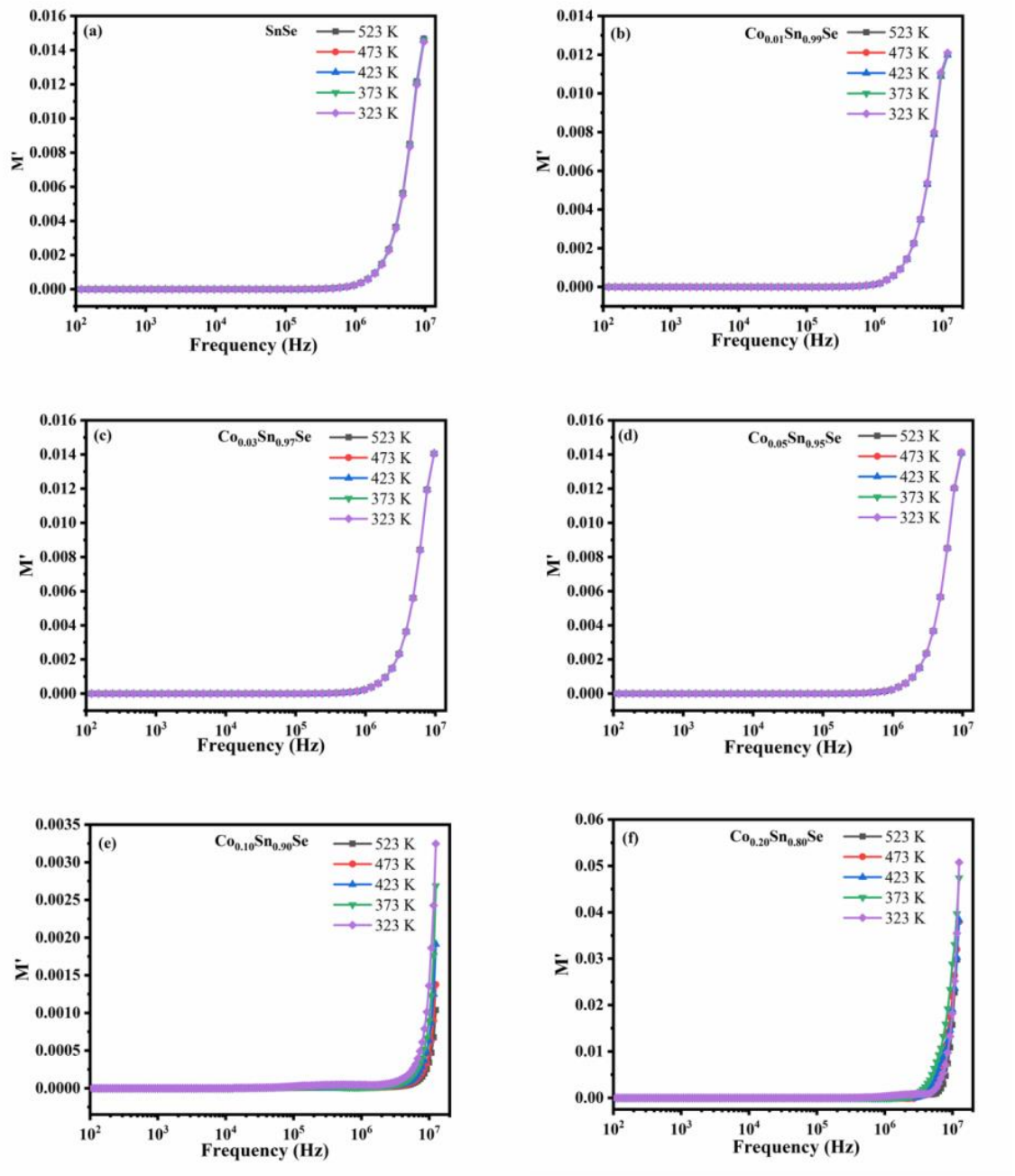

Figure 5.16 Variation of M' vs. Frequency of (a) SnSe, (b) $Co_{0.01}Sn_{0.99}Se$, (c) $Co_{0.03}Sn_{0.97}Se$, (d) $Co_{0.05}Sn_{0.95}Se$, (e) $Co_{0.10}Sn_{0.90}Se$, and (f) $Co_{0.20}Sn_{0.80}Se$ respectively in the temperature range of 323 K-523 K.

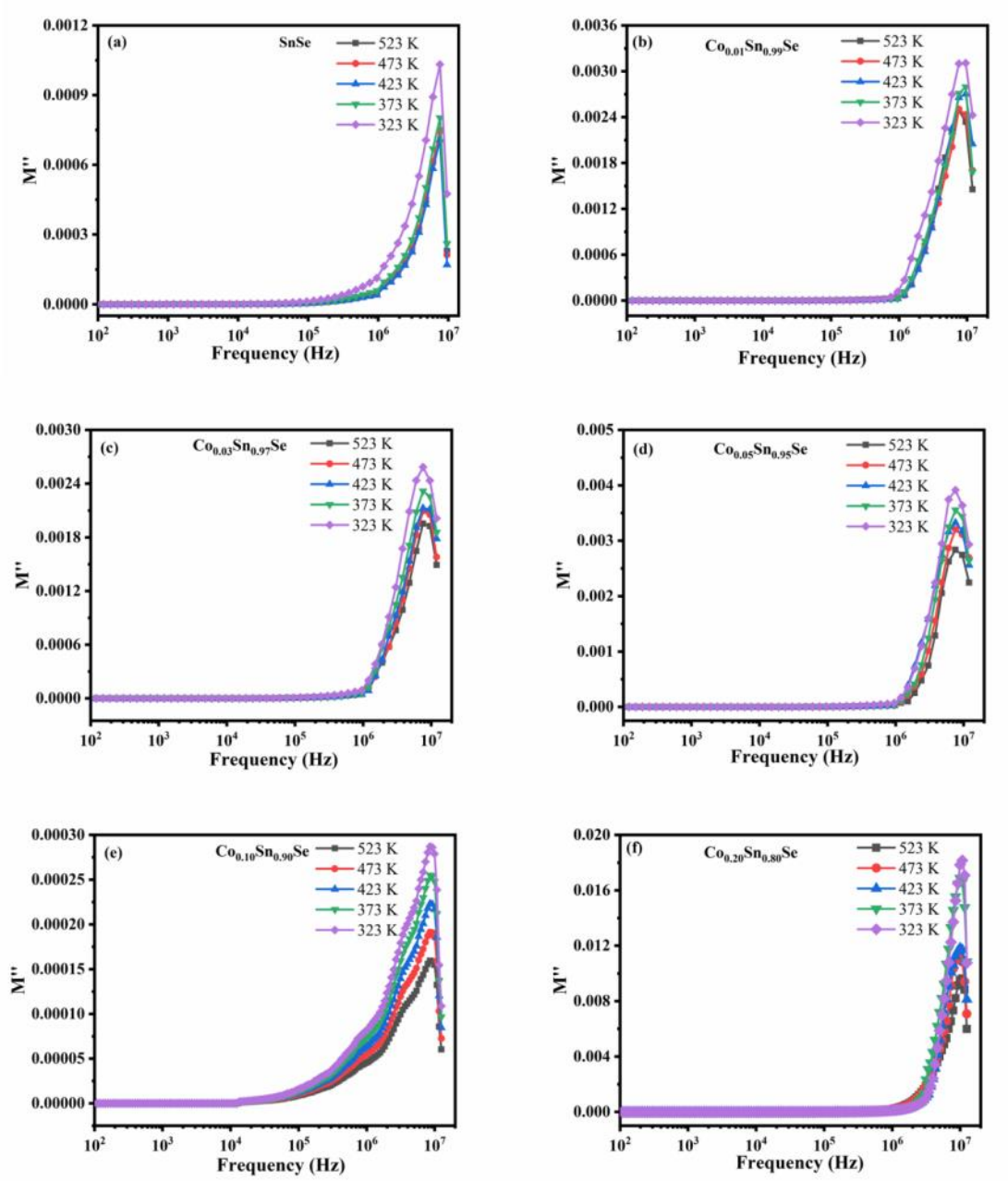

Figure 5.17 Variation of M'' vs. Frequency of (a) SnSe, (b) $Co_{0.01}Sn_{0.99}Se$, (c) $Co_{0.03}Sn_{0.97}Se$, (d) $Co_{0.05}Sn_{0.95}Se$, (e) $Co_{0.10}Sn_{0.90}Se$, and (f) $Co_{0.20}Sn_{0.80}Se$ respectively in the temperature range of 323 K-523 K.

Figure 5.18(a-f) depicts the variation of M' vs. M''. At all temperatures, single semi-circular arcs formed in all Co-doped samples, their centres are located below the x-axis. As the temperature increases, the radii of semi-circular arcs reduce in all the samples which indicate the conduction mechanism is a temperature-dependent hopping mechanism. The formation of semi-circular arcs in all samples at all temperatures is incomplete due to non-Debye type relaxation. The observed semi-circular arcs indicated the presence of grain boundaries in the low-frequency region.

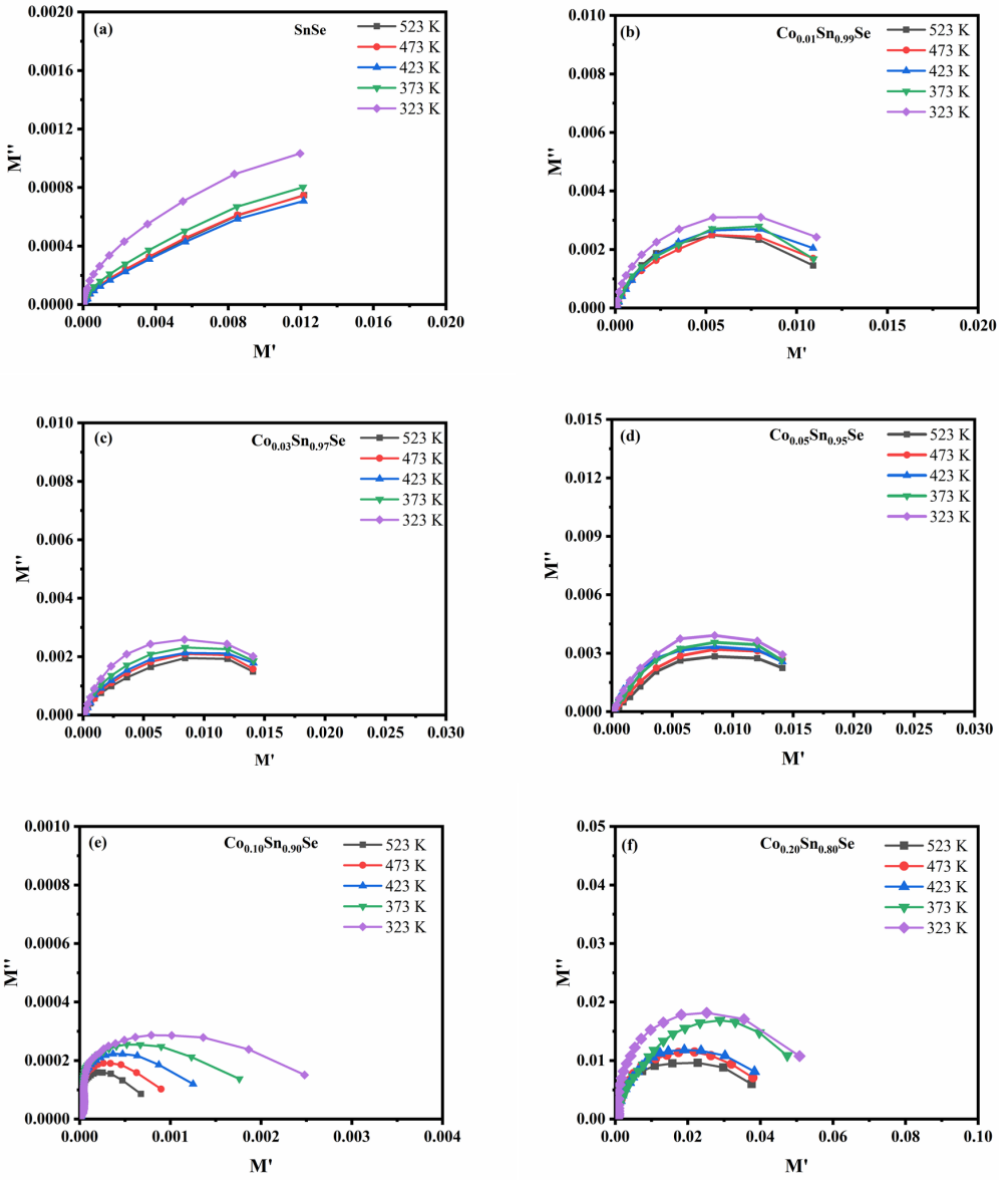

Figure 5.18 M'' vs. M' of (a) SnSe, (b) $Co_{0.01}Sn_{0.99}Se$, (c) $Co_{0.03}Sn_{0.97}Se$, (d) $Co_{0.05}Sn_{0.95}Se$, (e) $Co_{0.10}Sn_{0.90}Se$, and (f) $Co_{0.20}Sn_{0.80}Se$ respectively in the temperature range of 323 K-523 K.

5.3.6 Magnetic studies

Figure 5.19 depicts the M-H curves for $Co_xSn_{1-x}Se$ (x=0.00, 0.01, 0.03, 0.05, 0.10 and 0.20) polycrystals at room temperature. It is clear from fig. 5.19, that pure SnSe exhibits anti-ferromagnetic vortex behaviour at higher magnetic fields and experience ferromagnetism at low field areas. This ferromagnetic nature observed for undoped SnSe at low magnetic fields is due to the occurrence of residual defects as justified by many reports that explained the presence of ferromagnetism in undoped nonmagnetic semiconductor lattice [31,108]. All the $Co_xSn_{1-x}Se$ samples show ferromagnetic behaviour at room temperature having hysteresis loops with finite magnetization at 1.5 Tesla. The reasons for observed ferromagnetism at room temperature in all the doped

samples could be from several possibilities such as the formation of secondary phases related to Co or metallic Co, native defects, and carrier-related intrinsic property [101]. However native defects alone cannot produce ferromagnetism and no secondary phases related to Co were found in our case as evident from XRD, EDAX, and XPS. In general, two exact independent mechanisms are arising from two different processes which explain the causes for ferromagnetism in DMS. The first one is bound magnetic polarons (BMPs) generating long-range magnetic order and the second is carrier induced Ruderman-Kittel-Kasuya-Yosida substitute interaction (RKKY) [109]. From the XPS results, it is noticed that for the x=0.10 sample, Cobalt exists in +2 valence state. In the current study, the ferromagnetism observed in all Co-doped samples is attributed to the carrier-mediated intrinsic magnetic property as Co^{+2} ions being substituted for Sn^{+2} ions in the SnSe lattice without changing its original crystal structure. Distinct shapes and widths of hysteresis loops are obtained for different $Co_xSn_{1-x}Se$ Samples which are affected by many factors such as the presence of defects, the concentration of the dopant, and grain size [110]. The parameters such as coercivity (H_C), remnant magnetization (M_R), and saturation magnetization (M_S) are shown in Table 3, which do not follow any particular trend as Co concentration increases. The fluctuation in the magnetic parameter values might be due to the dislocations and defects that occurred during the growth process of $Co_xSn_{1-x}Se$ as observed from HRTEM studies (fig. 5.5(e-i)). From the hysteresis loops, strong ferromagnetism is observed for $Co_{0.10}Sn_{0.90}Se$ composition with a saturation magnetization (M_S) of 0.1342 emu/g. The increase in Co concentration leads to an increase in free delocalized carriers of host lattice and the localized d spins of Co^{+2} ions. The double exchange interaction (sp-d) between the delocalised charge carriers and the localised d spins of Co^{+2} ions become stronger with increase in Co concentration [111,112]. Further for $Co_{0.20}Sn_{0.90}Se$, the M_S decreases to 0.1083 emu/g. In general, two competing mechanisms can explain the ferromagnetism in DMS. One is long-range carrier-mediated mechanism is ferromagnetic and the other is short-range direct exchange mechanism is antiferromagnetic. The antiferromagnetic mechanism is neglected at lower concentrations of magnetic impurities. But, at a certain concentration of the magnetic ion, antiferromagnetic interactions play a crucial role and reduce the ferromagnetic nature of the sample [101]. The increase in Co concentration may reduce the distance between the Co ions that causes antiferromagnetic interactions between the neighbouring Co-Co ions and weakens the ferromagnetism in the SnSe matrix [110,113]. Hence the variation in the saturation magnetization (M_S) values of Co-doped

SnSe samples is due to the coupling between ferromagnetic and antiferromagnetic interactions.

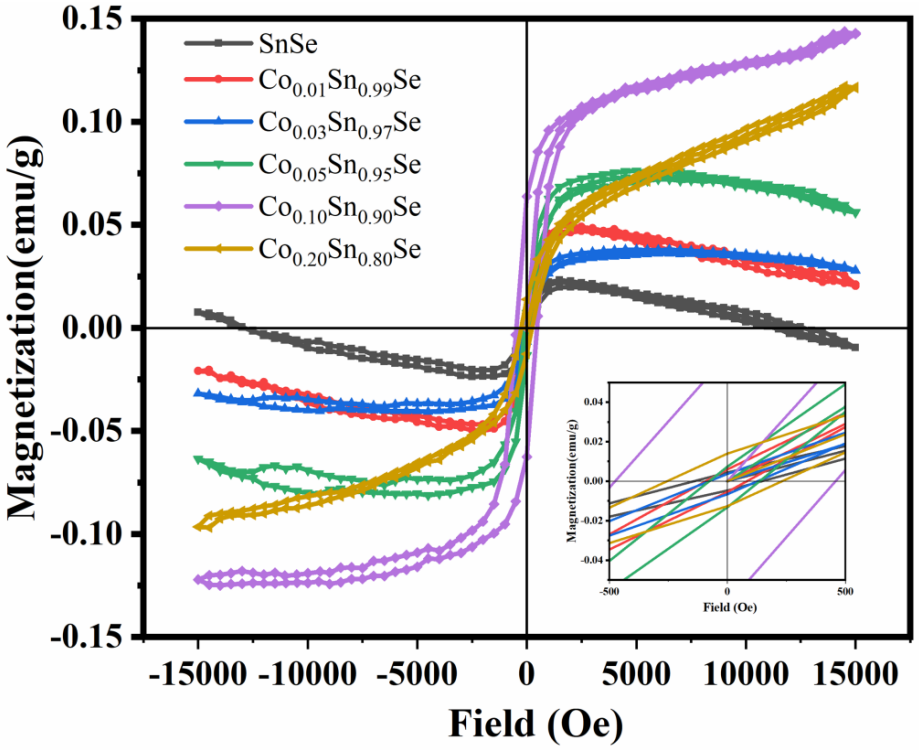

Figure 5.19 The hysteresis loops for all $Co_xSn_{1-x}Se$ samples measured at room temperature by VSM.

The value of remnant magnetization (M_R) rises from 0.00453 emu/g to 0.007 emu/g up to a cobalt concentration of 0.05. At Co concentration x= 0.10 the M_R value decreases to 0.0045 emu/g and increases to 0.0133 for x= 0.20. The coercivity is increased from 69 Oe to 153 Oe as the composition of Co increases from x= 0.01 to 0.05. This is due to the increase of anisotropy of the 3D flower-like structures formed for higher concentrations of Co [114,115]. The decrease in coercivity from 153 Oe to 33 Oe with increasing concentration from x= 0.05 to 0.10 could be because of the decrease in the anisotropy energy. A maximum coercivity of 244 Oe is obtained for x= 0.20, exhibiting uneven small rod-like structures having higher shape anisotropy. The increase in coercivity also might be caused by the largest value of magnetic ion impurity exhibiting a strong ferromagnetic coupling [31]. This is the first report on the magnetic properties of $Co_xSn_{1-x}Se$ samples showing room temperature ferromagnetic behaviour which can have potential applications in data storage and spintronic devices.

Table 5.3 Coercivity (H_C), Saturation Magnetization (M_S), and Remnant Magnetization (M_R) as a function of Co concentration.

Composition	H_C (Oe)	M_S (emu/g))	M_R (10^{-3} emu/g)
SnSe	69	0.0235	4.53
$Co_{0.01}Sn_{0.99}Se$	87	0.049	5.52
$Co_{0.03}Sn_{0.97}Se$	106	0.0426	5.10
$Co_{0.05}Sn_{0.95}Se$	153	0.0536	7.00
$Co_{0.10}Sn_{0.90}Se$	33	0.1342	4.50
$Co_{0.20}Sn_{0.80}Se$	244	0.1083	13.3

5.4 Conclusions

The $Co_xSn_{1-x}Se$ diluted magnetic semiconductors were successfully prepared using hydrothermal method. A single-phase with an orthorhombic structure for all the samples was concluded from XRD. The average crystallite size, strain, and dislocation densities were measured and they are well-matched with literature values. There is a small decay in the lattice constant values with an increase in Co concentration due to the ionic mismatch of Co and Sn. The surface morphology was observed by SEM, which revealed the 3D flower-like morphology that turned to small rod-like morphology for increasing compositions of Co. HR-TEM results are consistent with the SEM observations and revealed the presence of grain boundaries and dislocations. EDAX elucidated the presence of Cobalt in $Co_xSn_{1-x}Se$ samples. The optical studies obtained from UV-Vis-NIR DRS spectroscopy illustrate that both direct and indirect bandgaps decrease as the Co concentration increases up to x=0.05 after that they increased for x=0.10 and again decreased for x=0.20. The XPS studies confirmed the valence state of Sn, Se, and Co for the sample $Co_{0.10}Sn_{90}Se$. The room temperature dielectric studies revealed that $Co_{0.05}Sn_{0.95}Se$ has obtained high value of dielectric constant and ac conductivity. At low frequencies, the $Co_{0.05}Sn_{0.95}Se$ obtained the highest dielectric constant and dielectric losses at 523 K. The Co doping and change in temperature showed a significant effect on the AC conductivity and the $Co_{0.05}Sn_{0.95}Se$ sample exhibited the highest AC conductivity value at 523K. The CBH model is a possible mechanism for the charge carriers of the hopping mechanism, based on the calculated value of the parameter 's'. Electrical modulus studies revealed the impact of grain boundary effects, and all Co-doped SnSe samples showed non-Debye type relaxation. The findings suggest that the material could be used in microelectronic, capacitive storage electro-optic, and frequency-related devices. VSM measurements have described the ferromagnetism revealed by all the $Co_xSn_{1-x}Se$ SnSe at room temperature,

which suggests that these dilute magnetic semiconductors which exhibit thermoelectric behaviour can also have applications in spintronic devices.

CHAPTER 6: Investigation of Dielectric and Magnetic properties of Fe doped SnSe

6.1 Introduction

The doping effect of Co on optical, dielectric and magnetic properties of SnSe has been presented in the previous chapter. On the same lines doping of Fe into SnSe also can influence the optical, dielectric properties and it can induce magnetism in the host lattice. Researchers have theoretically investigated the magnetic properties of transition metal (Ni, Mn, Co, Fe, Mn) doped SnSe[50–53]. However experimental investigations are scant in this direction.

In the present study we have synthesized $Fe_xSn_{1-x}Se$ with x=0.00, 0.01, 0.03, 0.05, 0.10 and 0.20 using hydrothermal method. The influence of Fe on structural, morphological and optical parameters such as average crystallite size lattice parameters and bandgap are well studied. Further the effect of temperature on dielectric properties of Fe doped SnSe are investigated in detail. Furthermore room temperature magnetic studies were investigated for the prepared samples.

6.2 Synthesis of $Fe_xSn_{1-x}Se$ polycrystals

Analytical grades of $SnCl_2.2H_2O$ (99.9%), SeO_2 (98%), $FeCl_2.4H_2O$ (99.9%), NaOH (85%), $NaBH_4$ (99.9%) were procured from MERCK and utilized as received without conducting any further purification process. Initially, for Fe doped SnSe, stoichiometric amounts of $SnCl_2.2H_2O$, $FeCl_2.4H_2O$, and 4 g of NaOH were dissolved in 100 ml of DI water and stirred for 10 min. Then the colour of the solution is transformed to light green color. Stoichiometric amount of SeO_2 was added to the above solution and followed by stirring of 15 min. Finally to reduce the SeO_2, 1 g of $NaBH_4$ is mixed to the solution and stirred for 30 min. Then the resultant solution was transferred into an autoclave and subjected to 150 ^oC in a vacuum oven for 12h. After the reaction time is over, the autoclave was cooled naturally to room temperature and followed the post treatment of washing with ethanol and DI water many times. The obtained product was dried at 80 ^oC in a vacuum oven. Pristine SnSe was also prepared by similar procedure except the addition of Fe precursor.

6.3 Results and Discussion

6.3.1 X-Ray Diffraction

Figure 6.1(a) shows X-Ray diffraction pattern of $Fe_xSn_{1-x}Se$ for x = 0.00, 0.01, 0.03, 0.05, 0.10 and 0.20 polycrystals. Single-phase with the orthorhombic structure is found in undoped and all Fe-doped SnSe samples. From the fig. 6.1(a), it is noticed that the diffraction peaks occur mainly from the planes (2 0 1), (2 1 0), (0 1 1), (1 1 1), (4 0 0), (3 1 1), (4 1 1), (5 1 1) and (4 2 0). All the planes are well-indexed, and well-matched with standard PDF file no: #48-1224 [58,71,85]. There are two major peaks (111) and (4 0 0) are observed in all the samples. The diffraction intensity of both the planes (1 1 1) and (4 0 0) increases with increase in Fe concentration which shows increase in crystallinity. This type of behavior in the diffraction intensity of the planes (1 1 1) and (4 0 0) is due to the residual stresses that occur by the mismatch of ionic size between Fe^{+2} (0.78 Å) and Sn^{+2} (0.93 Å). The calculated lattice parameters are well-matched with the standard values (a = 11.49 Å, b = 4.153 Å, c = 4.44 Å, PDF#48-1224). The lattice parameter values reduce with increase in the Fe content, which could be due to the lower ionic radius of Fe^{+2} (0.78 Å) when compared to Sn^{+2} (0.93 Å), and hence, the lattice may leads to shrink which results in the reduction of lattice constant. The variation of lattice parameters with Fe concentration is shown in fig. 6.1(b). The calculated lattice parameters are shown in Table 1. The values of average crystallite size are calculated from the major peaks (1 1 1) and (4 0 0) through the Debye-Scherrer formula from Eqn. (2) [58,116]

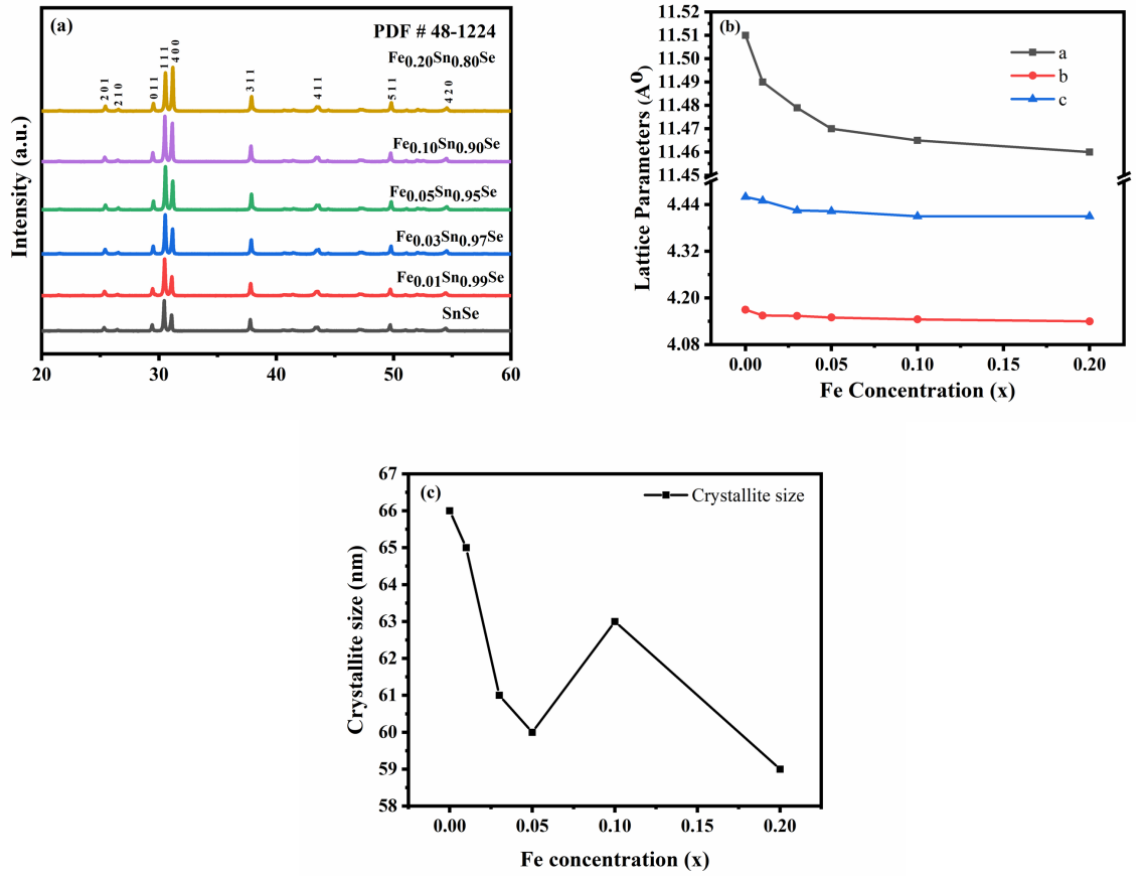

Figure.6.1 (a) XRD pattern of all $Fe_xSn_{1-x}Se$ samples, (b) Lattice parameter variation with concentration (x) of Fe, (c) crystallite size vs Fe doping concentration.

The calculated values are shown in Table 6.1. The value of D is found to be 66 nm for undoped SnSe. With increasing values of x from 0.00 to 0.05, the crystallite size decreased and thereafter attained a maximum value for x = 0.10 following which it decreased at x = 0.20. The calculated crystallite size values of undoped SnSe are in good agreement with existing literature values [91]. The noticed behavior of the average crystallite size is because of the lattice strains that are produced while synthesizing the $Fe_xSn_{1-x}Se$ samples [29]. The crystallite size is shown in the plot fig.6.1(c).

Table 6.1 XRD parameters of all $Fe_xSn_{1-x}Se$ compositions.

Sample	Lattice constants			Cell volume $(Å)^3$	D (nm)
	a (Å)	b (Å)	c (Å)		
SnSe	11.51	4.17	4.46	214.06	66
$Fe_{0.01}Sn_{0.99}Se$	11.49	4.155	4.45	212.45	65
$Fe_{0.03}Sn_{0.97}Se$	11.479	4.154	4.425	211.00	61
$Fe_{0.05}Sn_{0.95}Se$	11.47	4.15	4.423	210.54	60
$Fe_{0.10}Sn_{0.90}Se$	11.465	4.145	4.41	209.57	63
$Fe_{0.20}Sn_{0.80}Se$	11.46	4.14	4.41	209.22	59

6.3.2 Morphological studies and elemental analysis

Figure 6.2(a-f) revealed the morphology for all the $Fe_xSn_{1-x}Se$ samples. Pure SnSe exhibited the plate like morphology as shown in fig. 6.2(a). The plate like structures gradually deformed into rod like structures as Fe concentration into SnSe increases.. For x=0.20 composition small rods and nano particles are got agglomerated to form Sphere like structures. From fig. 6.3(a), the HRTEM image of $Fe_{0.10}Sn_{0.90}Se$ sample showing rod like structure at higher magnification. HRTEM image of $Fe_{0.20}Sn_{0.80}Se$ shows the agglomeration of small nanoparticle and rods as observed from fig. 6.3(b). Figure 6.3(c) shows the SAED pattern for $Fe_{0.10}Sn_{0.90}Se$ which consisting of set of rings corresponding to the lattice planes (1 1 1), (4 0 0), and (2 1 0) confirming the polycrystalline nature of the samples and the lattice planes are matched with the XRD data. Figure 6.3(d) depicts d-spacing of 3.3 Å corresponding to the plane (2 1 0). The elemental composition of pure and Fe-doped SnSe samples is confirmed through EDAX. Figure 6.4(a-c) shows the EDAX spectra for pure x=0.10 and 0.20 samples. The sharp peaks related to Sn, Se, and Fe are seen in fig. 6.4(d,k) which confirms the existence of Sn, Se, and Fe in the EDAX spectra. No other impurities were found other than the elements Sn, Se, and Fe. The elements Sn, Se, and Fe are distributed uniformly throughout the samples. The EDAX spectra show the near stoichiometric ratios of Sn, Se, and Fe in the respected compositions.

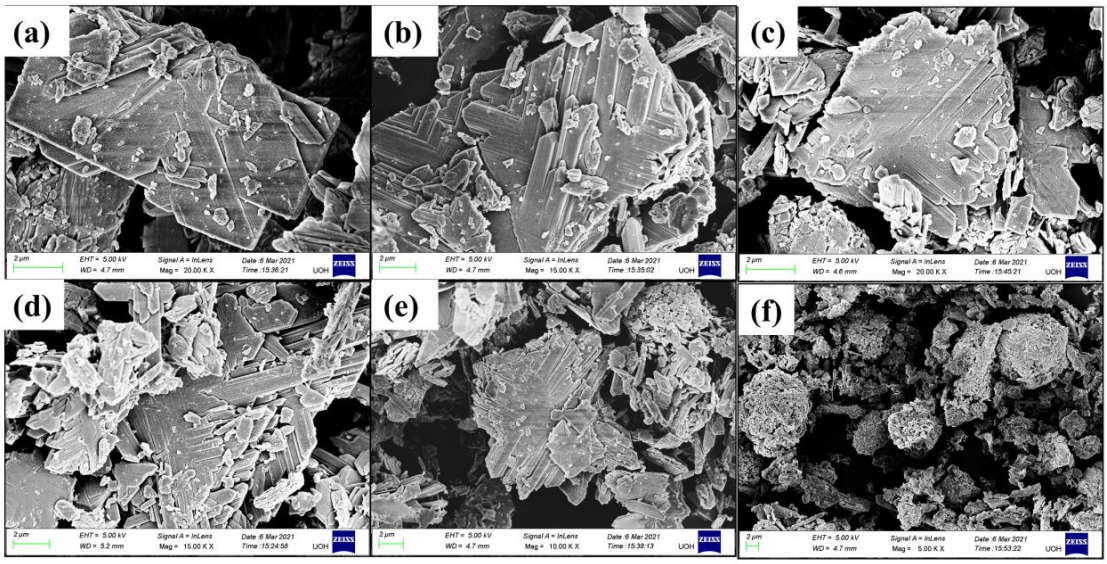

Figure 6.2 FESEM images of $Fe_xSn_{1-x}Se$ polycrystals (a) x = 0.00, (b) x = 0.01, (c) x = 0.03, (d) x = 0.05, (e) x = 0.10, and (f) x=0.20 at 2 μm range.

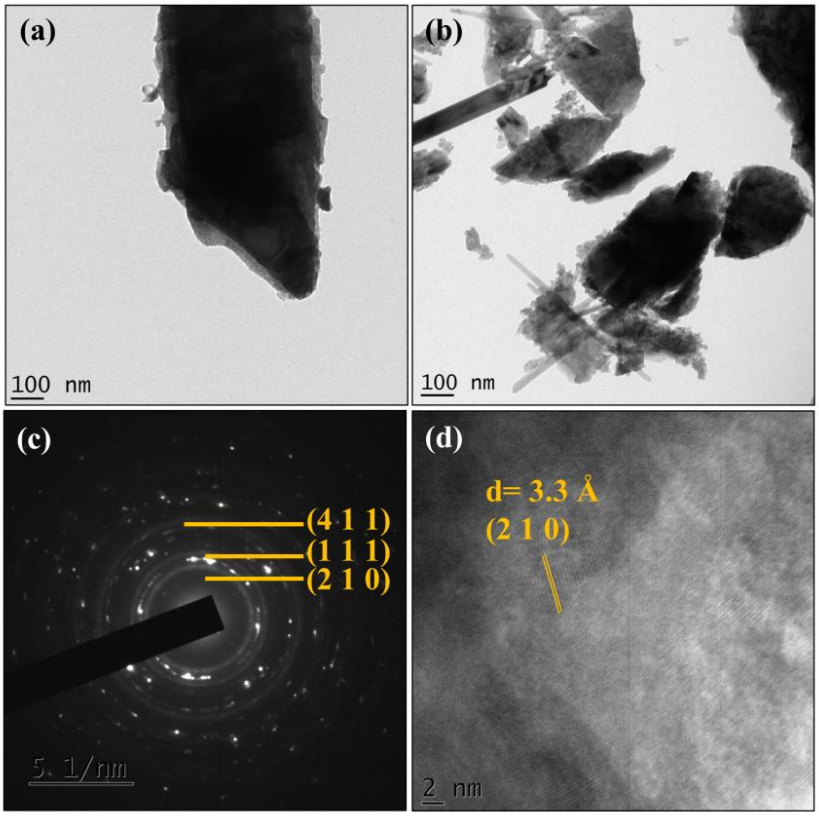

Figure 6.3 HRTEM images of $Fe_xSn_{1-x}Se$ polycrystals (a) x = 0.10, (b) x = 0.20, (c) SAED pattern of x = 0.10, and (d) d-spacing corresponding to the plane (2 1 0).

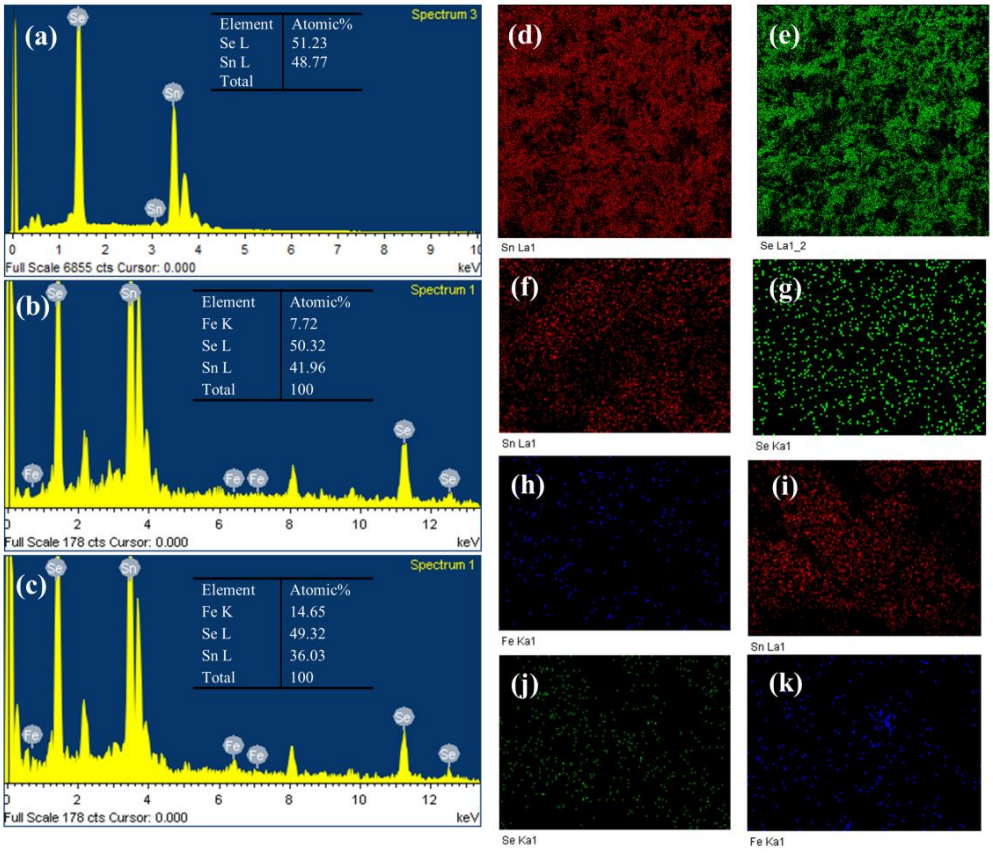

Figure 6.4 (a-c) EDAX spectra of SnSe, x=0.10 and x=0.20 samples, Elemental mapping of (d,e) pure SnSe, (f,g,h) x=0.10 and (i,j,k) x=0.20.

6.3.3 UV-VIS-NIR Diffuse Reflectance Spectroscopy

Figure 6.5(a) displays the reflectance spectra for all $Fe_xSn_{1-x}Se$ samples. The absorption edges are shifted toward the higher wavelength sides as Fe concentration increases into SnSe, indicating a redshift except for x= 0.10. The plot for indirect bandgap $((F(R)h\upsilon)^{1/2}$ versus $h\upsilon$) and direct bandgap $((F(R)h\upsilon)^2$ versus $h\upsilon$) are depicted in fig. 6.5(b-c) respectively. The optical bandgaps are calculated by extrapolating the linear region of the plots onto the $h\upsilon$ axis. Both the bandgap values decrease as Fe concentration increases till x= 0.05, followed by a slight increase at x=0.10 before it shows a decrease as the concentration approaches x= 0.20. The sp-d exchange interactions between the band electrons of the host lattice and the d electrons of Fe^{+2} ions cause changes in the bandgap values [98]. Further, the variation of bandgap values is related to the variation in the crystallite size for all the samples. The bandgap values decreased for values of x=0.00 to x=0.05 and also again for x=0.20. This is due to the decreasing trend of average crystallite size which will cause the grain size to decrease [72,99]. However, at x=0.10 the bandgap values show a slight increase. This can be attributed to an increase in the value of crystallite size. The bandgap values are shown in Table 6.2.

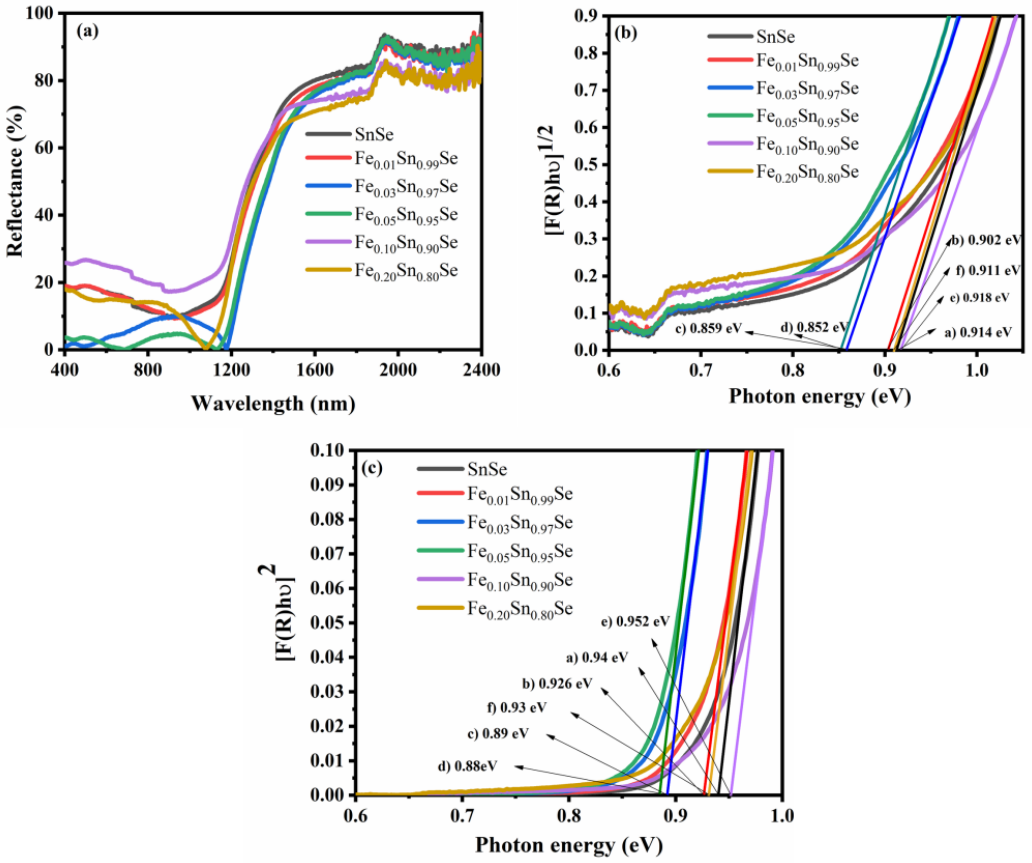

Figure 6.5 (a) Reflectance spectra of $Fe_xSn_{1-x}Se$ samples, (b) $(F(R)h\upsilon)^{1/2}$ versus $h\upsilon$ for indirect bandgap, and (c) $(F(R)h\upsilon)^2$ versus $h\upsilon$ Tauc plot for direct bandgap.

Table 6.2 Values of indirect and direct bandgaps of $Fe_xSn_{1-x}Se$ polycrystals

Composition	Indirect bandgap (eV)	Direct bandgap (eV)
SnSe	0.932	0.92
$Fe_{0.01}Sn_{0.99}Se$	0.922	0.905
$Fe_{0.03}Sn_{0.97}Se$	0.876	0.878
$Fe_{0.05}Sn_{0.95}Se$	0.869	0.871
$Fe_{0.10}Sn_{0.90}Se$	0.937	0.927
$Fe_{0.20}Sn_{0.80}Se$	0.928	0.899

6.3.4 X-ray Photoelectron spectroscopy

XPS is recorded for the sample $Fe_{0.10}Sn_{0.90}Se$ to know the chemical states and to confirm the formation of $Fe_{0.10}Sn_{0.90}Se$ as shown in fig. 6.6(a-c). Figure 6.6(a) shows a high-resolution spectrum of Sn 3d showing doublet peaks at 486.7 eV and 495.5 eV corresponding to $3d_{5/2}$ and $3d_{3/2}$ respectively which confirming that the valence state of Sn is +2. Figure 6.6(b) shows the deconvolution spectra of Se 3d showing two peaks at 53.7 eV and 55.7 eV are ascribed to $3d_{5/2}$ and $3d_{3/2}$ respectively which are associated with the -2 oxidation state of Se. The XPS results for both Sn and Se are in good agreement with the literature [91,100]. The peaks at 710.4 eV and 723.4 eV are corresponding to Fe $2p_{3/2}$ and Fe $2p_{5/2}$ respectively as depicted in fig. 6.6(c). The results reveal that the Fe in our sample is in +2 state.

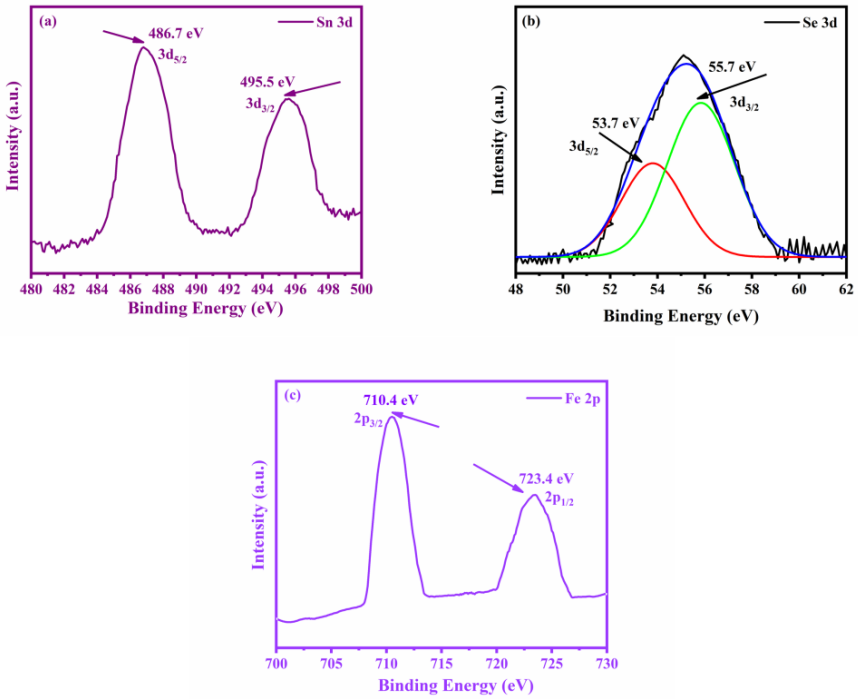

Figure 6.6 (a) XPS spectra of Sn3d, (b) Se3d, and (c) Fe2p of $Fe_{0.10}Sn_{0.90}Se$ sample.

6.3.5 Dielectric studies

6.3.5.1 Room temperature dielectric studies

The variation of ε' as a function of frequency is shown in fig. 6.7(a). The value of ε' is decreases with increase in frequency and becomes constant and independent of frequency after a certain point of frequency in all $Fe_xSn_{1-x}Se$ samples. This is due to the lag between the polarization and the applied field. Due to the lag, dipoles cannot rotate in the direction of the field in time which leads to decrease the value of ε'. The value of ε' is large for all the samples in the low frequency region is due to the trapping of charge carriers leads to the occurrence of space charge polarization which causes an increase in ε'. The value of ε' is increased as Fe concentration increases up to x= 0.05 in the low-frequency region. $Fe_{0.05}Sn_{0.95}Se$ exhibited large value of ε'. This is due to low value of average crystallite size having large number of grain boundaries. For the Fe concentration above x= 0.05, the microstructure exhibits small rod-like nature and the crystallite size is high for x= 0.20 compared to other compositions. The increase in the value of crystallite size causes a decrease in the number of grain boundaries which further decreases the dielectric constant. The loss of electrical energy of a material can be described by dielectric loss when an external ac field is applied. The ε" value for all Fe-doped SnSe samples is noticed to decrease with increasing frequency and becomes independent of frequency showing that losses vanish at high frequencies as seen from fig. 6.7(b). The decrease in ε" at high frequencies is due to the relaxation phenomenon. The ε" is high in the low-frequency region due to the enhancement in the carrier mobility by the free charge motion. The dielectric loss is observed to be the largest in the case of $Fe_{0.05}Sn_{0.95}Se$. It is seen from fig. 6.7(c); the dielectric loss tangent is constant and is independent of the frequency in the low-frequency region. It increases with frequency and peaks are observed in loss spectra for all compositions caused due to the dipole relaxation phenomenon. This is due to the space charges and defects in different defect states in Nano crystalline materials**.** The Maxwell Wagner model and Koop theories [103,104] are known to demonstrate the changes observed in the dielectric parameters. To understand the conduction phenomenon within the material, the ac conductivity is computed for all the $Fe_xSn_{1-x}Se$ samples and displayed in fig. 6.7(d). From the figure there is a plateau region at low frequencies which corresponds to dc conductivity $\sigma_{dc.}$ It is also seen that $\sigma_{dc,}$ increases with Fe composition till x=0.05 and thereafter decreases. The increasing portion of conductivity at high frequencies corresponds to ac conductivity. This conduction occurs due to the migration of ions inside the material. The σ_{ac} shows an increasing trend with Fe doping which indicates

that doping of Fe induces impurity sites within the bandgap of SnSe lattice. The $Fe_{0.05}Sn_{0.95}Se$ has achieved a high value of ac conductivity due to the reduction in the value of crystallite size. The decrement in the value of crystallite size with Fe concentration also improves grain boundary ionic diffusivity.

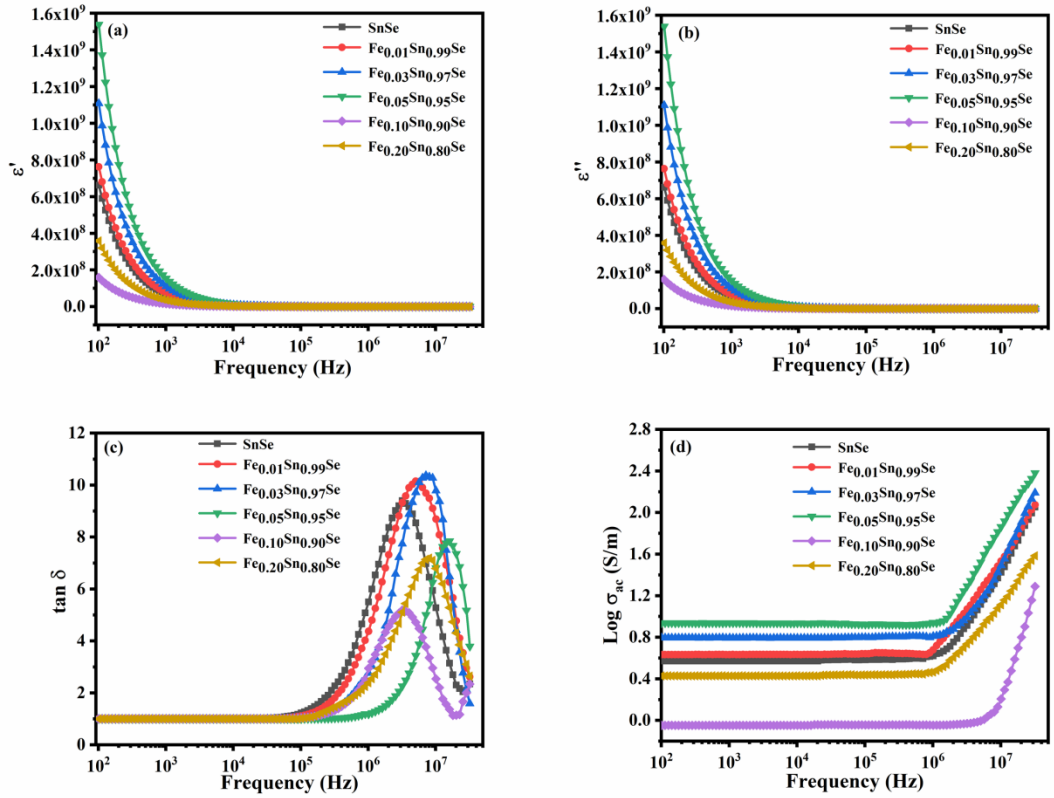

Figure 6.7 (a) Dielectric constant vs. frequency, (b) Dielectric loss vs. frequency, (c) Dielectric loss tangent vs. frequency, and (d) AC conductivity vs. frequency for all $Fe_xSn_{1-x}Se$ samples at room temperature.

Complex electrical modulus spectroscopy is helpful for the extraction of the electrical response and thus provides a better understanding of the relaxation phenomenon. It gives detailed information about the conduction mechanism in polycrystalline materials and describes the electrical relaxation phenomenon of ionic solids as a microscopic property of materials. The electrical modulus has been studied for all $Fe_xSn_{1-x}Se$ samples at room temperature. The variation of M' as a function of frequency for all $Fe_xSn_{1-x}Se$ samples is depicted in Fig. 6.8a. The M' values are low and tend to zero in the low-frequency region due to the non-contribution of electrode polarization. The M' values increase with frequency for all compositions due to the relaxation phenomenon and absence of space charge effect at high frequencies. The frequency dependence of M'' for $Fe_xSn_{1-x}Se$ system of samples is shown in Fig. 10(b). The M'' values increase with frequency and peaksare observed in the high-frequency region for all samples. The ions are free to move over long-range distances involving hopping mechanisms in the region below the peak maximum. In the region above the

peak maximum, the ions are restricted to potential wells and hence can move over short distances i.e., can move within the local site [105]. The area where the peak occurs specifies the transformation of long-range conduction of charge carriers to short-range conduction. The shifting of the peak towards the high frequencies for Fe concentration up to x=0.05 combined with the increase in peak strength. The peak shift towards the high-frequency region corresponds to conductivity. For Fe concentrations of x= 0.10 to 0.20, a shift towards low frequencies is observed with maximum peak strength being observed for x= 0.10. This shift towards the low-frequency side as the Fe composition increases is caused due to the increase in relaxation time [81].

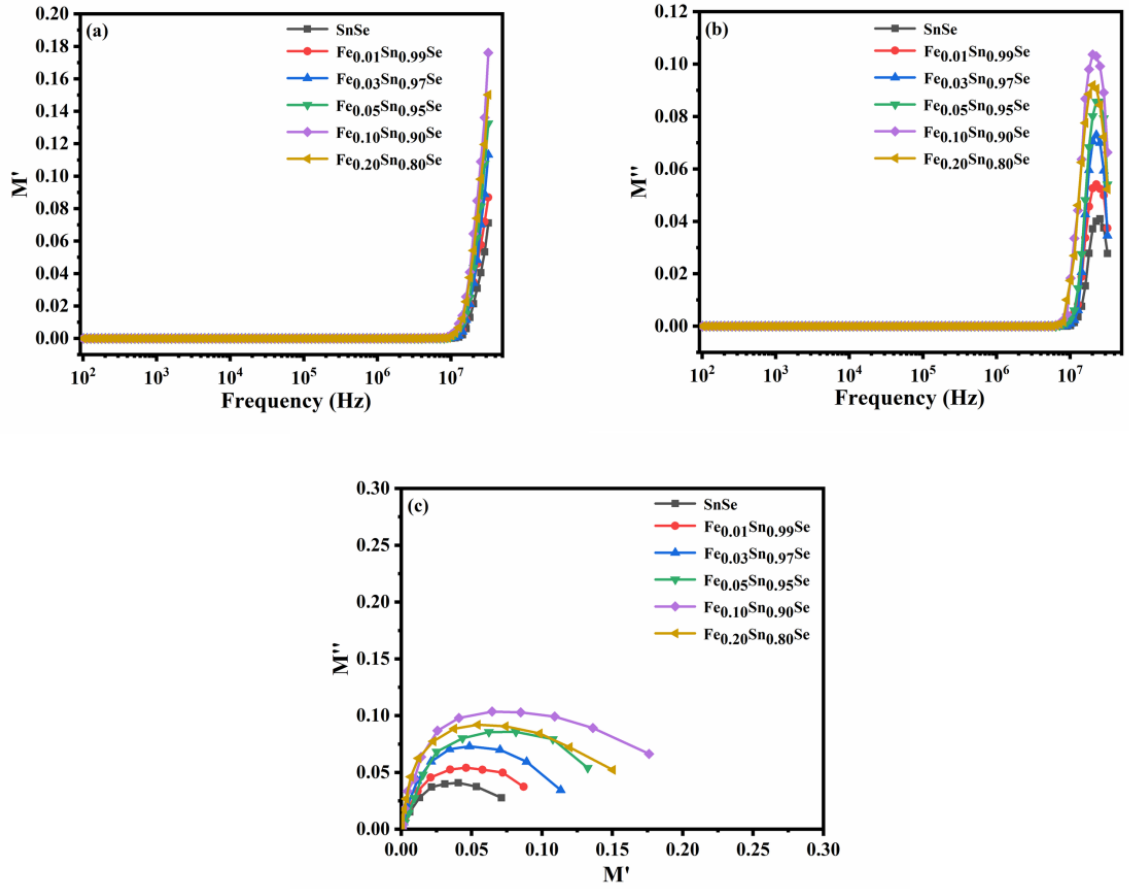

Figure 6.8 (a) Variation of M' as a function Frequency, (b) Variation of M'' as a function of Frequency, and (c) Variation M'' vs. M' for all $Fe_xSn_{1-x}Se$ samples.

The complex electrical modulus spectrum (M' vs M'') of all the $Fe_xSn_{1-x}Se$ samples at room temperature is shown in fig. 6.8(c). It is noticed that there is a formation of asymmetric semi-circular arc in every sample. This confirms the dominance of the bulk effect towards electrical conduction. The appearance of arcs in the spectra represents the single phase of the samples. The centers of the semi-circular arcs that lie below the x-axis indicate a non-Debye type relaxation. The semi-circular arcs observed in the low-frequency region represent the existence of grain boundaries.

The radii of semi-circular arcs decrease with an increase in Fe concentration till x= 0.05. The radius is maximum for x= 0.10, and thereafter decreases for x= 0.20. This would mean that the conduction processes depend on the doping concentration [106].

6.3.5.2 Temperature dependent dielectric studies

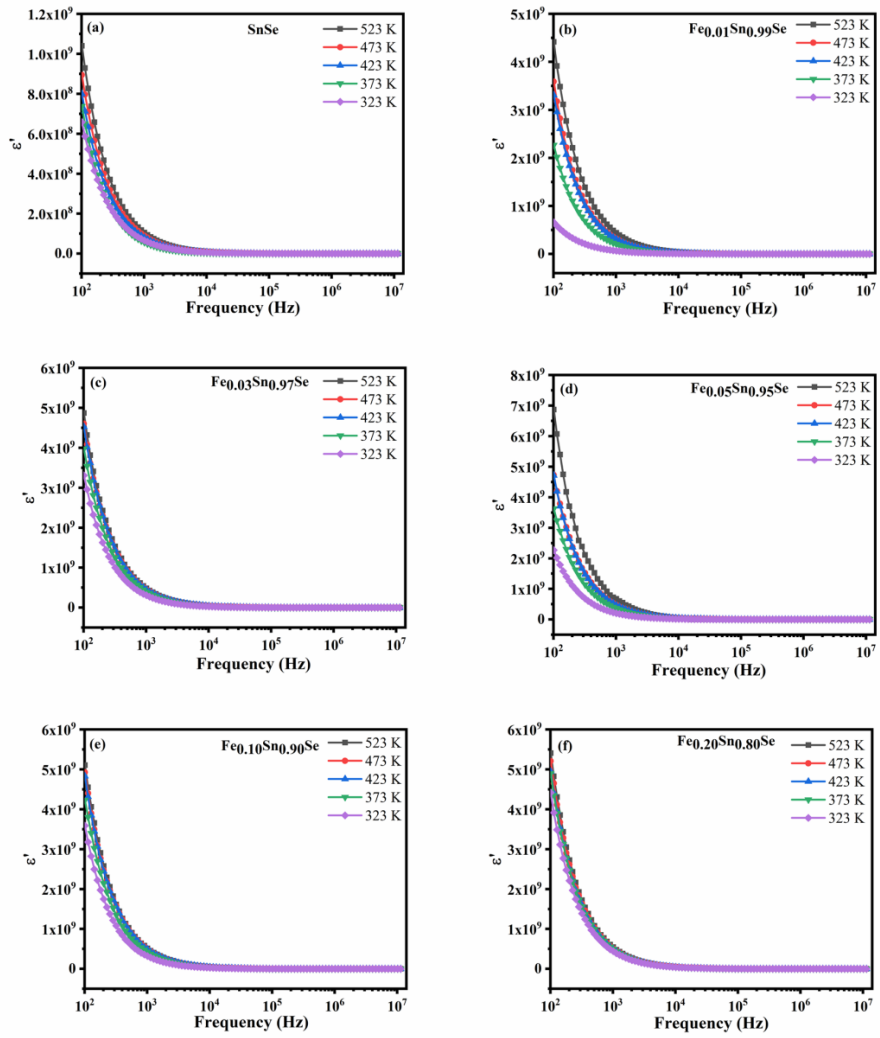

Figure 6.9 Variation of Dielectric constant vs. Frequency of (a) SnSe, (b) $Fe_{0.01}Sn_{0.99}Se$, (c) $Fe_{0.03}Sn_{0.97}Se$, (d) $Fe_{0.05}Sn_{0.95}Se$, (e) $Fe_{0.10}Sn_{0.90}Se$, and (f) $Fe_{0.20}Sn_{0.80}Se$ respectively in the temperature range of 323 K-523 K.

Figure. 6.9(a-f) depicts the frequency dependence of dielectric constants (ε') for all the $Fe_xSn_{1-x}Se$ samples in the temperature range 323 K-523 K. The value of ε' is large in the low-frequency region and decreases with frequency increase for all the compositions at all temperatures. It becomes independent of frequency above 10 kHz. There is no remarkable change observed in the ε' value at the high-frequency region in all cases at all temperatures. The combined contribution of interfacial, electronic, atomic, and ionic polarization results in net polarisation in the low-frequency region. When the measuring frequency is lower than the relaxation frequency, all kinds of polarizations will

influence the dielectric constant. The large value of the dielectric constant is due to interfacial polarization attributed to grain boundaries in the low-frequency region. The variation of dielectric constant with frequency is explained by Maxwell-Wagner's [10] theory of interfacial polarization. This theory agrees with Koop's theory [15]. According to this theory, interfacial polarization is prominent in the low-frequency region which causes charge trapping at grain boundaries. Because grain boundaries act as a barrier to charge carrier movement. Thus applying an external field will rotate the dipole moments at grain boundaries and contribute to increasing the dielectric constant value. value. In each case, the increase in dielectric constant with temperature can be attributed to charge carrier thermal conduction as the temperature rises. The value of ε' is increased with Fe-doping into SnSe and it is found to be large for the composition $Fe_{0.05}Sn_{0.95}Se$. When frequency increases, the dipoles do not have rapid orientation in the applied ac field direction. As a result, dipole oscillations lag behind frequency and ε' decreases in the high-frequency region. Further, the dipoles are no longer able to follow the applied ac field as the frequency rises, and their orientation is lost. Hence, at high frequencies, ε' reaches a constant value. The values of ε' obtained for the Fe-doped SnSe have possible applications in microelectronic and capacitive storage devices [19].

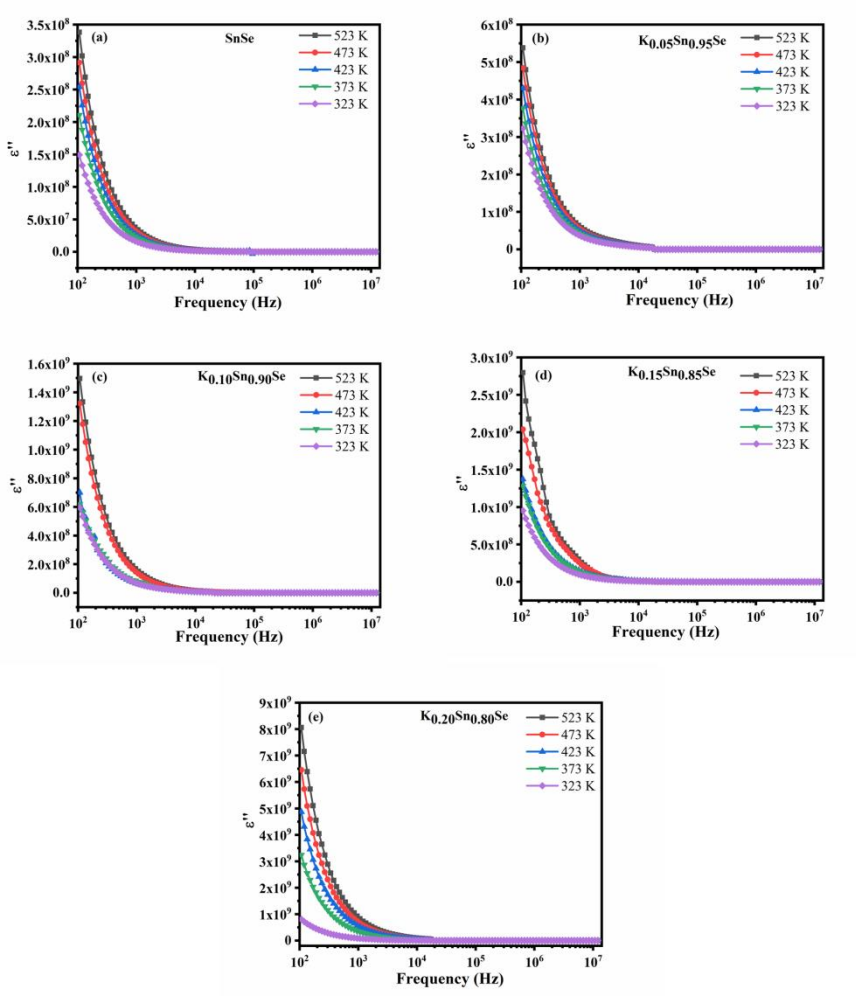

Figure 6.10 Variation of Dielectric loss vs. Frequency of (a) SnSe, (b) $Fe_{0.01}Sn_{0.99}Se$, (c) $Fe_{0.03}Sn_{0.97}Se$, (d) $Fe_{0.05}Sn_{0.95}Se$, (e) $Fe_{0.10}Sn_{0.90}Se$, and (f) $Fe_{0.20}Sn_{0.80}Se$ respectively in the temperature range of 323 K-523K.

Figure 6.10 (a-f) depicts the variation of dielectric loss (ε") as a function of frequency at different temperatures for all the Fe-doped SnSe. For all compositions, the value of ε" decreases with increasing frequency and increases with rise in temperature. It is high in the low-frequency region, and the composition $Fe_{0.05}Sn_{0.95}Se$ has the highest dielectric loss. Low dielectric constants and losses may have applications in electro-optic and high-frequency devices [21–23].

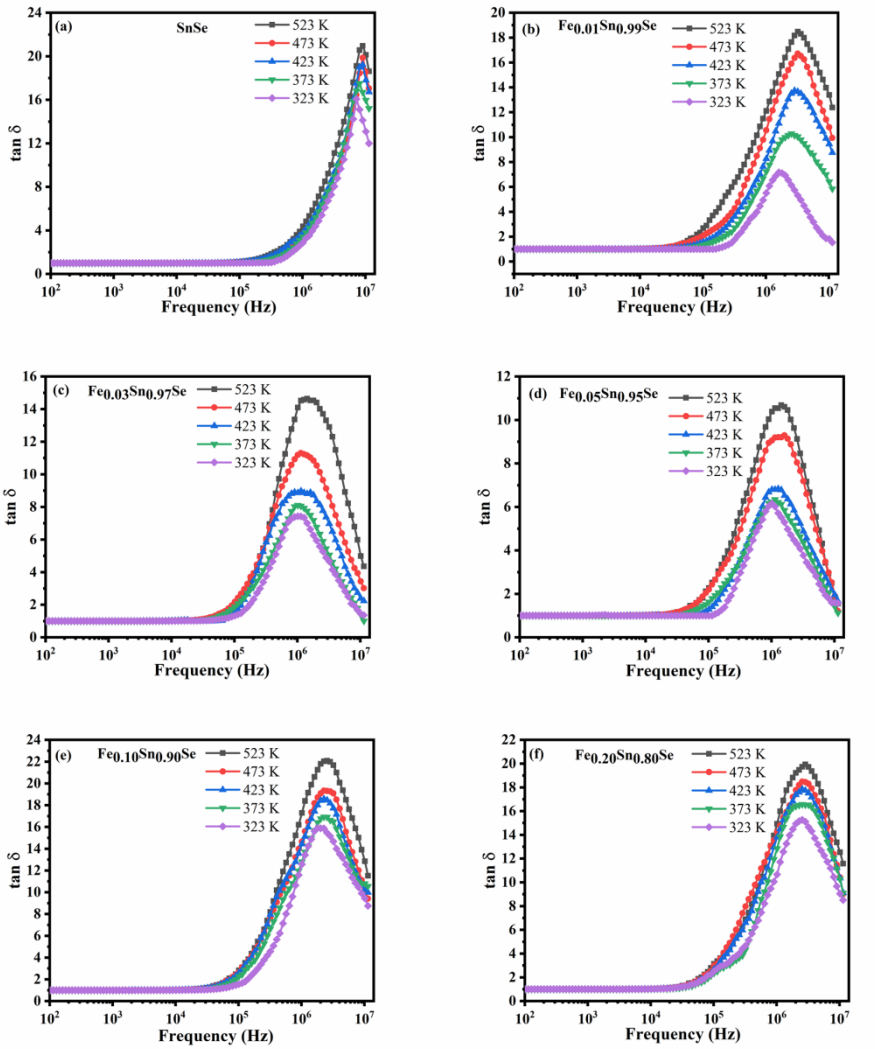

Figure 6.11 Variation of Dielectric loss tangent vs. Frequency of (a) SnSe, (b) $Fe_{0.01}Sn_{0.99}Se$, (c) $Fe_{0.03}Sn_{0.97}Se$, (d) $Fe_{0.05}Sn_{0.95}Se$, (e) $Fe_{0.10}Sn_{0.90}Se$, and (f) $Fe_{0.20}Sn_{0.80}Se$ respectively in the temperature range of 323 K-523 K.

In figure. 6.11(a-f), the variation of the dielectric loss tangent (tan δ) as a function of frequency is shown for all compositions. At low frequencies, the tan δ is low and frequency independent for all of the compositions, but it increases as the frequency increases. The tan δ shows a maximum value before it shows decreasing trend in the region of high frequencies. Relaxation peaks are observed for all the compositions in the high-frequency region of 1 MHz-10 MHz. After the occurrence of the relaxation peaks, the tan δ shows decreasing trends which indicates that the sample reveals almost zero dielectric loss at higher frequencies [24]. The peak intensity is increased as the temperature increases for all the compositions. The peaks are shifted to the low-frequency region as the temperature rises.

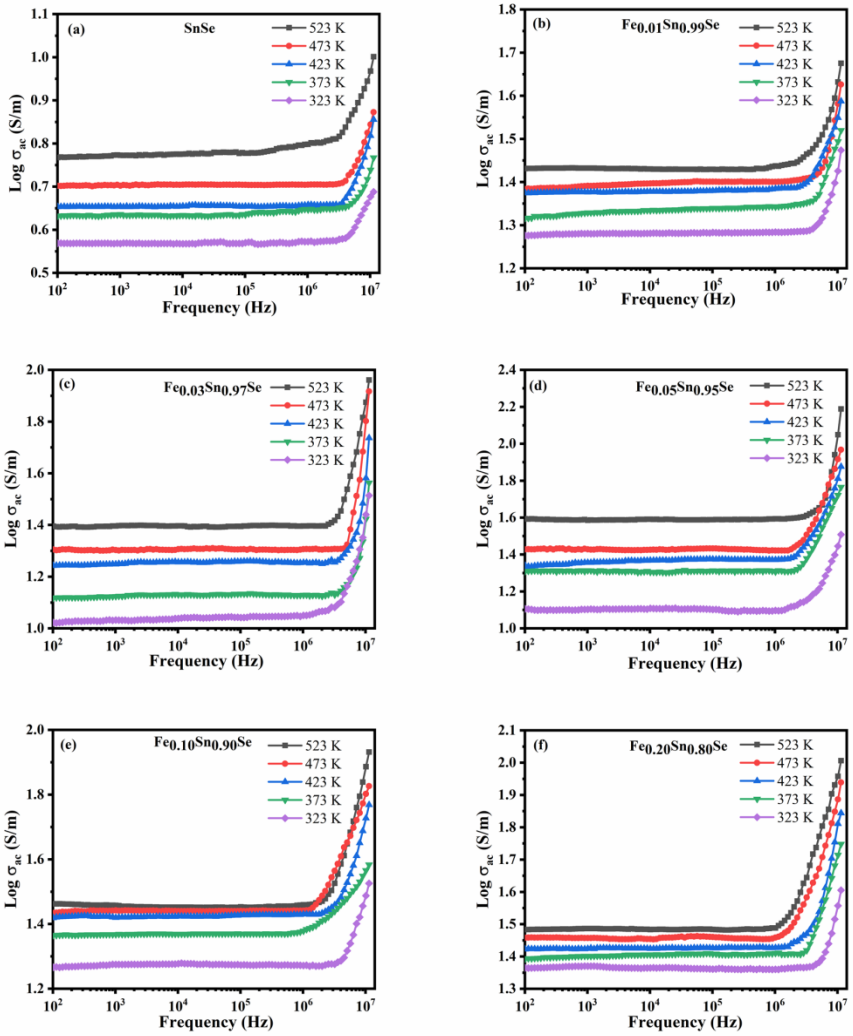

Figure 6.12 Variation of AC conductivity vs. Frequency of (a) SnSe, (b) $Fe_{0.01}Sn_{0.99}Se$, (c) $Fe_{0.03}Sn_{0.97}Se$, (d) $Fe_{0.05}Sn_{0.95}Se$, (e) $Fe_{0.10}Sn_{0.90}Se$, and (f) $Fe_{0.20}Sn_{0.80}Se$ respectively in the temperature range of 323 K-523 K.

Figure 6.12(a-f) depicts the effect of frequency on AC conductivity of the Fe-doped SnSe samples at various temperatures ranging from 323 K-523 K. From fig.6.12(a-f), the following two regions can be identified: (i) plateau region (100 Hz-100 kHz) which is frequency independent in the low-frequency region for all the compositions corresponding to DC conductivity, and (ii) the increasing portion in the frequency-dependent high-frequency region (100 kHz- 10 MHz) which indicates the AC conductivity. Thus the conduction mechanism in all the samples follows Jonscher's power law. The dispersion region in the AC conductivity shifted toward high frequencies as the temperature rises which shows the bulk relaxation of the materials [26]. The increase in temperature causes an increase in the thermal conduction of charge carriers in all compositions, resulting in an increase in AC conductivity in each case. The rise in temperature causes more charge carriers to move over the barrier and increase the electrical conductivity. The slopes of frequency vs. Logac (the increasing

portion of AC conductivity) plots for all $Fe_xSn_{1-x}Se$ samples are used to calculate the frequency exponent 's'. The values of 's' for all samples are found to decrease with temperature rise, and values ranging from 0.1 to 0.9, which are less than 1. From the manner of variation of 's', it can be concluded that the conduction process follows Correlated Barrier Hopping (CBH) mechanism. Table 6.3 shows the values of 's' for all of the samples at various temperatures. The valence band and conduction band are separated by localized states which are created due to the defects that occur in the material. Every localized state is separated by a barrier of height W_m. Under normal circumstances, charge carriers are confined to localized states. When external energy is supplied, charge carriers will move from filled localized states to unfilled localized states, resulting in hopping. Since the hopping mechanism is taking place over the barrier, activation energy (ΔE_a) is needed by the charge carriers to cross across the barrier. The slopes of temperature vs. (1-s) plot, as shown in fig. 6.13(b) and listed in Table 6.3, are used to calculate the W_m.

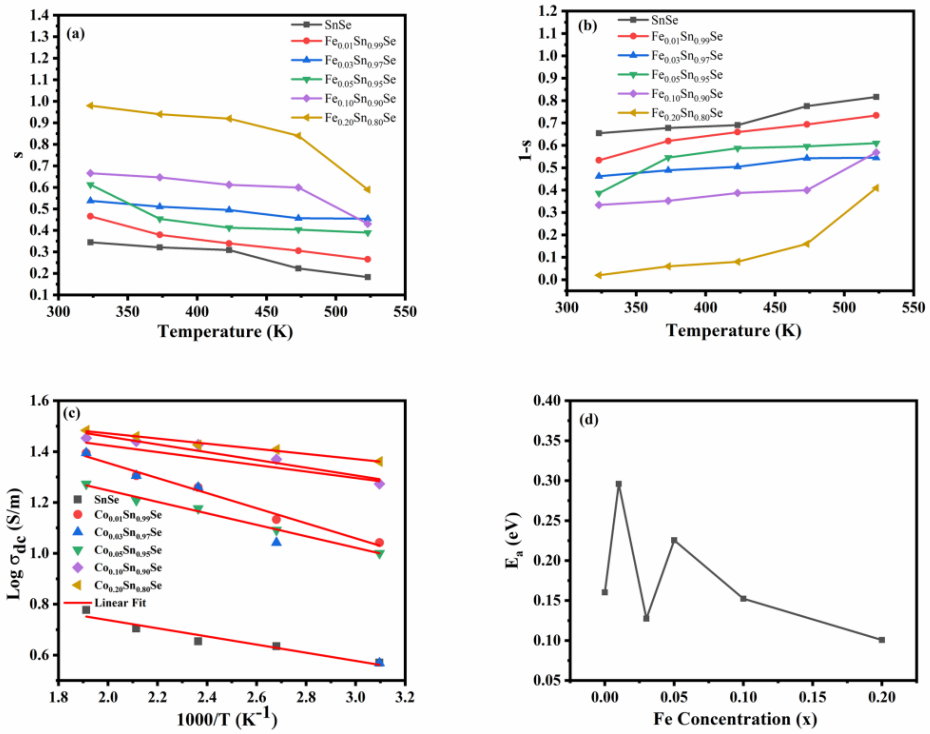

Figure 6.13 (a) Variation of frequency exponent 's' vs. temperature, (b) Variation of 1-s vs. Temperature, (c) Arrhenius plot for determining activation energy at 100 kHz, and (d) Activation energy vs. Dopant concentration (x).

Figure 6.13(c) shows the frequency dependence of dc conductivity for all $Fe_xSn_{1-x}Se$ samples at 100 kHz. The activation energy is estimated from the slopes of Frequency vs. Log σ_{dc} after linear fitting as depicted in fig. 6.13(c). It is found to increase with Fe doping till x=0.05, thereafter it decreases for x=0.10 slightly and further increases for

x=0.20 as displayed in fig. 6.13(d). Table 6.3 shows the activation energy (E_a) values for all of the samples.

Table 6.3 Frequency exponent 's', activation energy (E_a), and maximum barrier height (W_m) values at various temperatures for all Fe-doped SnSe samples

Composition	Temperature (K)	Frequency exponent (s)	Activation Energy (E_a) (eV)	W_m (meV)
SnSe	323	0.345		
	373	0.322		
	423	0.309	0.16	0.81
	473	0.224		
	523	0.183		
$Fe_{0.01}Sn_{0.99}Se$	323	0.466		
	373	0.380		
	423	0.340	0.296	1.00
	473	0.306		
	523	0.266		
$Fe_{0.03}Sn_{0.97}Se$	323	0.538		
	373	0.511		
	423	0.495	0.127	0.41
	473	0.457		
	523	0.455		
$Fe_{0.05}Sn_{0.95}Se$	323	0.613		
	373	0.454		
	423	0.412	0.225	1.11
	473	0.404		
	523	0.390		
$Fe_{0.10}Sn_{0.90}Se$	323	0.666		
	373	0.647		
	423	0.612	0.152	1.17
	473	0.600		
	523	0.431		
$Fe_{0.20}Sn_{0.80}Se$	323	0.980		
	373	0.940		
	423	0.920	0.100	1.95
	473	0.840		
	523	0.590		

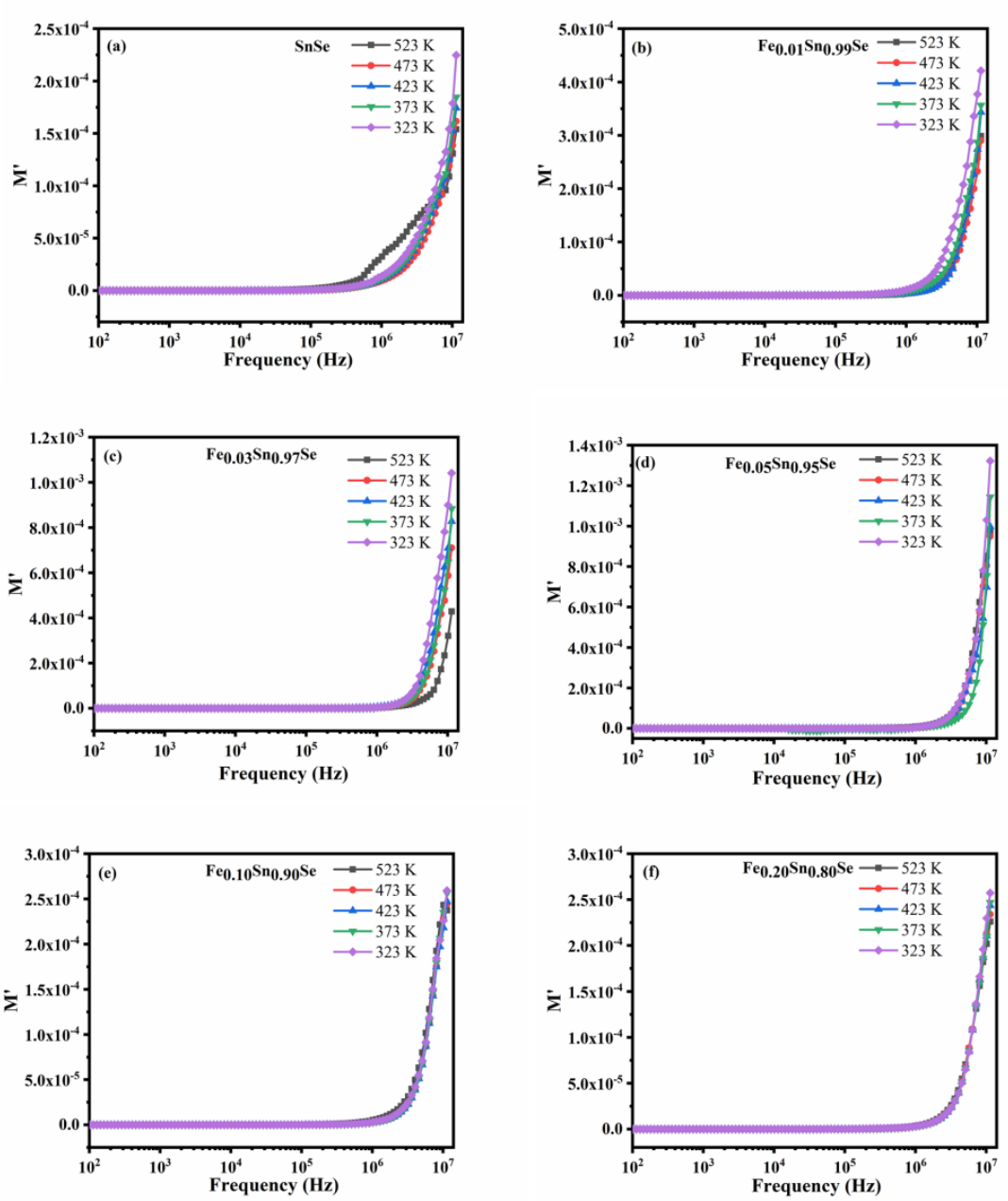

Figure 6.14 Variation of M' vs. Frequency of (a) SnSe, (b) $Fe_{0.01}Sn_{0.99}Se$, (c) $Fe_{0.03}Sn_{0.97}Se$, (d) $Fe_{0.05}Sn_{0.95}Se$, (e) $Fe_{0.10}Sn_{0.90}Se$, and (f) $Fe_{0.20}Sn_{0.80}Se$ respectively in the temperature range of 323 K-523 K.

The frequency dependence of the real part of electrical modulus (M') for all the Fe-doped SnSe samples at various temperatures are displayed in fig. 6.14(a-f). M' is nearly zero and frequency independent in the low-frequency region up to 1MHz. After that as frequency increases, M' value increased for all the compositions at all temperatures.

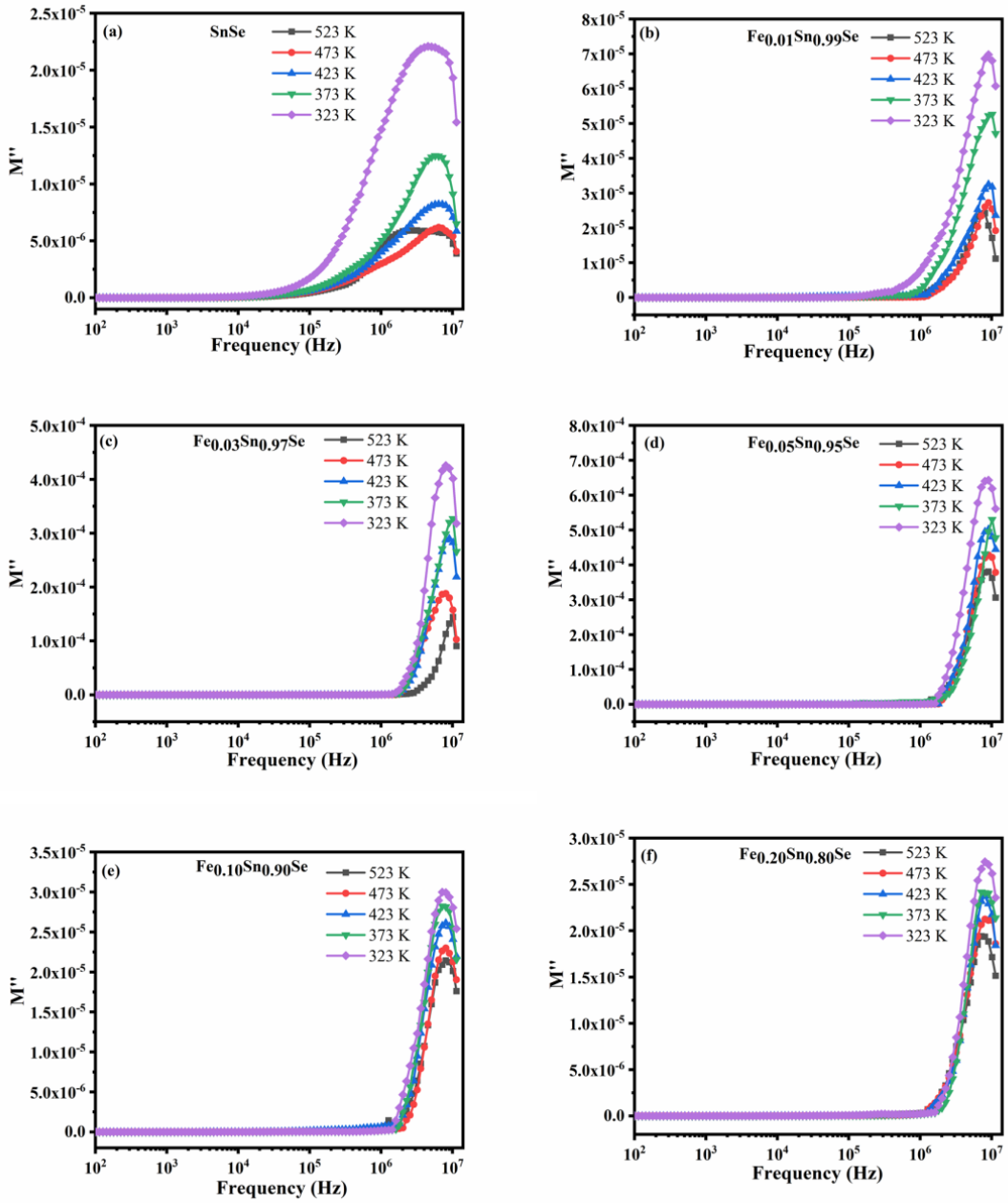

Figure 6.15 Variation of M'' vs. Frequency of (a) SnSe, (b) $Fe_{0.01}Sn_{0.99}Se$, (c) $Fe_{0.03}Sn_{0.97}Se$, (d) $Fe_{0.05}Sn_{0.95}Se$, (e) $Fe_{0.10}Sn_{0.90}Se$, and (f) $Fe_{0.20}Sn_{0.80}Se$ respectively in the temperature range of 323 K-523 K.

The variation of M'' with frequency is shown in fig. 6.15(a-f). The M'' is constant and frequency independent in the region of low frequencies. M'' increases with frequency, and relaxation peaks can be seen in the high-frequency region (1 MHz-10 MHz). The region beneath the peak maximum corresponds to charge carrier long-range conduction. Charge carriers are constrained to potential wells by short distances above the peak maximum. As the temperature rises, the relaxation peaks shift to the high-frequency side.

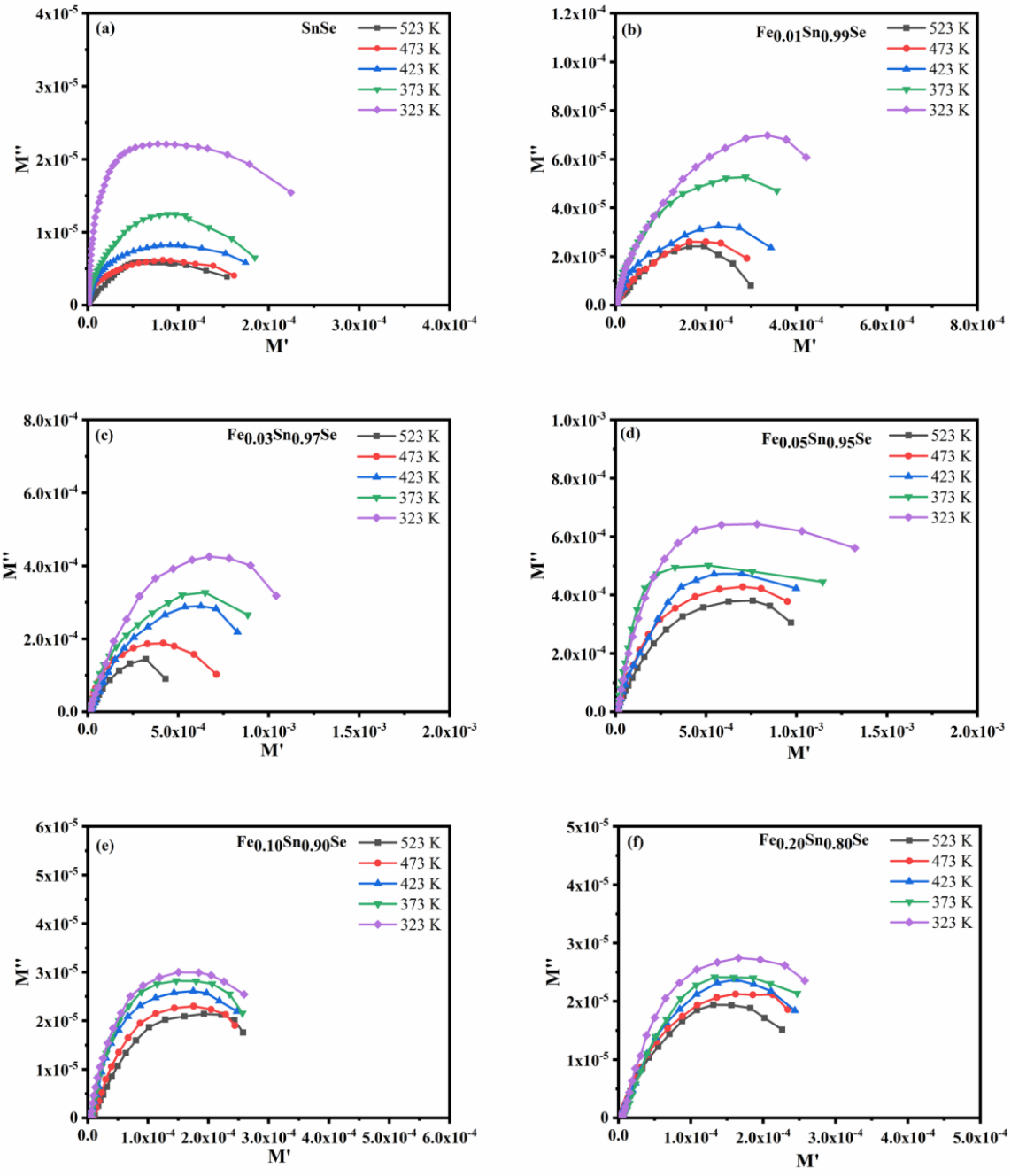

Figure 6.16 M'' vs. M' of (a) SnSe, (b) $Fe_{0.01}Sn_{0.99}Se$, (c) $Fe_{0.03}Sn_{0.97}Se$, (d) $Fe_{0.05}Sn_{0.95}Se$, (e) $Fe_{0.10}Sn_{0.90}Se$, and (f) $Fe_{0.20}Sn_{0.80}Se$ respectively in the temperature range of 323 K-523 K.

Figure 6.16(a-f) depicts the variation of M' vs. M''. At all temperatures, single semi-circular arcs formed in all Fe-doped samples, their centres are located below the x-axis. As the temperature increases, the radii of semi-circular arcs reduce in all the samples which indicate the conduction mechanism is a temperature-dependent hopping mechanism. The formation of semi-circular arcs in all samples at all temperatures is incomplete due to non-Debye type relaxation. The observed semi-circular arcs indicated the presence of grain boundaries in the low-frequency region.

6.3.7 Magnetic studies

The room temperature M-H curves for $Fe_xSn_{1-x}Se$ (x=0.00, 0.01, 0.03, 0.05, 0.10 and 0.20) polycrystals are depicted in fig.6.17. It is clear from fig.6.17, that pure SnSe exhibits ferromagnetism at low field areas and anti-vortex behaviour at higher magnetic fields. Many researchers justified that the ferromagnetic behaviour in an undoped semiconductor is due to the residual defects that occur in the host lattice [31,108]. All the $Fe_xSn_{1-x}Se$ samples exhibited room temperature ferromagnetism with hysteresis loops of finite magnetization at 1.5 Tesla. The reason for this ferromagnetism in doped samples could be raised from many possibilities such as formation of secondary phases defects, and carrier-related intrinsic property [101]. In our case we observed that no secondary phases are observed as observed from XRD, EDAX and XPS and defects its own cannot ferromagnetism. Thus, in the current work, the improved crystalline nature attained and the absence of hybrid phases in the synthesised samples ensure that the magnetism produced is solely the product of the addition of Fe to the SnSe host lattice. The saturation magnetization M_S value increases with increase in concentration of Fe into SnSe. Maximum value of M_S 0.10487 emu/g is obtained for x=0.10. It might be the result of the exchange interaction between the localised "d" spins of the Fe ions and the free, delocalized charge carriers of the host lattice. Thereafter it decreases to 0.04056 emu/g for x=0.20. This is due to the antiferromagnetic contribution generated by the large number of localised 3 d electrons in Fe atoms between adjacent Fe-Fe atoms. The ferromagnetic signals were quenched by the antiferromagnetic interactions caused by the increased Fe concentration [110,113]. Hence the variation in the saturation magnetization (M_S) values of Fe-doped SnSe samples is due to the coupling between ferromagnetic and antiferromagnetic interactions. The remnant magnetization (M_R) increases from 0.4893×10^{-4} emu/g to 3.9923 emu/g up to a Fe concentration of 0.05 thereafter it decreases at higher compositions. The coercivity (H_c) value is increased from 71.2 Oe to 212.39 Oe as the composition of Fe increases from x= 0.00 to 0.10. The increase in coercivity also might be caused by the large value of magnetic ion impurity exhibiting a strong ferromagnetic coupling [31].The decrease in coercivity for x=0.20 is might be due to the decrease in the anisotropy energy. The room temperature ferromagnetic behaviour exhibited by the $Fe_xSn_{1-x}Se$ samples will have potential applications in data storage and spintronic devices.

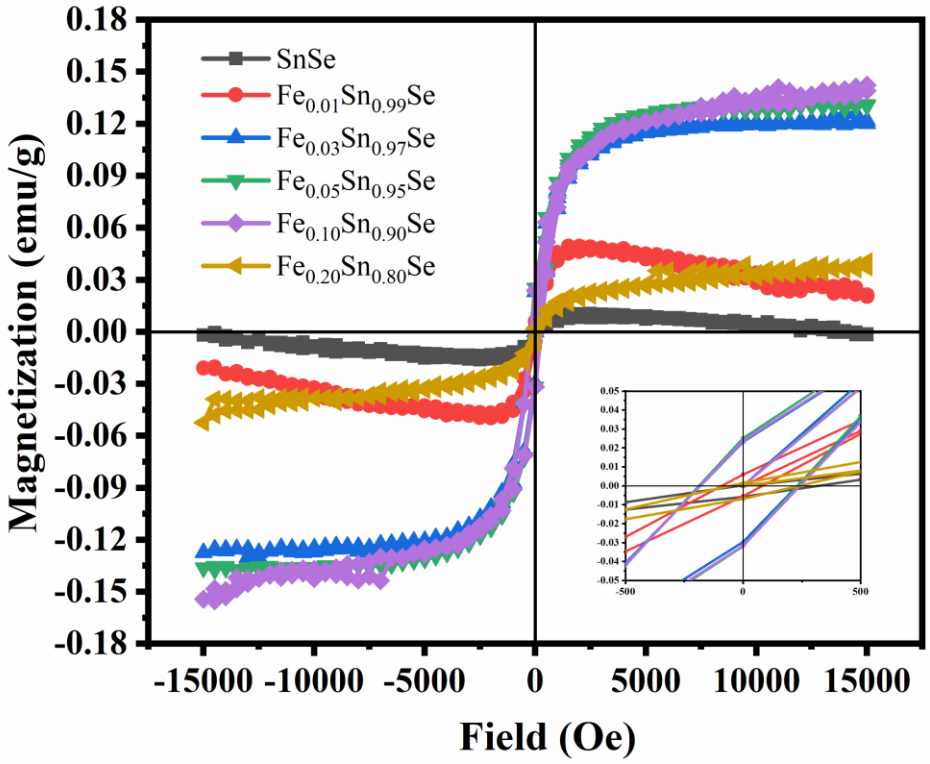

Figure 6.17 The hysteresis loops for all $Fe_xSn_{1-x}Se$ samples measured at room temperature by VSM.

Table 3 Coercivity (H_C), Saturation Magnetization (M_S), and Remnant Magnetization (M_R) as a function of Fe concentration.

Composition	H_C (Oe)	M_S (emu/g)	M_R (10^{-4} emu/g)
SnSe	71.2	0.00212	0.4893
$Fe_{0.01}Sn_{0.99}Se$	86.83	0.04941	0.9719
$Fe_{0.03}Sn_{0.97}Se$	205.92	0.12665	3.9667
$Fe_{0.05}Sn_{0.95}Se$	210.07	0.1325	3.9923
$Fe_{0.10}Sn_{0.90}Se$	212.39	0.14087	2.7745
$Fe_{0.20}Sn_{0.80}Se$	146.58	0.04056	0.588

6.4 Conclusions

The $Fe_xSn_{1-x}Se$ diluted magnetic semiconductors were successfully prepared using hydrothermal method. The surface morphology was observed by FESEM, which revealed the layered like morphology that turned to small ball like morphology for increasing compositions of Fe. The optical studies obtained from UV-Vis-NIR DRS spectroscopy illustrate that both direct and indirect bandgaps decrease as the Fe concentration increases up to x=0.05 after that they increased for x=0.10 and again decreased for x=0.20. The XPS studies confirmed the valence state of Sn, Se, and Fe for

the sample $Fe_{0.10}Sn_{0.90}Se$. The room temperature dielectric studies revealed that maximum value of dielectric constant and ac conductivity is obtained at x=0.05. the temperature dependent dielectric studies showed that $Fe_{0.05}Sn_{0.95}Se$ found large value of dielectric constant and ac conductivity at 523 K. VSM measurements have described the ferromagnetism revealed by all the $Fe_xSn_{1-x}Se$ SnSe at room temperature, which suggests that these dilute magnetic semiconductors can also have applications in spintronic devices.

CHAPTER 7: Summary and Conclusions

In this chapter summary and conclusions of the current thesis work are presented. The scope for future work in order to expand in the field of research work has also been suggested.

7.1 Summary of the thesis work

We have successfully prepared the alkali and transition metal doped SnSe polycrystals using hydrothermal method. We have observed change in the bandgap values with change in dopants. For undoped SnSe also a slight variation in the bandgap values are observed. This is due to different synthesis conditions that we have used for different dopants. We have obtained high dielectric constants and ac conductivity values for Na doped SnSe among the alkali doped SnSe and Fe doped SnSe among transition doped SnSe materials. The obtained dielectric properties show that our materials have possible applications in microelectronic and capacitive storage devices. Fe doped SnSe exhibits better room temperature ferromagnetic properties compare to Co doped SnSe showing applications in data storage and spintronic devices. The overall summary of the thesis work is given in below (Table 7.1-7.4)

Table 7.1 Values of Room temperature dielectric properties

Composition	**Dielectric constant (below 10 kHz)**	**Dielectric constant (above 10 kHz)**	**Log AC Conductivity(S/m)**
$Na_xSn_{1-x}Se$	$5x10^7$-$6.4x10^8$	450-1200	0.07-1.48
K_xSn_{1-x} Se	$1.2x10^8$-$5.6x10^8$	470-550	0.76-1.39
$Co_xSn_{1-x}Se$	$1.11x10^6$-$9.1x10^8$	440-460	0.94-1.64
Fe_xSn_{1-x} Se	$1.59x10^8$-$1.53x10^9$	545-1600	0.29-1.91

Table 7.2 Values of Temperature dependent dielectric properties

Composition	**Dielectric constant (below 10 kHz)**	**Dielectric constant (above 10 kHz)**	**Log AC Conductivity(S/m)**
$Na_xSn_{1-x}Se$	$7.05x10^7$-$1.35x10^{10}$	180-1200	0.04-1.98
K_xSn_{1-x} Se	$1.49x10^8$-$8x10^9$	80-200	0.49-1.37
$Co_xSn_{1-x}Se$	$4.18x10^8$ -$1.5x10^9$	50-1400	0.6-2.27
Fe_xSn_{1-x} Se	$6.58x10^8$-$6.86x10^9$	450-500	0.68-2.18

Table 7.3 Coercivity (H_C), Saturation Magnetization (M_S), and Remnant Magnetization (M_R) as a function of Co concentration.

Composition	H_C (Oe)	M_S (emu/g))	M_R (10^{-3} emu/g)
SnSe	69	0.0235	4.53
$Co_{0.01}Sn_{0.99}Se$	87	0.049	5.52
$Co_{0.03}Sn_{0.97}Se$	106	0.0426	5.10

$Co_{0.05}Sn_{0.95}Se$	153	0.0536	7.00
$Co_{0.10}Sn_{0.90}Se$	33	0.1342	4.50
$Co_{0.20}Sn_{0.80}Se$	244	0.1083	13.3

Table 7.4 Coercivity (H_C), Saturation Magnetization (M_S), and Remnant Magnetization (M_R) as a function of Fe concentration.

Composition	H_C (Oe)	M_S (emu/g)	M_R (10^{-4} emu/g)
SnSe	71.2	0.00212	0.4893
$Fe_{0.01}Sn_{0.99}Se$	86.83	0.04941	0.9719
$Fe_{0.03}Sn_{0.97}Se$	205.92	0.12665	3.9667
$Fe_{0.05}Sn_{0.95}Se$	210.07	0.1325	3.9923
$Fe_{0.10}Sn_{0.90}Se$	212.39	0.14087	2.7745
$Fe_{0.20}Sn_{0.80}Se$	146.58	0.04056	0.588

7.2 Conclusions

The conclusions derived from the thesis work performed on alkali and transition metal doped SnSe for dielectric and magnetic properties are given below:

$Na_xSn_{1-x}Se$ polycrystals (x = 0.00 to 0.20 with a step of 0.05) were successfully synthesized by hydrothermal method. XRD was performed to confirm the single phase of the compounds. Various structural parameters like average crystallite size, lattice parameters and cell volume were extracted. The average crystallite size decreased from 132 to 83 nm as Na doping increases. Morphological studies revealed by SEM and TEM exhibited 2D plate-like morphology for undoped SnSe. With increasing Na concentration, these 2D plate-like structures cross-linked to each other and formed 3D flower-like structure at x = 0.20. Further, this flower-like morphology helped in enhancing the dielectric properties of $Na_xSn_{1-x}Se$ polycrystals. The optical bandgap studies revealed that both direct and indirect bandgap values decreased as doping concentration increased which can contribute to an increase in AC conductivity. Room temperature dielectric studies showed that large value of dielectric constant and ac conductivity is obtained for $Na_{0.20}Sn_{0.80}Se$. The temperature-dependent dielectric studies showed that the maximum values of the real part of permittivity and dielectric losses were obtained for higher doping concentration at low frequencies and there is no remarkable change observed at higher frequencies. The low value of the dielectric constant and dielectric loss at high frequencies appears to be promising for electro-optic and solar cell devices. The doping concentration (Na) has a significant effect on AC conductivity and it is found to be maximum for $Na_{0.20}Sn_{0.80}Se$ sample at high temperature (523 K). The AC conductivity follows Jonscher's power-law relation and

the variation of the 's' parameter with temperature indicated that the CBH model is responsible for the charge carriers in the hopping mechanism. The electrical modulus studies revealed the dispersive nature and impact of grain boundary effects in all the $Na_xSn_{1-x}Se$ samples at room and high temperatures. The high values of the real part of permittivity and AC conductivity will find the possible application of $Na_xSn_{1-x}Se$ polycrystals in high-energy capacitive storage devices.

$K_xSn_{1-x}Se$ polycrystals (x = 0 to 20 mol % with a step of 5 mol %) were prepared by hydrothermal method. The structural parametrs confirmed the single phase of the compound using XRD. The average crystallite size is found to be varied from 97-136 nm with K doping increases into SnSe. Morphological studies revealed that there is a decrease in the size of the plate-like structures with K doping. The TEM analysis exhibited the combination of plate-like structures with small nanorods at high resolution. The indirect and direct bandgap values are reduced with an increase in K concentration and further lead to enhance the ac conductivity with K doping. The room and temperature-dependent dielectric studies exhibited maximum values of dielectric constant and dielectric losses for $K_{0.20}Sn_{0.80}Se$ at low frequencies. The K doping has significantly affected the AC conductivity and it is found to be maximum for the $K_{0.20}Sn_{0.80}Se$ sample at 523K. The calculated value of the parameter 's' suggested that the CBH model is the possible mechanism for the charge carriers of the hopping mechanism. The impact of grain boundary effects is revealed by electrical modulus studies and indicated non-Debye type relaxation in all the K-doped SnSe samples. The results suggest the possible application of the material in microelectronic, electro-optic, and capacitive storage devices.

The $Co_xSn_{1-x}Se$ diluted magnetic semiconductors were successfully prepared using hydrothermal method. A single-phase with an orthorhombic structure for all the samples was concluded from XRD. The average crystallite size, strain, and dislocation densities were measured and they are well-matched with literature values. The surface morphology was observed by SEM, which revealed the 3D flower-like morphology that turned to small rod-like morphology for increasing compositions of Co. HR-TEM results are consistent with the SEM observations and revealed the presence of grain boundaries and dislocations. The optical studies obtained from UV-Vis-NIR DRS spectroscopy illustrate that both direct and indirect bandgaps decrease as the Co concentration increases up to x=0.05 after that they increased for x=0.10 and again decreased for x=0.20. The XPS studies confirmed the valence state of Sn, Se, and Co for the sample $Co_{0.10}Sn_{0.90}Se$. The room temperature dielectric studies revealed that

$Co_{0.05}Sn_{0.95}Se$ showed high value of dielectric constant and ac conductivity. At low frequencies, the $Co_{0.05}Sn_{0.95}Se$ obtained the highest dielectric constant and dielectric losses at 523 K. The Co doping and change in temperature showed a significant effect on the AC conductivity and the $Co_{0.05}Sn_{0.95}Se$ sample exhibited the highest AC conductivity value at 523K. The CBH model is a possible mechanism for the charge carriers of the hopping mechanism, based on the calculated value of the parameter 's'. Electrical modulus studies revealed the impact of grain boundary effects, and all Co-doped SnSe samples showed non-Debye type relaxation. The findings suggest that the material could be used in microelectronic, capacitive storage electro-optic, and frequency-related devices. VSM measurements have described the ferromagnetism revealed by all the $Co_xSn_{1-x}Se$ SnSe at room temperature, which suggests that these dilute magnetic semiconductors have applications in spintronic devices.

The $Fe_xSn_{1-x}Se$ diluted magnetic semiconductors were successfully prepared using hydrothermal method. The morphological studies from SEM and TEM showed layered like morphology that turned to small ball like morphology for increasing compositions of Fe. The optical studies obtained from UV-Vis-NIR DRS spectroscopy illustrate that both direct and indirect bandgaps decrease as the Fe concentration increases up to x=0.05 after that they increased for x=0.10 and again decreased for x=0.20. The XPS studies confirmed the valence state of Sn, Se, and Fe for the sample $Fe_{0.10}Sn_{0.90}Se$. The room temperature and temperature dependent dielectric studies revealed that maximum value of dielectric constant and ac conductivity is obtained at x=0.05. Temperature dependent dielectric studies exhibited large value of dielectric constant and ac conductivity for x=0.05. VSM measurements have described the ferromagnetism revealed by all the $Fe_xSn_{1-x}Se$ SnSe at room temperature, which suggests that these dilute magnetic semiconductors can also have applications in spintronic devices.

7.3 Future scope of work

In the present work we have investigated the effect of alkali and transition metal doped SnSe for dielectric and magnetic properties. Other transition metals like Ni and Mn can be doped into SnSe and their dielectric and magnetic studies will be undertaken. Synthesis and characterization of other IV-VI metal chalcogenide materials such as SnS, PbS, PbSe and SnTe using hydrothermal method can be carried out for dielectric and magnetic device applications. Doping of transition metals (Co. Ni, Fe and Mn) into the above mentioned IV-VI metal chalcogenides can be carried out. Other transition metals

like Ni and Mn can be doped into SnSe and their dielectric and magnetic studies will be undertaken.

References

[1] X. Shi, X. Tao, J. Zou, Z. Chen, High-Performance Thermoelectric SnSe : Aqueous Synthesis , Innovations , and Challenges, Adv. Sci. 1902923 (2020). https://doi.org/10.1002/advs.201902923.

[2] R.M. Aspan, N. Fatima, R. Mohamed, U. Syafiq, M.A. Ibrahim, An overview of the strategies for tin selenide advancement in thermoelectric application, Micromachines. 12 (2021). https://doi.org/10.3390/mi12121463.

[3] H.C. Hsueh, J.X. Li, C.H. Ho, Polarization Photoelectric Conversion in Layered GeS, Adv. Opt. Mater. 6 (2018) 1–11. https://doi.org/10.1002/adom.201701194.

[4] V.R. Minnam Reddy, S. Gedi, B. Pejjai, C. Park, Perspectives on SnSe-based thin film solar cells: A comprehensive review, J. Mater. Sci. Mater. Electron. 27 (2016) 5491–5508. https://doi.org/10.1007/s10854-016-4563-9.

[5] F. Davitt, K. Stokes, T.W. Collins, M. Roldan-gutierrez, F. Robinson, H. Geaney, S. Biswas, S.L.Y. Chang, K.M. Ryan, G. Reid, J.D. Holmes, 2D SnSe Nanonetworks; Growth and Evaluation for Li-ion Battery Applications, ACS Appl. Energy Mater. (2020). https://doi.org/10.1021/acsaem.0c00776.

[6] D. Ni, Y. Chen, X. Yang, C. Liu, K. Cai, Microwave-assisted synthesis method for rapid synthesis of tin selenide electrode material for supercapacitors, J. Alloys Compd. 737 (2018) 623–629. https://doi.org/10.1016/j.jallcom.2017.12.037.

[7] A.G. Shiravizadeh, R. Yousefi, S.M. Elahi, S.A. Sebt, Effects of annealing atmosphere and rGO concentration on the optical properties and enhanced photocatalytic performance of SnSe/rGO nanocomposites, Phys. Chem. Chem. Phys. 19 (2017) 18089–18098. https://doi.org/10.1039/c7cp02995k.

[8] P. Mandal, B. Show, S.T. Ahmed, D. Banerjee, A. Mondal, Visible-light active electrochemically deposited tin selenide thin films: synthesis, characterization and photocatalytic activity, J. Mater. Sci. Mater. Electron. 31 (2020) 4708–4718. https://doi.org/10.1007/s10854-020-03027-0.

[9] K. Patel, G. Solanki, K. Patel, V. Pathak, P. Chauhan, Investigation of optical ,

electrical and optoelectronic properties of SnSe crystals, Eur. Phys. J. B. (2019).

[10] K.A. Campbell, C.M. Anderson, Phase-change memory devices with stacked Ge-chalcogenide/Sn-chalcogenide layers, Microelectronics J. 38 (2007) 52–59. https://doi.org/10.1016/j.mejo.2006.09.012.

[11] N.R. Mathews, Electrodeposited tin selenide thin films for photovoltaic applications, Sol. Energy. 86 (2012) 1010–1016. https://doi.org/10.1016/j.solener.2011.06.012.

[12] T. Arokiya Mary, A.C. Fernandez, P. Sakthivel, J.G.M. Jesudurai, A study on the role of surfactant on the layered growth of SnSe2 for electrical applications, J. Mater. Sci. Mater. Electron. 27 (2016) 11041–11048. https://doi.org/10.1007/s10854-016-5220-z.

[13] L.C. Gomes, A. Carvalho, Electronic and optical properties of low-dimensional group-IV monochalcogenides, J. Appl. Phys. 128 (2020). https://doi.org/10.1063/5.0016003.

[14] Y. Li, F. Li, J. Dong, Z. Ge, F. Kang, J. He, H. Du, B. Li, J.F. Li, Enhanced mid-temperature thermoelectric performance of textured SnSe polycrystals made of solvothermally synthesized powders, J. Mater. Chem. C. 4 (2016) 2047–2055. https://doi.org/10.1039/c5tc04202j.

[15] M. Kumar, S. Rani, Y. Singh, K.S. Gour, V.N. Singh, Tin-selenide as a futuristic material: properties and applications, RSC Adv. 11 (2021) 6477–6503. https://doi.org/10.1039/d0ra09807h.

[16] C. Zhang, H. Ouyang, R. Miao, Y. Sui, H. Hao, Y. Tang, J. You, X. Zheng, Z. Xu, X. Cheng, T. Jiang, Anisotropic Nonlinear Optical Properties of a SnSe Flake and a Novel Perspective for the Application of All-Optical Switching, Adv. Opt. Mater. 7 (2019). https://doi.org/10.1002/adom.201900631.

[17] D.I. Bletskan, Phase Equilibrium in Binary Systems AIVBVI. Part 3. Systems Sn—Chalcogenides, ChemInform. 37 (2006). https://doi.org/10.1002/chin.200630244.

[18] A.A. Ward, Dielectric materials for advanced applications, (2016) 51. https://doi.org/10.13140/RG.2.1.3481.5600.

[19] R.G. Geyer, Dielectric Characterization and Reference Materials, (n.d.).

[20] Fundamentals of Magnetism, n.d.

[21] C.O.M. Poun, M.A.N. Gan, Interaction between the d-Shells in the Transition Metals., 599 (1950).

[22] B. Torrance, T „, 1412 (1970).

[23] J.M.D. Coey, M. Venkatesan, C.B. Fitzgerald, T. College, Donor impurity band exchange in dilute ferromagnetic oxides, (2005) 173–179. https://doi.org/10.1038/nmat1310.

[24] S. Sakrani, Z. Othaman, K. Deraman, Y. Wahab, A study on a.c properties of tin selenide thin films, J. Fiz. UTM. 3 (2008) 99–108.

[25] P.M. P. SUGUNA, D. MANGALAMJ, SA. K. NARAYANDASS, Structure , Composition , Dielectric , and AC Conduction Studies on Tin Selenide Films, Phys. Status Sol. 405 (1996).

[26] G.K. Solanki, N.N. Gosai, K.D. Patel, Structural, Optical and Dielectric Properties of Tin Selenide Nanoparticles Prepared by Aqueous Solution Method, Res. J. Chem. Sci. 5 (2015) 1–5. http://www.isca.in/rjcs/Archives/v5/i3/1.ISCA-RJCS-2014-117.php.

[27] D. Properties, T. Crystals, G.K. Solanki, K.D. Patel, N.N. Gosai, P.R. B, Growth and Dielectric Properties of SnSe 0.5 Te 0.5 Crystals, Res. J. Chem. Sci. 2 (2012) 43–48.

[28] S. Suresh, C.G. Centre, Wet chemical synthesis of Tin Sulfide nanoparticles and its characterization Structural studies, 9 (2014) 380–385. https://doi.org/10.5897/IJPS2014.4176.

[29] B. Parveen, M. Hassan, S. Atiq, S. Riaz, S. Naseem, S. Zaman, Structural, dielectric and ferromagnetic properties of nano-crystalline Co-doped SnS, J. Mater. Sci. 52 (2017) 7369–7381. https://doi.org/10.1007/s10853-017-0972-2.

[30] B. Parveen, M. Hassan, S. Riaz, S. Atiq, S. Naseem, M. Irfan, M.F. Iqbal, Investigation of physical properties of SnS:Fe diluted magnetic semiconductor nanoparticles for spintronic applications, J. Magn. Magn. Mater. 460 (2018) 111–119. https://doi.org/10.1016/j.jmmm.2018.03.022.

[31] B. Parveen, M. Hassan, S. Atiq, S. Riaz, S. Naseem, M.A. Toseef, Structural and dielectric study of nano-crystalline single phase Sn1−xNixS (xNi=0–10%) showing room temperature ferromagnetism, Prog. Nat. Sci. Mater. Int. 27 (2017) 303–310. https://doi.org/10.1016/j.pnsc.2017.04.007.

[32] A.A. Azab, A.A. Ward, G.M. Mahmoud, E.M. El-Hanafy, H. El-Zahed, F.S. Terra, Structural and dielectric properties of prepared PbS and PbTe nanomaterials, J. Semicond. 39 (2018). https://doi.org/10.1088/1674-4926/39/12/123006.

[33] H. Zhou, G. Zhou, Q. Du, J. Zhou, Surfactant-assisted re fl ux synthesis of PbS nanostructures and their properties, (2012). https://doi.org/10.1557/jmr.2012.339.

[34] M.F. Afsar, A. Jamil, M.A. Rafiq, Ferroelectric, dielectric and electrical behavior of two-dimensional lead sulphide nanosheets, Adv. Nat. Sci. Nanosci. Nanotechnol. 8 (2017). https://doi.org/10.1088/2043-6254/aa8b3d.

[35] Effect of very fine nanoparticle and temperature on the electric and dielectric properties of MC-PbS polymer nanocomposite films _ Elsevier Enhanced Reader.pdf, (n.d.).

[36] A. Sultan, M. Ahmad, Z. Imran, S.S. Batool, K. Rasool, S. Hassan, M.A. Rafiq, Tailoring structural, dielectric and optical effects of PbS nanosheets with Ni doping, Phys. B Condens. Matter. 602 (2021). https://doi.org/10.1016/j.physb.2020.412571.

[37] M. Ahmad, M.A. Rafiq, M.M. Hasan, M. Ahmad, M.A. Rafiq, M.M. Hasan, Transport characteristics and colossal dielectric response of cadmium sulfide nanoparticles Transport characteristics and colossal dielectric response of cadmium sulfide nanoparticles, 133702 (2013). https://doi.org/10.1063/1.4823810.

[38] M. Ahmad, M.A. Rafiq, K. Rasool, Z. Imran, M.M. Hasan, Dielectric and transport properties of bismuth sulfide prepared by solid state reaction method, J. Appl. Phys. 113 (2013). https://doi.org/10.1063/1.4781004.

[39] A. Jamil, S.S. Batool, F. Sher, M.A. Rafiq, Determination of density of states, conduction mechanisms and dielectric properties of nickel disulfide nanoparticles, AIP Adv. 6 (2016). https://doi.org/10.1063/1.4952966.

[40] S. Liang, J. Xu, J.G. Noudem, H. Wang, X. Tan, G.Q. Liu, H. Shao, B. Yu, S. Yue, J. Jiang, Thermoelectric properties of textured polycrystalline Na0.03Sn0.97Se enhanced by hot deformation, J. Mater. Chem. A. 6 (2018) 23730–23735. https://doi.org/10.1039/c8ta07783e.

[41] H. Leng, M. Zhou, J. Zhao, Y. Han, L. Li, The thermoelectric performance of

anisotropic SnSe doped with Na †, RSC Adv. 6 (2016) 9112–9116. https://doi.org/10.1039/C5RA19469E.

[42] E.K. Chere, Q. Zhang, K. Dahal, F. Cao, J. Mao, Z. Ren, Studies on thermoelectric figure of merit of Na-doped p-type polycrystalline SnSe, J. Mater. Chem. A. 4 (2016) 1848–1854. https://doi.org/10.1039/c5ta08847j.

[43] Z. Yang, W. Chen, C. Liu, Synthesis and Electronic Transport of Hydrothermally Synthesized p -Type Na-Doped SnSe, J. Electron. Mater. (2016) 1–5. https://doi.org/10.1007/s11664-016-5084-2.

[44] F. Chu, Q. Zhang, Z. Zhou, D. Hou, L. Wang, Enhanced thermoelectric and mechanical properties of Na-doped polycrystalline SnSe thermoelectric materials via CNTs dispersion, J. Alloys Compd. 741 (2018) 756–764. https://doi.org/10.1016/j.jallcom.2018.01.178.

[45] N. Xin, Y. Li, G. Tang, L. Shen, Enhancing thermoelectric performance of K-doped polycrystalline SnSe through band engineering tuning and hydrogen reduction, J. Alloys Compd. 899 (2022) 163358. https://doi.org/10.1016/j.jallcom.2021.163358.

[46] C.C. Lin, D. Ginting, G. Kim, K. Ahn, J.S. Rhyee, High thermoelectric performance and low thermal conductivity in K-doped SnSe polycrystalline compounds, Curr. Appl. Phys. 18 (2018) 1534–1539. https://doi.org/10.1016/j.cap.2018.09.011.

[47] Y.X. Chen, Z.H. Ge, M. Yin, D. Feng, X.Q. Huang, W. Zhao, J. He, Understanding of the Extremely Low Thermal Conductivity in High-Performance Polycrystalline SnSe through Potassium Doping, Adv. Funct. Mater. 26 (2016) 6836–6845. https://doi.org/10.1002/adfm.201602652.

[48] K. Zhang, K. Deng, J. Li, H. Zhang, W. Yao, J. Denlinger, Y. Wu, W. Duan, S. Zhou, Widely tunable band gap in a multivalley semiconductor SnSe by potassium doping, Phys. Rev. Mater. 2 (2018). https://doi.org/10.1103/PhysRevMaterials.2.054603.

[49] T.R. Wei, G. Tan, X. Zhang, C.F. Wu, J.F. Li, V.P. Dravid, G.J. Snyder, M.G. Kanatzidis, Distinct Impact of Alkali-Ion Doping on Electrical Transport Properties of Thermoelectric p-Type Polycrystalline SnSe, J. Am. Chem. Soc. 138 (2016) 8875–8882. https://doi.org/10.1021/jacs.6b04181.

[50] M. Luo, Y.E. Xu, First-Principles Investigations on Magnetic and Optical Properties of Transition-Metal Dopants in β-SnSe, J. Supercond. Nov. Magn. 33 (2020) 2801–2807. https://doi.org/10.1007/s10948-020-05540-z.

[51] J. Lu, L. Guo, G. Xiang, Y. Nie, X. Zhang, Electronic and Magnetic Tunability of SnSe Monolayer via Doping of Transition-Metal Atoms, J. Electron. Mater. 49 (2020) 290–296. https://doi.org/10.1007/s11664-019-07701-w.

[52] M. Luo, Y. Xu, Y. Shen, Magnetic properties of SnSe monolayer doped by transition-metal atoms: A first-principle calculation, Results Phys. 17 (2020). https://doi.org/10.1016/j.rinp.2020.103126.

[53] X.L. Wang, W. Li, T.X. Wang, X.Q. Dai, Modulation of magnetic properties of bilayer SnSe with transition-metals doping in the interlayer, Phys. E Low-Dimensional Syst. Nanostructures. 75 (2016) 106–111. https://doi.org/10.1016/j.physe.2015.09.020.

[54] S. Isber, X. Gratens, Crystal growth and magnetic properties of tin selenide-doped europium Sn1-xEuxSe, J. Magn. Magn. Mater. 322 (2010) 1113–1116. https://doi.org/10.1016/j.jmmm.2009.09.015.

[55] S. Liu, M. Lan, G. Li, Y. Yuan, B. Jia, Q. Wang, Co dopant drives surface smooth and improves power factor of evaporated SnSe films, Ceram. Int. 46 (2020) 16578–16582. https://doi.org/10.1016/j.ceramint.2020.03.229.

[56] B.E. Warren, X-ray diffraction methods, J. Appl. Phys. 12 (1941) 375–383. https://doi.org/10.1063/1.1712915.

[57] C.G. Pope, X-ray diffraction and the bragg equation, J. Chem. Educ. 74 (1997) 129–131. https://doi.org/10.1021/ed074p129.

[58] K. Assili, O. Gonzalez, K. Alouani, X. Vilanova, Structural, morphological, optical and sensing properties of SnSe and SnSe2 thin films as a gas sensing material, Arab. J. Chem. 13 (2020) 1229–1246. https://doi.org/10.1016/j.arabjc.2017.10.004.

[59] M. de Assumpcão Pereira-da-Silva, F.A. Ferri, Scanning Electron Microscopy, in: Nanocharacterization Tech., Springer, Boston, MA, Boston, MA, 2017: pp. 1–35. https://doi.org/10.1016/B978-0-323-49778-7.00001-1.

[60] P. Echlin, Handbook of Sample Preparation for Scanning Electron Microscopy and X-Ray Microanalysis, Springer US, 2009. https://doi.org/10.1007/978-0-387-

85731-2.

[61] G.R. Chalmers, R.M. Bustin, I.M. Power, Characterization of gas shale pore systems by porosimetry, pycnometry,surfacearea,andfield emission scanning electron microscopy/ transmission electron microscopy image analyses: Examples from the Barnett, Woodford, Haynesville, Marcellus,andDoig units, Am. Assoc. Pet. Geol. Bull. 96 (2012) 1099–1119. https://doi.org/10.1306/10171111052.

[62] J.M. Bonard, K.A. Dean, B.F. Coll, C. Klinke, Field Emission of Individual Carbon Nanotubes in the Scanning Electron Microscope, Phys. Rev. Lett. 89 (2002) 197602. https://doi.org/10.1103/PhysRevLett.89.197602.

[63] J. Ayache, L. Beaunier, J. Boumendil, G. Ehret, D. Laub, Sample Preparation Handbook for Transmission Electron Microscopy, Springer New York, 2010. https://doi.org/10.1007/978-0-387-98182-6.

[64] C.J. Powell, P.E. Larson, Quantitative surface analysis by X-ray photoelectron spectroscopy, Appl. Surf. Sci. 1 (1978) 186–201. https://doi.org/10.1016/0378-5963(78)90014-4.

[65] J.D. Andrade, X-ray Photoelectron Spectroscopy (XPS), in: Surf. Interfacial Asp. Biomed. Polym., Springer, Boston, MA, Boston, MA, 1985: pp. 105–195. https://doi.org/10.1007/978-1-4684-8610-0_5.

[66] S. Oswald, X-Ray Photoelectron Spectroscopy in Analysis of Surfaces, in: Encycl. Anal. Chem., John Wiley & Sons, Ltd, 2013. https://doi.org/10.1002/9780470027318.a2517.pub2.

[67] A. Escobedo-Morales, I.I. Ruiz-López, M. de L. Ruiz-Peralta, L. Tepech-Carrillo, M. Sánchez-Cantú, J.E. Moreno-Orea, Automated method for the determination of the band gap energy of pure and mixed powder samples using diffuse reflectance spectroscopy, Heliyon. 5 (2019). https://doi.org/10.1016/j.heliyon.2019.e01505.

[68] A. Radoń, D. Łukowiec, M. Kremzer, J. Mikuła, P. Włodarczyk, Electrical conduction mechanism and dielectric properties of spherical shaped Fe3O4 nanoparticles synthesized by co-precipitation method, Materials (Basel). 11 (2018). https://doi.org/10.3390/ma11050735.

[69] P. Oruç, N. Turan, Y. Demirölmez, A. Seçkin, Ş. Çavdar, H. Koralay, N.

Tuğluoğlu, AC conductivity, dielectric and electrical modulus studies of bulk Zn0.95Co0.05O ceramic, J. Mater. Sci. Mater. Electron. 32 (2021) 15837–15850. https://doi.org/10.1007/s10854-021-06136-6.

[70] T.R. Wei, C.F. Wu, X. Zhang, Q. Tan, L. Sun, Y. Pan, J.F. Li, Thermoelectric transport properties of pristine and Na-doped SnSe1-xTex polycrystals, Phys. Chem. Chem. Phys. 17 (2015) 30102–30109. https://doi.org/10.1039/c5cp05510e.

[71] P. Boudjouk, D.J. Seidler, D. Grier, G.J. McCarthy, Benzyl-substituted tin chalcogenides. Efficient single-source precursors for tin sulfide, tin selenide, and Sn(SxSe1-x) solid solutions, Chem. Mater. 8 (1996) 1189–1196. https://doi.org/10.1021/cm9504347.

[72] R. Shakoury, A. Arman, Ş. Ţălu, D. Dastan, C. Luna, Stereometric analysis of -TiO 2 thin films deposited by electron beam ion assisted, Opt. Quantum Electron. 52 (2020) 1–12. https://doi.org/10.1007/s11082-020-02388-4.

[73] N. Ghobadi, F. Hafezi, S. Naderi, F. Amiri, C. Luna, A. Arman, Microstructure and Optical Bandgap of Cobalt Selenide Nanofilms, 53 (2019) 1751–1758. https://doi.org/10.1134/S1063782619130074.

[74] S. Meti, S. Prutvi, H.M.R. Rahman, U.K. Bhat, A single step unique microstructural growth of porous colossal dielectric constant titanium oxide, Appl. Phys. A. 125 (2019) 1–10. https://doi.org/10.1007/s00339-019-2477-0.

[75] R. Shakoury, S. Rezaee, F. Mwema, C. Luna, thin films deposited by electron gun method, (2020).

[76] K. Khurana, N. Jaggi, Modifications in structural, optical, and dielectric properties of CdS nanostructures: role of different solvents, J. Mater. Sci. Mater. Electron. 31 (2020) 10334–10346. https://doi.org/10.1007/s10854-020-03581-7.

[77] M.G. Todd, F.G. Shi, Molecular Basis of the Interphase Dielectric Properties of Microelectronic and Optoelectronic Packaging Materials, IEEE Trans. Components Packag. Technol. 26 (2003) 667–672. https://doi.org/10.1109/TCAPT.2003.817862.

[78] K.W. Wagner, Zur Theorie der unvollkommenen Dielektrika, Ann. Phys. 345 (1913) 817–855. https://doi.org/10.1002/andp.19133450502.

[79] B. Cai, J. Li, H. Sun, P. Zhao, F. Yu, L. Zhang, D. Yu, Y. Tian, B. Xu, Sodium

doped polycrystalline SnSe: High pressure synthesis and thermoelectric properties, J. Alloys Compd. 727 (2017) 1014–1019. https://doi.org/10.1016/j.jallcom.2017.08.223.

[80] T. Šalkus, E. Kazakevičius, J. Banys, M. Kranjčec, A.A. Chomolyak, Y.Y. Neimet, I.P. Studenyak, Influence of grain size effect on electrical properties of Cu 6PS5I superionic ceramics, Solid State Ionics. 262 (2014) 597–600. https://doi.org/10.1016/j.ssi.2013.10.040.

[81] A. Bagum, M.B. Hossen, F.U.Z. Chowdhury, Complex impedance and electric modulus studies of Al substituted Co0.4Cu0.2Zn0.4Al xFe2-xO4 ferrites prepared by auto combustion technique, Ferroelectrics. 494 (2016) 19–32. https://doi.org/10.1080/00150193.2016.1137467.

[82] M. Mumtaz, M. Naveed, S. Akhtar, M. Imran, M.N. Khan, Complex Electric Modulus Spectroscopy of (MnFe2O4)x/CuTl-1223 Nanoparticles-Superconductor Composites, J. Supercond. Nov. Magn. 31 (2018) 2691–2698. https://doi.org/10.1007/s10948-017-4547-x.

[83] M. Nerella, M.B. Suresh, S. Bathulapalli, Effect of Na doping on structural, optical, and dielectric properties of SnSe polycrystals, J. Mater. Sci. Mater. Electron. 32 (2021) 4347–4362. https://doi.org/10.1007/s10854-020-05177-7.

[84] Z.H. Ge, D. Song, X. Chong, F. Zheng, L. Jin, X. Qian, L. Zheng, R.E. Dunin-Borkowski, P. Qin, J. Feng, L.D. Zhao, Boosting the Thermoelectric Performance of (Na,K)-Codoped Polycrystalline SnSe by Synergistic Tailoring of the Band Structure and Atomic-Scale Defect Phonon Scattering, J. Am. Chem. Soc. 139 (2017) 9714–9720. https://doi.org/10.1021/jacs.7b05339.

[85] B. Pejjai, V.R. Minnam Reddy, K. Seku, M.R. Pallavolu, C. Park, Eco-friendly synthesis of SnSe nanoparticles: Effect of reducing agents on the reactivity of a Se-precursor and phase formation of SnSe NPs, New J. Chem. 42 (2018) 4843–4853. https://doi.org/10.1039/c7nj04547f.

[86] R. Rajesh, S. John Ethilton, K. Ramachandran, K. Ramesh Kumar, S.S. Vadla, I.B. Shameem Banu, Effect of Sr doping on the magnetocapacitive effect in Bi0.6Sr0.4FeO3−δ polycrystalline ceramics, Appl. Phys. A Mater. Sci. Process. 124 (2018) 0. https://doi.org/10.1007/s00339-018-1941-6.

[87] F.K. Butt, M. Mirza, C. Cao, F. Idrees, M. Tahir, M. Safdar, Z. Ali, M. Tanveer, I. Aslam, Synthesis of mid-infrared SnSe nanowires and their optoelectronic

properties, CrystEngComm. 16 (2014) 3470–3473. https://doi.org/10.1039/c4ce00267a.

[88] G. Han, S.R. Popuri, H.F. Greer, J.W.G. Bos, W. Zhou, A.R. Knox, A. Montecucco, J. Siviter, E.A. Man, M. MacAuley, D.J. Paul, W.G. Li, M.C. Paul, M. Gao, T. Sweet, R. Freer, F. Azough, H. Baig, N. Sellami, T.K. Mallick, D.H. Gregory, Facile surfactant-free synthesis of p-type snse nanoplates with exceptional thermoelectric power factors, Angew. Chemie - Int. Ed. 55 (2016) 6433–6437. https://doi.org/10.1002/anie.201601420.

[89] D. Feng, Z.H. Ge, D. Wu, Y.X. Chen, T. Wu, J. Li, J. He, Enhanced thermoelectric properties of SnSe polycrystals via texture control, Phys. Chem. Chem. Phys. 18 (2016) 31821–31827. https://doi.org/10.1039/c6cp06466c.

[90] S. Suresh, C. Arunseshan, Dielectric Properties of Cadmium Selenide (CdSe) Nanoparticles synthesized by solvothermal method, Appl. Nanosci. 4 (2014) 179–184. https://doi.org/10.1007/s13204-012-0186-5.

[91] M.N. Ashiq, S. Irshad, M.F. Ehsan, S. Rehman, S. Farooq, M. Najam-Ul-Haq, A. Zia, Visible-light active tin selenide nanostructures: Synthesis, characterization and photocatalytic activity, New J. Chem. 41 (2017) 14689–14695. https://doi.org/10.1039/c7nj04030j.

[92] M. El-Hagary, E.R. Shaaban, S.H. Moustafa, G.M.A. Gad, The particle size-dependent optical band gap and magnetic properties of Fe-doped CeO 2 nanoparticles, Solid State Sci. 91 (2019) 15–22. https://doi.org/10.1016/j.solidstatesciences.2019.03.005.

[93] H. Yousaf, S.M. Muzaffar, S. Riaz, N. Ahmad, S. Shahzadi, S. Naseem, Tuning of opto-electrical properties of hematite thin films using Co 2+ doping, J. Mater. Sci. Mater. Electron. 30 (2019) 4203–4218. https://doi.org/10.1007/s10854-019-00712-7.

[94] B. Parveen, Mahmood-ul-Hassan, Z. Khalid, S. Riaz, S. Naseem, Room-temperature ferromagnetism in Ni-doped TiO2 diluted magnetic semiconductor thin films, J. Appl. Res. Technol. 15 (2017) 132–139. https://doi.org/10.1016/j.jart.2017.01.009.

[95] K.C. Kumar, N.M. Rao, S. Kaleemulla, G.V. Rao, Structural, optical and magnetic properties of Sn doped ZnS nano powders prepared by solid state reaction, Phys. B Condens. Matter. 522 (2017) 75–80.

https://doi.org/10.1016/j.physb.2017.07.071.

[96] L. Xie, D. He, J. He, SnSe, the rising star thermoelectric material: A new paradigm in atomic blocks, building intriguing physical properties, Mater. Horizons. 8 (2021) 1847–1865. https://doi.org/10.1039/d1mh00091h.

[97] M. Rengachari, A. Bikowski, K. Ellmer, Defect analysis by transmission electron microscopy of epitaxial Al-doped ZnO films grown on (0001) ZnO and a - sapphire by RF magnetron sputtering, J. Appl. Phys. 120 (2016). https://doi.org/10.1063/1.4955064.

[98] E. Bacaksiz, M. Tomakin, M. Altunbaş, M. Parlak, T. Çolakoğlu, Structural, optical and magnetic properties of Cd1-xCo xS thin films prepared by spray pyrolysis, Phys. B Condens. Matter. 403 (2008) 3740–3745. https://doi.org/10.1016/j.physb.2008.07.006.

[99] R. Shakoury, S. Rezaee, F. Mwema, C. Luna, K. Ghosh, S. Jurečka, Ş. Ţălu, A. Arman, A. Grayeli Korpi, Multifractal and optical bandgap characterization of Ta2O5 thin films deposited by electron gun method, Opt. Quantum Electron. 52 (2020) 1–13. https://doi.org/10.1007/s11082-019-2173-5.

[100] S. Kundu, S.I. Yi, C. Yu, Gram-scale solution-based synthesis of SnSe thermoelectric nanomaterials, Appl. Surf. Sci. 459 (2018) 376–384. https://doi.org/10.1016/j.apsusc.2018.07.190.

[101] G. Giribabu, G. Murali, D. Amaranatha Reddy, C. Liu, R.P. Vijayalakshmi, Structural, optical and magnetic properties of Co doped CdS nanoparticles, J. Alloys Compd. 581 (2013) 363–368. https://doi.org/10.1016/j.jallcom.2013.07.082.

[102] B.J. Tan, K.J. Klabunde, P.M.A. Sherwood, XPS Studies of Solvated Metal Atom Dispersed Catalysts. Evidence for Layered Cobalt—Manganese Particles on Alumina and Silica, J. Am. Chem. Soc. 113 (1991) 855–861. https://doi.org/10.1021/ja00003a019.

[103] H.A. Hashem, S. Abouelhassan, Dielectric and thermodynamic properties of tin (II) sulfide thin films, Chinese J. Phys. 43 (2005) 955–966.

[104] H. Şafak, M. Merdan, Ö.F. Yüksel, Dispersion analysis of SnS and SnSe, Turkish J. Phys. 26 (2002) 341–347.

[105] S. Das, A. Dutta, B. Ghosh, S. Banerjee, T.P. Sinha, Dielectric relaxation of

CdSe nanoparticles, J. Phys. Chem. Solids. 75 (2014) 1245–1251. https://doi.org/10.1016/j.jpcs.2014.06.008.

[106] R. V. Barde, K.R. Nemade, S.A. Waghuley, AC conductivity and dielectric relaxation in V 2 O 5 -P 2 O 5 -B 2 O 3 glasses, J. Asian Ceram. Soc. 3 (2015) 116–122. https://doi.org/10.1016/j.jascer.2014.11.006.

[107] S.R. Elliott, A theory of a.c. conduction in chalcogenide glasses, Philos. Mag. 36 (1977) 1291–1304. https://doi.org/10.1080/14786437708238517.

[108] S. Jindal, P. Sharma, Optical and magnetic properties of Dy3+ doped CdS dilute magnetic semiconductor nanoparticles, Mater. Sci. Semicond. Process. 108 (2020) 104884. https://doi.org/10.1016/j.mssp.2019.104884.

[109] M. Alzaid, M. Alwshih, M.N. Abd-el Salam, N.M.A. Hadia, Role of Cu dilute on microstructures, optical, photoluminescence, magnetic and electrical properties of CdS film, Mater. Sci. Semicond. Process. 127 (2021) 105687. https://doi.org/10.1016/j.mssp.2021.105687.

[110] S. Ravishankar, A.R. Balu, S. Balamurugan, K. Usharani, D. Prabha, M. Suganya, J. Srivind, V.S. Nagarethinam, TG–DTA analysis, structural, optical and magnetic properties of PbS thin films doped with Co2+ ions, J. Mater. Sci. Mater. Electron. 29 (2018) 6051–6058. https://doi.org/10.1007/s10854-018-8579-1.

[111] S. Kumar, N.S. Negi, S.C. Katyal, P. Sharma, V. Sharma, Structural, morphological and magnetic analysis of Cd-Co-S dilute magnetic semiconductor nanofilms, J. Magn. Magn. Mater. 367 (2014) 1–8. https://doi.org/10.1016/j.jmmm.2014.04.065.

[112] J. Singh, N.K. Verma, Structural, optical and magnetic properties of cobalt-doped CdSe nanoparticles, Bull. Mater. Sci. 37 (2014) 541–547. https://doi.org/10.1007/s12034-014-0671-4.

[113] N. Sreelekha, K. Subramanyam, D. Amaranatha Reddy, G. Murali, S. Ramu, K. Rahul Varma, R.P. Vijayalakshmi, Structural, optical, magnetic and photocatalytic properties of Co doped CuS diluted magnetic semiconductor nanoparticles, Appl. Surf. Sci. 378 (2016) 330–340. https://doi.org/10.1016/j.apsusc.2016.04.003.

[114] C. Gong, J. Tian, J. Zhang, X. Zhang, L. Yu, Z. Zhang, Effect of processing

conditions on the structure and collective magnetic properties of flowerlike nickel nanostructures, Mater. Res. Bull. 45 (2010) 682–687. https://doi.org/10.1016/j.materresbull.2010.03.002.

[115] H. Chen, C. Xu, C. Chen, G. Zhao, Y. Liu, Flower-like hierarchical nickel microstructures: Facile synthesis, growth mechanism, and their magnetic properties, Mater. Res. Bull. 47 (2012) 1839–1844. https://doi.org/10.1016/j.materresbull.2012.04.079.

[116] A.Y. Kuznetsov, R. MacHado, L.S. Gomes, C.A. Achete, V. Swamy, B.C. Muddle, V. Prakapenka, Size dependence of rutile TiO2 lattice parameters determined via simultaneous size, strain, and shape modeling, Appl. Phys. Lett. 94 (2009) 2–5. https://doi.org/10.1063/1.3139078.

LIST OF PUBLICATIONS

1. **Manjula Nerella**, Suresh, M.B. & Bathulapalli, S. Effect of Na doping on structural, optical, and dielectric properties of SnSe polycrystals. J Mater Sci: Mater Electron 32, 4347–4362 (2021). https://doi.org/10.1007/s10854-020-05177-7
2. **Manjula Nerella**, Suresh, M.B. & Bathulapalli, S. Room temperature ferromagnetism and dielectric properties of cobalt doped Tin Selenide for spintronic application. Physica B: Physics of Condensed matter, 627,2022, 413534. https://doi.org/10.1016/j.physb.2021.413534
3. **Manjula Nerella**, Suresh, M.B. & Bathulapalli, S. Optical and dielectric properties of potassium-doped tin selenide polycrystals. J Mater Sci: Mater Electron 33, 2869-2887 (2022). https://doi.org/10.1007/s10854-021-07574-y
4. **Manjula Nerella,** Nagaraju Macherla, Suresh, M.B. & Bathulapalli, Effect of temperature on dielectric properties of cobalt-doped SnSe polycrystals. J Mater Sci: Mater Electron 34, 120 (2023). https://doi.org/10.1007/s10854-022-09521-x

PAPERS PRESENTED AT NATIONAL AND INTERNATIONAL CONFERENCES

1. **Manjula Nerella** and Sobha Bathulapalli, Study of Structural, Morphological and Optical Properties of nanostructured Sodium doped Tin Selenide crystals in an international conference on "Recent Trends in Material Science and Technology" organised by the Indian Institute of Space Science and Technology, Thiruvananthapuram, Kerala, jointly with Material Society of India, dated from 10th October 2018 to 13th October 2018.
2. **Manjula Nerella** and Sobha Bathulapalli, Study on Optical properties of hydrothermally synthesized Na-doped SnSe polycrystals in an international conference on Advanced Functional Materials and Devices (ICAFMD – 2019) organised by Department of physics NIT Warangal during 26th-28th February, 2019.
3. **Manjula Nerella**, Madireddy Buchi Suresh and Sobha Bathulapalli on Dielectric properties of Na-doped SnSe polycrystals in 65th DAE-Solid State Physics Symposium, Organized by Bhabha Atomic Research Centre, Mumbai, India, during 15th-19th December 2021.
4. **Manjula Nerella**, Nagaraju Macherla, Madireddy Buchi Suresh and Sobha Bathulapalli, Room Temperature Dielectric Properties of Na, K Doped SnSe Polycrystals Prepared By Hydrothermal Method in an International conference on Advances in Chemical and Materials Sciences will be organized by Indian Institute of Chemical Engineers, Calcutta during April 14-16, 2022